

KWAME NKURUMAH UNIVERSITY OF SCIENCE AND TECHNOLOGY, KUMASI

COLLEGE OF SCIENCE

FACULTY OF PHYSICAL AND COMPUTATIONAL SCIENCES

DEPARTMENT OF CHEMISTRY

**SYNTHESES AND CHARACTERIZATION OF BISMUTH AND LEAD
CHALCOGENIDES AND THEIR TERNARY ALLOYS FROM SINGLE SOURCE
PRECURSORS**

A thesis submitted to the Department of Chemistry, Kwame Nkrumah University of Science
and Technology, Kumasi, in partial fulfilment of the requirement for the award of
DOCTOR OF PHILOSOPHY IN INORGANIC CHEMISTRY DEGREE

By

Selina Ama Saah

(B.Sc. Chemistry; MPhil Polymer Science and Technology)

July, 2018

CERTIFICATION OF AUTHORSHIP

I hereby declare that this submission is my own work and that, to the best of my knowledge and belief, it contains no material previously published or written by another person nor material which to a substantial extent has been accepted for the award of any other degree or diploma at Kwame Nkrumah University of Science and Technology, Kumasi or any other educational institution, except where due acknowledgment is made in the thesis.

Selina Ama Saah, (PG1217913) Date

Student Name & ID Signature

Certified by: Prof. Johannes A. M. Awudza Date

Supervisor Signature

Certified by: Dr. Osei Akoto Date

Head of Department Signature

DEDICATION

This work is dedicated to my father, Mr. John Hayford Ahwir of blessed memory.

KNUST



ABSTRACT

This research describes the syntheses and characterization of lead and bismuth chalcogenide nanoparticles and thin films from single source precursors. The single source precursors used were dithiocarbonates, dithio- and diselenoureas, and dithiocarbamates. These precursors were characterized using micro-elemental analyses, thermogravimetric analyses, infrared spectroscopy, nuclear magnetic resonance spectrometry and mass spectrometry. The single crystal structures of bismuth ethyl xanthate and its 1, 10 phenanthroline adduct were determined. The complexes were used for the syntheses of nanoparticles using the hot injection and thin films using the spin coating technique. The as-synthesized nanoparticles and thin films were characterized by X-ray diffraction, scanning electron microscopy, transmission electron microscopy, inductively coupled plasma, energy dispersive X-ray spectroscopy and absorption measurements. Optical band gaps were estimated from the absorption data using Tauc's plots. For the PbS thin films from lead dithiocarbonates, the effect of the alkyl chain length on the morphology and size of the nanocrystals were investigated. There was a change in morphology from cubes to fibrous structures as the alkyl chain changed from ethyl to dodecyl, thus confirming the anisotropic nature of PbS. SEM analyses of Bi₂S₃ thin films also showed a change in shape from nanowires of the bismuth ethyl xanthate to clusters of nanorods (triethylamine, pyridine) and nanodots (1,10 phenanthroline) depending on the choice of nitrogen adduct.

Ternary PbS_xSe_(1-x) thin films deposited from lead xanthate and lead selenourea showed a gradual shift in p-XRD pattern to lower 2 theta values as the mole fraction of the lead selenourea complex in the coating mixture changed from 0 to 1 at an interval of 0.1. Estimated optical band gaps for the parent binaries (PbS and PbSe) and their ternary alloys (PbS_xSe_(1-x)) were all blue shifted from their respective bulk materials. PbS_xSe_(1-x) nanoparticles synthesized from lead thio- and selenourea complexes also exhibited a similar trend in both p-XRD and

optical band gap. EDX analyses confirmed the presence of Pb, S and Se in all the $\text{PbS}_x\text{Se}_{(1-x)}$ alloys formed at different atomic percentages depending on the ratios of the starting materials.

The effects of different concentrations of Bi doping on the optical and structural properties of PbS nanoparticles have been investigated. Morphological studies showed cubes at 50% Bi doping suggesting the incorporation of the Bi atoms into the crystal lattice of the PbS nanoparticles. However, an interplay between rods and cubes were seen at 80% Bi doping. The estimated band gaps for PbS and Bi_2S_3 were 0.72 and 1.94 eV respectively with the alloy having band gaps in between the two binaries.

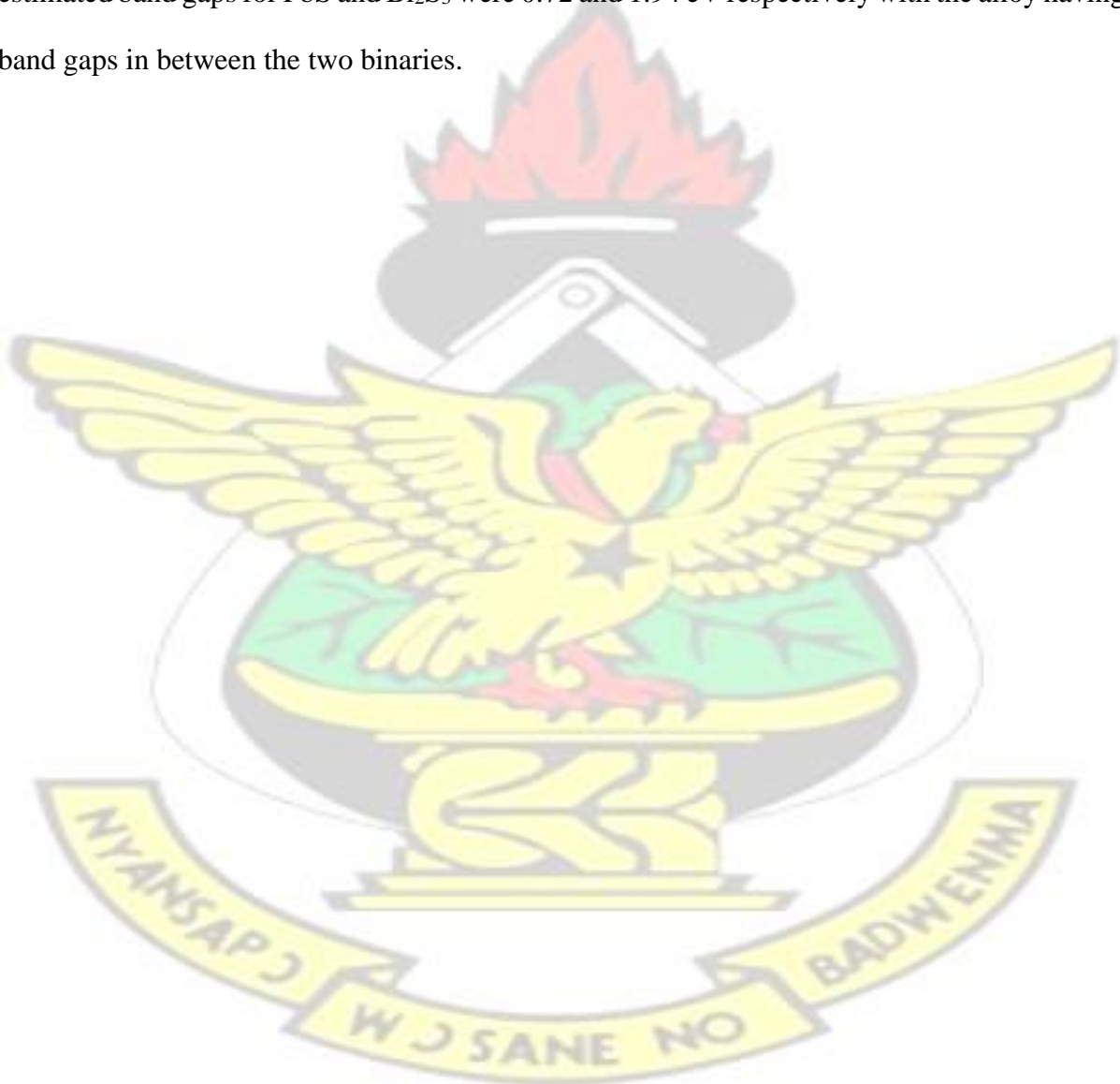


TABLE OF CONTENTS

CERTIFICATION OF AUTHORSHIP	ii
DEDICATION	iii
ABSTRACT.....	iv
TABLE OF CONTENTS	vi
LIST OF FIGURES	x
LIST OF TABLES	xv
LIST OF ABBREVIATIONS	xiv
ACKNOWLEDGEMENTS	xviii
CHAPTER 1: INTRODUCTION	1
1.1 Background	1
1.2 Problem statement and justification	5
1.3 Main aim	7
1.3.1 Specific objectives	7
1.4 Scope of study	7
CHAPTER 2: LITERATURE REVIEW	8
2.1 Semiconductors as inorganic materials	8
2.2 Classification of semiconductors	10
2.2.1 Intrinsic semiconductor	10
2.2.2 Extrinsic semiconductor	11
2.2.3 Direct and indirect band gap semiconductors	13
2.3 Applications of semiconductors	14

2.4 Nanotechnology	15
2.4.1 Origin of nanotechnology	15
2.5 Nanomaterials	16
2.5.1 Approaches to nanomaterial syntheses	17
2.5.1.1 Bottom-up approach	17
2.5.1.2 Top-down approach	18
2.5.2 Properties of nanomaterials	18
2.6 Applications of nanotechnology and nanomaterials	18
2.7 Semiconductor nanocrystals	19
2.7.1 Properties of semiconductor nanocrystals	19
2.7.1.1 Electronic properties	20
2.7.1.2 Optical properties	21
2.7.1.3 Quantum size effect of semiconductor nanocrystals	22
2.8 Lead chalcogenides	23
2.8.1 Lead sulfide nanocrystals	25
2.8.2 Lead selenide nanocrystals	27
2.8.3 Lead telluride nanocrystals	28
2.9 Applications of lead chalcogenides	30
2.10 Ternary lead sulfide selenide ($\text{PbS}_x\text{Se}_{(1-x)}$) nanomaterials	30
2.11 Application of $\text{PbS}_x\text{Se}_{(1-x)}$ nanomaterials.....	33
2.12 Single source precursors (SSPs)	34
2.12.1 Lead dithiocarbonato complexes (xanthates)	35

2.12.2 Lead dichalcogenocarbamate complexes	39
2.12.3 Lead dichalcogenophosphinato complexes	42
2.12.4 Lead dichalcogenoimidodiphosphinato complexes	44
2.12.5 Lead dichalcogenoureato complexes	45
2.12.6 Lead chalcogenobiuret complexes	47
2.13 Synthetic route to nanomaterials preparation using single source precursors	48
2.13.1 Chemical bath deposition	48
2.13.2 Chemical vapour deposition	50
2.13.3 Interface between two immiscible liquids	53
2.13.4 Spin coating	54
2.13.5 Melt reactions	57
2.13.6 Colloidal syntheses	58
2.13.6.1 Hot injection	58
2.13.6.2 Heat up	60
2.13.6.3 Green syntheses of nanoparticles	61
CHAPTER 3: METHODOLOGY	64
3.1 Summary	64
3.2 Syntheses and characterization of ligands and complexes	66
3.2.1 Synthesis of <i>bis</i> (diethyldithiocarbonato)lead(II) complex (1)	66
3.2.2 Synthesis of <i>bis</i> (dipropyldithiocarbonato)lead(II) complex (2)	67

3.2.3	Synthesis of <i>bis</i> (dibutyldithiocarbonato)lead(II) complex (3)	67
3.2.4	Synthesis of <i>bis</i> (dihexyldithiocarbonato)lead(II) complex (4)	67
3.2.5	Synthesis of <i>bis</i> (dioctyldithiocarbonato)lead(II) complex (5)	68
3.2.6	Synthesis of dodecyldithiocarbonato ligand (6)	68
3.2.7	Synthesis of <i>bis</i> (didodecyldithiocarbonato) lead(II) complex (7).....	69
3.2.8	Synthesis of potassium ethylxanthogenate ligand (8)	69
3.2.9	Synthesis of bismuth ethyl xanthate complex (9)	70
3.2.10	Synthesis of tetramethylethylenediamine (TMEDA) adduct of bismuth ethyl xanthate complex (10)	70
3.2.11	Synthesis of triethylamine adduct of bismuth ethyl xanthate complex (11)	71
3.2.12	Synthesis of 1, 10 phenanthroline adduct of bismuth ethyl xanthate complex (12)	71
3.2.13	Synthesis of pyridine adduct of bismuth ethyl xanthate complex (13)	71
3.2.14	Synthesis of <i>N, N</i> -diethyl- <i>N'</i> -naphthoylselenourea ligand (14)	72
3.2.15	Synthesis of <i>bis</i> (<i>N, N</i> -diethyl- <i>N'</i> -naphthoylselenoureato) lead(II) complex (15)	72
3.2.16	Synthesis of <i>N, N</i> -diethyl- <i>N'</i> -naphthoylthiourea ligand (16)	73
3.2.17	Synthesis of <i>bis</i> (<i>N, N</i> -diethyl- <i>N'</i> - naphthoylthioureato) lead(II) complex (17)	74
3.2.18	Synthesis of sodium piperidine dithiocarbamate ligand (18)	74
3.2.19	Synthesis of lead piperidine dithiocarbamate complex (19)	75
3.2.20	Synthesis of bismuth piperidine dithiocarbamate complex (20)	75
3.3	Characterization of complexes	75
3.3.1	Nuclear magnetic resonance spectroscopy (NMR)	75
3.3.2	Melting point	77

3.3.3 Micro-elemental analyses	77
3.3.4 Infrared spectroscopy (IR)	78
3.3.5 Mass spectrometry (MS)	79
3.3.6 Thermogravimetric Analysis (TGA)	80
3.4 Syntheses of metal chalcogenide nanomaterials	82
3.4.1 Deposition of the thin films by spin coating method	82
3.4.2 Syntheses of nanoparticles	83
3.5 Characterization techniques of thin films and nanoparticles	84
3.5.1 Powder X-Ray diffraction (p-XRD)	84
3.5.2 Scanning electron microscopy (SEM)	88
3.5.3 Energy dispersive X-ray spectroscopy analysis (EDX)	90
3.5.4 Transmission electron microscopy (TEM).....	91
3.5.5 UV-VIS-NIR Spectroscopy	92
CHAPTER 4: RESULTS AND DISCUSSIONS ON THE SYNTHESSES AND CHARACTERIZATION OF BINARY LEAD SULFIDE AND BISMUTH SULFIDE THIN FILMS	94
4.1 Summary of results on lead and bismuth sulfides	94
4.2 Syntheses of lead xanthate single source precursors.....	94
4.3 Characterization of lead xanthate single source precursors	95
4.4 Characterization of PbS thin films	100
4.4.1 Powder XRD of PbS thin films	100
4.4.2 Scanning electron microscope (SEM) images of PbS thin films	112
4.4.3 Energy dispersive X-ray (EDX) analyses of PbS thin films	118

4.5 Syntheses of bismuth ethyl xanthate and its N-adduct complexes.....	119
4.6 Characterization of bismuth ethyl xanthate and its N-adduct complexes	120
4.6.1 Crystal structure of complexes (9) and (12)	122
4.7 Characterization of Bi ₂ S ₃ thin films	124
4.7.1 P-XRD characterization of the Bi ₂ S ₃ thin films	124
4.7.2 Scanning electron microscopic analyses of the Bi ₂ S ₃ thin films	126
4.7.3 Energy dispersive X-ray analyses of the Bi ₂ S ₃ thin films	128
CHAPTER 5: RESULTS AND DISCUSSIONS ON THE SYNTHESSES AND CHARACTERIZATION OF TERNARY LEAD CHALCOGENIDES AND BISMUTH DOPED LEAD SULFIDE THIN FILMS AND NANOPARTICLES.....	129
5.1 Summary of results for ternary PbS _x Se _(1-x) and Bi doped PbS nanomaterials	129
5.2 Syntheses of complexes (7) and (15)	129
5.3 Characterization of complexes (7) and (15)	130
5.4 Characterization of PbS _x Se _(1-x) thin films	132
5.4.1 p-XRD analyses of PbS _x Se _(1-x) thin films	132
5.4.2 Scanning electron microscopy images of PbS _x Se _(1-x) thin films	140
5.4.3 Energy dispersive X-ray spectroscopy analyses of PbS _x Se _(1-x) thin films	143
5.4.4 Optical studies of PbS _x Se _(1-x) thin films	145
5.5 Characterization of complexes (15) and (17)	148
5.5.1 Thermal properties of complexes (15) and (17)	149
5.6 Characterization of PbS _x Se _(1-x) nanoparticles	150
5.6.1 Powder-X ray diffraction patterns of PbS _x Se _(1-x) nanoparticles.....	150

5.6.2	Transmission electron microscopy (TEM) images of $\text{PbS}_x\text{Se}_{(1-x)}$ nanoparticles	154
5.6.3	Energy dispersive X-ray (EDX) analyses of the $\text{PbS}_x\text{Se}_{(1-x)}$ nanoparticles	156
5.5.4	Optical properties of the $\text{PbS}_x\text{Se}_{(1-x)}$ nanoparticles	157
5.7	Syntheses of sodium, lead and bismuth piperidine dithiocarbamate complexes.....	158
5.8	Characterization of sodium, lead and bismuth piperidine dithiocarbamate complexes	159
5.8.1	TGA of metal piperidine dithiocarbamate ligand and complexes	159
5.8.2	Fourier transform infrared spectra of metal piperidine dithiocarbamate complexes	160
5.9	Characterization of Bi doped PbS nanoparticles	162
5.9.1	Powder X-ray diffraction (p-XRD) of Bi doped PbS nanoparticles	162
5.9.2	Transmission electron microscopy images of Bi doped PbS nanoparticles	166
5.9.3	Energy dispersive X-ray spectroscopy of Bi doped PbS nanoparticles	168
5.9.4	Inductively coupled plasma analyses of Bi doped PbS nanoparticles	169
5.9.5	Optical properties of Bi doped PbS nanoparticles	170
CHAPTER 6: CONCLUSIONS AND RECOMMENDATIONS		
		174
6.1	Conclusions	174
6.2	Recommendations	176
REFERENCES		177
APPENDIX		
		211

LIST OF FIGURES

Figure 2.1	Molecular orbitals of hydrogen atom (Zhang <i>et al.</i> , 2015)	9
Figure 2.2	Pictorial representation of an intrinsic semiconductor showing equal number of holes and electrons (Zhang <i>et al.</i> , 2015)	11
Figure 2.3	Pictorial representation of pure silicon doped as n-type and p-type semiconductors (Hsiang <i>et al.</i> , 2013)	13

Figure 2.4 Pictorial representation of direct and indirect band gap semiconductors (Hsiang <i>et al.</i> , 2013)	13
2.5 Comparison of material sizes	16
Figure 2.6 Electronic band structure of quantum dots due to the quantum confinement effect (Iqbal <i>et al.</i> , 2012)	20
2.7 Quantum size effect in inorganic materials	23
Figure 2.8 Schematic presentation of spin coating (a) deposition of the solution containing the mixture, (b) and (c) rotation of the support and (d) evaporation of the solvent	55
2.9 Stages in colloidal syntheses	62
Figure 3.1 Pictorial representation of nuclear magnetic resonance spectroscopy	76
Figure 3.2 Pictorial representation of Stuart Scientific melting point apparatus	77
Figure 3.3 Pictorial representation of Flash 2000 elemental analyser	78
Figure 3.4 Pictorial representation of Perkin Elmer FT-IR spectrum two	79
Figure 3.5 Pictorial representation of Waters SQD2 quadrupole mass spectrometer	80
Figure 3.6 Pictorial representation of Perkin-Elmer TGA7	81
Figure 3.7 Pictorial representation of a spin coater.....	83
Figure 3.8 Pictorial representation of hot injection set up	84
Figure 3.9 A photograph of Bruker D8 X-ray diffractometer	88
Figure 3.10 A photograph of Philips XL30 FEG scanning electron microscope	90
Figure 3.11 A photograph of JEOL 1010 transmission electron microscope	92
Figure 3.12 A photograph of Perkin Elmer uv-vis-nir lambda 1050 spectrophotometer.....	93
Figure 4.1 Structures of the lead alkyl xanthate single source precursors	96
Figure 4.2 TGA thermograms of complexes (1), (2), (3), (4), (5) and (7) under nitrogen gas	98
Figure 4.3 p-XRD pattern of PbS thin films obtained from heating complex (1) at (a) 125, (b) 150, (c) 200, (d) 250 and (e) 300 °C	101
Figure 4.4 p-XRD pattern of PbS thin films obtained from heating complex (2) at (a) 125, (b) 150, (c) 200, (d) 250 and (e) 300 °C	102
Figure 4.5 p-XRD pattern of PbS thin films obtained from heating complex (3) at (a) 125, (b) 150, (c) 200, (d) 250 and (e) 300 °C	103
Figure 4.6 p-XRD pattern of PbS thin films obtained from heating complex (4) at (a) 125, (b) 150, (c) 200, (d) 250 and (e) 300 °C	104
Figure 4.7 p-XRD pattern of PbS thin films obtained from heating complex (5) at (a) 125, (b) 150, (c) 200, (d) 250 and (e) 300 °C	105

Figure 4.8 p-XRD pattern of PbS thin films obtained from heating complex (7) at (a) 125, (b) 150, (c) 200, (d) 250 and (e) 300 °C	106
Figure 4.9 A plot of crystallite sizes against heating temperature of the complexes	107
Figure 4.10 A plot of dislocation density against heating temperature of the coated glass slides	108
Figure 4.11 Effect of alkyl chain length on the lattice constant “a” of PbS thin films at 250 °C	109
Figure 4.12 Williamson-Hall plot for PbS thin films obtained from complex (3) at 250 °C	110
Figure 4.13 SEM images of PbS obtained from complex (1) at 20000x magnification by heating coated films at (a) 150, (b) 200, (c) 250, (d) 300 °C and (e) effect of temperature on size	113
Figure 4.14 SEM images of PbS obtained from complex (2) at 20000x magnification by heating coated films at (a) 125, (b) 150, (c) 200, (d) 250 and (e) 300 °C	114
Figure 4.15 SEM images of PbS obtained from complex (3) at 20000x magnification by heating coated films at (a) 125, (b) 150, (c) 200, (d) 250 and (e) 300 °C	115
Figure 4.16 SEM images of PbS obtained from complex (4) at 20000x magnification by heating coated films at (a) 125, (b) 150, (c) 200, (d) 250 and (e) 300 °C	116
Figure 4.17 SEM images of PbS obtained from complex (5) at 20000x magnification by heating coated films at (a) 125, (b) 150, (c) 200, (d) 250 and (e) 300 °C	117
Figure 4.18 SEM images of PbS obtained from complex (7) at 20000x magnification by heating coated films at (a) 125, (b) 150, (c) 200, (d) 250 and (e) 300 °C	118
Figure 4.19 Representative EDX spectrum for PbS thin films	119
Figure 4.20 Structure of bismuth ethyl xanthate complex and its adducts	120
Figure 4.21 X-ray crystal structure of C ₉ H ₁₅ BiO ₃ S ₆ (9)	122
Figure 4.22 X-ray crystal structure of C ₂₁ H ₂₃ BiN ₂ O ₃ S ₆ (12)	124
Figure 4.23 p-XRD pattern of Bi ₂ S ₃ thin film from (a) complex (9) (b) complex (10), (c) complex (11) (d) complex (12) and (e) complex (13)	125
Figure 4.24 SEM images of Bi ₂ S ₃ thin film from (a) complex (9), (b) complex (10), (c) complex (11) (d) complex (12) and (e) complex (13)	127
Figure 5.1 Structures of the single source precursors used in this study (a) <i>bis</i> (didodecylxanthato)lead(II) (7) and (b) <i>bis</i> (<i>N,N</i> -diethyl- <i>N'</i> naphthoylselenoureato) lead (II) (15).	130
Figure 5.2 Thermogravimetric analysis (TGA) profile of complexes (7) and (15)	132
Figure 5.3 Powder XRD patterns of (a) PbS and (b) PbSe thin films deposited by spin coating of complex (7) and (15) respectively following heating for 30 minutes at various temperatures as indicated.	133
Figure 5.4 (a) p-XRD patterns of PbS _x Se _(1-x) obtained by spin coating mixtures of precursors following heating for 30 minutes at 250 °C and (b) expanded form of (a) along the (220) plane with corresponding (triangle) PbSe and (circle) PbS.	135
Figure 5.5 Relation between the cubic lattice constant ‘a’ to the ratio of [Se]/[S+Se]	

in the precursor concentration used for spin coating.	139
Figure 5.6 SEM images of PbS nanoparticles deposited on glass substrate obtained from decomposition of complex (7) at (a) 250, (b) 300, (c) 350 and (d) 400 °C.	140
Figure 5.7 SEM images of PbSe nanoparticles deposited on glass substrate obtained from decomposition of complex (15) at (a) 250, (b) 300, (c) 350 and (d) 400 °C.	142
Figure 5.8 SEM images of PbS _x Se _(1-x) thin films obtained from mixing (7):(15) at (a) 1:0, (b) 0.9:0.1, (c) 0.8:0.2, (d) 0.7:0.3, (e) 0.6:0.4, (f) 0.5:0.5 and (g) 0:1	143
Figure 5.9 Representative EDX spectrum of PbS _x Se _(1-x) thin film prepared at 250 °C	144
Figure 5.10 Percentage Se quantified from EDX as a function of mole fraction of Se in coating mixture	145
Figure 5.11 Absorption spectra of PbS _x Se _(1-x) thin films obtained at mole fraction of complex (15) in coating mixture at 0, 0.1, 0.2, 0.3, 0.4, 0.5 and 1	146
Figure 5.12 Representative Tauc plot of PbS _x Se _(1-x) thin film prepared at 250 °C	147
Figure 5.13 A linear plot band gap against mole fraction of [Se]/[S+Se] in feed precursor	148
Figure 5.14 The chemical structures of the single source precursors used in this study. (a) <i>bis(N, N</i> -diethyl- <i>N'</i> naphthoylthioureato)lead(II) (17) and (b) <i>bis(N, N</i> -diethyl- <i>N'</i> naphthoylselenoureato)lead (II) (15)	148
Figure 5.15 Thermogravimetric analysis (TGA) of complex (15) and (17) at a heating rate of 10 °C min ⁻¹ under nitrogen.	149
Figure 5.16 p-XRD patterns of PbS _x Se _(1-x) nanoparticles synthesized at 200 °C with standard matching lines of PbS (dash) and PbSe (line).	151
Figure 5.17 Effect of selenium mole fraction on crystallite size (left y-axis, circle) and dislocation density (right y-axis, square) of PbS _x Se _(1-x) nanoparticles	153
Figure 5.18 Relation between the cubic lattice constant “a” to the ratio of [Se]/[S+Se] in the injection mixture	154
Figure 5.19 TEM images of PbS _x Se _(1-x) obtained at x values of (a) 0, (b) 0.3, (c) 0.5, (d) 0.8, (e) 1.	156
Figure 5.20 EDX spectrum for PbS _{0.5} Se _{0.5} nanoparticles	157
Figure 5.21 (a) Representative Tauc plot of PbS _x Se _(1-x) nanoparticles and (inset) effect of mole fraction (15) in the injecting mixture on the band gap of the nanoparticles	158
Figure 5.22 TGA thermograms of ligand and complexes, (inset) TGA data	160
Figure 5.23 IR spectra of complex (18), (19) and (20)	161
Figure 5.24 p-XRD pattern of PbS, Bi ₂ S ₃ and Bi doped PbS nanoparticles with (orange) Bi ₂ S ₃ pattern and (blue) PbS pattern	163
Figure 5.25 Effect of % bismuth content in the injection mixture on crystallite size (circles) and dislocation density (squares) of PbS nanoparticles	165
Figure 5.26 TEM images of Bi doped PbS nanoparticles at %Bi doping of (a) 0, (b) 50, (c) 80, (d) 90, (e) 100.	167
Figure 5.27 EDX spectrum of Bi doped PbS nanoparticles	168

Figure 5.28 Absorption spectra of Bi doped PbS nanoparticles	171
Figure 5.29 Representative Tauc plots of PbS and Bi ₂ S ₃ nanoparticles	172
Figure 5.30 Effect of % Bi content in injection mixture on the band gap of Bi doped PbS nanoparticles	173

KNUST

LIST OF TABLES

Table 2.1 Physical properties of lead chalcogenides	25
Table 3.1 List of chemicals and reagents	64
Table 4.1 Effect of alkyl chain length on yield of lead xanthate complexes	95
Table 4.2 TGA data for complexes	99
Table 4.3 Effect of alkyl chain length on the sizes of PbS nanomaterials determined from the p-XRD profile	111
Table 4.4 Effect of temperature on the sizes of PbS nanomaterials determined from the p-XRD profile	111
Table 4.5 Effect of temperature on the strain of PbS nanomaterials determined from W-H plots	112
Table 4.6 Single crystal data for complexes (9) and (12)	123
Table 4.7 Structural parameters of Bi ₂ S ₃ thin films.	126
Table 5.1 Effect of temperature on the lattice constant of as-deposited PbSe and PbS thin films	134
Table 5.2 Effect of temperature on the strain in PbSe and PbS thin films	136
Table 5.3 Effect of selenium mole fraction on crystallite sizes and dislocation density	

of $\text{PbS}_x\text{Se}_{(1-x)}$ thin film	137
Table 5.4 Effect of the mole fraction of complex (15) in the precursor mixture on the strain of $\text{PbS}_x\text{Se}_{(1-x)}$ thin films	138
Table 5.5 Effect of %Bi doping on lattice constant of Bi doped PbS nanoparticles	166
Table 5.6 Percentage incorporation of Bi into the PbS crystal lattice	169

KNUST



LIST OF ABBREVIATIONS

Å	Angstrom
AACVD	Aerosol assisted chemical vapour deposition
APCVD	Atmospheric pressure chemical vapour deposition
Bi	Bismuth
Bi_2S_3	Bismuth sulfide

Calc.	Calculated
CS ₂	Carbon disulfide
CBD	Chemical bath deposition
CVD	Chemical vapour deposition
CDCl ₃	Deuterated chloroform
CdS	Cadmium sulfide
CdSe	Cadmium selenide
CdTe	Cadmium telluride
CIS	Copper indium selenide
CuS	Copper sulfide
°C	Degrees Celsius
DSSCs	Dye sensitized solar cells
E	Chalcogen
eV	Electron volts
E _g	Band gap
EDX	Energy dispersive X-ray spectroscopy
FF	Fill factor
FWHM	Full width at half maximum
GaAs	Gallium arsenide
g	gram

$^1\text{H NMR}$	Proton nuclear magnetic resonance
HOMO	Highest occupied molecular orbital
HSAB	Hard and soft acids and bases
ICDD	International Centre for Diffraction Data
IR	Infrared
ITO	Indium tin oxide
ICP	Inductively coupled plasma
Jsc	Short circuit current
K	Kelvin
LUMO	Lowest unoccupied molecular orbital
MS	Mass spectrometry
mmol	millimole
M^+	Molecular ion peak
MOCVD	Metal – organic chemical vapour deposition
MOT	Molecular orbital theory
OLA	Oleylamine
ODE	Octadecene
Pb	Lead
$\text{Pb}(\text{S}_2\text{CNRR}')_2$	Lead dialkyldithiocarbamate

PbE	Lead chalcogenide
PbSe	Lead selenide
PbS	Lead sulfide
PbS _x Se _(1-x)	Lead sulfur selenide
PbTe	Lead telluride
PCE	Power conversion efficiency
PV	Photovoltaic
p-XRD	Powder X-ray diffraction
QDSSC	Quantum dot sensitized solar cell
QSE	Quantum size effect
S	Sulfur
Sccm	Standard cubic centimetre per minute
Se	Selenium
Si	Silicon
SEM	Scanning electron microscope
SSPs	Single source precursors
TGA	Thermogravimetric analysis
TEM	Transmission electron microscope
TMEDA	Tetramethylethylenediamine
TOP	Trioctylphosphine

TiO₂ Titanium oxide

UV-VIS-NIR Ultra-violet visible near infrared

V_{oc} Open circuit voltage

W-H Williamson Hall

ACKNOWLEDGEMENTS

First and foremost, I would like to thank the Leverhulme Trust - Royal Society Africa Awards and The Royal Society-DFID Africa Capacity Building Schemes for their financial support.

I am grateful to Prof. Johannes A. M. Awudza, Department of Chemistry, KNUST, for his advice and guidance throughout my research and for being an outstanding example of successful research supervisor.

I would like to thank Prof. Paul O'Brien (CBE, FRS), Dr. Chris Wilkins, Dr. Mohammed Azad Malik, Dr. John Waters, Dr. John Warren, Mr. Martin Jennings, Dr. Gary Harrison, Dr. Inigo Vitorica-Yrezabal, Dr. George Whitehead, Dr. Chris Muryn, Mr. Masqood, Dr. Mike Faulkner, Miss Christine Taylor, Mr. Gareth Smith, Dr. Peter Matthews, Dr. David Lewis, Dr. Claire Lydon, Dr. Paul McNaughter and Dr. Nicky Savjani; all of the University of Manchester, United Kingdom. I would also like to thank Prof. Neerish Revaprasadu, Prof. Motaung Tshwafo, Prof Opoku, Dr. Sixberth Mlowe and Mr Johannes Buthelezi; all of the University of Zululand, South Africa, for their encouragement and support in various analyses.

I would like to appreciate the important contributions made by all the lecturers of the Department of Chemistry, KNUST, especially Dr. Nathaniel Owusu Boadi, who collaborated closely with me on many aspects of this research.

To Michael Baah Mensah, Saadatu Shahaban, Getrude Opoku and Musa Seidu Makinka, I say a big thank you for your inspiration.

Finally, I would like to thank my family for their continuing love and support.

KNUST



CHAPTER 1 INTRODUCTION

1.1 Background

One of the major industries which has seen enormous applications of nanotechnology is the energy sector through solar cells (Le Donne *et al.*, 2011). Solar energy is one of the most environmentally benign sources of energy. A solar cell is an electrical device that converts sunlight into electricity by the photovoltaic (PV) effect (Landsberg and Markvart, 2013). Solar cells are among the most promising candidates for alternative energy sources to meet the global energy demand (Le Donne *et al.*, 2011). Their ability to produce electricity at a cheaper cost make them robust, reliable and long lasting. The search for new materials for the PV industry has increased greatly in the last few decades owing to the increasing energy crises faced by most developing countries (Ramasamy *et al.*, 2013). Most of the commercially available solar cells take advantage of the well-studied p-n junction structures for the separation of charge carriers, which are produced by absorption of sunlight (Green and Blakers, 1983). Worldwide, crystalline silicon (Si) cells with thickness ranging from 180 to 300 μm dominate the PV market (Mauk *et al.*, 2013). However, despite the many advantages of this unlimited and clean resource, the first generation solar devices, which are based on Si suffer from high cost of manufacturing and installation although they exhibit the highest power conversion efficiencies (Angmo *et al.*, 2012; Yun *et al.*, 2013). Another challenge is the waste of low-energy photons due to vanishing absorption below the band gap energy (Aeberhard *et al.*, 2012). The high production cost as a result of the sophisticated technologies used to avoid carrier recombination prior to their extraction are all factors that make the Si based solar cells extremely expensive (Yun *et al.*, 2013). This has given rise to the search for new hybrid solar cells which are cost effective and efficient.

These hybrid solar cells comprise of conjugated polymers, nanomaterials, electrodes and substrate (Bhat *et al.*, 2011; Zhao *et al.*, 2014). Due to their advantage of combining the low cost fabrication of organic molecules with the stability of inorganic semiconductors, hybrid solar cells are promising systems for PV application and therefore the subject of intensive work (Gondek, 2014; Yu *et al.*, 2013; Zimmermann *et al.*, 2011). Examples of these hybrid solar cells include tandem (Bolanda *et al.*, 2011; Yang *et al.*, 2012), perovskite (Abdelhady *et al.*, 2016; Dharani *et al.*, 2014), dye sensitized (Oftadeh *et al.*, 2012; Pimanpang *et al.*, 2014), quantum dots sensitized (Choi *et al.*, 2014; Pan *et al.*, 2014) and polymer based solar cells (Freitas *et al.*, 2014; Scarongella *et al.*, 2014). Although these devices are still at the research stage, they have recorded high power conversion efficiencies of about 20 %, which make them good alternatives to the conventional Si based devices (Baik *et al.*, 2009; Freitas *et al.*, 2014; Hao *et al.*, 2012; Yang *et al.*, 2012).

One of the commonly employed nanomaterials in these systems are the lead chalcogenides. At the nanometer region, lead chalcogenides possess similar properties which include large excitonic Bohr radius from *ca.* 20 to 50 nm and narrow bulk band gap ranging from 0.41 to 0.27 eV at 300 K from S to Te (Boadi *et al.*, 2012; Christensen *et al.*, 2016; Dai *et al.*, 2010; Leventis *et al.*, 2010; McNaughton *et al.*, 2016; Preetha and Remadevi, 2014; Sagadevan *et al.*, 2017). These properties offer technological advantages for strong quantum confinement of charge carriers both individually and in excitonic modes (Boadi *et al.*, 2012; Shyju *et al.*, 2012). The ability to produce lead chalcogenide nanoparticles with sizes below their respective Bohr exciton radii allow band gap engineering to access the entire ultraviolet, visible and near infrared spectrum through quantum confinement (Boadi *et al.*, 2016). Solar cells based on binary lead chalcogenides have been reviewed recently (Freitas *et al.*, 2014; Kershaw *et al.*, 2013).

Due to the toxicity issues around the use of lead, bismuth sulfide (Bi_2S_3) nanomaterials have been exploited. Bi_2S_3 is a well-known n-type semiconductor which is chemically stable. Bi_2S_3 has been identified as non-toxic, abundant, biocompatible and environmentally friendly material and hence the interest in investigating into its properties (Ayodhya and Veerabhadram, 2017; Han *et al.*, 2015; Yu *et al.*, 2016). The direct energy band gap of Bi_2S_3 which is between 1.3 and 1.7 eV, lies within the optimal band gap value for a single junction solar cell and therefore makes it a suitable material in the fabrication of photodiode arrays and photovoltaic devices (Arumugam *et al.*, 2017). The properties of Bi_2S_3 make it a suitable material as solar absorbers, compared to the widely used cadmium tellurides, which are toxic and expensive (Song *et al.*, 2016). Bi_2S_3 possesses relatively high carrier mobility ($\mu_e = 200 \text{ cm}^2/\text{Vs}$), enabling full light absorption and photogenerated carrier collection within a film of a few micrometers thick (Song *et al.*, 2016). The bulk Bi_2S_3 has refractive index between 1.3 to 1.9 (Ali *et al.*, 2017) and has been reported to crystallize with a lamellar structure having the Bi_2S_3 units interconnected with weak van der Waals interactions (Liu *et al.*, 2003). Solar cells based on bismuth sulfide have also been reported (Moreno-García *et al.*, 2011; Saha and Pal, 2015; Song *et al.*, 2016).

Ternary alloys are three elements system that either contain a single metal and two chalcogens (example, $\text{PbS}_x\text{Se}_{(1-x)}$) or two metals and one chalcogen (example, $\text{Cd}_{(1-x)}\text{Zn}_x\text{Se}$) (Bagade *et al.*, 2015; Kumar *et al.*, 2010). These are usually formed through doping. Electronic doping of quantum dots have led to several breakthroughs in technological industries (Abdelhady *et al.*, 2016). For example, in the solar cell industries, doping is crucial in the optimization of p-n junctions, which in turn improves charge collection efficiencies. In electronics, doping refers to the process of changing the electrical properties of a semiconductor without altering significantly its crystal phase or structure (Abdelhady *et al.*, 2016). The materials used are usually referred to as ‘dopants or impurities’. Usually, the impurities act as acceptors, donors

or traps which affect the Fermi level and, therefore, its carrier density, carrier mobility and conductivity (Portillo *et al.*, 2017).

The use of metal doped PbS semiconductor nanomaterials are regarded as the most promising candidates for absorbers of low-cost but highly-efficient technological devices (Balasubramanian and Suriyanarayanan, 2013). Common elements that have been used to dope PbS for specific technological applications include calcium for PV devices (Yücel and Yücel, 2017), strontium for PV devices (Yücel and Yücel, 2016), copper for PV devices (Lee *et al.*, 2016; Touati *et al.*, 2016), bismuth for optoelectronic and thermionic devices (Du *et al.*, 2017; Papagiorgis *et al.*, 2017), aluminium for PV devices (Sagadevan *et al.*, 2017; Suganya *et al.*, 2016), iodine for solar cells (Stavrinadis *et al.*, 2017), iron for magnetic imaging devices (Balu *et al.*, 2017), manganese for solar cell devices and magnetic resonance imaging labels (Rajashree *et al.*, 2016; Rimal *et al.*, 2016; Turyanska *et al.*, 2016), nickel for PV application (Kumar *et al.*, 2015; Rajashree and Balu, 2016), gold and antimony for solar cell applications (Patra *et al.*, 2017), cadmium for solar cell (Lee *et al.*, 2016), lithium for multiple exciton generation devices (Portillo *et al.*, 2017) and tin for optoelectronic devices (Lin *et al.*, 2011; Liu *et al.*, 2013). In nanotechnology, these alloys have gained significant attention because their optical as well as structural properties can be tuned. For example, alloys containing Pb, Bi and S atoms have high electrical conductivity as compared to their parent binary PbS and Bi₂S₃ counterparts. These alloyed nanomaterials are usually synthesized using multiple source starting materials and techniques such as chemical vapour deposition (Bente and Anton, 1995), solid state reactions (Ohta *et al.*, 2014), thermal evaporation (Abd-Elkader and Deraz, 2014), and chemical bath deposition (Pring and Etschmann, 2002).

Bismuth is an element with +3 valency which is isoelectronic with Pb²⁺. It is, therefore, able to replace Pb atoms in a crystal lattice (Abdelhady *et al.*, 2016; Stavrinadis *et al.*, 2013). Bi doped PbS is a new class of materials that can be used as absorbers in photovoltaic cells. These

materials are less expensive, therefore promoting their use in the PV industry (Moreno-García *et al.*, 2011). Bi doped PbS materials are less toxic as compared to some widely used solar cell materials, such as GaAs, CdTe and CIS (Balasubramanian and Suriyanarayanan, 2013). The addition of Bi atoms to PbS based solar cell improves the electron-conduction process and the overall power conversion efficiency (Saha *et al.*, 2015). In thermoelectric devices, Bi doped PbS thin films have been used as a cheaper and less toxic substitute to lead sulfides, selenides and tellurides (Du *et al.*, 2017). This conclusion was based on the improved electrical conductivity and decreased thermal conductivity of the Bi doped PbS as compared to the parent binary PbS nanomaterials.

The common chalcogens that have been used to dope PbS include selenium and tellurium (Labidi *et al.*, 2011; Smith *et al.*, 2011). Ternary alloys of the type $\text{PbS}_x\text{Se}_{(1-x)}$ ($0 \leq x \leq 1$) are potentially useful materials that allow band gap engineering in thin films or a particulate form and also the exploitation of size-dependent quantum confinement effects (Lin *et al.*, 2011). PbS and PbSe are closely related in a structural sense; their anionic radii differ by only *ca.* 15 % of each other and the lattice mismatch between the two halite phases is only *ca.* 2 % (Ma *et al.*, 2009), thus, making these two materials compactible at the nanometer region (Akhtar *et al.*, 2011). Perhaps most importantly, $\text{PbS}_x\text{Se}_{(1-x)}$ can yield efficient photovoltaic devices (with power conversion efficiency of about 10 %) through the combination of open circuit voltage (V_{OC}) and short circuit current (J_{SC}) unavailable in either of the parent PbSe or PbS materials (Akhtar *et al.*, 2011; Nam *et al.*, 2012; Yu *et al.*, 2011).

1.2 Problem statement and justification

The depletion of natural resources (example, coal) has greatly affected the energy sector in most developing countries (Bao *et al.*, 2007). It is therefore necessary to develop alternative mechanisms to produce energy that is cost effective and environmentally friendly. Si based

solar cells have been widely used despite their high cost; due to the abundance of sunshine in Ghana and most part of world. Therefore, there is a great need for inexpensive routes for the preparation of advanced materials for the PV industry. Examples of such routes include colloidal syntheses and spin coating (Lee *et al.*, 2014; Xiong *et al.*, 2015). These routes are simple and technically straight forward. By changing the reaction conditions such as temperature and time, the size of the nanocrystals can be varied, which have a direct effect on other properties such as band gap (Lewis *et al.*, 2015). Despite the toxicity of lead based materials, they have been reported as efficient solar absorbers (Tan *et al.*, 2011; Zhao *et al.*, 2010). One approach to reduce the toxicity involved in the material synthesis is through the use of single source precursors (Boadi *et al.*, 2012). Several single source precursors have been used in the syntheses of binary lead chalcogenides, which include lead dithiocarbonates (McNaughten and Saah *et al.*, 2016), lead dichalcogenocarbamates (Romano *et al.*, 2015), lead dichalcogenophosphates (Zyl and Woollins, 2013) and lead dichalcogenophosphinates (Boadi *et al.*, 2016). There are however, only a hand full of reports on the use of these SSPs as starting materials in the syntheses of ternary nanoparticles and thin films. Furthermore, most of the reports on ternary alloys have considered doping percentages less than 10 (Du *et al.*, 2017; Papagiorgis *et al.*, 2017).

This research, therefore, sought to explore the syntheses of nanoparticles and thin films from single source precursors which can be used as absorbers in solar cells. Practically, this research investigated the effects of alkyl chain length of lead alkyl xanthate precursors on the properties such as size and shape of PbS thin films. It also explored the effect of nitrogen adduct on the morphology of Bi₂S₃ thin films. It further investigates the effect of higher dopant (Se and Bi) percentages (up to 90%) on the structural, morphological and optical properties of ternary PbS nanoparticles and thin films.

1.3 Main aim

The main aim of this research was to synthesize and characterize lead and bismuth chalcogenides and ternary alloyed thin films and nanoparticles using different single source precursors.

KNUST

1.3.1 Specific objectives

- (a) To deposit PbS thin films from a series of lead alkyl xanthate complexes using spin coating method.
- (b) To investigate the effect of nitrogen adduct of bismuth ethyl xanthate on the properties of Bi₂S₃ thin films deposited from xanthates using spin coating method.
- (c) To investigate the effect of selenium concentration in selenourea on the properties of PbS_xSe_(1-x) thin films and nanoparticles.
- (d) To investigate the effect of bismuth concentration on the properties of Bi doped PbS nanoparticles from dithiocarbamates using the hot injection method.

1.4 Scope of study

This work is limited to the syntheses and characterization of nanomaterials from single source precursors.

CHAPTER 2 LITERATURE REVIEW

2.1 Semiconductors as inorganic materials

Semiconductor materials are crystalline or amorphous solids with distinct abilities in conducting electricity (Oener *et al.*, 2016). Their properties such as carrier mobility, band gap and resistivity lie in between conductors and insulators (Tominaka *et al.*, 2015). Conductors are materials that have low resistance to the flow of electricity (i.e. good conductors of electricity). These group of materials have partially filled outermost bands. Common examples of conductors are nickel, copper and sodium (Hwang, 2015). Insulators on the other hand are materials that have high resistance to the flow of electricity (bad conductors of electricity). All the valence electrons are strongly bound and therefore are not able to move to the conduction band under the influence of an external electric field (Cheek and Mertens, 1983; Oener *et al.*, 2016). Typical examples are glass, plastics and wool. Semiconductors have properties in between conductors and insulators. Temperature, magnetic field and illumination are some parameters that affect the electrical conductivity of semiconductors (Grätzel, 2001; Hwang, 2015). They have fully filled valence band and an empty conduction band which is separated by a forbidden gap (Gupta and Gupta, 2017). The valence electrons are therefore able to move to the conduction band under the influence of energy (Tominaka *et al.*, 2015), thus, creating a temporary hole in the valence band (Zhang *et al.*, 2015). Silicon, lead sulfide, and cadmium selenide are some common examples of semiconductors.

In order to successfully apply semiconducting materials in opto-electronic devices, their band structures, which is derived from their molecular orbital theory, are of great importance. Molecular orbital theory (MOT) is a method for determining molecular structure in which electrons are not assigned to individual bonds between atoms, but are treated as moving under the influence of the whole molecule (Jain *et al.*, 2008). According to MOT, the linear combination of atomic orbitals (LCAO) approximation results in the formation of molecular

orbitals on the basis of interaction of wave functions (Koca *et al.*, 2012). These molecular orbitals are usually divided into bonding, non-bonding and anti-bonding orbitals. A bonding orbital basically concentrates electron density in the region between a given pair of atoms. The electron density in turn attracts each of the two nuclei toward each other, therefore holding the two atoms together. Electrons in non-bonding orbitals on the other hand do not interact with others and therefore have no contribution to bond strength. Anti-bonding orbitals concentrate electron density on the side of each atom which is farthest from the other atom and tend to pull each of the two nuclei away from each other. This weakens the bond between the two nuclei (Tussupbayev *et al.*, 2015).

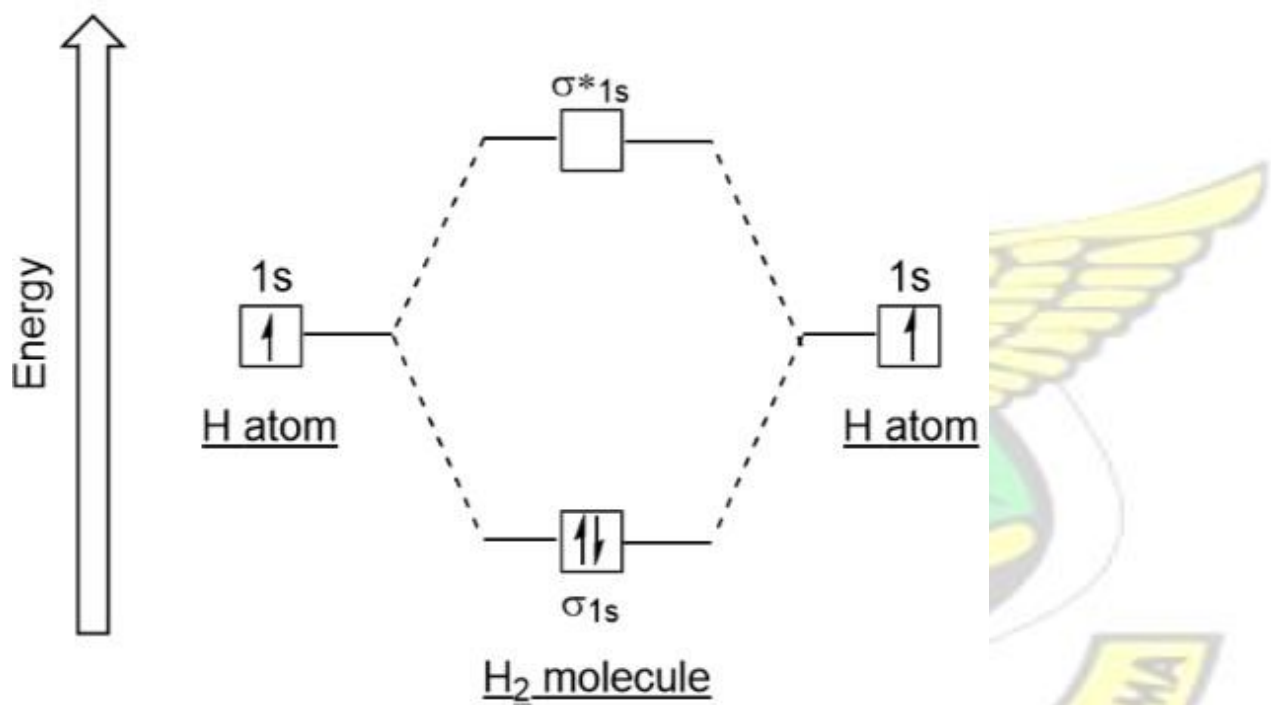


Figure 2.1 Molecular orbitals of hydrogen atom (Zhang *et al.*, 2015)

A typical example is the hydrogen molecule; in which the single “s” electron wave function (usually represented by χ_A and χ_B) interact with all possible linear combinations to generate a bonding and anti-bonding orbital (ψ_1 and ψ_2) respectively.

$$\psi_1 = (\chi_A + \chi_B) \quad \text{Equation 2.1} \quad \psi_2 = (\chi_A - \chi_B) \quad \text{Equation 2.2}$$

From Figure 2.1, the two “s” electrons in the hydrogen molecule occupy the bonding orbital which has the lowest energy whereas the anti-bonding orbital remains unoccupied (Lei *et al.*, 2014). These two orbitals are separated by an energy gap. Usually, when an electron absorb enough energy, it moves from the valence band to the conduction band. Each material has a unique energy for this transition which is measured in electron volt (eV) (Zhang *et al.*, 2015).

2.2 Classification of semiconductors

Semiconductors are grouped into intrinsic and extrinsic semiconductors based on their electronic structures and into direct and indirect semiconductors based on their electronic transitions.

2.2.1 Intrinsic semiconductor

An intrinsic semiconductor is a chemically pure semiconductor material with no impurity (Saha *et al.*, 2015). Although they have poor conductivity, their conductivity increases with temperature. These semiconductors display electrical properties based on their inherent electronic structures. Upon excitation, electrons are promoted from the valence band into the conduction band thereby creating a hole in the valence band. This process is an electron-hole pair creation. They possess equal number of holes (positive carriers) in the valence band and electrons (negative carriers) in the conduction band. This is because each electron produces only one hole (Lei *et al.*, 2014; Oener *et al.*, 2016). A typical example is a pure silicon crystal. Under the influence of an applied energy, both the electrons and holes can move across the material. Both charge carriers contribute to the conduction of electricity (Figure 2.2). These semiconductors have limited applications because of their relatively small number of valence

electrons that obtain enough energy to move to the conduction band. For example, at room temperature, silicon is of the typical order of 10^{10} electrons/cm³ (Shchennikov *et al.*, 2002). One way to increase the number of charge carriers in intrinsic semiconductor is through doping. Doping basically involves the addition of impurities to a material. This process increases the applications of semiconductors since they can be functionalised to various applications (Zhang *et al.*, 2015).

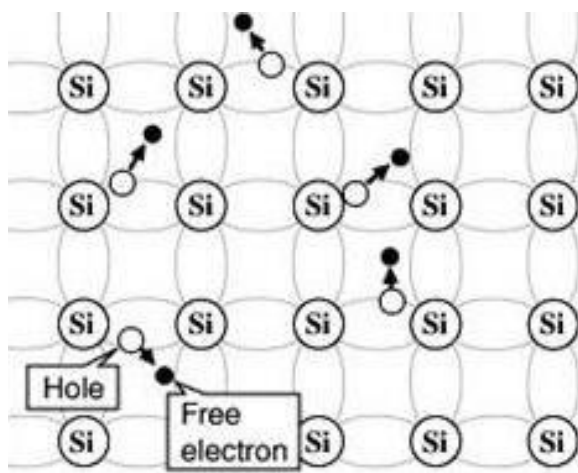


Figure 2.2 Pictorial representation of an intrinsic semiconductor showing equal number of holes and electrons (Zhang *et al.*, 2015)

2.2.2 Extrinsic semiconductor

Extrinsic semiconductors are materials whose electrical properties are based on the presence of impurities (Gupta and Gupta, 2017; Singh and Green, 1981). These impurities are referred to as dopants (Abdelhady *et al.*, 2016). Doping basically involves the addition of specific atoms with different valency to a pure semiconductor to change the electron and hole carrier concentrations at thermal equilibrium (Kang *et al.*, 2013). In an extrinsic semiconductor, the number of electrons and holes are not equal since factors other than electron-hole pair generation is used to produce charge carriers. As such the optical and electrical properties of extrinsic semiconductors depend on the type and amount of dopant introduced into the pure

semiconductor, thus, allowing the engineering of semiconductors for specific applications (Saha *et al.*, 2015). The choice of dopant gives rise to two classifications of extrinsic semiconductors namely, p- and n-type semiconductors (Figure 3). If the donor atoms have more valence electrons (usually the group 5 elements) than the pure semiconductor (example silicon), extra electrons are donated into the conduction band of the pure semiconductor. The extra electrons increase the electron carrier concentration, thereby making it an n-type semiconductor. The 'n' refers to the negative charge of the electrons. The extra non-bond electron remains bound to the pentavalent dopant (Hsiang *et al.*, 2013). When this electron absorbs enough energy, it is promoted to the conduction band, creating a positive charge on the dopant which acts as an immobile hole. At this charge imbalance, Fermi level (a term used to describe the top of the collection of electron energy level at absolute zero temperature) shift closer to the conduction band, thereby creating a new energy level. On the other hand, if the dopant atom has fewer valence electrons than the pure semiconductor, then the dopant accepts electrons. Typical example is the doping of silicon with a trivalent atom such as boron. This results in excess holes in the pure semiconductor, which gives rise to an unequal number of holes and electrons. The increase in the number of hole carriers create a p-type semiconductor. The 'p' denotes the positive charge of the holes (Kosacki *et al.*, 2000).

Interestingly, a number of semiconductors can act as p-type or n-type based on vacant sites in their crystal lattices. A typical example is PbS, which can either be a p-type or n-type semiconductor depending on its stoichiometric imbalance (Clark *et al.*, 2011; Oh *et al.*, 2013; Preetha and Remadevi, 2013).

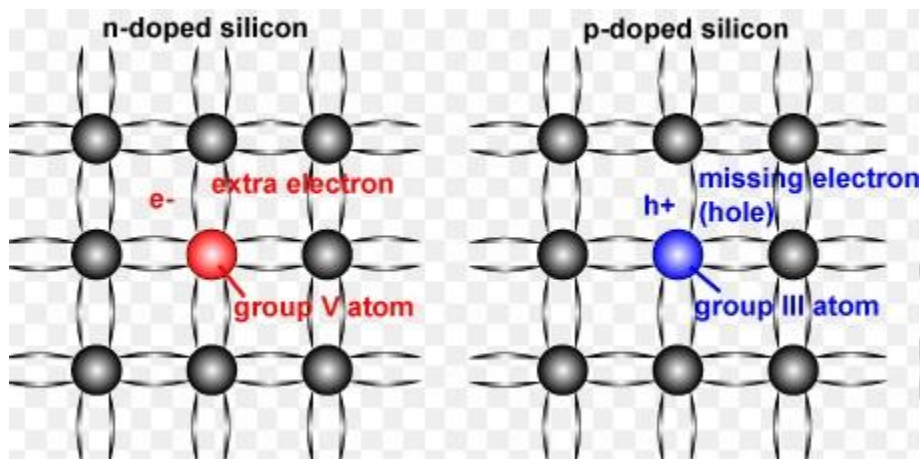


Figure 2.3 Pictorial representation of pure silicon doped as n-type and p-type semiconductors (Hsiang *et al.*, 2013)

2.2.3 Direct and indirect band gap semiconductors

In semiconductors, the minimal energy between the conduction and valence bands are characterized by a crystal momentum (k-factor) in the Brillouin zone (Lei *et al.*, 2014; Wang *et al.*, 2017). If the k-factors are the same, then it is a direct band gap semiconductor and if the k-factor are different, an indirect band gap semiconductor is formed (Chen *et al.*, 2010; Reiss, 2008). In direct band gap semiconductors, there is a direct transition of an electron from the valence to conduction band upon the absorption of energy. Therefore, the energy difference between the valence band and conduction band represents the band gap energy of the material (Chen *et al.*, 2010; Midgett *et al.*, 2013; Zhang *et al.*, 2015). Examples include lead sulfides and bismuth sulfides.

In indirect band gap semiconductors, there is no direct excitation of electrons from the valence band to the conduction band. Therefore, an additional energy is required to enable transition to occur (Dey *et al.*, 2013; Reiss, 2008). Common examples are silicon and gallium arsenides.

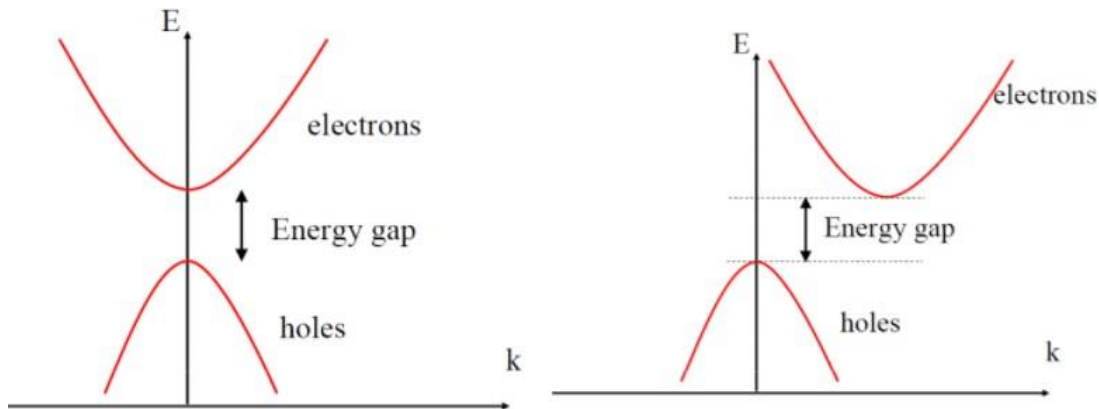


Figure 2.4 Pictorial representation of direct and indirect band gap semiconductors (Hsiang *et al.*, 2013)

2.3 Applications of semiconductors

The semiconductor industry represents one of the important industries that has a great effect on modern electronics. Some technological devices from this industry include computers, cellular phones, light emitting diodes, photo-detectors, solar cells, lasers and various types of transistors, such as bipolar junction transistors and field-effect transistors (Afzaal and O'Brien, 2006; Dharani *et al.*, 2014; Hiszpanski and Loo, 2014; Ohzeki *et al.*, 2014). Furthermore, the contribution of semiconductors to modern electronics also provides a platform to investigate into some fundamentals in physics and device fabrication. Some of these fundamental processes that have been studied in semiconductors include multiple exciton generation and quantum hall effects (Alam *et al.*, 2015; Hwang, 2015; Midgett *et al.*, 2013; Rimal *et al.*, 2016; Zhang, 2000).

2.4 Nanotechnology

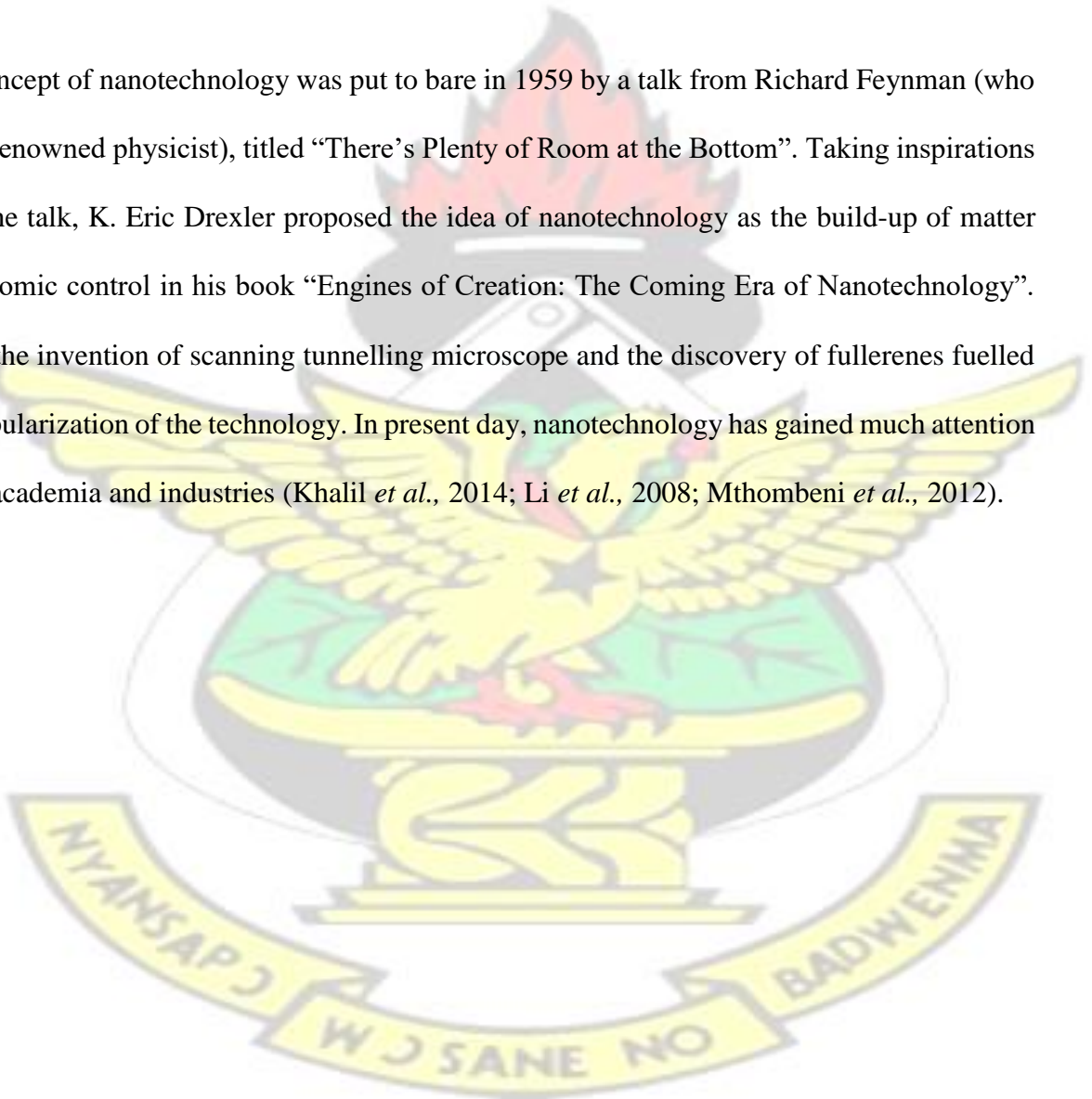
Nanotechnology involves the understanding and engineering of functional materials on an atomic or molecular scale where unique phenomena enable novel applications (Gubin *et al.*,

2005). It comprises imaging, measuring, modelling and manipulating of matter with typical dimensions between 1 to 100 nm (Figure 2.5) (Iqbal *et al.*, 2012). This technology has widespread applications although research is still ongoing (Bhawana and Fulekar, 2012; Gautam *et al.*, 2013; Nowack, 2008).

KNUST

2.4.1 Origin of nanotechnology

The concept of nanotechnology was put to bare in 1959 by a talk from Richard Feynman (who was a renowned physicist), titled “There’s Plenty of Room at the Bottom”. Taking inspirations from the talk, K. Eric Drexler proposed the idea of nanotechnology as the build-up of matter with atomic control in his book “Engines of Creation: The Coming Era of Nanotechnology”. Later, the invention of scanning tunnelling microscope and the discovery of fullerenes fuelled the popularization of the technology. In present day, nanotechnology has gained much attention in the academia and industries (Khalil *et al.*, 2014; Li *et al.*, 2008; Mthombeni *et al.*, 2012).



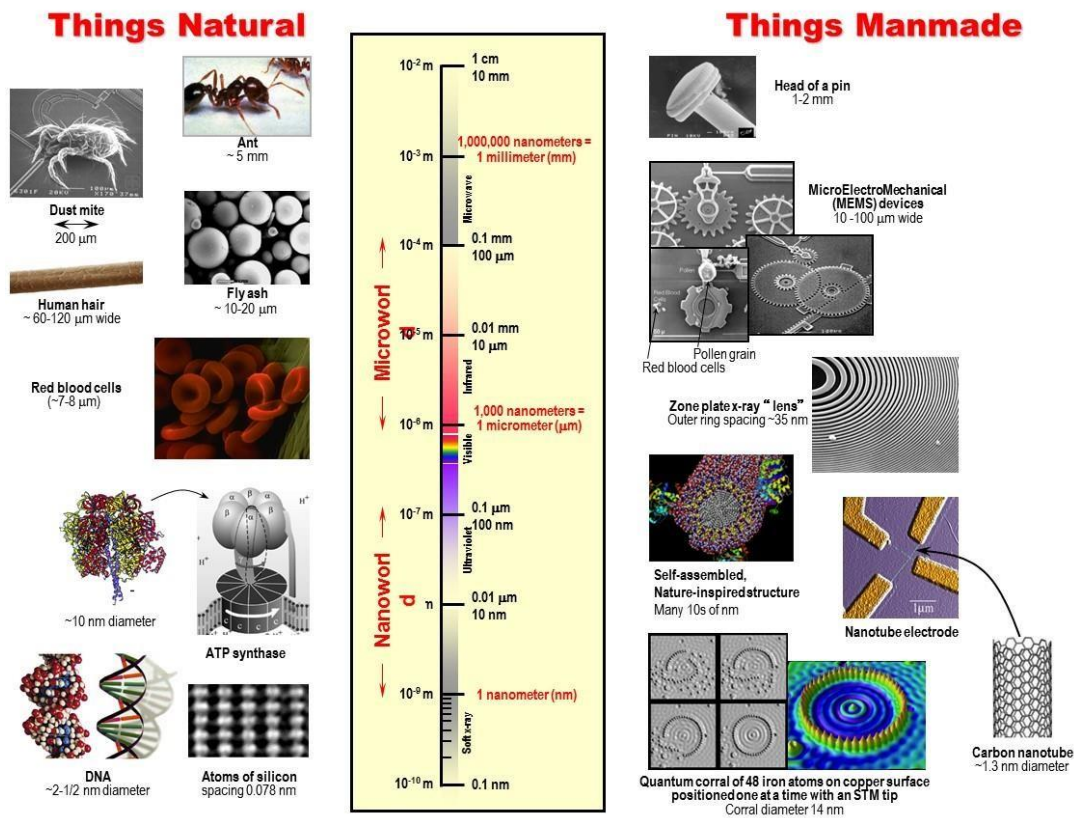


Figure 2.5 Comparison of material sizes

2.5 Nanomaterials

Nanomaterials are usually referred to as particles or materials with at least one of its dimension between 1 to 100 nm (Fan *et al.*, 2007). Nanomaterials include zero-dimensional nanocrystals and quantum dots, one-dimensional nanotubes and nanowires, two-dimensional nanofilms and three-dimensional clustered structures (Rao *et al.*, 2007). Nanomaterials have been the hotspot for science because they exhibit varieties of novel and remarkable structural and surface related properties, including increased strength, enhanced diffusivity, hardness, reduced elastic modulus, higher thermal expansion coefficient, lower thermal conductivity, large surface-to-volume ratio, reduced roughness and superior soft magnetic properties as compared to their bulk materials (Patil *et al.*, 2007). As the particle size is reduced to the nanometer ranges, material properties such as band gap is also increased (Panneerselvam and Green, 2013). In this

novel state of matter, the valence band and conduction band split, giving rise to discrete energy levels rather than a continuous band as observed in bulk materials. The close proximity of the electron and hole pair in nanosized semiconductors makes it impossible to ignore the Coulombic interaction between the electron and hole and they consequently assume a higher state of kinetic energy than the bulk (O'Brien *et al.*, 2005). The successful applications of nanomaterials into functional devices depend upon the synthetic pathway and surface modification which improve their inherent characteristics (Wang and Hong, 2010).

2.5.1 Approaches to nanomaterial syntheses

There are two main approaches to nanomaterial syntheses. These are the bottom-up and topdown approaches (Han *et al.*, 2011; Li *et al.*, 2013).

2.5.1.1 Bottom-up approach

The bottom-up approach to nanoparticle synthesis involves the putting together of atoms and molecular entities in a gas phase or a solution (Panneerselvam and Green, 2013). This approach has the potential to produce nanomaterials with a comparable level of control over the size, shape, composition and phase of the crystal domains (Ibanez *et al.*, 2013). It also involves vapour methods such as chemical vapour deposition, chemical bath deposition, solution methods, colloidal and sol-gel approaches. The integration of nanoscale building blocks into functional assemblies and further into multifunctional devices can be achieved through the “bottom–up” method. Compared to the top-down approach, this process has more flexibility in building up functional macro and nanostructures (Li *et al.*, 2011). This is by far the widely used synthetic approach to nanoparticle syntheses (Kershaw *et al.*, 2013; Young and Kinloch, 2013).

2.5.1.2 Top-down approach

The top-down approach on the other hand involves the breaking down of a bulky material to obtain finely divided particles. Widely used processes include crushing, milling and grinding although other technologies such as etching, ink printing and lithography have been considered under this approach (Trindade *et al.*, 2001). This approach has been extensively applied in the silicon industry where electron beam pattern generators are used to divide single silicon crystal which is about 1.3 m long into the nanometer dimensions (Iqbal *et al.*, 2012). In materials chemistry, $\text{Cd}_x\text{Pb}_{1-x}\text{S}$ nanocrystals with average particle size of about 9 nm have been synthesized using mechanical alloying process which is an example of a top-down approach (Tan *et al.*, 2014).

2.5.2 Properties of nanomaterials

The numerous applications of nanomaterials in various aspects of life are as a result of their unique magnetic, chemical, physical and mechanical properties which differ from their bulk materials (Abe *et al.*, 1998). These unique properties are size and shape dependent (Chen *et al.*, 2009). Due to their unique size-dependent properties, they are conventionally referred to as “artificial” atoms (Khanna *et al.*, 2006). For example, the dimensions of CdSe nanoparticles have a great effect on the colour of their colloidal suspension and hence their optical properties. These unique properties guide researchers in band gap engineering and tailoring material properties by increasing or decreasing the size of nanoparticles to suit specific applications.

2.6 Applications of nanotechnology and nanomaterials

Based on the versatile applications of nanomaterials in various disciplines of science and technology, the concept of nanotechnology has attracted practitioners from both academia and

industries. Nanomaterials have widespread applications in the electronics, food and agriculture, cosmetic, textile, healthcare, energy production and engineering industries (Ananthakumar *et al.*, 2014; Fan *et al.*, 2007; Ibanez *et al.*, 2013; Liu *et al.*, 2013; Nguyen *et al.*, 2014; Perex *et al.*, 2005; Prastani *et al.*, 2013). Nanotechnology has also been applied in a wide range of household products including sports gears, cosmetics, sunscreen lotions, food packaging materials, clothings, household appliances, electronic devices, disinfectants, paints, furniture varnishes and building materials (Iqbal *et al.*, 2012).

2.7 Semiconductor nanocrystals

Although several researchers have focused on the syntheses of monodispersed semiconductor nanocrystals, much attention has been on metal chalcogenides especially the sulfides and selenides. The semiconductor nanocrystal is usually capped by an organic layer which provides sufficient repulsion between the crystals, thus preventing aging and agglomeration (Marimuthu *et al.*, 2012). The interest in these class of materials reside in the change of their physical and chemical properties with respect to size and shape. This is due to their large surface-to-volume ratio and their reduced dimensions in relation to the excitonic radius of the bulk material. For instance, their optical band gaps can be tuned by controlling their shape and size thereby enhancing their performance in the fabrication of devices as compared to their bulk counterparts.

2.7.1 Properties of semiconductor nanocrystals

The properties of semiconductor nanocrystals result mainly from their quantum confinements.

This is basically the changes in electronic structure caused by the confinement of the electronic wave function to the dimensions of the particle, which is less than the mean free path of electrons (Fu and Tsang, 2012).

2.7.1.1 Electronic properties

At the nanometer regime, the valence and conduction bands split, giving rise to discrete energy levels rather than a continuous band as observed in the bulk material (O'Brien *et al.*, 2005). When the sizes of semiconductor nanocrystals are less than their Bohr exciton radii, their electronic properties change resulting in quantum size effect (Choi *et al.*, 2013). The quantum size effect is a consequence of the confinement of the charge carriers within the dimensions of the nanocrystals which result in them being treated quantum mechanically as particles in a box (Figure 2.6) (Su *et al.*, 2001). However, the magnitude of quantum size effect can be controlled by the synthetic approach to the nanocrystal production.

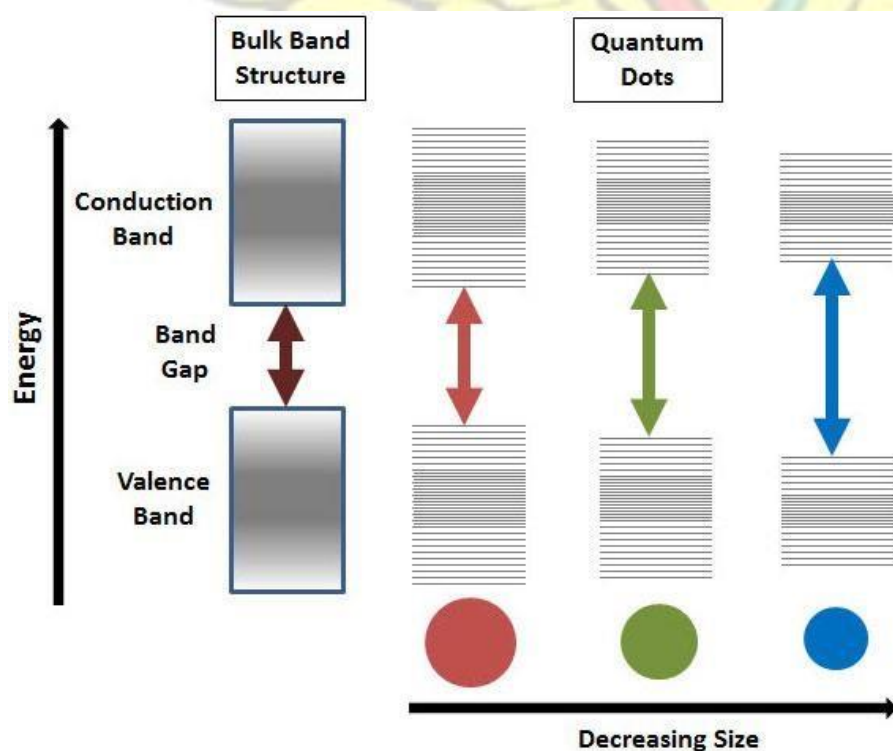


Figure 2.6 Electronic band structure of quantum dots due to the quantum confinement effect

(Iqbal *et al.*, 2012)

2.7.1.2 Optical properties

Optical properties of nanocrystals have a great potential both in fundamental studies and in practical applications (Ebnalwaled *et al.*, 2013). At the nanometer dimensions, there is usually size-dependent absorption and emission features in the optical spectra (Corricelli *et al.*, 2012). The optical properties are divided photoluminescence and absorption.

2.7.1.2.1 Photoluminescence

Photoluminescence refers to the emission of light from any material after the absorption of photons (Kaci *et al.*, 2010). It is usually divided into fluorescence and phosphorescence, depending upon the electronic configuration of the excited state and the emission pathway (Fuentes-Martínez *et al.*, 2009). During fluorescence transitions, the electron absorbs a photon with energy greater than its band gap. The electron then loses energy so that re-emitted photons will have lower energy than the absorbed photons. The process is typically fast. In phosphorescence transitions, the absorbed photon undergoes intersystem crossing where it enters into a triplet spin state thereby having a much longer excited state lifetime. After emitting a photon of energy corresponding to the band gap of the material, the electron then transitions back to the lower singlet energy state (Wagner *et al.*, 2005). This process occurs at a slower rate, sometimes lasting for minutes or up to hours. Therefore by changing the size of the nanoparticle, the emission colour can be changed to various colours on the electromagnetic spectrum (Reiss, 2008; Tani *et al.*, 2008).

2.7.1.2.2 Absorption

When the energy of a photon exceeds the band gap of a semiconductor nanocrystal, absorption occurs. Due to quantum confinement, decreasing the particle size results in a hypsochromic (blue-) shift of the absorption onset therefore allowing the tuning of the band gap energy. For a typical absorption, the smaller the size of the nanocrystal, the larger the number of spectral features and more distinctly resolved the spectrum (Reiss, 2008).

2.7.1.3 Quantum size effect of semiconductor nanocrystals

Quantum size effect (QSE) can be defined as the increase in band gap of a semiconductor with decreasing particle size (Pedrueza *et al.*, 2013). QSE is usually observed when the diameter of the nanocrystal is of the same order of magnitude as the wavelength of absorption. QSE gives rise to discrete energy levels depending on the size of the nanocrystal (Figure 2.7). The understanding of QSE is important in many potential applications. For example, when the size of the nanocrystal is of few nanometers (below the Bohr exciton radius), the electronic transitions are not restricted to specific energy levels which in turn widens the energy band gap of the nanocrystals as compared to that of the bulk material (Raniero *et al.*, 2010). At this unique state of materials, altering the number of atoms or changing the surface geometry of the nanocrystal has a great effect on its band gap (Osherov *et al.*, 2010).

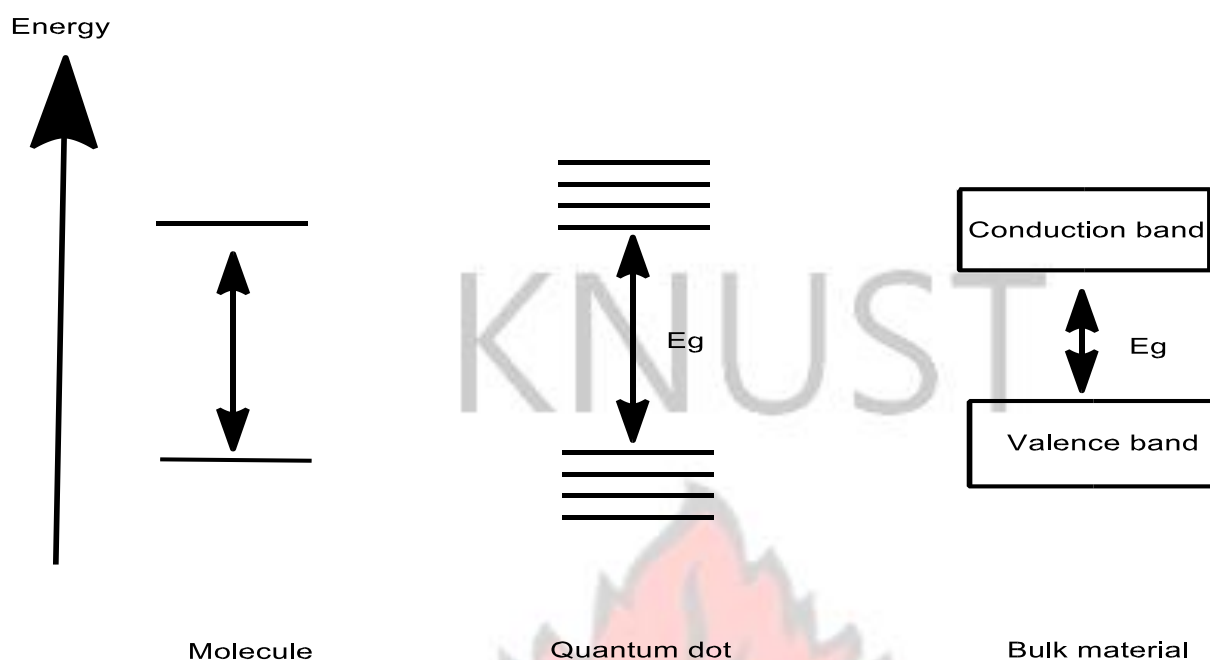


Figure 2.7 Quantum size effect in inorganic materials

2.8 Lead chalcogenides

Lead chalcogenides (PbE) comprising of sulfides, selenides and tellurides are currently receiving widespread attention because of their size-quantized optical transitions that extend from the near to the mid infrared region of the electromagnetic spectrum (Anthony *et al.*, 2009; Bian *et al.*, 2014; Kalebaila and Brock, 2012). Bulk PbE materials exhibit cubic (rock salt) crystal structures (Table 2.1). PbE can be considered as exhibiting a face-centered cubic structure with the Pb^{2+} occupying the octahedral holes or the anion (E) occupying the octahedral holes. In both case, they exhibit six coordination number structures. The nature of bond between Pb and E has been reported to be either ionic, covalent or both (Boadi *et al.*, 2012). Notwithstanding, ionic bonding in PbE is considered more important and it decreases as the size of chalcogenide species increase from sulfides to tellurides (Li *et al.*, 2015). Lead chalcogenides are direct band gap semiconductors with optical band gap energy of 0.28–0.41 eV at 300 K, and both valence and conduction bands maxima being a fourfold degenerate at

the L point of the Brillouin zone (Boadi *et al.*, 2012). By controlling their size, the absorption wavelength of the first exciton peak can easily be extended into the infrared region of the electromagnetic spectrum (Hyun *et al.*, 2008). They exhibit high carrier mobilities, strong size tunability and comparatively low forbidden gaps (Ghamsari *et al.*, 2011; Nabi *et al.*, 2000). Furthermore, they exhibit nonlinear optical properties which have been postulated to arise from a variety of physical mechanisms. When electrons in nanocrystals are excited by photons with energy greater than the band gap energy of the nanocrystal, free carrier absorption, trapped state absorption, and multiphoton absorption are thought to be the underlying physical mechanisms behind nonlinear absorption (Asunskis *et al.*, 2009). The nonlinear optical properties of PbE play an important role in the technology of photonics, especially in optical switches and signal processors (Chen *et al.*, 2014). This property of PbE also plays an important role in future nanoelectronics and quantum optics applications (Abel *et al.*, 2010; Meng *et al.*, 2014). PbE are known to exhibit variations in their polarity transport based on their stoichiometric imbalance. Pb-rich or E-rich materials have been shown to become n-type or p-type semiconductors respectively (Afzaal *et al.*, 2004; Oh *et al.*, 2013). Both n-type and p-type bulk PbE crystals exhibit unusual positive temperature coefficients of resistance (Otto and Yu, 2013). Their photosensitivity is dependent on the surface morphology, grain size and the topography of the film; that is on the uniformity of the grain size distribution and the degree of compaction of the structure formed (Larramendi *et al.*, 2001). Nanocrystals with sizes below their excitonic Bohr radii exhibit large blue shift of the absorption onset, and this can be achieved without having to prepare very small particles (Kalebaila and Brock, 2012). The interest in PbE nanocrystals result largely from the possibility to tune their optoelectronic properties by variation in composition, size and shape (Ghamsari *et al.*, 2011). Different structures of PbE have been obtained including nano and micro-rods (Aerts *et al.*, 2013; Cunningham *et al.*, 2014), nano and micro-cubes (Cui *et al.*, 2012; Emadi and Salavati-Niasari, 2013), nanowires (Akhtar *et al.*, 2012a; Foos *et al.*, 2011; Kim *et al.*, 2011), nanospheres

(Akhtar *et al.*, 2011), dendrite nanostructures (Akhtar *et al.*, 2010) and nanospheres (An *et al.*, 2006; Andreev and Lipovski, 1999).

Their optoelectronic properties arise from their three-dimensional quantum size confinement effects on carriers (Pedrueza *et al.*, 2013). For instance, their multiple exciton generations, large dielectric constants and high carrier mobilities make PbE attractive for use as photoactive materials in solar cells (Witt *et al.*, 2012). Qiu *et al.*, (2010) reported that PbE were the first materials used to demonstrate the effectiveness of nano engineering in improving thermoelectric properties.

Table 2.1 Physical properties of lead chalcogenides

Properties	Lead sulfides (PbS)	Lead selenides (PbSe)	Lead tellurides (PbTe)
Band gap in eV at 373 K	0.44	0.31	0.34
Bohr radius of bulk	18	46	46
Static dielectric constant	169	204	414
Lattice spacing (Å)	5.936	6.124	6.460
Density of mass (g/cm ³)	7.61	8.27	8.24
Youngs' modulus (GPa)	39.3	36.9	27.7
Crystal lattice	Cubic	Cubic	Cubic

2.8.1 Lead sulfide nanocrystals

PbS (commonly known as galena) is a group IV-VI semiconductor and the most widely studied among the lead chalcogenides (Emadi and Salavati-Niasari, 2013). It has a narrow direct band gap of 0.41 eV. Its large Bohr radius of 18 nm owing to a nearly equal contribution from electrons and holes allow an enhanced level of quantum confinement, making them advantageous over II-IV or III-V type materials (Boadi *et al.*, 2012; Patla *et al.*, 2007). It has a

high dielectric constant of 18, very high carrier mobility of $0.44 \text{ cm}^2 \text{ V}^{-1} \text{ S}^{-1}$ and small effective masses of electron and hole ($m_e^* = m_h^* = 0.085 m_e$). These are responsible for the third order nonlinear optical response which is 30 times that of GaAs and 1000 times that of CdS nanoparticles of similar dimensions (Akhtar *et al.*, 2010). These unique properties offer opportunities for achieving strong quantum confinement of both charge carriers individually as well as in an excitonic mode (Alam *et al.*, 2015). Different synthetic routes to PbS nanomaterials have resulted in tunable shapes and sizes thus, serving as a basis for studying the effect of shape and size on the electronic and optical properties. The choice of reaction conditions are aimed at producing uniformly shaped and sized nanoparticles. These synthetic approach ranges from using mild to very harsh conditions. The growth of uniformly sized spherical PbS nanocrystals with diameters of 4.1, 4.6, 5.6 and 9.0 nm in toluene solution of different polymeric materials (polystyrene, poly (1-decene), poly (1-butene) and polyethylene) have been studied (Asunskis *et al.*, 2008). The nature of the polymer had a great effect on the sizes of the PbS nanocrystals, further confirming better capping activity with higher molecular weight polymers. The growth of PbS nanowires with length of 300 nm and width of 50 nm *via* a solvothermal route by reacting lead stearate with elemental sulfur in the presence of tetralin has been reported (Gautam and Seshadri, 2004). The effect of temperature on the morphology of PbS synthesized from the thermal decomposition of lead tetrahydroquinoline dithiocarbamate SSP in oleyamine has been studied. The decompositions were performed at 180 and 270 °C. At 180 °C, nanocubes with sides of 24 nm were confirmed from the transmission electron microscope (TEM) images. However, at 270 °C, rods with length of 99 nm and width of 16 nm were formed (Nyamen *et al.*, 2014). One possibility of the formation of the rod could be from head-on agglomeration of cubes in one direction. The same group of researchers reported the syntheses of uniformly sized PbS nanocubes from the thermal decomposition of lead tetrahydroquinoline dithiocarbamate SSP in olive oil at 180 °C (Nyamen

et al., 2014). Salavati-Niasari and co-workers (2010) have investigated the effect of time on the morphology of PbS synthesized using a hydrothermal process of lead thiosemicarbazide complex at 150 °C. Cubic, fish-bone like and star shaped morphologies were observed at 6, 9 and 12 hours respectively from the TEM images. The decomposition of lead hexadecylxanthate in trioctylamine at a relatively low temperature of 90 °C has been reported to yield ultra-narrow rods with length of *ca.* 15 nm and diameter of *ca.* 1.8 nm (Patla *et al.*, 2007).

2.8.2 Lead selenide nanocrystals

PbSe (commonly known as clausthalite) is a group IV-VI direct semiconductor with a band gap of 0.27 eV (Boadi *et al.*, 2012). It is a grey crystalline solid which forms cubic crystals with a rock salt structure. It has a high dielectric constant of 22 and a small effective masses between electron and hole ($m_e^* = m_h^* = 0.05 m_e$) which results in relatively large effective electron and hole pair. It has a relatively large effective Bohr radius of 46 nm which is eight times larger than that of CdSe (Anwar *et al.*, 2015; Zhou *et al.*, 2006), thus size quantization effects are strongly pronounced in PbSe nanocrystals (Sashchiuk *et al.*, 2004). Furthermore, these nanocrystals are predicted theoretically to have absorptive and dispersive nonlinearities which is 1000 times larger than those of CdSe nanocrystals of the same size and shape (Lifshitz *et al.*, 2003; Ma and Cheng, 2013). Among the lead chalcogenides, PbSe is a promising candidate because of its superior chemical stability and simplicity of film deposition (AlGhamdi *et al.*, 2013). PbSe also show multiple exciton generation (MEG), in which the impact of a single photon produces two or more excitons (Argeri *et al.*, 2011). PbSe exhibits good grade of polarity, with bonds formed through electrostatic interactions among the ions of the crystal lattice (Ali and Saleh, 2014). By varying the size and shape of PbSe nanomaterials, their electrical and optical properties can also be tuned. One of the approaches to vary the properties

is usually achieved from the synthetic pathway and the reaction conditions. The effect of temperature on the sizes and optical properties of PbSe nanocrystals synthesized using the melt method has been reported (Yu *et al.*, 1997). An increase in temperature from 460 to 540 °C at an increment of 20 °C at constant time of 6 hours resulted in spherical PbSe nanocrystals with average radius ranging from 1.6 to 7.3 nm. The size effect on the optical band gap of the nanocrystals was found to decrease from 0.73 to 0.55 eV as the size increased from 1.6 to 7.3 nm. PbSe nanocrystals are also known to possess excellent carrier multiplication properties. However, 1-dimensional PbSe nanomaterials have enhanced carrier - carrier Coulomb interactions which might lead to increase carrier multiplication as compared to 0-dimensional PbSe nanomaterials (Padilha *et al.*, 2013). PbSe nanorods have been synthesized by injecting *tris*(diethylamino)phosphine selenide solution into octadecene containing lead oxide at 170 °C (Padilha *et al.*, 2013). The researchers studied the size dependence of PbSe nanorods on Auger recombination and carrier multiplicity. They concluded that there is a linear dependence on the length of the nanorods with a fixed cross-sectional size on Auger recombination and carrier multiplicity. Thus longer Auger lifetime in nanorods make them promising materials for a practical exploitation in next generation PV devices. For a better future of technology, it is essential to have nanoparticles with perfect morphology as well as well-defined spatial separation (Khanna *et al.*, 2006).

2.8.3 Lead telluride nanocrystals

PbTe (which occurs naturally as altaite) is a group IV-VI direct semiconductor with a band gap of 0.32 eV at 300 K and Bohr exciton radius of 46 nm (Ziqubu *et al.*, 2010). It appears as a grey cubic crystal with a sodium chloride crystal structure. The Pb and Te atoms occupy the cationic and anionic lattice respectively. It has a dielectric constant of 10 and a small effective

masses between electron and hole ($m_e^* = m_h^* = 0.01 m_e$). It has an electron mobility of $6000 \text{ cm}^2\text{V}^{-1}\text{S}^{-1}$ at 300 K (Fu and Tsang, 2012). Despite the immense interest in the use PbTe nanocrystals, few researches have focussed on their syntheses and characterization as compared to the other lead chalcogenides. For example, the effect of temperature on the morphology of PbTe had been investigated by Ziqibu and co-workers using a hot injection technique. Spherical PbTe nanocrystals with radius of 10 and 15 nm were obtained at 190 and 230 °C respectively. At 270 °C, nanorods with width of 7.3 and length of 45 nm were obtained (Ziqibu *et al.*, 2010). This observation further confirmed that reaction conditions can be changed to obtain specific properties of nanomaterials. Octahedral PbTe nanocrystals with average dimension of 20 nm was synthesized in diphenylether solution using oleic acid as the stabilizing ligand (Scheele *et al.*, 2011). Another contributor to difference in the size and shape of nanocrystals is time. The effect of time on the size and shape of PbTe nanocrystals have been reported. The synthetic approach involved the injection of trioctylphosphine telluride into a mixture of lead acetate trihydrate, oleic acid and 1-octadecene maintained at 400 °C. The PbTe nanocrystal obtained after a growth time of 3 minutes were found to be spherical with an average particle size of 9.0 nm, whereas nanoparticles obtained after a growth time of 5 minutes were found to be cubic with an average size of 15.8 nm (Ganguly and Brock, 2011). The researchers explained the transition from spherical to cubic morphology as thermodynamically driven as the size increases, favouring the growth of the {100} facets (lowest total surface energy) leading to the cubic morphology at longer reaction time. PbTe nanorods with length of *ca.* 600 nm and width of *ca.* 100 nm have been grown on silicon substrates by thermal evaporation method under high vacuum (Sridharan *et al.*, 2012). These researches confirm that synthetic approach and reaction conditions have a great effect on the size and shape of the nanocrystals formed.

2.9 Applications of lead chalcogenides

PbS is commonly used in infrared detectors and emitters owing to its high photosensitivity in the infrared region of the electromagnetic spectrum and high ‘electron and hole’ mobilities.

Nanostructured PbS has found useful applications as solar absorbers (Guchhait *et al.*, 2011; Rafea and Roushdy, 2010). Its exceptional third-order nonlinear optical properties enhance their applications in devices such as optical signal processors and switches, photoresistors, laser diodes, photo sensors, light emitting diodes, humidity and temperature sensors (Altiokka *et al.*, 2013; Dolatyari *et al.*, 2011). A demonstration of the use of PbS nanomaterials for thermoelectric application has been reported based on its thermal transport properties (Pei and Liu, 2012). Due to its large Bohr radius, PbSe nanomaterials have great potential applications in near IR lasers, optical switches, and telecommunications operating at wavelength between 1.5 – 5.2 μm without the need for cryogenic cooling (Al-Ghamdi *et al.*, 2013; Lifshitz *et al.*, 2003; Ramasamy *et al.*, 2011). PbSe nanomaterials have found useful applications in multiple exciton generators (Aerts *et al.*, 2011; Ahmad *et al.*, 2010). Other uses include thermoelectric devices (Al-Ghamdi *et al.*, 2013; Pei and Liu, 2012), near-infrared detectors (Ahmad *et al.*, 2010) and sensors (Akhtar *et al.*, 2012). PbTe nanomaterials have been reported to be superior materials for solid state thermoelectric cooling and electrical power generation devices (Ganguly *et al.*, 2011; Kungumadevi and Sathyamoorthy, 2013). They have also been used in optical switches, solar cells, photodetectors and electroluminescent devices (Murphy *et al.*, 2006; Ziqubu *et al.*, 2010).

2.10 Ternary lead sulfide selenide ($\text{PbS}_x\text{Se}_{(1-x)}$) nanomaterials

Most of the researches on nanocrystalline semiconductors reported so far have been restricted to the study of binary PbS and PbSe semiconductors with little attention on ternary lead sulfide selenide ($\text{PbS}_x\text{Se}_{(1-x)}$) nanomaterials. However, the particle-size dependence of electronic and optical properties in ternary semiconductors is now of major interest since they give access to

new families of materials with distinct properties (Bagade *et al.*, 2015). Ternary alloys are usually formed with either a common cation or a common anion but of different band gaps. Alloyed semiconductor quantum dots pose an advantage over their binary systems such as band gaps tuning can be achieved by varying the constituent stoichiometries of the binaries. Ternary systems also provide a wide range of emission colours independently of their size and can achieve emission colours which are difficult to get using a single component material (Joshi *et al.*, 2003). Ternary nanomaterials also have a possible increase in the multiple exciton generation through altering the lattice or tuning the electronic properties of the excited state (Abdelhady *et al.*, 2014). This serves as an additional property to the size-dependent quantum confinement effects, thus giving rise to a family of materials with distinct properties (Akhtar *et al.*, 2011). PbS and PbSe are materials which can be mixed to form an ideal substitutional alloy of $\text{PbS}_x\text{Se}_{(1-x)}$. Technologically, binary PbS and PbSe are known to be ideal materials for thermoelectric applications due to their large Bohr exciton radii and low thermal conductivity. However, by mixing these materials to form a ternary alloy, the thermal conductivity could be further lowered, which leads to even better thermoelectric properties (Gao *et al.*, 2013). Despite the unique properties of ternary $\text{PbS}_x\text{Se}_{(1-x)}$, their syntheses are of great challenge. The challenge is usually as a result of the sulfur being far more reactive and therefore rapidly consumed during the nucleation phase as compared to the selenium. This causes the ratio of sulfur to selenium in the injection mixture to differ from that of the alloy formed (Akhtar *et al.*, 2011). For the syntheses of homogenous ternary alloys, the growth rates of the two constituent materials must be close and the growth conditions for one constituent should not impede that of the other. One way of achieving this is to choose starting materials with similar decomposition behaviours. Thereby opening a research window to new routes for the syntheses of homogenous ternary alloys.

Solar cells based on binary compositions of PbSe and PbS nanocrystals have been investigated by most researches (Ma *et al.*, 2011; Wang *et al.*, 2012). Those based on PbSe nanocrystals generate larger short circuit currents while PbS nanocrystals devices with similar bandgap show larger open circuit voltage (Ma *et al.*, 2009). Therefore, ternary $\text{PbS}_x\text{Se}_{(1-x)}$ system can simultaneously optimize both the current and voltage in the solar cell (Gao *et al.*, 2013). Over the past decade, researchers have reported numerous approaches to the syntheses of homogenous $\text{PbS}_x\text{Se}_{(1-x)}$ nanomaterials with the hot injection technique being the most exploited towards nanoparticles and chemical bath deposition towards thin films (Akhtar *et al.*, 2011; Brumer *et al.*, 2006; Kumar *et al.*, 2010; Lifshitz *et al.*, 2006; Ma *et al.*, 2009; Nam *et al.*, 2012; Onicha *et al.*, 2012; Safrani and Golan, 2015; Song *et al.*, 2016; Thomson *et al.*, 2012; Yu *et al.*, 2011). Suitable compatible starting materials, have encompassed the use of lead salts with separate sources for sulfur and selenium, in which compatible decomposition characteristics have aided stoichiometric control (Akhtar *et al.*, 2011; Ma *et al.*, 2009; Nam *et al.*, 2012). The common chalcogen sources used are trioctylphosphine sulfur or selenium, *bis*(trimethylsilyl) sulfur or selenium and octadecene sulfur or selenium (Akhtar *et al.*, 2011; Ma *et al.*, 2009). These sources are fairly expensive and some are also potentially noxious and toxic. Hence, there is an interest in the syntheses of $\text{PbS}_x\text{Se}_{(1-x)}$ nanoparticles by simpler and safer routes. The Ozin group have used a single selenium sulfur precursor (Se_mS_n) in the syntheses of $\text{PbS}_x\text{Se}_{(1-x)}$ (Thomson *et al.*, 2012). The use of oleylamine as a reagent in the molten syntheses of Se_mS_n further increased the cost thereby limiting scale up. This limitation can be solved with the use of SSPs. The use of single source precursors (SSPs) of lead (II) imido(*bis*(selenodiisopropylphosphinate)) and lead (II) diethyldithiocarbamate species in trioctylphosphine oxide in the presence of trioctylphosphine using the hot injection technique has been reported by Onicha *et al.*, (2012). The report demonstrates the efficient use of SSPs

in producing compositionally alloyed systems. By varying the composition of the starting materials; the optical, electrical, and thermal properties can be engineered (Onicha *et al.*, 2012). The structural, optical and thermodynamic properties of binary PbS and PbSe and their alloys $\text{PbS}_{1-x}\text{Se}_x$ have been studied using Ab initio calculations employing density functional theory (DFT). The research described a nonlinear behaviour of the lattice constant, bulk modulus and band gap dependence on the mole fraction of selenium in the alloy. They attributed the bowing to be caused mainly by the charge transfer effect, while the volume deformation and the structural relaxation contribute to the bowing parameter at smaller magnitude (Labidi *et al.*, 2011).

2.11 Application of $\text{PbS}_x\text{Se}_{(1-x)}$ nanomaterials

Ternary semiconductor alloys of $\text{PbS}_x\text{Se}_{(1-x)}$ are of great interest and have been reported to have potential applications in transistors, infrared detectors, infrared emitters, optical fibres, light emitting diodes and photoconductors (El-Shazly *et al.*, 2011; Ferne *et al.*, 2009; Ganaie and Zulfeqar, 2015; Ghosh *et al.*, 2012; Khan *et al.*, 2011; Rojas-Chávez *et al.*, 2012; Yanover *et al.*, 2012). For example, Ma *et al.*, (2009) synthesized ternary $\text{PbS}_x\text{Se}_{(1-x)}$ nanocubes for photovoltaic studies using a mixed chalcogenide system in a hot injection method. Typically, a mixture of trioctylphosphine selenide and *bis*(trimethylsilyl) sulfide with diphenyl phosphine in octadecene (ODE) was injected into the hot lead oleate solution at 150 °C for 90 seconds. The ternary $\text{PbS}_{0.7}\text{Se}_{0.3}$, PbS and PbSe were employed in the fabrication of a hybrid solar cells and efficiencies compared. Efficiencies of 1.7, 1.4 and 3.3 % were obtained for PbS, PbSe and $\text{PbS}_{0.7}\text{Se}_{0.3}$ hybrid solar cells. Further confirming that alloyed $\text{PbS}_{0.7}\text{Se}_{0.3}$ possess better performance than either of the parent binary materials. The researchers attributed this performance to the combination of material properties as well as a redistribution of the trap states in the ternary $\text{PbS}_{0.7}\text{Se}_{0.3}$.

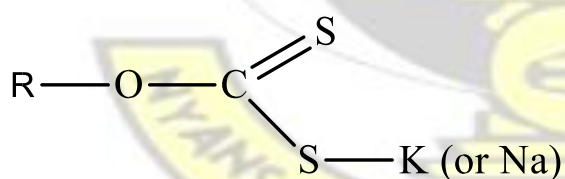
2.12 Single source precursors (SSPs)

Single source precursors (SSPs) are metal-organic complexes containing all the constituent elements needed to synthesize a desired product in a single molecule (Akhtar *et al.*, 2011). Technically, these SSPs are designed to contain the required elements in their right stoichiometries (Bendt *et al.*, 2016). Under right conditions, these precursors can be used for the syntheses of thin films and nanoparticles. Over the past three decades, many researchers have reported on the use of SSPs as efficient synthetic route to high quality, crystalline and mono-dispersed metal chalcogenide nanomaterials (Abdelhady *et al.*, 2013; Akhtar *et al.*, 2012a; Al-Dulaimi *et al.*, 2016; Thomson *et al.*, 2012). These starting materials have numerous advantages over multiple route sources which include suppressing impurities and extent of side reactions, potential to reduce the environmental impact of material processing. This is as a result of the limited volumes of solvents used in the process (Dutta *et al.*, 2012). The existence of preformed metal to chalcogen bonds and the absence of metal to carbon bonds in these precursors lead to the successful formation of metal chalcogens in an inert atmosphere (Pawar *et al.*, 2017). A major role in tailoring the properties of the materials reside in a proper choice of the precursors; whose nature strongly affects the composition, size and morphology of the final product. For example, the bulkier the SSP, the better self-capping activity on the nanomaterials formed (McNaughten and Saah *et al.*, 2016). In particular, SSPs containing all the desired elements to be deposited in a unique molecule can be used conveniently as building blocks for the single-step transformation of molecules into nanomaterials (Ji *et al.*, 2017). The thermal decomposition of these precursors result in nanoparticles with high yields. Some of the commonly used ligands for the preparation of SSPs include dichalcogenocarbonate, dichalcogenourea, dichalcogenophosphinate, dichalcogenocarbamate,

dichalcogenoimidodiphosphinate, dichalcogenobiuret and dichalcogenophosphate (Boadi *et al.*, 2012; Malik *et al.*, 2010; Malik and O'Brien, 2005). There are enormous researches on the use of SSPs for the syntheses of nanomaterials which include binary are PbE (Akhtar *et al.*, 2012b; Boadi *et al.*, 2016), CdS (Maji *et al.*, 2012; Thupakula *et al.*, 2012), CuS (Abdelhady *et al.*, 2011; Maji *et al.*, 2012), ZnS (Maji *et al.*, 2011), In₂S₃ (Abdelhady *et al.*, 2013), Bi₂S₃ (Dutta *et al.*, 2014; Kun *et al.*, 2016), EuE (Hasegawa *et al.*, 2008; Mirkovic *et al.*, 2005), FeS (Dutta *et al.*, 2012; Khalid *et al.*, 2015) and ternary CdSSe (Abdelhady *et al.*, 2011; Kevin *et al.*, 2015), ZnCdS (Abdelhady *et al.*, 2014; Zhang *et al.*, 2015) and PbSSe (Gao *et al.*, 2013; Onicha *et al.*, 2012).

2.12.1 Lead dithiocarbonato complexes (xanthates)

Xanthates deriving their name from their characteristic yellow colour are the alkyl derivatives of dithiocarbonic acid (Kayatürk *et al.*, 1999; Yanev *et al.*, 2000). They are synthesized by a reaction between an alkoxide and carbon disulfide (Kaltenhauser *et al.*, 2013; Zohir *et al.*, 2009). The chemical properties of xanthates can be modified with the alkyl chain length of the starting alcohol (Lewis *et al.*, 2015). For example, their thermal stability increases with a corresponding increase in the chain length of the starting alcohol (Akhtar *et al.*, 2011).

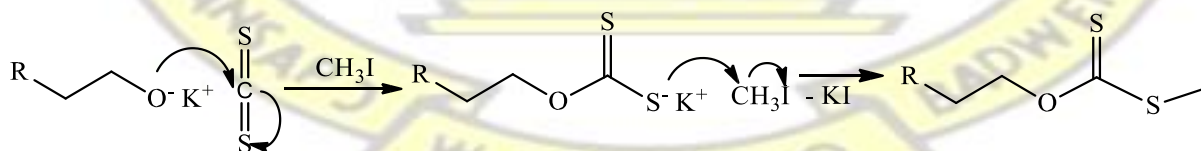


Scheme 2.1: Structure of xanthate ligand

Among the absorbents used for the removal of hazardous metals in froth flotation, sulfur containing ligands have shown high affinity for heavy metals. According to the hard and soft acids and bases (HSAB) classification system, sulfur is considered to bind strongly to a number

of metals; such as lead, cadmium, mercury and copper which are soft acids (Torres-Blancas *et al.*, 2013). Xanthate, which is a sulfur containing ligand has been reported to form strong bonds with sulfide minerals and most metal ions (Bag *et al.*, 2011; Nedjar and Barkat, 2012). Industrially, xanthates have been employed as flotation agents for the thiophilic minerals for most metals (Morey *et al.*, 1999; Mustafa *et al.*, 2004; Ndzebet *et al.*, 1994; Peng *et al.*, 2012; Peng and Grano, 2010). Xanthate adsorption on galena, which is the major ore for lead, has been widely studied experimentally, and a number of adsorption mechanisms have been proposed (Porento and Hirva, 2003). The use of sodium ethyl and butyl xanthates as flotation agents in the removal of galena from wastewater have been studied (Plescia, 1993). Theoretical considerations have been used to investigate the effect of alkyl chain length of xanthate on its interaction with copper ion. Stronger electronic interactions were observed with increased alkyl chain length of the xanthate (Bag *et al.*, 2011). These ligands usually form bidentate chelates, or monodentate discrete or network solids, showing a wide range of coordination behaviour depending on the metal. The xanthate ligands are also used for the removal of heavy metals in aqueous waste streams of many metal plating, mining, and tannery industries (Ghosh *et al.*, 2012; Ghosh *et al.*, 2013). Xanthates have also been reported to be attractive alternatives as oxygen-containing fuel additives (Guo *et al.*, 2012).

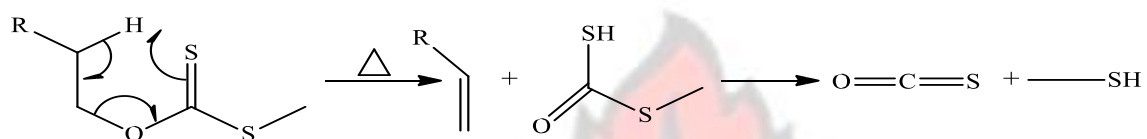
The chemistry of xanthates is dominated by the thiocarbonyl (O-CS₂) functionality. The reaction mechanism of presented in Scheme 2.2.



Scheme 2.2: Reaction for the synthesis of alkyl xanthate ligand

The decomposition pathway of xanthate is similar to the Chugaev elimination mechanism. This pathway is cleaner and can occur at relatively lower temperatures than those of other SSPs

(Goh *et al.*, 2013; Lewis *et al.*, 2015). This property of xanthates enable their *insitu* growth in polymer matrix (Lewis *et al.*, 2015). The Chugaev elimination usually occur at temperatures lower than 200 °C, where an alkene is formed by a concerted syn-elimination, *via* a 6membered cyclic transition state and the hydrogen atom is moved from the β -C-atom to the sulfur. The side product decomposes to carbonyl sulfide and methylthiol which are all volatile (Alam *et al.*, 2008; Goh *et al.*, 2013; Lewis *et al.*, 2015).



Scheme 2.3: Chugaev elimination reaction

Metal xanthates as a class of inorganic complexes have been successfully used as SSPs for the syntheses of high purity metal sulfide nanomaterials at relatively low temperatures (< 250 °C) (Alam *et al.*, 2008; Pradhan *et al.*, 2003). The use of metal xanthates have been of interest due to their high solubility in organic solvents, air-stability and decomposition properties (Dowland *et al.*, 2011; Fan *et al.*, 2007). The binding energy of alkyl xanthate to metals increase with increasing alkyl chain length. This was confirmed by theoretical calculations performed to understand the nature of interaction between alkyl xanthates and copper atom (Bag *et al.*, 2011). The use of xanthates in nanomaterial syntheses serve two important roles. Firstly, their use as efficient capping agents for stabilizing the metal sulfide nanoparticles and secondly modifying the surface properties of the nanomaterials. Although there seem to be extensive research on xanthates, most of them are limited to the ethyl derivative (Akhtar *et al.*, 2010; Barreca *et al.*, 2005; Dowland *et al.*, 2011; Ghosh *et al.*, 2013; Nair *et al.*, 2002; Ramasamy *et al.*, 2013). And therefore, little is known about the properties and use of higher alkyl chain xanthate complexes. The effect of temperature on PbS thin films deposited on kapton substrates from lead butyl xanthate at 150 °C by AACVD at atmospheric pressure has been reported by Akhtar *et al.*,

(2011). XRD analyses of the films showed no additional peak from the substrate or an impurity. TEM images of the films deposited at 170 °C composed of distorted cubes which might have resulted from agglomeration of smaller cubes (Akhtar *et al.*, 2011). Ethyl and butyl derivatives of lead xanthate complexes have been synthesized and characterized by Clark and co-workers. Their report also bring to account the properties of new lead xanthate adducts with N-donor ligands such as bipyridine, tetramethylethylenediamine and pentamethyldiethylenetriamine (Clark *et al.*, 2011). The research confirmed that lead xanthates and their N-adducts are efficient SSPs for the syntheses of PbS nanomaterials. The effect of alkyl chain on the morphology of PbS thin films grown in polystyrene matrix using the spin coating technique have been reported by the O'Brien group. The researchers observed that as the alkyl chain of the xanthate moiety increased from ethyl to octyl, it caused an anisotropic growth from cubic to wires (Lewis *et al.*, 2015). The effect of alkyl chain on the dimensions of lead sulfide nanocubes using the melt method showed a decreased in size with increasing alkyl chain length from 157 to 77 nm in edge length from ethyl to octyl (McNaughter *et al.*, 2016). Furthermore, the growth of uniform and ultra narrow PbS nanowires with diameter of 1.8 nm and length of 120 nm from lead hexadecyl xanthate at 90 °C has been reported (Patla *et al.*, 2007). Using the same precursor, another group of researchers have synthesized ultra-narrow PbS nanorods with diameter size of 1.7 nm using trioctylamine (TOA) as coordinating solvent at 65 °C (Khan *et al.*, 2011).

The selenium derivative of xanthate (selenocarbonato) complexes can be synthesized by reacting carbon diselenide with an alkoxide. However, there seem to be little or no report on such complexes because of the difficulty in synthesizing the toxic and noxious carbon diselenide involved in the reaction since it is not commercially available (Afzaal *et al.*, 2012; Embden *et al.*, 2015).

2.12.2 Lead dichalcogenocarbamate complexes

Dithiocarbamates are formed by the reaction of amines with carbon disulfide in the presence of either a sodium or potassium salt, although most researchers have used the sodium salt (Afzaal *et al.*, 2012; Nyamen *et al.*, 2011).

Their syntheses can be represented as follows:



Scheme 2.4: Reaction for the synthesis of dithiocarbamates

Dithiocarbamates are highly versatile ligands which form stable complexes with most metal ions (Afzaal *et al.*, 2012). They have been applied widely in agriculture as anti-fungal agents and in mining industry as flotation agents (Pedras *et al.*, 2012; Queiroz *et al.*, 1999). Dithiocarbamates have been reported as active accelerators in the vulcanization of rubber (Jung *et al.*, 2010). In materials chemistry, metal dithiocarbamates have been used for the syntheses of metal sulfide thin films and nanoparticles (Davidovich *et al.*, 2010). By contrast, dithiocarbamates do not undergo Chugaev elimination since the C=N bond is stronger as compared to the C=O bond in xanthates (Castro *et al.*, 2008).

The past two decades have seen extensive researches on lead dithiocarbamate complexes due to their strong metal binding properties (Malik *et al.*, 2010). The O'Brien group was the first to report on the use of lead (II) dithiocarbamate complexes $[\text{Pb}(\text{S}_2\text{CNRR}')_2]$ (R, R' = ethyl, butyl, *i*-butyl) as SSPs for the syntheses of PbS nanoparticles (Trindade and O'Brien, 1997). Using TOPO as capping agents, they synthesized nanocrystalline PbS by thermolyses of the precursors. It was observed that the optical and morphological properties of the PbS nanocrystallites depended strongly on the temperature rather than the chemical nature of the precursors. For example, at 100 °C, spherical PbS nanocrystallites with average diameters of

6.3 nm were obtained whereas a mixture of cubic and spherical crystallites were obtained at 150 °C. In a related research by the same group, heterolytic lead dithiocarbamate complexes, $[\text{Pb}(\text{S}_2\text{CNRR}')_2]$ (R = methyl, ethyl; R' = iso propyl, n-butyl) were used as SSPs for the deposition of PbS thin films using CVD techniques (Afzaal *et al.*, 2004). There was a great effect of deposition temperature on the morphology. For example, PbS decomposed from the complex with RR' being ethyl and iso-propyl respectively showed granular, cubic with some platelet and acicular platelets morphologies at deposition temperatures of 400, 425 and 450 °C respectively. A further research by the same group involving the decomposition of a series of lead dithiocarbamate complexes in oleyamine at different temperatures was carried out. They observed that the lower chain complexes decomposed to a clean PbS phase at much higher temperatures as compared to the higher chain complexes. This observation was attributed to the greater thermal stability of the higher chain derivatives (Akhtar *et al.*, 2010). Sun and Buhro, (2008) have reported the use of lead ethyl carbamate for the solution liquid solid growth of high quality PbS nanowires with TOP and TOPO as the solvent and capping agent respectively. The nanowires had diameters between 9-31 nm and length of several microns. The examples above demonstrate the effect of synthetic technique on the size and shape of the nanomaterials formed. The Revaprasadu group has reported extensively on the use of heterocyclic dithiocarbamates and their adducts as efficient SSPs for the syntheses of high quality metal sulfide nanomaterials. The heterocyclic ring provides improved capping activity due to the steric effect. Anisotropic PbS nanostructures have been synthesized from lead tetrahydroquinoline dithiocarbamate at a temperature of 250 °C. Shapes of rod, quasi-cubic, cubic and rectangular shaped PbS were obtained using hexadecylamine, TOPO, OLA and decylamine as capping agents respectively (Nyamen *et al.*, 2012). Almost uniformly sized cubic PbS nanoparticles with average side length of 18 nm have been synthesized from lead piperidine dithiocarbamate using olive oil as capping agent (Nyamen *et al.*, 2014).

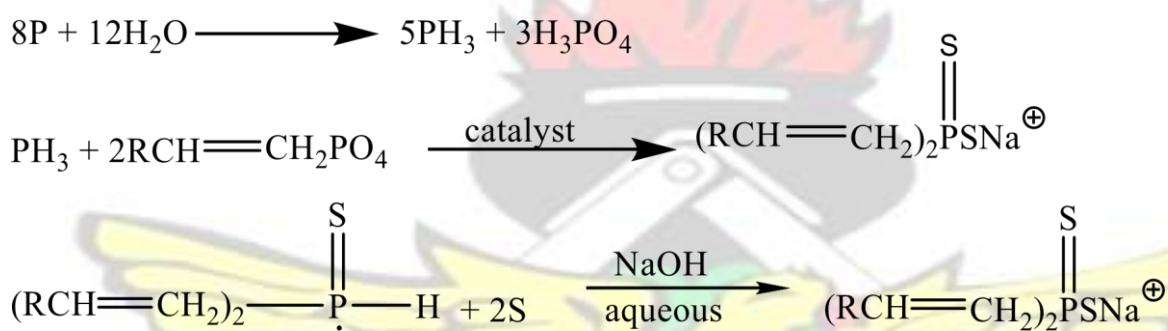
The selenium derivatives are synthesized by reacting the carbon diselenide or selenocyanate with the amine in the presence of an alkali salt at low temperatures (Hursthouse *et al.*, 1992). Few reports include the syntheses of a series of group 12 metals to determine their cytotoxic and radical scavenging properties. Some of the complexes exhibited promising broad spectrum antiproliferative activity (Romano *et al.*, 2015). Selenocarbamate complexes of chromium, cobalt, nickel and palladium have been synthesized and their absorption properties investigated (Furlani *et al.*, 1968). The absorption spectra showed two intensive ultraviolet bands and a shoulder in the visible region depending on the colour of the complex. The superoxide anion scavenging selenocarbamates have been investigated *in vitro* (Takahashi *et al.*, 2005). Heterolytic dialkylselenocarbamate complexes with one of the alkyl groups being ethyl and the other (phenyl, methylphenyl and naphthyl) have been investigated for their anti-oxidant properties using the 1,1-diphenyl-2-picrylhydrazyl radical (DPPH) assay. The phenyl and naphthyl derivatives turned out to be more active than some well-known antioxidants like ascorbic acid and trolox (Merino-Montiel *et al.*, 2013). Selenocarbamates have also been investigated as effective superoxide anion scavengers (Takahashi *et al.*, 2005).

In materials chemistry, there have been few reports on the use of metal selenocarbamate for the syntheses of metal selenides thin films and nanoparticles (Hursthouse *et al.*, 1992). Zinc and cadmium ethyl selenocarbamate have been used for the deposition of the respective metal selenide thin films (Hursthouse *et al.*, 1992). The thin films had a high selenium contamination however, there was no explanation for this behaviour of the nanomaterials. Later, a research by Chunggaze and co-workers using ethyl and hexyl selenocarbamate of zinc and cadmium explained the reason for the selenium contamination. The researchers demonstrated that the choice of alkyl chain attached to the nitrogen atom has a great effect on the decomposition of the complex. Using the gas chromatography mass spectrometer (GC-MS) technique, they observed that the lower chain (ethyl) formed a selenium cluster whereas the cluster was not

found in the higher chain complex (Chunggaze *et al.*, 1999). Their conclusion was to use higher chain length selenocarbamate complexes for deposition of metal selenide nanomaterials.

2.12.3 Lead dichalcogenophosphinato complexes

Phosphines are produced from hydrolysis of elemental phosphorus which in turn reacts with isobutylene to form a secondary phosphine intermediate. The phosphine intermediate is then reacted with sulfur in alkaline solution to give di-isobutyl dithiophosphinate (Zyl and Woollins, 2013). The reaction processes are shown below:



Scheme 2.5: Reaction for the synthesis of dithiophosphinates

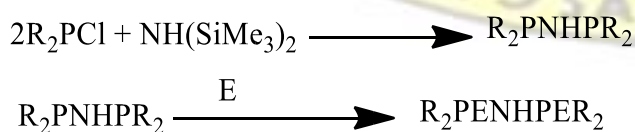
The dichalcogenophosphinato SSPs contain the metal, phosphorous and chalcogen source in the same structure, therefore making them efficient precursors for the growth of metal phosphides and metal chalcogenide nanomaterials at relatively low temperatures under ambient conditions (Maneeprakorn *et al.*, 2009). The structural chemistry of dichalcogenophosphinato complexes have been reviewed (Davidovich *et al.*, 2010; Haiduc and Yoong, 2002). Both reviewers mainly discussed the coordination chemistry, molecular structures and supramolecular associations of metal dichalcogenophosphinato although those of Pb (II), is rather limited. Dithiophosphinates have been reported as flotation agent although few reports exist as compared to xanthates (Davidovich *et al.*, 2010). They possess important biological properties and may also inhibit hydrocarbon oxidation (Maspero *et al.*, 2003). Duan *et al.*,

(2007) have synthesized high quality cubic PbS nanocrystals by the solvothermal decomposition of $[\text{Pb}(\text{S}_2\text{POR})_2]$ (R = butyl, octyl, dodecyl) in OLA at temperatures between 140 to 180 °C. The PbS nanocubes had side length of 14.8, 58.5, and 74.5 nm, corresponding to dodecyl, octyl, and butyl derivatives respectively. It was clear that, the average size of PbS nanocrystals decreased largely with an increase in the alkyl chain length of precursors. This may have resulted from the increased capping activity of the precursors with higher alkyl chains.

Diselenophosphinate ligands have been shown to form monomeric, cluster and polymeric complexes with a wide variety of metal ions due to their capability of adopting several binding modes through the two selenium atoms (Artem *et al.*, 2014; Chang *et al.*, 2010; Nguyen *et al.*, 2007). Until recently, examples of the use of selenophosphinates for the syntheses of nanoparticles were rare. Cubic and eight-horned dendrite morphologies were observed for poly(vinyl pyrrolidone) and ethylenediamine capped PbSe nanomaterials have been grown from lead diselenophosphinate (Chang *et al.*, 2010). Theoretical consideration on the gas phase decomposition of $\text{Pb}(\text{tPr})_2\text{PSSe}_2$ showed that, the formation of ternary $\text{PbSe}_x\text{S}_{1-x}$ is more favourable than parent binaries based on DFT calculations (Opoku *et al.*, 2015).

2.12.4 Lead dichalcogenoimidodiphosphinato complexes

The synthetic pathway of imidophosphinates occur *via* two step as shown in Scheme 2.6 below. The first step involves the formation of the intermediate which is then reacted with the chalcogen to form the dichalcogenoimidodiphosphinates.



Scheme 2.6: Reaction for the synthesis of dichalcogenoimidodiphosphinates

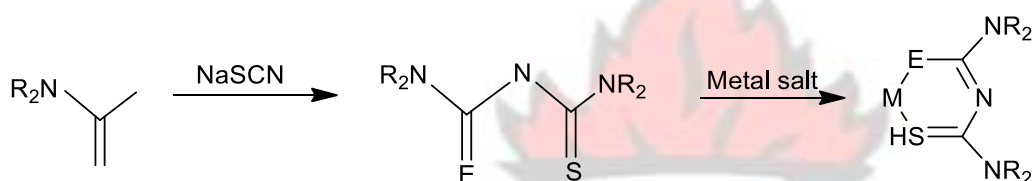
Dichalcogenoimidodiphosphinato complexes are known to exhibit various binding geometries about the metal center. This depends on the choice of chalcogen, organic group and complexing metal (Demko and Wasylishen, 2008a; Silvestru and Drake, 2001). Since the first report on imidodiphosphinates by Schmidpeter and co-workers, several researchers have adopted the synthetic process to make various metal dichalcogenoimidodiphosphinato complexes (Cupertino *et al.*, 1996, 1999; Ritch *et al.*, 2010). Report on some early applications of dichalcogenoimidodiphosphinato complexes included their use as lanthanide shift reagents, in luminescent materials, or in metal-extraction processes (Chivers *et al.*, 2010). Lead dichalcogenoimidodiphosphinato complexes have been reported to be efficient SSPs for the deposition of PbE thin films using various techniques (Afzaal *et al.*, 2004; Ritch *et al.*, 2010). The syntheses of diselenoimidodiphosphinate complexes occur from the facile oxidation of the corresponding *bis*(dialkylphosphine)amine with elemental selenium unlike the use of noxious carbon diselenide in the syntheses of diselenocarbamates (Demko and Wasylishen, 2008b).

Although the S and Se analogues are air stable, the Te analogue are prone to oxidation in air (Boadi *et al.*, 2012). Both the sulfur and selenium derivatives of lead dichalcogenoimidodiphosphinate complexes have been used to deposit PbS and PbSe thin films using AACVD. SEM images of the thin films revealed the formation of cubic nanocrystals with sizes of 670.6 ± 42.2 nm and 440.7 ± 66.4 nm for PbS and PbSe films respectively (Boadi *et al.*, 2016). Research on the Te analogue by Chivers and co-workers resulted in the development of a new synthetic pathway. This involves the metalation of R_2PNHPR_2 by sodium hydride to form $Na[R_2PNHPR_2]$ followed by the addition of tellurium powder in hot toluene in the presence of TMEDA. This ligand, when reacted with metal ions produce complexes with most metals. This approach has been used to deposit submicrometer-sized rectangular prisms PbTe

Dichalcogenourea ligands are potentially multidentate, therefore, capable of coordination through nitrogen and/or chalcogen atoms with a range of metals (Golovnev *et al.*, 2010). Therefore exhibiting rich and diverse coordination chemistry (Henderson *et al.*, 2003). The lead complex is usually prepared by a reaction between a lead salt and ethanolic solution of the chalcogenourea ligand at room temperature. *Bis*[N,N-disobutyl-N-(4-nitrobenzoyl)selenoureato]lead (II) have been used for the syntheses of PbSe nanoparticles. The morphology of the PbSe nanoparticles was greatly affected by temperature. For example, 200 °C gave spherical particles, whilst the growth at 250 °C were cubes (Akhtar *et al.*, 2011). The same group have successfully synthesized *bis*[N,N-diethyl-N'-naphthoylselenoureato] lead (II) complex and used to grow PbSe nanowires in TOPO at 290 °C. They were able to tune the dimensions of the PbSe nanowires between 8-25 nm in diameter and length of several micrometres by tailoring the reaction time (Akhtar *et al.*, 2012). PbSe nanohexagons have been synthesized by injecting selenourea dissolved N,N- dimethylformamide and phenyl ether into lead acetate solution at 160 °C (Sliem *et al.*, 2011). Using chemical bath technique, the effect of pH on PbSe thin films from lead nitrate and selenourea has been investigated (Bhardwaj *et al.*, 2007). The p-XRD patterns of the PbSe thin films shifted slightly towards higher 2 theta values indicating a decrease in lattice parameter with increasing pH of the bath solution increased from 10 to 11.5. The effect of deposition technique (chemical bath deposition, sonochemical bath deposition and microwave-assisted chemical bath deposition) on PbS from lead thiourea has been reported (Patel *et al.*, 2012). Morphologies observed from the SEM images were spherical with an intricate network of flakes, spherical and layers of thin flakes for the three techniques respectively. PbS nanoparticles with average size of 60 nm have been prepared by chemical precipitation from aqueous solutions of thiourea and lead acetate (Belova and Rempel, 2004).

2.12.6 Lead chalcogenobiuret complexes

Thio and seleno-biurets have attracted considerable attention due to their chemotherapeutic properties (Thomas *et al.*, 2015). This class of compounds have been reported to have versatile biological applications in areas such as anti-malarial, anti-inflammatory agents, fungicidal, insecticidal, herbicidal and pesticidal actions (Rastogi *et al.*, 2001). The thiobiuret ligand is formed by the reaction between N, N'-dialkylcarbonyl chloride and sodium thiocyanate. The metal complex is formed by precipitation of the ligand with the metal salt.



Scheme 2.8: Reaction for the synthesis of thiobiurets

Ramasamy and co-workers were the first group of researchers to investigate the use of metal thiobiurets as SSPs for the syntheses of a wide range of metal sulfide nanomaterials. The metals included Co, Fe, Zn, Cd, In, Ni and Cu (Ramasamy *et al.*, 2010). The same group have extensively reported on different transition metal thiobiurets as efficient starting materials to metal sulfide nanomaterials (Abdelhady *et al.*, 2013; Abdelhady *et al.*, 2014). Lead thiobiurets have been dissolved in toluene and layered upon an aqueous solution of sodium sulfide nonahydrate to deposit interconnected networks PbS thin films with dimensions of 10-20 nm (Cant *et al.*, 2015). Using the same synthetic technique with oil as the organic phase, spherical PbS have been synthesized from lead thiobiuret complexes (Thomas *et al.*, 2015). Report on seleno derivate of biuret is rather scarce and limited to Ab initio considerations. Calculations of minimum-energy conformers were carried out at the Hartree-Fock and second-order MøllerPlesset levels. The researchers concluded that the *cis-trans* was the most stable

conformation as compared to the *cis-cis* and *trans-trans* within the limit of the calculations (Jabalameili *et al.*, 1997).

2.13 Synthetic route to nanomaterials preparation using single source precursors

Several routes have been exploited for the syntheses of nanoparticles and thin films from SSPs. These include chemical bath deposition, chemical vapour deposition, spin coating, deposition at the interface between two immiscible solvents, doctor blading, dip coating, melt reactions, colloidal syntheses and precipitation methods. The choice of the synthetic technique has a great effect on the morphology, size and properties on the nanomaterials.

2.13.1 Chemical bath deposition

Chemical bath deposition (CBD) method is based on successive adsorption and reaction of species on the surface of a substrate from an aqueous solutions (Bhatt *et al.*, 2014; Hussain *et al.*, 2013; Rajashree and Balu, 2016). CBD requires relatively mild, cost effective, scalable and technically straight-forward conditions. In CBD, thin films are grown in a single bath solution hence the morphologies and dimensions of the crystallites can be varied by controlling deposition parameters such as time, temperature, reagent concentrations and pH (Abbas *et al.*, 2011; Bhatt *et al.*, 2014; Gertman *et al.*, 2014). This approach has some drawbacks which have been identified. For example, researchers have observed that the thermal treatment process has effect on the rate of absorptivity of the films and consequently influence their optical properties. The single bath system can cause particulate contamination which causes yield loss in semiconductor processing. Another major defect of CBD is the formation of an oxide layer on the wafer when it is rinsed with water. Moreover, the presence of dissolved oxygen in water may cause the oxidation of the nanomaterials during deposition. This can however be corrected

by purging the bath with nitrogen gas in order to reduce the levels of oxygen and carbon dioxide before deposition (Altiokka *et al.*, 2013). This further increases the cost of deposition. In addition, CBD has a terminal thickness defect which indicates the point where the growth of thin film stopped due to depletion of starting materials in the bath. This defect is usually observed when the film thickness is between 300–500 nm. Therefore, in order to get a film with sufficient thickness, e.g., about 1 μm , several successive depositions must be done (Abbas *et al.*, 2011). Although most reports on CBD have employed dual source approaches, a few of them have reported on the use of SSPs as starting materials. Kariper and Özpozan, (2013) have reported on the deposition of cobalt xanthate thin films using cobalt nitrate and isopropyl xanthate at a pH of 6.5. They studied the effect of temperature on the film thickness. An increase in the temperature from 30 to 50 °C caused a corresponding increase in film thickness from 198 to 454 nm. Altiokka *et al.*, (2013) have reported the deposition of PbS thin films with crystallite sizes between 23 and 37 nm by reacting lead nitrate, sodium hydroxide, thiourea in the presence of sodium sulfide as an oxygen scavenger using CBD. The effect of temperature on the band gap of orthorhombic PbBiS_2 thin films have been investigated using CBD. A decrease in temperature from 80 to 60 °C increased the band gap from 1.56 to 1.97 eV (Balasubramanian and Suriyanarayanan, 2013). The effect of the lead source (acetate, nitrate, chloride and sulphate) on the properties of chemically deposited PbS thin films have been investigated. Although XRD characterization of the films showed polycrystalline PbS nanomaterials with face centred cubic structure, morphology studies proved otherwise. The acetate source produced uniformly sized spherical grains with strong quantum confinements. The chloride and nitrate showed randomly oriented grains and agglomerated crystals of varying sizes respectively whereas the sulphate showed uniformly distributed nano-sized grains (Preetha and Remadevi, 2013). The same group of researchers have investigated the effect of substrate on chemically deposited PbSe thin films using soda lime and gold coin corning glass

slides. The PbSe deposited on soda lime glass substrate favoured crystallite growth by micro strain reduction. They concluded that the PbSe deposited on soda lime glass substrates have superior properties such as optical, morphological and structural properties as compared to the deposit on the gold coin corning glass slide (Preetha and Remadevi, 2014). PbSe thin films with thickness of 250 nm and crystallite diameter of 30–35 nm have been deposited from a chemical bath containing N, N-dimethylselenourea and lead nitrate at temperatures ranging from 30 to 60 °C at a deposition time of 2 hours (Barrios-Salgado *et al.*, 2011).

2.13.2 Chemical vapour deposition

Chemical vapour deposition (CVD), as a thin film fabrication method, has gained increasing attention due to its obvious advantages such as low cost, simplicity, high homogeneity at the molecular level, lower crystallization temperatures, controllability of film microstructures, good adhesion and scalability (Benjamin *et al.*, 2014). In order for a precursor to be suitable for CVD, it must be:

- (a) of high purity to prevent contamination of the deposited thin films.
- (b) reactive at the substrate surface to give the desired deposited thin film.
- (c) volatile to be brought into the gas phase at relatively low temperatures.
- (d) stable in air to avoid the need for specialist storage systems.
- (e) less toxic to avoid the environmental impact of the deposition process (Bakar *et al.*, 2012; Malik *et al.*, 2010).

There are several types of CVD based on the conditions used. These include metal-organic, aerosol assisted and atmospheric pressure chemical vapour deposition.

2.13.2.1 Metal-organic chemical vapour deposition (MOCVD)

MOCVD, which is sometimes referred to as metal organic vapour phase epitaxy, is one of the CVD techniques that relies on the gas phase transfer of volatile metal-organic or metal nitride complexes to be deposited on a substrate at high temperatures to form layers of thin films (Akhtar *et al.*, 2011; Choi and Park, 2014). The formation of the thin film is driven by the decomposition of the precursor and the chemical reaction that occurs at the surface of the substrate. Highly uniform films can be deposited using this technique because the sample can be rotated at high speed. However, the major drawback of this method is the unwanted side reactions that can occur at the high processing temperatures (Lemberger *et al.*, 2007). Therefore, it has not been an attractive pathway to the syntheses of thin films to most researchers. MOCVD is regarded as a suitable technique for the growth of highly oriented arrays of nanowires because of its good in-plane alignment on the substrate surface. However, its capability is somewhat limited in terms of ‘mass production’ of the nanowires (Lee *et al.*, 2004; Yang *et al.*, 2004). Bismuth telluride thin films have been deposited on GaAs substrate at 400 °C by MOCVD. Angle-resolved photoemission spectroscopy analysis on the deposited films showed that they could be used as topological insulators (Cao *et al.*, 2012).

2.13.2.2 Aerosol assisted chemical vapour deposition (AACVD)

AACVD, which is a sub-class of CVD, solves the volatility restrictions of most CVD method, thus, allowing the use of a wide range of precursors to deposit multi-component layers, thereby ensuring both reproducibility and homogeneity in the deposited layer. It is by far the most widely used among the CVD techniques. The morphology and size of the deposit can be closely controlled by the choice of solvent, deposition temperature, deposition time and by controlling

the frequency of the ultrasonic modulator (Abdelhady *et al.*, 2011; Bakar *et al.*, 2012; Ehsan *et al.*, 2012; Kevin *et al.*, 2015).

In AACVD, the precursor solution can be used to fabricate multi-component layers ensuring both reproducibility and the presence of all the components in the deposited layer. Furthermore, AACVD does not depend on the vapour pressure of the precursor or its volatility but rather the solubility of the precursor in the solvent (Akhtar *et al.*, 2011). More importantly, the aerosol droplet size can easily be varied by the frequency of the ultrasonic aerosol generator, which allows for the control of the deposition rate. With this degree of control, highly crystalline and uniform films can easily be tailored using this method (Bakar *et al.*, 2012). However, this method is expensive due to the extra cost of solvents and instrumentation (Akhtar *et al.*, 2011). AACVD has been widely used in the deposition of thin films at relatively high temperatures (Dilshad *et al.*, 2016). For example, in a research by Afzaal and co-workers (2004) using asymmetric lead dithiocarbamates, no significant deposition was observed below 400 °C whereas uniformly sized PbS cubes were observed at 400 °C. PbS nanocubes with approximate dimensions of 200 nm have been deposited from lead ethyl xanthate and its N donor - adducts at 350 °C using the AACVD techniques (Clark *et al.*, 2011). Ahmed *et al.*, (2010) confirmed that 300 °C was too low a temperature to initiate deposition of PbSe from lead phosphinodiselenoato SSPs using AACVD. However, a pure PbSe phase was obtained at a higher temperature of 400 °C.

2.13.2.3 Atmospheric pressure chemical vapour deposition (APCVD)

APCVD involves the deposition of thin films from both single and dual source starting materials at high temperatures. Uniformly deposited thin films can be achieved through control of temperature and gas flow. The morphologies can also be controlled by adjusting the

deposition position, temperature and the flux of the carrier gas (Li *et al.*, 2004). In the APCVD technique, the starting material is placed in a ceramic boat and inserted into a tube furnace. Substrates are arranged at the downstream end of the furnace. The carrier gas which is usually inert then acts as a transport medium to the deposition. The rate of flow of the inert gas results in the growth of the nanomaterials (Ge *et al.*, 2005). Some of the challenges associated with this technique include the extremely susceptibility of the nanomaterials to oxidation due to the greater gas density and residence time. Another challenge is the large volumes of liquid nitrogen used which makes it very expensive on commercial scale (Woods and Meyers, 2002). Titanium dioxide coatings on glass substrates have been achieved by the reaction of titanium chloride and a co-oxygen source (water, ethanol and methanol) at 500 °C using APCVD. The coatings show excellent uniformity, surface coverage and adherence (O'Neill *et al.*, 2003). Thin films of tungsten doped vanadium (IV) oxide on glass substrates prepared by APCVD have been used as a window coating (Manning and Parkin, 2004).

2.13.3 Interface between two immiscible liquids

The deposition of thin films at the interface between two immiscible liquids have been used to deposit thin films with nanoscopic grains from molecular precursors (Thomas *et al.*, 2013).

The two liquids are usually immiscible (Rao and Kalyanikutty, 2007). Typical examples include water-toluene, water-air and water-oil interfaces (Kim *et al.*, 2010; Sayed-Sweet *et al.*, 1997; Stansfield *et al.*, 2010). Deposition parameters such as concentration, time and temperature have a great effect on the assembly of the particulates (Fan *et al.*, 2008a). Largescale ordered arrays of nanoparticles may be obtained at the air–water interface using the Langmuir–Blodgett method (Duan *et al.*, 2004; Fan *et al.*, 2008a; Kalyanikutty *et al.*, 2006). PbS thin films have been deposited by the reaction of a toluene solution of lead cupferronate with the aqueous solution of sodium sulfide at 30 °C (Kalyanikutty *et al.*, 2006). PbS pyramids

have been deposited at the interface between a toluene solution of lead diethyldithiocarbamate and an aqueous solution of sodium sulfide at 50 °C for 2 hours (Fan *et al.*, 2008b). The pyramids had a square base and four triangular faces which spread across the entire watertoluene interface. Lead thiobiuret and lead diethyldithiocarbamate have been used as lead source for the syntheses of PbS thin films at a water toluene interface using Na₂S as sulfur source (Cant *et al.*, 2015).

2.13.4 Spin coating

Spin coating is a process of spreading a solution from the center of a wafer to the edges by centrifugal force (Wang and Möhwald, 2004). The spin coating process consists of several distinct stages (Figure 2.8). In the first stage, a drop of colloidal solution is deposited onto a substrate. Secondly, the substrate is then accelerated to a certain rotational speed and the liquid droplet spreads out to cover the whole substrate. In the third stage, the film becomes thinner due to equilibrium between centrifugal force and viscous shear force. Finally, the solvent evaporate, where the film thickness reduces to the same order as particle size (Fierro and Comninellis, 2010). The transition between the different stages depend notably on the volatility of the solvent (Colson *et al.*, 2011; Conceicao *et al.*, 2010; Ogi *et al.*, 2007).

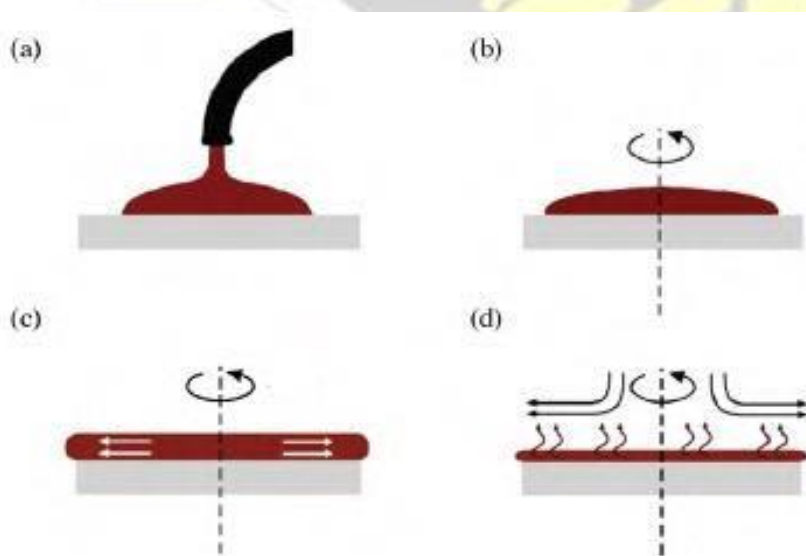


Figure 2.8 Schematic presentation of spin coating. (a) Deposition of the solution containing the mixture, (b) and (c) rotation of the support and (d) evaporation of the solvent

The spin coating technique, has recently become a favourite deposition technique to produce nanostructured thin films (Al-Juaid *et al.*, 2013; Aradia *et al.*, 2008; Jardim *et al.*, 2014). Spin coating is well established in the electronic and coating industries. For example, the spin coating technique has been used in the manufacture of compact discs, flat-screen televisions, light-emitting diodes, thin film transistors, electrochromic cells and photovoltaic devices (Mangrola *et al.*, 2013; McIntyre and Brush, 2010; Toolan *et al.*, 2013). In solid oxide fuel cell fabrication, the spin coating technique has gained attention because of its ability to produce thin electrolyte layers (Jasinski *et al.*, 2009). The advantage of spin coating technique over other deposition techniques is that the thickness of the deposited film can be varied based on the concentration of the solution, spinning speed and spinning time (Dunbar *et al.*, 2010; Lima and de Andrade, 2006; Nur *et al.*, 2012). A research on the effect on spinning speed on the morphology of TiO₂ showed that at a spinning speed of 600, 1000 and 2000 rpm, the morphology of the TiO₂ as seen from the TEM images were cubic, mixture of cubic and hexagonal, and hexagonal respectively (Pan and Lee, 2005). It is also reproducible and able to produce highly uniform multi-layered thin films (Burmam *et al.*, 2014). Furthermore, it is low cost and technically straight forward (Mitzi *et al.*, 2004; Nur *et al.*, 2012). The spin coating technique also provides a full coverage of the substrate easily (Aernouts *et al.*, 2004). Its application in the layer by layer deposition of hybrid solar cell materials have also been exploited (Al-Juaid *et al.*, 2013; Galagan *et al.*, 2013). Excellent compositional control, high homogeneity at the molecular level, lower crystallization temperatures, controllability of film microstructures, good adhesion and scalability are all attribute of the spin coating technique (Dunbar *et al.*, 2010; Ko *et al.*, 2011; Miyazaki *et al.*, 2013). The initial amount of solution deposited on the substrate has no adverse effect on the final film thickness since the solution

quickly equilibrate on the substrate (Chou *et al.*, 2005). Reproducibility has been reported as one remarkable property in the spin-coating process, which is well known since its early use for painting plane surfaces (Jardim *et al.*, 2014). A recent review spells out the spin coating technique as robust for producing polycrystalline films (Pichumani *et al.*, 2013). The approach is also advantaged in its short deposition time as compared with the traditional immersion methods (Leuw *et al.*, 2010; Liu *et al.*, 2003; Ogi *et al.*, 2007). The spin coating technique of device fabrication is also compatible with many traditional pre- or post-patterning processes (Liu *et al.*, 2013). Reports on both single and dual source starting materials are available although the former has been well researched into. The few reports on the latter include the deposition of CdSe thin films by spin coating a solution that contained 0.1M of cadmium chloride and 0.1 M of sodium selenosulphate (Rosmani *et al.*, 2013). The growth of Ag nanoparticles by reducing AgNO₃ spin coated onto a glass substrate has been reported (Sartale and Ansari, 2013). Polymeric multi-layered mirrors based on polyvinylcarbazole and cellulose acetate for application in the optics and lasers have been fabricated by spin coating technique (Komikado *et al.*, 2007). Metal-oxide-semiconductor capacitors embedded with gold nanoparticles which show good memory properties has been successfully fabricated by a spin coating approach (Leuw *et al.*, 2010). The effect of the spinning time on the efficiency of a polymer based solar cell has been investigated. Their results proved that the *J*_{sc} increased with increasing spinning time. This translates to a decreasing PCE with increasing time. The researchers varied the spinning time from 10 to 120 seconds and the highest PCE of 3.67% was obtained at 10 seconds of spinning time (Ohzeki *et al.*, 2014).

2.13.5 Melt reactions

Melt reactions involve the solventless thermolyses of complexes to form nanoparticles. It has been found to be a cost effective, simple and straight forward approach for the syntheses of

nanoparticles of metals and metal chalcogenides (Chen *et al.*, 2007). In this synthetic approach, the starting material serves as the source of metal, chalcogen and capping agent; which increases with bulkiness (Lewis *et al.*, 2014). Usually, the starting material is a solid at room temperature and nanoparticle synthesis is achieved through heating in the absence of a solvent, causing the precursor to melt and inducing thermal decomposition. The major advantage of this technique relies on the absence of solvent which offers potential for scale up and confers potential economic and environmental advantages including atom efficiency as compared to hot-injection and related methods (McNaughter and Saah *et al.*, 2016). The absence of solvent also eliminates collisions and interparticle diffusion during the syntheses, thus, having an effect on size and shape distributions (Sigman and Korgel, 2005). In literature, few researches exist on the solventless synthesis of nanoparticles. The first demonstration of the solventless syntheses of nanoparticles involved the thermal decomposition of the silver salts of fatty acids at 250 °C (Abe *et al.*, 1998). After this report, thiolates and xanthates have been reported to be efficient molecular precursors for solventless synthesis of nanoparticles. In all these class of complexes, the organic moiety around the central metal atom acts as the capping agent and therefore the bulkier the group, the better its self-capping activity (Chen *et al.*, 2007; Lewis *et al.*, 2014). The organic part of the complex is blown off the nanoparticle formed by the carrier gas which is usually inert. Tin ethyl xanthate has been used in the syntheses of tin sulfide with stoichiometries of Sn_{1.3}S and SnS by varying the reaction conditions in melt reaction (Alshakban *et al.*, 2016). A series of lead xanthate complexes have been explored as efficient starting materials to PbS at 150 °C. Analysis by SEM showed that the choice of the alkyl chain length had an influence on nanocrystal size and shape. The ethyl derivative showed a cubic morphology whereas the octyl showed the growth of a rod with a cube at the tip (McNaughter and Saah *et al.*, 2016).

2.13.6 Colloidal syntheses

The colloidal synthesis is regarded as the most widely studied approach to nanoparticle syntheses. Based on the synthetic pathway, colloidal syntheses are grouped into hot injection and heat up.

2.13.6.1 Hot injection

Generally, the hot injection approach involves the rapid injection of a precursor into a solvent at high temperature. This aids in the breaking down of the precursor to form highly crystalline nanoparticles. The rapid injection of the precursor solution leads to an instantaneous burst of homogenous nuclei by relieving the excess free energy in the supersaturated solution (Abdulwahab *et al.*, 2013; Park *et al.*, 2007). However, the gradual depletion of starting precursor and sudden drop in temperature associated with the injection of the precursor solution prevents further nucleation. This stage is followed by growth which is consistent with “Ostwald ripening”, where the high surface energy of small crystallites make them less stable therefore dissolving in the solvent as described in the LaMer model (Murray *et al.*, 1993). In order to synthesise uniformly sized monodispersed nanoparticles, the nucleation and growth stages must be separated. This is achieved through the rapid injection of the precursor solution at a temperature lower than the hot solvent. The drop in temperature reduces the rate of nucleation and all the nuclei grow at the same rate leading to highly monodispersed nanoparticles (Cui *et al.*, 2012). Murray and co-workers (1993) were the first group of researchers to report the syntheses of nanoparticles using this technique. The researchers employed dimethyl cadmium and trioctylphosphine selenium as sources of metal and chalcogen to synthesize CdSe nanoparticles (Murray *et al.*, 1993). However, the use of pyrophoric and air sensitive starting materials limit this technique to be employed on industrial scale. This challenge opened a new

window to the single source approach which is less toxic. To date, there are numerous reports on the use of SSPs for the syntheses of metal chalcogenide nanoparticles. The interest in this route relies on the careful design of complexes which provide relevant elements (metal and chalcogen) whilst suppressing impurity and toxic by-products associated with the multiple source route. Reports on hot injection encompass the use of both single and multiple source starting materials although much attention has focussed on the single source approach in recent times (Nyamen *et al.*, 2014). Some of the commonly used solvents and capping agents include phosphines (eg. trioctylphosphine and trioctylphosphine oxide), carboxylic acids (eg. oleic acid), thiols (eg. dodecanethiol) and long chain amines (eg. hexadecyl amine and oleylamine). The choice of solvent and capping agent has a great effect on the properties of the nanoparticles formed. The effect of capping agent on the morphology of PbS nanocrystals synthesized at 200 °C have been reported (Wang *et al.*, 2012). Different shapes such as octahedral, star like, cubic and truncated cubic were obtained when dodecanethiol, octadecene, oleic acid and oleylamine were used as capping agent respectively. The difference in shape is as a result of the different growth mechanisms due to the binding effect.

2.13.6.2 Heat up

This approach to nanoparticle synthesis is also referred to as non-injection method. In this reaction pathway, all reagents are mixed into a reaction vessel and heated controllably to induce the nucleation and growth of nanoparticles (Kwon and Hyeon, 2011). In this approach, the nucleation and growth processes are driven by temperature. For instance, at low temperatures, the reaction solution is largely comprised of the starting material either as single or dual source. As the reaction continues to heat, the starting materials experience an increased thermodynamic driving force to form monomers (Timonen *et al.*, 2011). This eventually triggers nucleation followed by growth of the nanoparticles (Embden *et al.*, 2015). The heat up approach addresses

some challenges associated with the hot injection technique. For example, in the hot injection technique, the injection time often varies which can affect the reaction kinetics which hinders reproducibility. There is also the possibility of large scale syntheses of nanoparticles which is not achievable in the hot injection technique (Chiang *et al.*, 2011; Shavel *et al.*, 2016). It is also simple and technically straight-forward (Park *et al.*, 2007). However, some challenges associated with the heat up approach is that there must be a great understanding into the chemistry of the starting materials and the solvents used. In addition, nucleation is very rapid and a large amount of nuclei are generated within a relatively short period of time. This can lead into the formation of large particles over a short period of time because of the high surface energy of the nanoparticles high temperatures ($> 200\text{ }^{\circ}\text{C}$) (Kwon and Hyeon, 2011; Yang *et al.*, 2005). Monodispersed CdSe nanospheres with diameters of 4 nm have been synthesized using the heat up method with ODE as solvent and cadmium myristate as the precursor at $240\text{ }^{\circ}\text{C}$ (Yang *et al.*, 2005). A similar pathway has been used to synthesize monodispersed iron oxide from iron oleate precursor at $320\text{ }^{\circ}\text{C}$ (Kwon *et al.*, 2007).

2.13.6.3 Green syntheses of nanoparticles

Conventional colloidal syntheses rely on the use of organic chemicals as capping agents and solvents. These chemicals limit large scale production of nanoparticles due to cost and toxicity. Poor surface passivation and photosensitivity with capping agents such as phosphines and thiols can accelerate the degradation of nanoparticles after their preparation (Akhtar *et al.*, 2010). Another challenge is that most of the precursors have low solubility in the solvent, therefore reducing the concentration of the precursor in the injection solution. One of the solutions to these challenges is to consider greener approaches to nanoparticle syntheses. The fundamental principle underlying the greener synthetic route to nanoparticle synthesis, is to reduce chemical hazards and cost without compromising on the properties of the nanoparticles.

Akhtar *et al.*, (2010) developed a synthetic pathway using a dual source route to the syntheses of PbS quantum dots at 60 °C using olive oil as an alternative for the conventional air sensitive, toxic and expensive capping agent. A single source approach using heterocyclic dithiocarbamate complexes have been investigated in the syntheses of PbS nanoparticles in olive oil. Nearly uniformly shapes PbS nanocubes with average size of about 20 nm were obtained using olive oil stabilized at 180 °C (Nyamen *et al.*, 2014). Olive oil capped CdSe nanoparticles have been used in the fabrication of a light emitting device with the structure ITO/P3HT/CdSe/Al using the bi-layer approach. The device showed strong electroluminescent characteristics (Bera *et al.*, 2012). Anacardic acid, which is a non-edible green solvent has been used as capping agent for the syntheses of PbE nanoparticles at temperatures of 140 or 160 °C. The anacardic acid was capped to the surface of the nanoparticles, resulting to the formation of highly monodispersed nanospheres and cubes (Mlowe *et al.*, 2013). Castor oil has also been employed in the syntheses of spherical CdSe nanoparticles with diameters ranging between 3.81 to 6.80 nm depending on the reaction conditions (Kyobe *et al.*, 2015). Biosynthesis of nanoparticles from plant sources have been reported to be more stable, and the rate of synthesis is faster (Ramesh *et al.*, 2014). Silver nitrate have been reduced in the presence of the leaf extract of *Lantana camera L.* and fruit extract of *Momordica charantia* to form silver nanoparticles. The formation of the nanoparticles were confirmed with p-XRD analyses (Nahar *et al.*, 2015; Sambandan *et al.*, 2015). Gold nanoparticles have been synthesized using hot aqueous olive leaf extract (Khalil *et al.*, 2012). Flower extract of *Cassia auriculata* has been used as a stabilizing and reducing agent for the synthesis of zinc oxide nanoparticles (Ramesh *et al.*, 2014).

2.13.6.4 Stages in colloidal syntheses

The major stages in the colloidal syntheses include nucleation and growth as reported in the LaMer model (Figure 2.9) (Kwon and Hyeon, 2011). However, balancing the nucleation and growth rates represent one of the major challenges associated with this method, as both processes have different activation energies and reaction orders (Kovalenko *et al.*, 2008).

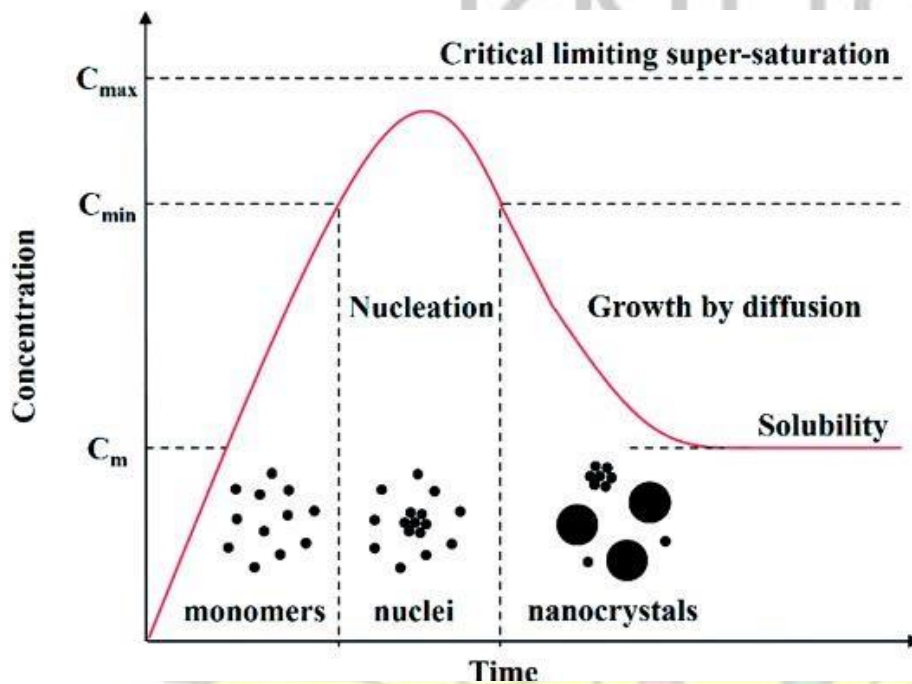


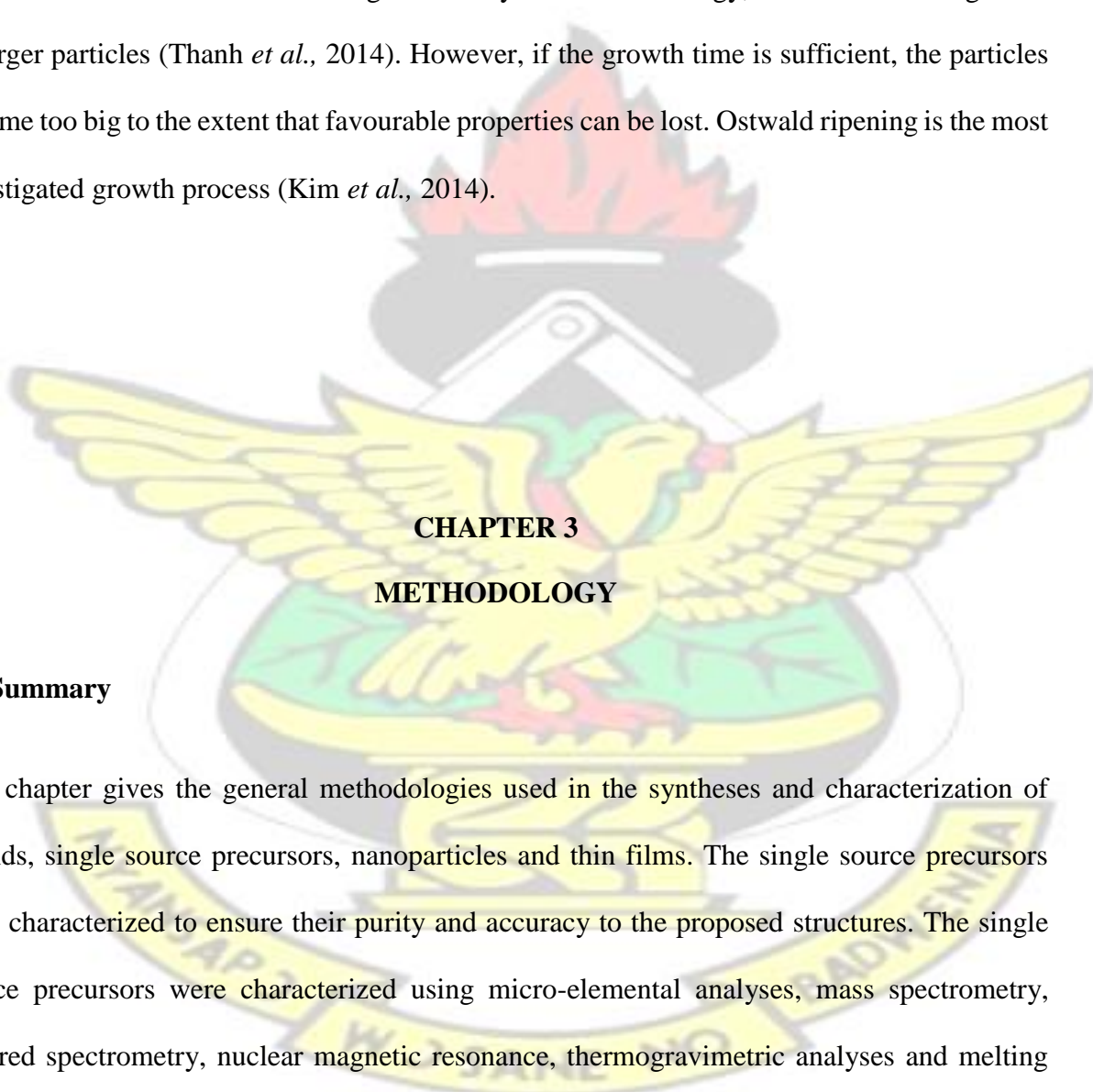
Figure 2.9 Stages in colloidal syntheses

2.13.6.4.1 Nucleation

Nucleation is defined as the process whereby a seed is produced either homogeneously or heterogeneously (Thanh *et al.*, 2014). Homogeneous nucleation occurs away from the surface whereas heterogeneous nucleation occurs on the surface of the system (Chatterjee *et al.*, 2017). In classical nucleation theory, heterogeneous nucleation occurs much faster and slows exponentially with the height of a free energy barrier. This barrier comes from the free energy penalty at the surface of the growing nucleus (Park *et al.*, 2007). In colloidal systems, homogeneous nucleation is paramount (Kügler *et al.*, 2016). The nuclei form uniformly within the solvent. However, the presence of impurities cause a level of inhomogeneity. Nucleation can be controlled by temperature kinetics (Timonen *et al.*, 2011).

2.13.6.4.2 Growth

Growth basically involves the coming together of nuclei with different sizes and shapes. It occurs either by diffusion or coalescence. This growth mechanism is caused by the change in solubility of the different sizes of the nuclei. The smaller particles break down and re-dissolve back into the solution due to their high solubility and surface energy, which lead to the growth of larger particles (Thanh *et al.*, 2014). However, if the growth time is sufficient, the particles become too big to the extent that favourable properties can be lost. Ostwald ripening is the most investigated growth process (Kim *et al.*, 2014).



CHAPTER 3 METHODOLOGY

3.1 Summary

This chapter gives the general methodologies used in the syntheses and characterization of ligands, single source precursors, nanoparticles and thin films. The single source precursors were characterized to ensure their purity and accuracy to the proposed structures. The single source precursors were characterized using micro-elemental analyses, mass spectrometry, infrared spectrometry, nuclear magnetic resonance, thermogravimetric analyses and melting point determination. After these, the single source precursors were used as starting precursors for the syntheses of thin films and nanoparticles. The thin films and nanoparticles were also characterized using powder X-ray diffractometry (p-XRD), scanning electron microscopy

(SEM), transmission electron microscopy (TEM), energy dispersive X-ray spectroscopy (EDX), ultra violet-visible-near infrared spectroscopy (uv-vis-nir) and inductively coupled plasma analyses (ICP).

Table 3.1 List of chemicals and reagents

Number		Grade	% Purity
1	Ethanol	Laboratory reagent	≥99.8
Chemicals and reagents			
2	1-Propanol	Laboratory reagent	99.5
3	1-Butanol	Laboratory reagent	99.8
4	1-Hexanol	Laboratory reagent	99.8
5	1-Octanol	Laboratory reagent	≥99
6	1-Dodecanol	Laboratory reagent	98
7	Tetramethylethylenediamine	Laboratory reagent	98
8	Bismuth nitrate pentahydrate	Laboratory reagent	95
<hr/>			
9	Oleylamine	Laboratory reagent	95
10	Carbon disulphide	Laboratory reagent	≥99
11	Lead acetate trihydrate	Laboratory reagent	≥99.99
12	2-naphthoyl chloride	Laboratory reagent	99.8
13	Potassium selenocyanate	Laboratory reagent	95
14	Diethylamine	Laboratory reagent	≥99.5
15	Sodium ethoxide	Laboratory reagent	95
16	Sodium thiocyanate	Laboratory reagent	95
17	Trioctylphosphine	Technical reagent	90
18	1-Octadecene	Technical reagent	90
19	Piperidine	Laboratory reagent	98

20	Diethyl ether	Laboratory reagent	≥99.9
21	Acetone	Laboratory reagent	≥99.9
22	Acetonitrile	Laboratory reagent	99.8
23	Hexane	Laboratory reagent	95
24	Chloroform	Laboratory reagent	≥99
25	Petroleum ether	Laboratory reagent	≥90
26	Toluene	Laboratory reagent	99.8
27	Potassium hydroxide	Laboratory reagent	≥85
28	Sodium hydroxide	Laboratory reagent	≥85
29	Methanol	Laboratory reagent	99.5
30	Triethylamine	Laboratory reagent	95
31	1, 10 phenanthroline	Laboratory reagent	99.9
32	Pyridine	Laboratory reagent	99

3.2 Syntheses and characterization of ligands and complexes

All chemicals and reagents were purchased and used as received from Sigma-Aldrich, United Kingdom with no further purification unless otherwise stated. Generally, the metal salt was reacted with the appropriate ligand to form a precipitate. The precipitate was then filtered, washed, recrystallized and dried to obtain the pure complex. The complex was then characterized using techniques such as micro-elemental analyses, ^1H NMR, FT-IR, melting point determination, thermogravimetric analyses and mass spectrometry.

3.2.1 Synthesis of *bis*(diethyldithiocarbonato)lead(II) complex (1)

In a round bottom flask, ethanol (1.8 g, 40.0 mmol), sodium hydroxide (1.6 g, 40.0 mmol) and distilled water (50 ml) were stirred until complete dissolution at room temperature. The mixture was then cooled to 0 °C and CS₂ (3.1 g, 40.0 mmol) added. After an hour of stirring, lead acetate trihydrate (7.6 g, 20.0 mmol) dissolved in distilled water (50 ml) was added to the ligand. The precipitate formed was filtered, washed with water and dried. The crude sample was recrystallized from acetone to yield *bis*(diethyldithiocarbonato)lead(II) as a yellowish complex. The yield was 86.4 %. The micro-elemental results were as follows; Calc (found): C, 16.0 (16.1); H, 2.3 (2.3); S, 28.5 (28.5); and Pb, 46.1 (45.9). The melting point was 108 °C. MS (ESI), m/z = [M⁺] 450. $\nu_{(C-O)}$ 1098 cm⁻¹, $\nu_{(C-S)}$ 1020 cm⁻¹. ¹H NMR (400 MHz, CDCl₃), δ : 1.45 (t, *J* = 7.1 Hz, 6H; CH₃) and 4.71 (m, *J* = 7.1 Hz, 4H; CH₂).

3.2.2 Synthesis of *bis*(dipropyldithiocarbonato)lead(II) complex (2)

This was synthesized through similar steps described for complex (1) with ethanol (1.8 g, 40.0 mmol) replaced with 1-propanol (2.4 g, 40.0 mmol). The crude sample was recrystallized from acetone and dried under vacuum to yield *bis*(dipropyldithiocarbonato)lead(II) as a yellowish complex. The yield was 85.9 %. The micro-elemental results were as follows; Calc (found): C, 20.1 (19.8); H, 2.9 (2.7); S, 26.8 (26.6) and Pb, 43.3 (42.3). The melting point was 85 °C. MS (ESI), m/z = [M⁺] 478. $\nu_{(C-O)}$ 1085 cm⁻¹, $\nu_{(C-S)}$ 1015 cm⁻¹. ¹H NMR (400 MHz, CDCl₃), δ : 1.08 (t, *J* = 7.4 Hz, 6H; CH₃), 1.92 (m, 6H, CH₂) and 4.61 (t, *J* = 6.7 Hz, 4H; CH₂).

3.2.3 Synthesis of *bis*(dibutyldithiocarbonato)lead(II) complex (3)

This was synthesized through similar steps described for complex (1) with ethanol (1.8 g, 40.0 mmol) replaced with 1-butanol (3.0 g, 40.0 mmol). The crude sample was recrystallized from acetonitrile and dried under vacuum to yield *bis*(dibutyldithiocarbonato)lead(II) as a yellowish complex. The yield was 85.8 %. The results from the micro-elemental analyses were as follows; Calc (found): C, 23.8 (23.9); H, 3.6 (3.6); S, 25.4 (25.4); and Pb, 40.9 (40.9). The melting point was 81 °C. MS (ESI), $m/z = [M^+]$ 506. $\nu_{(C-O)}$ 1056 cm^{-1} , $\nu_{(C-S)}$ 1011 cm^{-1} . 1H NMR (400 MHz, $CDCl_3$), δ : 0.97(t, $J = 7.3$ Hz, 4H; CH_3), 1.48 (m, 6H; CH_2), 1.88 (m, 4H; CH_2) and 4.65 (t, $J = 6.6$ Hz, 4H, CH_2).

3.2.4 Synthesis of *bis*(dihexyldithiocarbonato)lead(II) complex (4)

This was synthesized through similar steps described for complex (1) with ethanol (1.8 g, 40.0 mmol) replaced with 1-hexanol (4.1 g, 40.0 mmol). The crude sample was recrystallized from acetonitrile and dried under vacuum to yield *bis*(dihexyldithiocarbonato)lead(II) as a yellowish complex. The yield was 83.9 %. The results from the micro-elemental analysis were as follows; Calc (found): C, 29.9 (30.1); H, 4.7 (4.7); S, 22.8 (22.8); and Pb, 36.8 (36.6). The melting point was 60 °C. MS (ESI), $m/z = [M^+]$ 562. $\nu_{(C-O)}$ 1072 cm^{-1} , $\nu_{(C-S)}$ 1045 cm^{-1} . 1H NMR (400 MHz, $CDCl_3$), δ : 0.91(t, $J = 7.1$ Hz, 4H; CH_3), 1.39 (m, 5H; CH_2), 1.89 (m, 4H; CH_2) and δ : 4.64 (t, $J = 6.7$ Hz, 4H, CH_2).

3.2.5 Synthesis of *bis*(dioctyldithiocarbonato)lead(II) complex (5)

This was synthesized through similar steps as (1) with ethanol (1.8 g, 40.0 mmol) replaced with 1-octanol (5.2 g, 40.0 mmol). The crude sample was recrystallized from acetonitrile and dried

under vacuum to yield *bis*(dioctyldithiocarbonato)lead(II) as a yellowish complex. The yield was 82.4 %. The results from the micro-elemental analysis were as follows; Calc (found): C, 34.9 (35.0); H, 5.5 (5.9); S, 20.7 (20.5); and Pb, 33.6 (33.5). The melting point was 78 °C. MS (ESI), $m/z = [M^+]$ 618. $\nu_{(C-O)}$ 1084 cm^{-1} , $\nu_{(C-S)}$ 1014 cm^{-1} . 1H NMR (400 MHz, $CDCl_3$), δ : 0.89(t, $J = 6.9$ Hz, 4H; CH_3), 1.36 (m, 5H; CH_2), 1.89 (m, 4H; CH_2) and 4.64 (t, $J = 6.7$ Hz, 4H, CH_2).

3.2.6 Synthesis of dodecyldithiocarbonato ligand (6)

In a round bottom flask, 1-dodecanol (7.4 g, 40.0 mmol) and potassium hydroxide (2.2 g, 40.0 mmol) were melted together at 200 °C. Upon melting, heating was stopped and the hot suspension allowed to cool to 100 °C. At this temperature, toluene (25 ml) was added and stirring continued. The suspension was cooled further below 25 °C and carbon disulfide (4.6 g, 60.0 mmol) added drop wise and the resulting mixture stirred for an hour. After this, petroleum ether (100 ml) was added and the mixture stirred further for two hours. The precipitate was filtered, washed with water/petroleum ether at 1:2 ratio and vacuum dried to yield the dodecyldithiocarbonato ligand. The yield was 90.2 %. The micro-elemental results were as follows; Calc (found): C, 59.7(59.6); H, 9.6 (9.7); and S, 24.6 (24.4).

3.2.7 Synthesis of *bis*(didodecyldithiocarbonato) lead(II) complex (7)

In a three-necked flask, didodecyldithiocarbonato ligand (6); (5.0 g, 19.2 mmol) was stirred in methanol (20 ml) until complete dissolution. A lead acetate solution containing lead acetate trihydrate (3.6 g, 9.6 mmol) was added drop wise to the ligand which caused the formation of a precipitate. The resulting mixture was stirred for an hour, filtered, washed several times with water and vacuum dried. The crude sample was recrystallized from toluene and air dried to

yield *bis*(didodecyldithiocarbonato) lead(II) as a brown complex. The yield was 82.1 %. The micro-elemental results were as follows; Calc (found): C, 42.8 (43.3); H, 6.9 (7.0); S, 17.6 (17.4); and Pb 28.4 (27.6). The melting point was 87 °C. MS (ESI), $m/z = [M^+Na]$ 754. $\nu_{(C-O)}$ 1099 cm^{-1} , $\nu_{(C-S)}$ 1015 cm^{-1} . 1H NMR (400 MHz, $CDCl_3$), δ : 0.89 (t, $J = 7.1$ Hz, 4H; CH_3), 1.34 (m, 5H; CH_2), 1.88 (m, 4H; CH_2), 3.65 (t, $J = 6.6$ Hz, 4H, CH_2) and 4.64 (t, $J = 6.7$ Hz, 4H, CH_2).

3.2.8 Synthesis of potassium ethylxanthogenate ligand (8)

In a round bottom flask, ethanol (1.8 g, 40.0 mmol) and potassium hydroxide (2.2 g, 40.0 mmol) were stirred until complete dissolution at room temperature. The mixture was then cooled to 0 °C and carbon disulfide (3.1 g, 40.0 mmol) added drop wise to the resulting mixture which was stirred further for an hour. The yellow precipitate was filtered and air dried. The crude product was then recrystallized in acetone to yield the pure potassium ethylxanthogenate ligand. The micro-elemental results were as follows; Calc (found): C, 22.5 (22.4); H, 3.1 (3.0); and S, 20.0 (19.9). The melting point was 226 °C.

3.2.9 Synthesis of bismuth ethyl xanthate complex (9)

Potassium ethylxanthogenate ligand (8); (12.0 g, 74.8 mmol) was dissolved in distilled water (100 ml). Bismuth nitrate pentahydrate (12.1 g, 24.9 mmol) was stirred in distilled water (100 ml) in a round bottom flask. The aqueous potassium ethylxanthogenate ligand was transferred into a dropping funnel and added drop-wise to the bismuth nitrate pentahydrate solution resulting in the formation of the precipitate. The precipitate was filtered, washed several times with distilled water and air dried. The crude sample was recrystallized from acetone and dried under vacuum to yield bismuth ethyl xanthate as a yellowish complex. The yield was 82.7 %.

The micro-elemental results were as follows; Calc (found): C, 18.8 (18.7); H, 2.6 (2.5); S, 33.6 (33.5); and Bi, 36.5 (36.3). The melting point was 103 °C. ¹H NMR (400 MHz, CDCl₃), δ: 1.46 ppm (t, 9H; CH₃) and 4.66 ppm (m, *J* = 7.1 Hz, 6H; CH₂). $\nu_{(C-O)}$ 1096 cm⁻¹, $\nu_{(C-S)}$ 1020 cm⁻¹.

3.2.10 Synthesis of tetramethylethylenediamine (TMEDA) adduct of bismuth ethyl xanthate complex (10)

In a round bottom flask, bismuth nitrate pentahydrate (12.1 g, 24.9 mmol) and TMEDA (2.9 g, 24.9 mmol) were stirred in distilled water (100 ml) in a round bottom flask. An aqueous solution of ligand (8) containing potassium ethylxanthogenate (12.0 g, 74.8 mmol) was added resulting in the formation of a precipitate. The precipitate was filtered, washed several times with distilled water and air dried. The crude sample was recrystallized from acetone and dried under vacuum to yield TMEDA adduct of bismuth ethyl xanthate as a yellowish complex. The yield was 80.7 %. The micro-elemental results were as follows; Calc (found): C, 26.2 (26.0); H, 4.5 (4.4); N, 4.1 (4.0); S, 27.9 (27.7); and Bi, 30.3 (30.5). The melting point was 79 °C. ¹H NMR (400 MHz, CDCl₃), δ: 1.54 ppm (t, *J* = 7.1 Hz, 6H; CH₃), 1.60 ppm (s, 6H; CH₃), 2.20 ppm (m, 4H; CH₂) and 4.75 ppm (m, *J* = 6.9 Hz, 6H; CH₂). $\nu_{(C-O)}$ 1105 cm⁻¹, $\nu_{(C-S)}$ 1020 cm⁻¹, $\nu_{(C-N)}$ 1282 cm⁻¹.

3.2.11 Synthesis of triethylamine adduct of bismuth ethyl xanthate complex (11)

This was synthesized through the same steps as (10) with TMEDA replaced with triethylamine (2.5 g, 24.9 mmol). The yield was 81.3 %. The micro-elemental results were as follows; Calc (found): C, 26.7 (26.5); H, 4.5 (4.3); N, 2.1 (2.0); S, 28.6 (28.7); and Bi, 31.0 (30.9). Melting point 80 °C. ¹H NMR (400 MHz, CDCl₃), δ: 1.40 ppm (t, *J* = 7.3 Hz, 9H; CH₃), 1.53 ppm (m,

6H; CH₂), 3.25 ppm (m, $J = 7.4$ Hz 9H; CH₃) and 4.73 ppm (m, $J = 7.3$ Hz, 6H; CH₂). $\nu_{(C-O)}$ 1105 cm⁻¹, $\nu_{(C-S)}$ 1013 cm⁻¹, $\nu_{(C-N)}$ 1282 cm⁻¹.

3.2.12 Synthesis of 1, 10 phenanthroline adduct of bismuth ethyl xanthate complex (12)

This was synthesized through the same steps as (10) with TMEDA replaced with 1, 10 phenanthroline (4.5 g, 24.9 mmol). The yield was 80.5 %. The micro-elemental results were as follows; Calc (found): C, 33.5 (33.6); H, 3.1 (3.0); N, 3.7 (3.7); S, 25.6 (27.2); and Bi, 27.8 (28.1). The melting point was 102 °C. ¹H NMR (400 MHz, CDCl₃), δ : 1.50 ppm (t, $J = 7.0$ Hz, 9H; CH₃), 1.58 ppm (m, 6H; CH₂), 2.20 ppm (s, CH) and 4.69 ppm (m, $J = 7.1$ Hz, 6H; CH₂). $\nu_{(C-O)}$ 1105 cm⁻¹, $\nu_{(C-S)}$ 1013 cm⁻¹, $\nu_{(C-N)}$ 1289 cm⁻¹.

3.2.13 Synthesis of pyridine adduct of bismuth ethyl xanthate complex (13)

This was synthesized through the same steps as (10) with TMEDA replaced with pyridine (2.0 g, 24.9 mmol). The yield was 79.9 %. The micro-elemental results were as follows; Calc (found): C, 25.8 (25.9); H, 3.1 (2.9); N, 2.2 (2.1); S, 29.5 (29.4); and Bi, 32.1 (32.1). The melting point was 99 °C. MS (ESI), $m/z = [M^+Cl^-]$ 692. ¹H NMR (400 MHz, CDCl₃), δ : 1.30 ppm (t, 9H; CH₃), 2.20 ppm (m, 5H; CH) and 4.75 ppm (m, $J = 7.3$ Hz, 6H; CH₂). $\nu_{(C-O)}$ 1105 cm⁻¹, $\nu_{(C-S)}$ 1020 cm⁻¹, $\nu_{(C-N)}$ 1274 cm⁻¹.

3.2.14 Synthesis of *N, N*-diethyl- *N'*-naphthoylselenourea ligand (14)

In a roundbottom flask, acetone solution of 2-naphthoyl chloride (9.2 g, 48.6 mmol) was added to acetone solution of potassium selenocyanate (7.0 g, 48.6 mmol) under nitrogen gas and refluxed. The content of the flask changed from white to greenish yellow. Addition of diethyl

amine (5.0 ml, 48.6 mmol) in acetone changed the colour of the mixture from dirty green to orange red. After five minutes of stirring, 100 ml of anhydrous diethyl ether was added and the flask left undisturbed. The *N, N*-diethyl- *N'*-naphthoylselenourea was extracted into the ether layer (top layer) and separated from the bottom layer. The ether layer was left to evaporate to yield a red solid which was recrystallized from ethanol to yield yellow crystals of *N, N*-diethyl- *N'*-naphthoylselenourea ligand. The yield was 85.4 %. The micro-elemental results were as follows; Calc (found): C, 57.7 (57.5); H, 5.5 (5.8); N, 8.4 (8.4). The melting point was 126 °C. $\nu_{(C-O)}$ 1680 cm^{-1} , $\nu_{(C-N)}$ 1390 cm^{-1} and $\nu_{(C-Se)}$ 1190 cm^{-1} . $^1\text{HNMR}$ (CDCl_3 , 400 MHz), δ : 1.32 (t, CH_3), 1.41 (t, CH_3), 3.64 (q, CH_2), 4.14 (q, CH_2), 7.87 (m, Ar), 8.36 (s, NH).

3.2.15 Synthesis of *bis(N, N*-diethyl- *N'*-naphthoylselenoureato) lead(II) complex (15)

Ligand (14), (4.0 g, 12.0 mmol) was stirred in 100 ml of ethanol until complete dissolution under nitrogen gas. Then sodium ethoxide (0.8 g, 12 mmol) was added followed by a lead acetate solution containing lead (II) acetate (2.3 g, 6.0 mmol) also dissolved in distilled water (60 ml). The addition of the lead solution resulted in the formation of a precipitate. The mixture was stirred for 30 minutes to ensure complete reaction. The precipitate was filtered, washed with water and vacuum dried. The crude product was recrystallized from toluene and precipitated with hexane. The yield was 81.7 %. The micro-elemental results were as follows; Calc (found): C, 44.1 (44.6); H, 3.9 (3.5); N, 6.4 (6.3); Pb, 23.8 (23.9). The melting point was 152 °C. MS (ESI), $m/z = [M^+]$ 873. $\nu_{(C-O)}$ 1490 cm^{-1} , $\nu_{(C-N)}$ 1400 cm^{-1} and $\nu_{(C-Se)}$ 883 cm^{-1} . $^1\text{HNMR}$ (CDCl_3 , 400 MHz): 1.09 (t, CH_3), 1.26 (t, CH_3), 3.79 (q, CH_2), 3.87 (q, CH_2), 7.81 (m, Ar).

3.2.16 Synthesis of *N, N*-diethyl- *N'*-naphthoylthiourea ligand (16)

Ligand (16) was synthesized through similar steps as ligand (14) with slight modifications. Typically, acetone solution of 2-naphthoyl chloride (9.2 g, 48.6 mmol) was added to acetone solution of sodium thiocyanate (7.0 g, 48.6 mmol) under nitrogen gas and refluxed. The mixture changed from white to greenish yellow. Addition of diethyl amine (5.0 ml, 48.6 mmol) in 20 ml acetone changed the colour from dirty green to orange red. After five minutes of stirring, 100 ml of anhydrous diethyl ether was added and the flask left undisturbed. The *N, N*-diethyl-*N'*-naphthoylthiourea was extracted into the ether layer (top layer) and separated from the bottom layer. The ether layer was left to evaporate to yield a red solid which was recrystallized from ethanol to yield yellow cubic crystals of *N, N*-diethyl-*N'*-naphthoylthiourea ligand. The yield was 86.4 %. The micro-elemental results were as follows; Calc (found): C, 57.7 (57.5); H, 5.5 (5.8); N, 8.4 (8.4). The melting point was 106 °C. $\nu_{(C-O)}$ 1650 cm^{-1} , $\nu_{(C-N)}$ 1380 cm^{-1} and $\nu_{(C-Se)}$ 1210 cm^{-1} . $^1\text{H NMR}$ (CDCl_3 , 400 MHz), δ : 1.32 (t, CH_3), 1.41 (t, CH_3), 3.64 (q, CH_2), 4.14 (q, CH_2), 7.87 (m, Ar), 8.36 (s, NH).

3.2.17 Synthesis of *bis*(*N, N*-diethyl- *N'*- naphthoylthioureato) lead(II) complex (17)

Complex (17) was synthesized through the same steps as complex (15) with ligand (14) replaced with ligand (16). Typically, ligand (16), (3.4 g, 12.0 mmol) was stirred in 100 ml of ethanol until complete dissolution under nitrogen gas. Sodium ethoxide (0.8 g, 12.0 mmol) was added followed by a lead acetate solution containing lead (II) acetate (2.3 g, 6.0 mmol) also dissolved in distilled water (60 ml). The addition of the lead solution resulted in the formation of a precipitate which was filtered, washed several times with water and vacuum dried. The crude product was recrystallized from toluene and precipitated with hexane. The yield was 81.7

% . The micro-elemental results were as follows; Calc (found): C, 49.4 (49.7); H, 4.4 (4.7); N, 7.2 (7.1); S, 8.2 (8.1); Pb, 26.6 (26.4). The melting point was 190 °C. MS (ESI), $m/z = [M^+]$ 779. $\nu_{(C-O)}$ 1490 cm^{-1} , $\nu_{(C-N)}$ 1400 cm^{-1} and $\nu_{(C-Se)}$ 893 cm^{-1} . 1H NMR ($CDCl_3$, 400 MHz): 1.09 (t, CH_3), 1.26 (t, CH_3), 3.79 (q, CH_2), 3.87 (q, CH_2), 7.81 (m, Ar).

3.2.18 Synthesis of sodium piperidine dithiocarbamate ligand (18)

In a round bottom flask, piperidine (8.5 g, 100.0 mmol), sodium hydroxide (4.0 g, 100.0 mmol) and distilled water (25 ml) was stirred for an hour at room temperature. The mixture was cooled to 0 °C and carbon disulfide (7.6 g, 100.0 mmol) added drop wise to the mixture to form a precipitate. After 15 minutes, the precipitate was filtered and air dried to yield the sodium piperidine dithiocarbamate ligand. The yield was 92.5%. The micro-elemental results were as follows; Calc (found): C, 35.8 (35.7); H, 6.0 (6.0); N, 7.0 (6.9). $\nu_{(O-H)}$ 3362 cm^{-1} , $\nu_{(C-N)}$ 1418 cm^{-1} and $\nu_{(C-S)}$ 964 cm^{-1} .

3.2.19 Synthesis of lead piperidine dithiocarbamate complex (19)

Ligand (18), (5.5 g, 30.0 mmol) was stirred in distilled water (25 ml) until complete dissolution. Lead acetate trihydrate (5.7 g, 10.0 mmol) dissolved in distilled water (25 ml) was added drop wise to the sodium piperidine dithiocarbamate ligand. The reaction mixture was stirred for one hour, and the precipitate was filtered, washed with excess distilled water and dried overnight in an oven at 70 °C. The yield was 90.3 %. The micro-elemental results were as follows; Calc (found): C, 27.3 (27.3); H, 3.8 (3.7); N, 5.3 (5.2). The melting point was 239 °C. $\nu_{(C-N)}$ 1427 cm^{-1} and $\nu_{(C-S)}$ 968 cm^{-1} .

3.2.20 Synthesis of bismuth piperidine dithiocarbamate complex (20)

Complex (20) was synthesized through similar steps as complex (19). Typically, aqueous solution of sodium piperidine dithiocarbamate ligand (5.5 g, 30.0 mmol) was added drop wise to bismuth nitrate pentahydrate (4.9 g, 10.0 mmol) dissolved in distilled water (25 ml) to form a precipitate. The precipitate was filtered, washed with excess distilled water and dried overnight in an oven at 70 °C. The yield was 87.8 %. The micro-elemental results were as follows; Calc (found): C, 31.3 (31.2); H, 4.4 (4.3); N, 6.1 (6.0). Melting point 195 °C. $\nu_{(C-N)}$ 1435 cm^{-1} and $\nu_{(C-S)}$ 977 cm^{-1} .

3.3 Characterization of complexes

3.3.1 Nuclear magnetic resonance spectroscopy (NMR)

Nuclear magnetic resonance spectroscopy (NMR) is an analytical tool that examines the magnetic properties of atomic nuclei with carbon and hydrogen being the most common. It relies on the principle of nuclear magnetic resonance and can provides information about the reaction state, structure and chemical environment of molecules. The intra molecular magnetic field around an atomic nuclei in a molecule changes the resonance frequency, thus, giving access to details of the electronic structure of a molecule. It is used to determine the physical and chemical properties of atoms or the molecules in which they are contained.

^1H NMR was carried out using Ultrashield Advance Bruker 400 NMR (Figure 3.1). The samples to be analysed were prepared by dissolving ~0.3 mg of each complex in chloroformd at room temperature. The complex solution (5 ml) was filled into an 8 inches thin walled NMR tube and analysed. The chemical shifts, splitting patterns and J coupling of the different hydrogen atoms were then compared to literature. For the ^{78}Se NMR analyses, ~0.3 mg of the complex

was dissolved in minimum amount of CDCl_3 and 0.15 mg of diphenyldiselenide added to it as a standard. The solution was then introduced into the NMR tube as above.



Figure 3.1 Pictorial representation of nuclear magnetic resonance spectroscopy

3.3.2 Melting point

The melting point of a solid is the temperature at which it changes from a solid to a liquid state at atmospheric pressure. At this temperature, the solid and liquid phases are in equilibrium and it is a characteristic figure used to determine the purity of compounds.

The melting point of the complexes were determined using a Stuart Scientific melting point apparatus (Figure 3.2). To do that, a capillary tube, sealed at one end, was filled through the other with the sample and inserted into the melting point apparatus. The sample was then monitored through the eyepiece as the melting point apparatus was heated. The temperature at

which the sample began to melt and completely melted were then recorded. The average of these two temperatures was then recorded as the melting point of the sample.



Figure 3.2 Pictorial representation of Stuart scientific melting point apparatus

3.3.3 Micro-elemental analyses

Micro-elemental analysis is a technique used to determine the elemental composition of substances. Micro-elemental analysis can either be for qualitative (determining what elements are present), quantitative (determining how much of each element is present) or both determinations.

The micro-elemental analyses of the as-synthesized complexes were performed by the University of Manchester Micro-analytical facility using a Flash 2000 elemental analyser for CHNS and Thermo iCap 6300 Inductively Coupled Plasma Optical Emission Spectroscopy (ICP-OES) for the metals (Figure 3.3). It was used to ascertain the purity of the complexes. To do this, 15 mg of the sample was weighed into a tin capsule. This was then transferred into the furnace where combustion occurred. The theoretical elemental percentages of the complexes were then compared with the experimental determined elemental percentages. The closer the two values, the higher the purity of the complex.



Figure 3.3 Pictorial representation of Flash 2000 elemental analyser

3.3.4 Infrared spectroscopy (IR)

Infrared refers to that part of the electromagnetic spectrum between the visible and microwave regions (between 700 nm to 1 mm). In IR spectroscopy, an organic molecule is exposed to infrared radiation and the absorbed radiation converted into energy of molecular vibration. When the radiant energy matches the energy of a specific molecular vibration, absorption occurs. Infrared spectra were obtained on a Perkin Elmer FT-IR spectrum two with Bruker detector (Figure 3.4). The samples were placed on the platinum crystal and corked. The samples were then scanned from 4000–400 cm^{-1} and the spectra recorded.



Figure 3.4 Pictorial representation of Perkin Elmer FT-IR spectrometer

3.3.5 Mass spectrometry (MS)

Mass spectrometry is a technique that identifies the amount and type of chemicals present in a sample by measuring the mass-to-charge ratio and abundance of gas-phase ions. It works by ionizing chemical compounds to generate charged molecular fragments and measuring their mass-to-charge ratios.

Mass spectrometry was performed by the Lilly Mass Spectrometry unit (University of Manchester) using electron spray ionization technique (ESI) and atmospheric pressure chemical ionization (APCI) method with dichloromethane as solvent on Waters SQD2 quadrupole mass spectrometer (Figure 3.5).

Typically, 0.1 mg of the sample was dissolved in dichloromethane and ionized, for example by bombarding with electrons. This causes the sample's molecules to break into charged fragments. The ions are separated according to their mass-to-charge ratios. Ions of the same

mass-to-charge ratio are deflected and detected. Results are displayed as a spectrum of the relative abundance of detected ions as a function of the mass-to-charge ratio. The different fragments were identified by correlating known masses to the identified masses or through a characteristic fragmentation pattern.



Figure 3.5 Pictorial representation of Waters SQD2 quadrupole mass spectrometer

3.3.6 Thermogravimetric Analysis (TGA)

Thermogravimetric analysis (TGA) is a method of thermal analysis, in which changes in mass of a substance is monitored as a function of temperature as the substance is subjected to a controlled temperature program in a controlled atmosphere. TGA provides information about the decomposition pattern of the complex.

TGA analyses were carried out by University of Manchester Micro-analytical Facility using Perkin-Elmer TGA7 analyzer (Figure 3.6). Typically, about 1.5 mg of the complex was

weighed into an aluminium pan and inserted into the sample compartment of the Perkin-Elmer TGA7 analyzer. The furnace was heated from 25 to 600 °C under a flow of nitrogen gas at a heating rate of 10 °C min⁻¹. The change in weight of the sample as a function of temperature is recorded as a thermogram. The thermogram gives information about decomposition steps and percentage weight of residue after the decomposition process. The percentages of the residues remaining are then compared to the theoretical weight of the inorganic portion in the different complexes to ascertain to feasibility of using the complexes as starting for the syntheses of the various metal chalcogenides present in them.



Figure 3.6 Pictorial representation of Perkin-Elmer TGA7

3.4 Syntheses of metal chalcogenide nanomaterials

The complexes synthesized earlier were used as single source precursors for the syntheses of thin films and nanoparticles using different techniques. The thin films were deposited using spin coating whereas hot injection technique was employed for the syntheses of the nanoparticles.

3.4.1 Deposition of the thin films by spin coating method

Prior to the deposition, glass substrates with dimensions of 1.5 x 2 cm were cleaned by sonicating them in isopropanol, distilled water and acetone for 15 minutes each. The cleaned glass slides were air dried and kept for further use. The precursor solution was then prepared by dissolving 0.2 mmol of the complex in chloroform (1.5 ml). Afterwards, a glass substrate was placed into the sample component of the spin coater and a drop of the precursor solution introduced onto the glass slide using an eppendorf pipette (Figure 3.7). The substrate was spun at a speed of 1500 rpm for 20 seconds to spread the precursor over the entire surface of the glass substrate. The coated glass substrates were placed in the center of a quartz tube and inserted into a pre-heated carbolite furnace. The coated glass substrates were then heated from 125 to 300 °C under the flow of nitrogen gas for specific times. At the end of the 30 minutes, the quartz tube was pulled from the carbolite furnace and the heating stopped. The thin films were allowed to cool and kept in petri dishes for further characterizations.

For the deposition of the ternary thin films, different mole ratios of the two starting precursors were mixed to an overall concentration of 0.20 mmol. The mixture was then dissolved in 1.5 ml of chloroform and sonicated to form the coating precursor solution. The precursor solution was then spin coated onto glass substrates and heated as above at 250 °C.



Figure 3.7 Pictorial representation of a spin coater with part labelled

3.4.2 Syntheses of nanoparticles

Hot injection, which is one of the colloidal synthetic techniques was employed for the syntheses of the nanoparticles. All the syntheses were carried out using standard Schlenk line conditions. In a typical synthesis, 7 ml of oleyamine was degassed at 110 °C and purged with nitrogen gas. The temperature of the oleyamine was increased to 200 °C and allowed to stabilize. In another flask, 0.2 mmol of the precursor was dissolved in 2 ml of octadecene under nitrogen gas and injected rapidly into the hot oleyamine while stirring. A temperature decrease of 15-20 °C (from 200-180 °C) was observed. The temperature was allowed to stabilize and heating continued for 30 minutes. At the end of the 30 minutes, heating was stopped and the reaction mixture allowed to cool. At about 60 °C, excess methanol was added to the content of the flask to precipitate the nanoparticles and transferred into a centrifuge tube. The precipitate was separated by centrifuging at 3000 rpm for 15 minutes. The obtained solid nanoparticles were then washed with methanol trice by centrifugation and re-dispersed in toluene after which it was kept for characterization.

For the ternary nanoparticles, different mole ratios of the two precursors were weighed to an overall concentration of 0.2 mmol and dissolved in 2 ml of solvent. The precursor solution was then injected rapidly into the hot capping agent at the required temperature as above for the binary nanoparticles.



Figure 3.8 Pictorial representation of hot injection set up

3.5 Characterization techniques of thin films and nanoparticles

3.5.1 Powder X-Ray diffraction (p-XRD)

Powder X-ray diffraction (p-XRD) is a technique primarily used for phase identification of a crystalline material and can provide information about unit cell dimensions. Powder X-ray diffraction is a technique for the study of crystal structures, atomic spacing, preferred crystal orientation, average grain size, crystallinity, strain and chemical composition of materials.

Powder X-ray diffraction is based on constructive interference of monochromatic X-rays and a crystalline sample. These X-rays are generated by a cathode ray tube, filtered to produce monochromatic radiation, concentrated and directed towards the sample. The interaction of the

incident rays with the sample produces constructive interferences which are then diffracted. These diffracted X-rays are then detected, processed and counted. By scanning the sample through a range of 2θ angles, all possible diffraction directions of the lattice are attained due to the random orientation of the sample. Conversion of the diffraction peaks to d-spacings allow identification of the material since each material has a set of unique d-spacing values. Typically, this is achieved by comparison of d-spacings with standard reference libraries such as International Centre of Diffraction Data (ICDD) or Joint Committee on Powder Diffraction Standards (JCPDS) (Warren, 1969).

Powder X-ray diffraction analyses were carried out on a Bruker D8 AXS diffractometer using monochromated Cu-K α radiation (Figure 3.9). For the thin films, the back of the glass substrates were mounted onto the sample holders using a gum. For the nanoparticles, few drops were deposited onto a cleaned glass slide and left undisturbed for the solvent to evaporate. This was then mounted onto the sample holders as in the case of the thin films. Afterwards, the sample holders were loaded into the sample compartment and scanned at various 2θ values depending on the metal chalcogenides under consideration (Warren, 1969). For instance, the lead chalcogenides were scanned between 2θ values of 20 and 85 degrees at a step size of 0.020° and a count rate of 3 seconds at room temperature (Lewis *et al.*, 2015). From the p-XRD pattern, structural parameters such as crystallite size, dislocation density, lattice parameter and strain were determined.

The crystallite sizes of the nanomaterials were calculated using the Scherrer equation. The equation is limited to nanoscale particle and not applicable if the size is $> 0.1 \mu\text{m}$ (Monshi *et al.*, 2012). This equation relates the crystallite size to the peak broadening in the diffraction pattern. Peak broadening in p-XRD pattern may result from other factors other than the size effect. These include instrumental broadening which was corrected using a standard silicon wafer.

The crystallite size ‘ D ’ was calculated using to the Scherrer equation,

$$D = \frac{k\lambda}{B \cos \theta} \quad \text{Equation 3.1}$$

where:

D is the crystallite size (nm), k is a dimensionless shape factor, with a typical value of about 0.9, λ is the wavelength of the radiation, B is the full width at half maximum (FWHM), and θ is the angle of diffraction (Bragg angle).

Dislocation density (δ) is defined as a measure of the number of dislocations in a unit volume of a crystalline material. Dislocations represent irregularities or defects within a crystal lattice (Hussain *et al.*, 2013). The dislocation density was calculated from Williamson and Smallman’s equation (Williamson and Smallman, 1956).

$$\delta = \frac{1}{D^2} \quad \text{Equation 3.2}$$

where:

D is the average crystallite size.

The lattice constant “ a ” refers to the physical dimensions of the unit cell in a crystal lattice. Usually, lattices are represented by three constants “ a ”, “ b ”, and “ c ” which are referred to lattice parameters. However, in a special case of a cubic crystal, the three lattices are equal and usually referred to as “ a ”. The lattice constant of the cubic crystals were calculated from the equation;

$$a = d\sqrt{(h^2 + k^2 + l^2)} \quad \text{Equation 3.3}$$

where:

d is the spacing between the planes in the atomic lattice and (hkl) are the Miller indices in the xyz planes of the crystal lattice.

For an orthorhombic phase, lattice parameters are calculated from the equation;

$$\frac{1}{d^2} = \frac{h^2}{a^2} + \frac{k^2}{b^2} + \frac{l^2}{c^2} \quad \text{Equation 3.4}$$

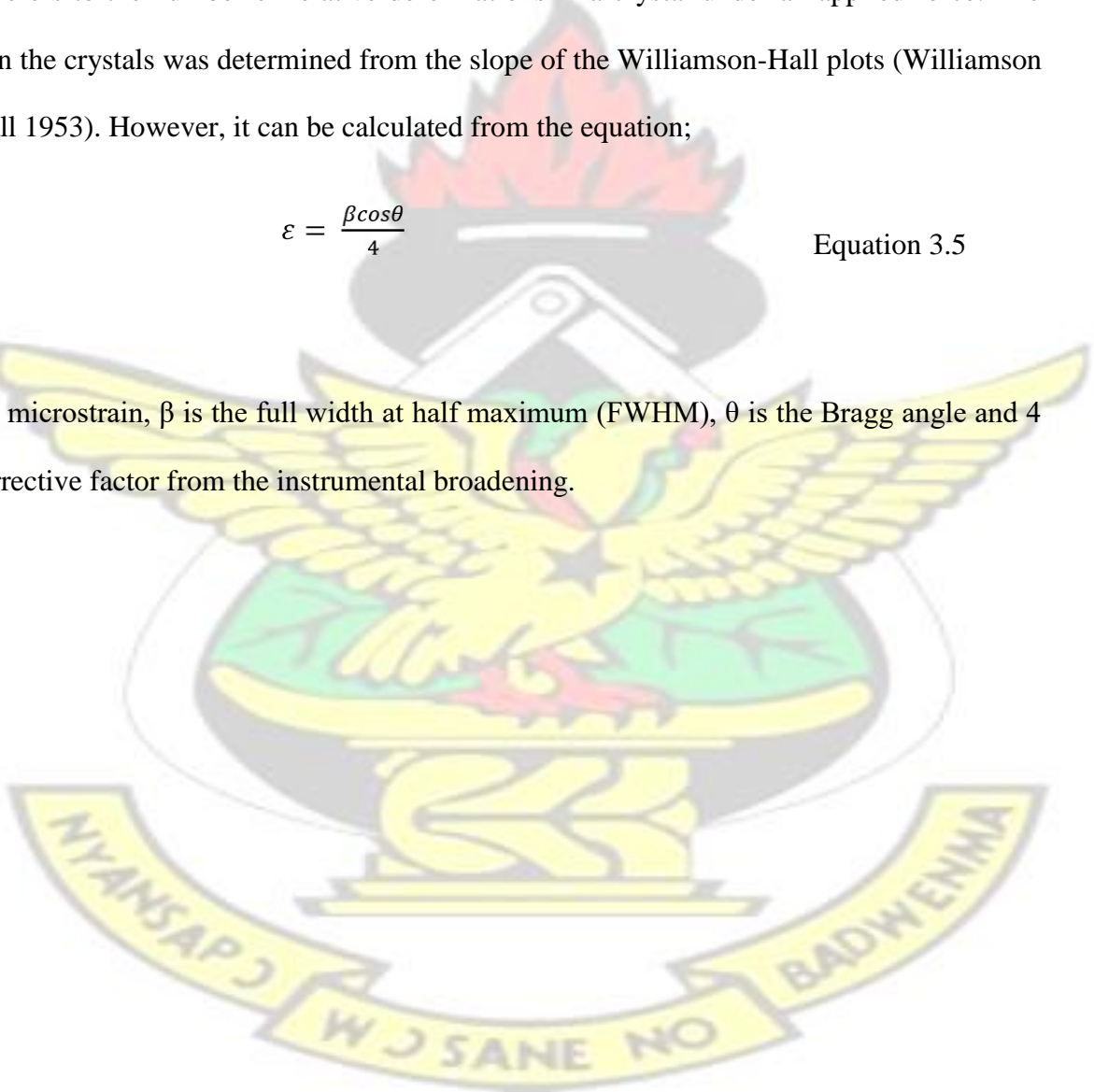
where: d is the d-spacing, hkl are the Miller indices and abc are the lattice parameters.

Strain refers to the number of relative deformations in a crystal under an applied force. The strain in the crystals was determined from the slope of the Williamson-Hall plots (Williamson and Hall 1953). However, it can be calculated from the equation;

$$\varepsilon = \frac{\beta \cos \theta}{4} \quad \text{Equation 3.5}$$

where:

ε is the microstrain, β is the full width at half maximum (FWHM), θ is the Bragg angle and 4 is a corrective factor from the instrumental broadening.



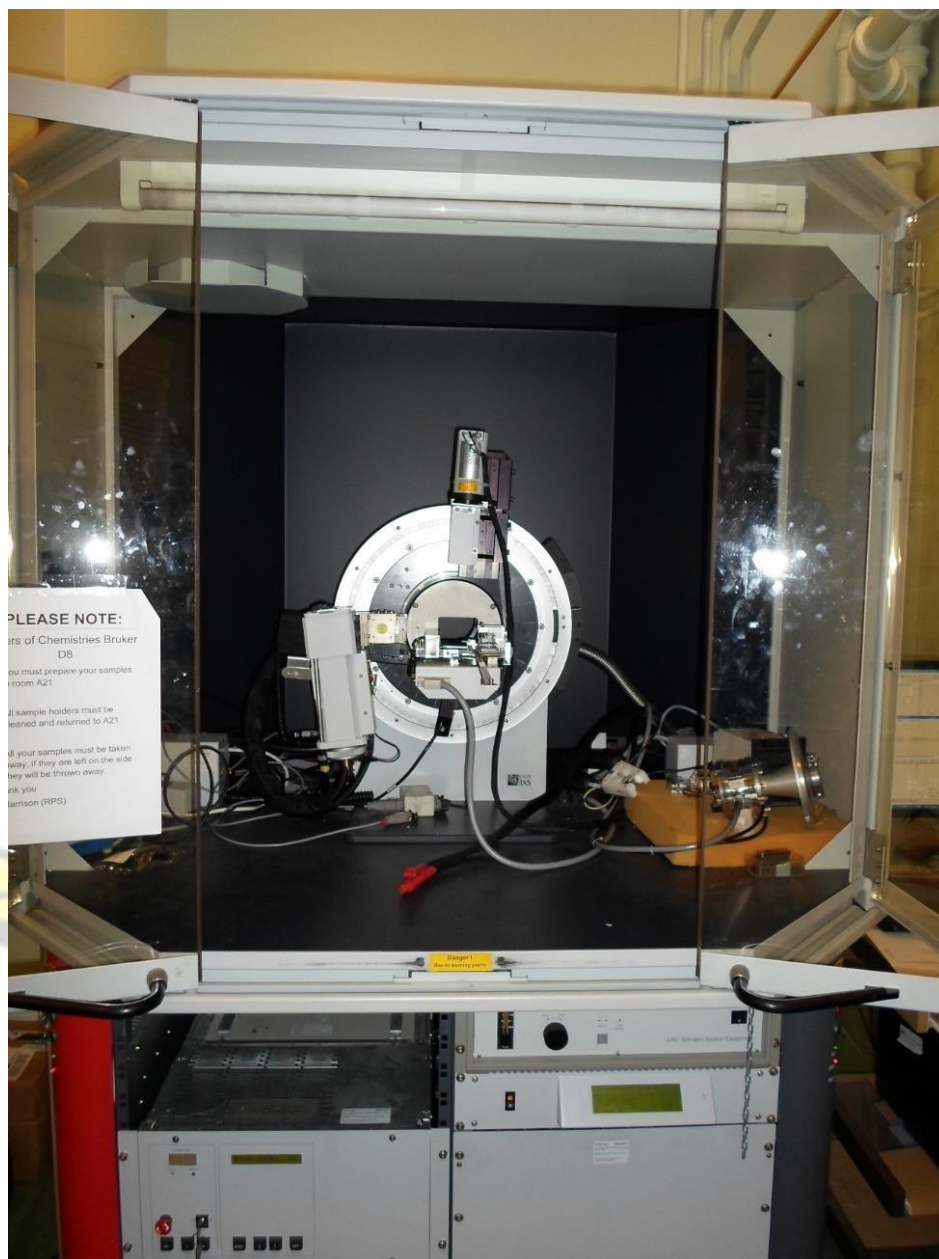


Figure 3.9 A photograph of Bruker D8 X-ray diffractometer

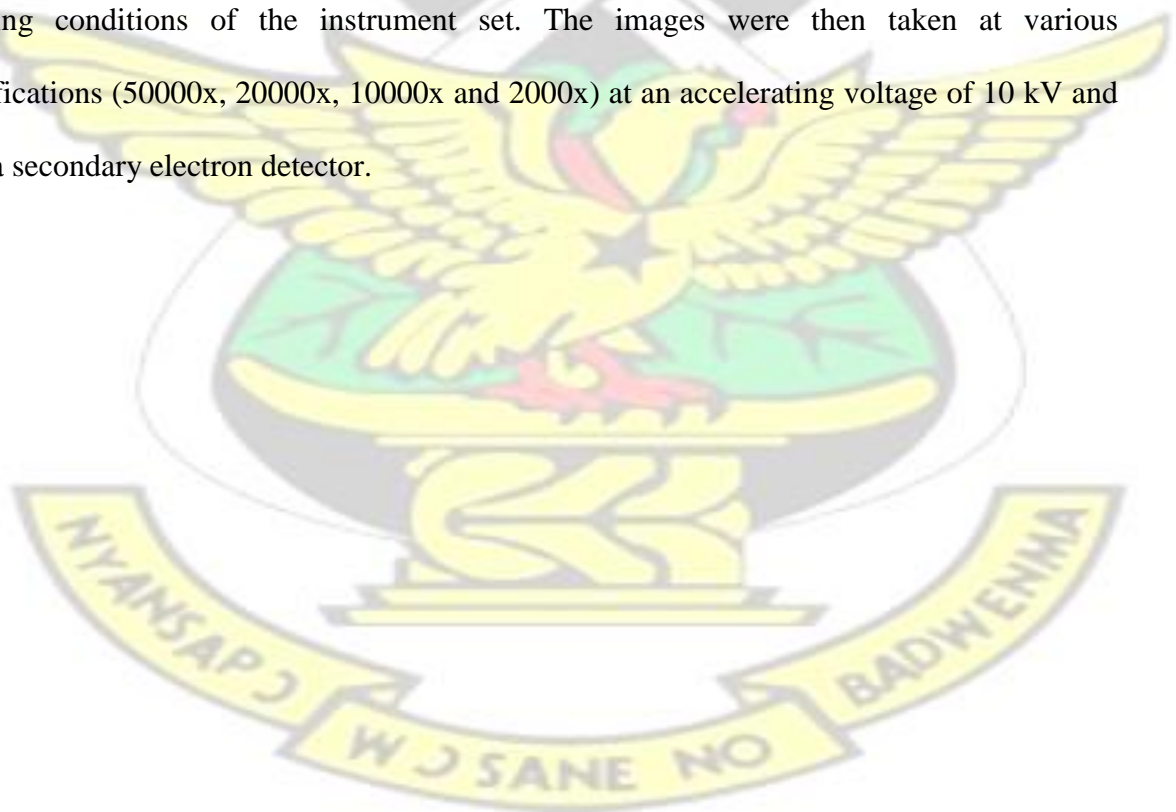
3.5.2 Scanning electron microscopy (SEM)

Scanning electron microscope is a type of electron microscope that produces an image of a sample by scanning it with a focused beam of electrons. The electrons interact with atoms in the sample, producing various signals that can be detected and contain information about the sample's surface topography. The signals include X-rays, secondary electrons and back

scattered electrons. The electron beam is generally scanned in a raster pattern, and the beam's position is combined with the detected signal to produce a 2-dimensional image of the selected area of the sample.

SEM was carried out on a Philips XL30 FEG Scanning Electron Microscope (Figure 3.10). The deposited thin films were mounted onto SEM stubs using a copper tape or carbon stub. The nanoparticles were deposited onto glass substrates from toluene solution after which the solvent was allowed to evaporate. It was also mounted onto the stubs just like the thin films.

The samples were then carbon coated using Edward's E306A coating system prior to the analyses. After coating, the deposited thin films were silver painted to create a pathway for the charges produced. The samples were then mounted into the sample compartment of the SEM at a working distance of 10 cm. Vacuum was then created in the system and the standard operating conditions of the instrument set. The images were then taken at various magnifications (50000x, 20000x, 10000x and 2000x) at an accelerating voltage of 10 kV and using a secondary electron detector.



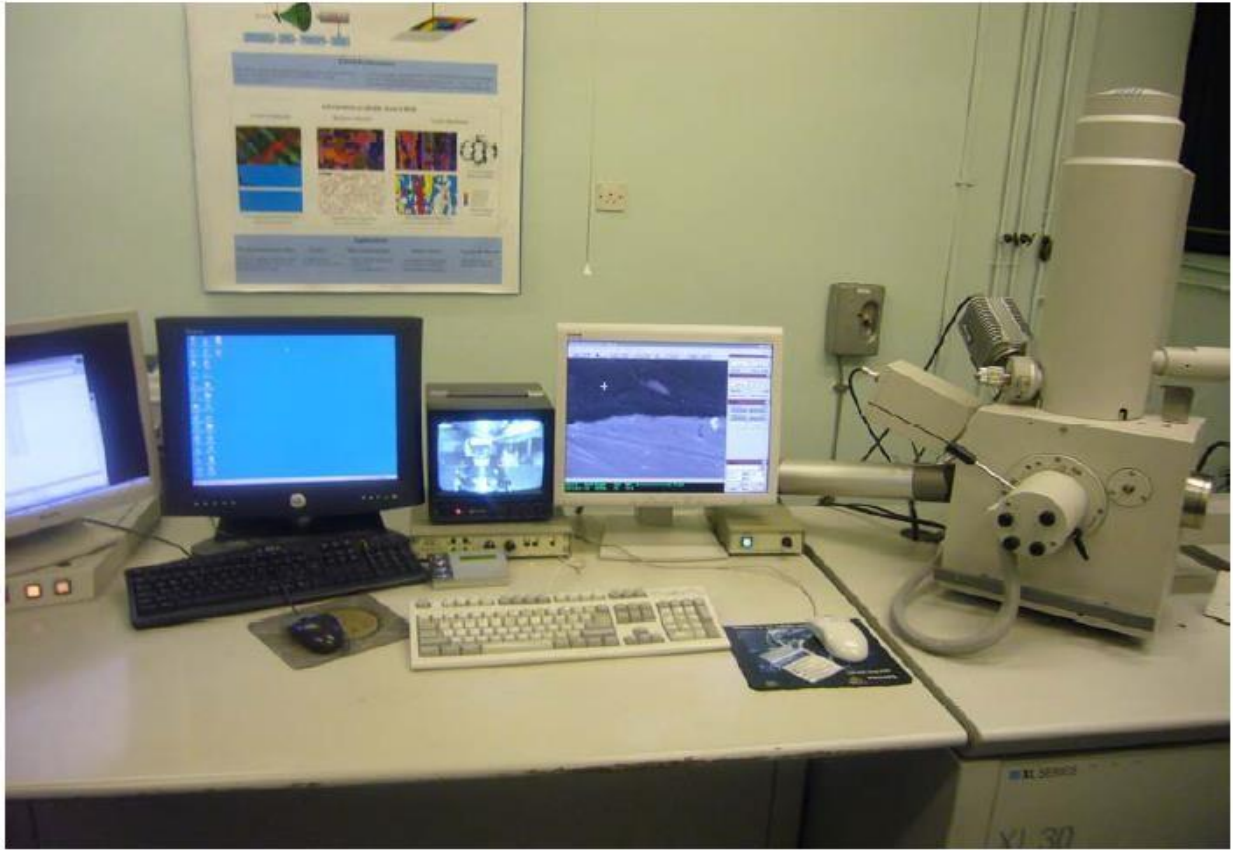


Figure 3.10 A photograph of Philips XL30 FEG Scanning electron microscope

3.5.3 Energy dispersive X-ray spectroscopy analysis (EDX)

Energy dispersive X-ray spectroscopy analysis (EDX) is a technique used for the elemental analysis of samples. Its setup comprise basically of the excitation source, X-ray detector, pulse processor and analyser. It relies on an interaction between a source of Xray excitation and a sample. Its characterization capabilities are due to the fundamental principle that each element has a unique atomic structure allowing unique set of peaks on its X-ray emission. The principle of EDX is that, when the incident beam interacts with a sample, secondary electrons are ejected and this leaves holes in the electron shells where the secondary electrons used to be. Electrons from outer shells release energy to drop into the inner shells to stabilize the atoms. This energy is in the form of X-rays which is characteristic of the element.

Therefore, a measure of the energy of the X-rays determines the type of elements are present in the sample.

EDX was performed on a DX4 interfaced to the Philips XL30 FEG Scanning Electron Microscope at an accelerating voltage of 20 kV. The elemental composition of the nanomaterials were determined and quantified. The quantification was performed using Esprit 1.8 software.

3.5.4 Transmission electron microscopy (TEM)

Transmission electron microscopy (TEM) is an imaging technique in which an electron beam is transmitted through an ultra-thin specimen to form an image on a fluorescent screen or on a layer of photographic film. TEM is able to image at significantly higher resolutions than light microscope owing to the small de Broglie wavelength of the electrons. In operation, electrons are emitted (either by thermionic or field electron emission) from the “gun” which is usually a tungsten filament or a lanthanum hexaboride (LaB_6) source typically at voltages ranging from 100 to 300 kV into the vacuum. The electrons are then consolidated and directed through the upper lenses of the TEM and subsequently interact with the sample to produce an image. In addition, TEM can also provide information on selected area electron diffraction (SAED) and diffraction pattern.

TEM was carried on JEOL 1010 TEM with an accelerating voltage of 100 kV, Megaview III camera, and Soft Imaging Systems iTEM software (Figure 3.11). The TEM samples were prepared by diluting a drop of the nanoparticle solution in 10 ml of toluene. The dilute solution was sonicated to ensure uniform dispersion of the nanoparticles in the solvent. Few drops of the nanoparticles suspended in toluene were transferred on a copper grid. The solvent was allowed to evaporate and the deposit analysed.



Figure 3.11 A photograph of JEOL 1010 Transmission electron microscope

3.5.5 UV-VIS-NIR Spectroscopy

Uv-vis-nir spectroscopy refers to the absorption or reflectance characteristics of a sample in the ultraviolet, visible and near infrared spectral region. The electromagnetic radiation wavelengths range for ultraviolet, visible and near infrared are 300 to 400 nm, 400 to 700 nm and 700 to 10^6 nm respectively. Practically, when a radiation source of a particular wavelength is used to illuminate a sample, absorption occurs. Molecules containing π -electrons or nonbonding electrons can absorb the energy to excite to higher anti-bonding molecular orbitals. The easier the electrons are excited, the longer the wavelength of light it can absorb. It is this absorption phenomenon which is used to characterize materials. Absorption of radiation may occur in a transmission or reflection mode.

Absorption measurements were performed on Perkin Elmer UV-VIS-NIR lambda 1050 spectrometer (Figure 3.12). For the thin films, the deposited glass substrates were stacked to the sample compartment and a blank glass substrate was stacked to the reference compartment using a gum. With the nanoparticles, a dilute toluene solution of the nanoparticles was transferred into a 1 cm path length glass cuvette. This was placed into the sample compartment of the instrument. In another cuvette, toluene was transferred into it and inserted into the reference compartment to serve as the reference solvent (blank). The samples were scanned at different wavelength ranges based on the nanomaterials under consideration. For example, the PbS nanomaterials were scanned from 1000 to 3000 nm to obtain the absorption spectra.

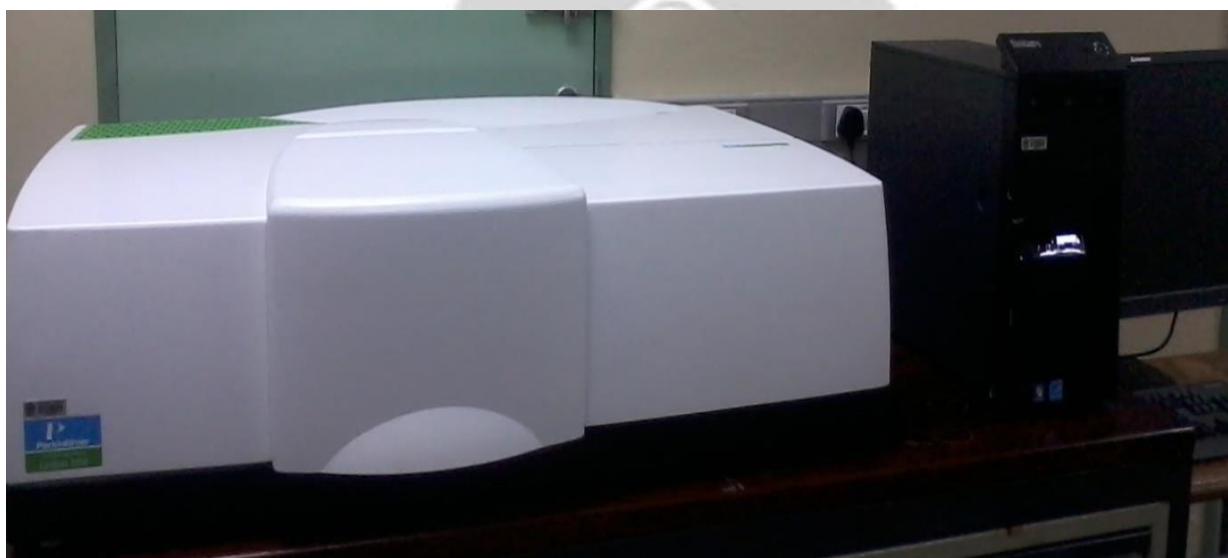


Figure 3.12 A photograph of Perkin Elmer UV-VIS-NIR lambda 1050 spectrometer
CHAPTER 4

RESULTS AND DISCUSSIONS ON THE SYNTHESSES AND CHARACTERIZATION OF BINARY LEAD SULFIDE AND BISMUTH SULFIDE THIN FILMS

4.1 Summary of results on lead and bismuth sulfides

A series of *bis*(dialkyldithiocarbonato) lead (II); (alkyl = ethyl, propyl, butyl, hexyl, octyl and dodecyl) labelled as ((1), (2), (3), (4), (5) and (7)), bismuth ethyl xanthate labelled as ((9), its adduct of TMEDA (10), triethylamine (11), 1,10 phenanthroline (12) and pyridine (13)) have been synthesized and characterized. These complexes have been used as single source precursors for the deposition of binary lead sulfide and bismuth sulfide thin films. The thin films were characterized using p-XRD, SEM and EDX analyses.

4.2 Syntheses of *bis*(dialkyldithiocarbonato) lead (II) single source precursors

A series of *bis*(dialkyldithiocarbonato) lead (II); (alkyl = ethyl, propyl, butyl, hexyl, octyl, and dodecyl) labelled as (1), (2), (3), (4), (5) and (7) have been synthesized and characterized (Figure 4.1). The complexes were obtained in good yields with simple reaction routes by the addition of an aqueous solution of the metal salt to the ligand. There was a decrease in the yield of the pure complexes as the alkyl chain increased from ethyl to dodecyl as presented in Table 4.1. This can be due to the formation of dixanthogens which are favoured in higher alkyl chain xanthates (Bag *et al.*, 2011; Shankaranarayana and Patel, 1961).

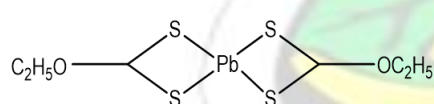
As the alkyl chain in the starting alcohol changes from ethyl to dodecyl, there is a change in the physical properties of the alcohol. For example, ethanol is a liquid whereas dodecanol is a solid at room temperature. This difference in properties may have caused the difference in polarity of the solvents used for recrystallizing the crude complexes. The lower chain complexes were soluble in polar solvents (acetone and acetonitrile) whereas the highest chain (dodecyl derivatite) was soluble in toluene which is a non polar solvent. The choice of solvents for recrystallization was determined by dissolving minute amount of the crude product in a range of solvents and the one that was able to purify the crude in high yield was selected.

Table 4.1 Effect of alkyl chain length on the yield of lead xanthate complexes

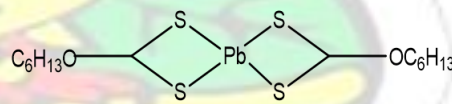
Complex	Alkyl group	Carbon length	% Yield
(1)	Ethyl	2	86.4
(2)	Propyl	3	85.9
(3)	Butyl	4	85.8
(4)	Hexyl	6	83.9
(5)	Octyl	8	82.4
(7)	Dodecyl	12	82.1

4.3 Characterization of *bis*(dialkyldithiocarbonato) lead (II) single source precursors

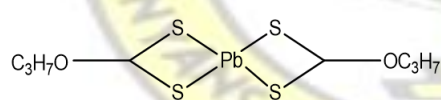
Micro-elemental analyses of the complexes showed closeness of experimentally determined percentages to the theoretical requirements based on their proposed structures. This showed that the complexes were pure and could be used as starting materials for the syntheses of PbS nanoparticles and thin films. The experimentally determined elemental percentages of the lead alkyl xanthate complexes were comparable to work done by other researchers (Clark *et al.*, 2011; Lewis *et al.*, 2015).



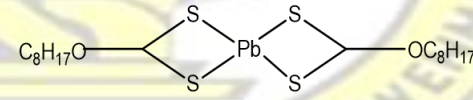
Bis(diethylthiocarbonato) lead (II) complex (1)



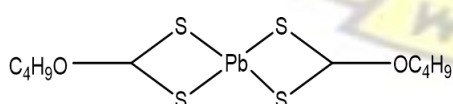
Bis(dihexylthiocarbonato) lead (II) complex (4)



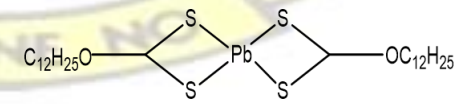
Bis(dipropylthiocarbonato) lead (II) complex (2)



Bis(dioctylthiocarbonato) lead (II) complex (5)



Bis(dibutylthiocarbonato) lead (II) complex (3)



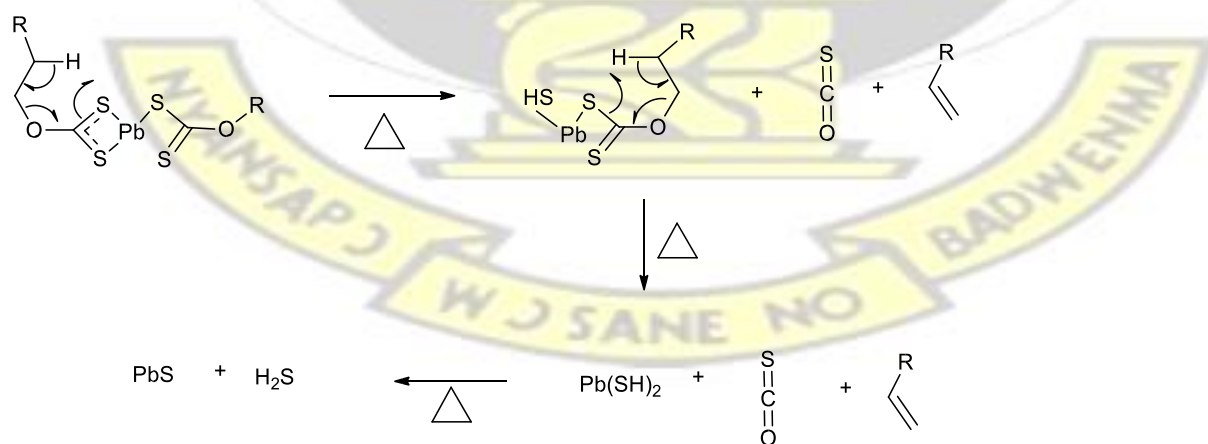
Bis(didodecylthiocarbonato) lead (II) complex (7)

Figure 4.1 Structures of *bis*(dialkyldithiocarbonato) lead (II) single source precursors

The IR spectra of the *bis*(dialkyldithiocarbonato) lead (II) SSPs showed major absorptions at 1056-1099 cm^{-1} and 1011-1045 cm^{-1} which correspond to C-O and C-S stretches respectively. Similar wavenumbers have been reported for these stretches in *bis*(dialkyldithiocarbonato) lead (II) complexes as per workdone in our group (Lewis *et al.*, 2015) and by others (Clark *et al.*, 2011).

Mass spectroscopic analyses of the lead xanthate complexes were carried out using electro spray ionization. In *bis*(dialkyldithiocarbonato) lead (II) complexes, electro spray ionization activates several decomposition pathways (Barreca *et al.*, 2005). The molecular ion peak observed using the electro spray ionization method in all the complexes confirmed their respective relative masses which were comparable to the calculated masses based on the proposed structures of the complexes. Molecular ion peaks at m/z ratio of 450, 478, 506, 562 and 618 for complexes (1 to 5) showed the attachment of a hydrogen to the molecular ion peak. However, complex (7) showed the attachment of sodium at m/z ratio of 754. Both hydrogen and sodium are used as bombarding atoms in the positive electro spray ionization and hence the tendency of attachment to the molecular ion peak (Fenn *et al.*, 1989).

The thermal decomposition of metal xanthates have been reported to be similar to the Chugeav elimination as shown in Scheme 4.1 (McNaughter and Saah *et al.*, 2016).



Scheme 4.1 A possible breakdown mechanism based upon the Chugeav elimination for lead xanthate complexes (McNaughter and Saah *et al.*, 2016)

The thermal behaviours of the complexes were examined using a Perkin Elmer Pyris 7 TGA at a heating rate of 10 °C min⁻¹. Complexes (1), (2), (3) and (4) showed a clean, one-step decomposition to form stable residue at offset decomposition temperatures of 160, 165, 168 and 200 °C respectively (Figure 4.2). There was a gradual increase in offset temperatures as the alkyl chain changed from ethyl to hexyl. Similar decomposition steps have been reported for these complexes. For instance, several researchers have reported a single step decomposition for lower alkyl chain xanthates such as complexes (1) (Clark *et al.*, 2011), (3) (Akhtar *et al.*, 2011) and (4) (McNaughter and Saah *et al.*, 2016). In complexes (1) to (4), the two bidentate xanthate ligands decomposed cleanly in one step.

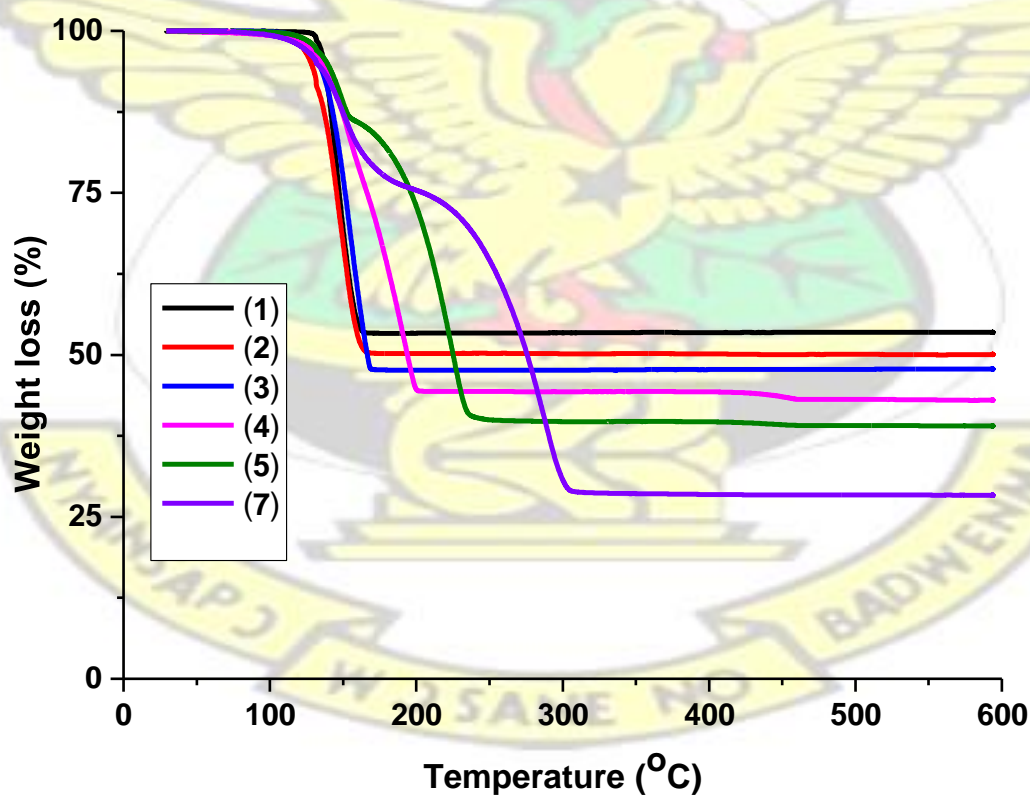


Figure 4.2 TGA thermograms of complexes (1), (2), (3), (4), (5) and (7) under nitrogen gas

The thermal stability of *bis*(dialkyldithiocarbonato) complexes have been reported to increase with increasing alkyl chain length (Figure 4.2) (Akhtar *et al.*, 2011). This is observed in the increasing offset decomposition temperatures with increasing alkyl chain length of *bis*(dialkyldithiocarbonato) lead (II) which ranged from 165 to 305 °C for complexes (1 to 7) respectively. Also, the constant residual weight observed after the offset temperatures in each of the complexes suggest the formation of a stable PbS residue at those temperatures as earlier observed by Bakar *et al.*, (2012). The relatively low offset temperatures observed for all the complexes are due to the low decomposition temperatures of *bis*(dialkyldithiocarbonato) lead (II) complexes (Fan *et al.*, 2007). Complexes (5) and (7) showed a two-step decomposition pathway that suggests the formation of an intermediate which decomposed further to form PbS as the residue. This could be attributed to the relatively longer alkyl chain and bulky nature of the complexes as the alkyl chain increases. For instance, the first decomposition step in complex (5) occurred in the temperature range of 125-155 °C, which was associated with a 13.86 % weight loss. This weight loss corresponds to the loss of -C₆H₁₃ group from one of the bidentate *bis* (dialkyldithiocarbonato) ligands attached to the Pb atom. The second decomposition step which ranged from 161-252 °C was associated with the loss of all the remaining organic moiety around the PbS (45.83 %). Pandey (1988) has studied the effect of inert gas on the thermal decomposition of *bis*(dialkyldithiocarbonato) zirconium (II) complexes and reported that the choice of inert atmosphere has little or no effect on the decomposition pathway of complexes. In this current study, the use of nitrogen gas was as a result of its cost effectiveness and availability.

Generally, the calculated weight of PbS in the complexes were similar to the experimentally determined weight of residue remaining since the difference was less than 5% conversion of

the complexes to PbS (Table 4.2). This trend has been reported earlier by Akhtar *et al.*, (2011) and Lewis *et al.*, (2015).

Table 4.2 TGA data for complexes

Complex	% Calculated weight of PbS	% Found weight of PbS	% Difference
(1)	53.21	54.56	1.35
(2)	50.09	50.10	0.01
(3)	47.30	47.76	0.46
(4)	42.58	45.06	2.48
(5)	38.83	40.31	1.48
(7)	32.72	29.46	3.26

From Table 4.2, the higher experimental residue for (1), (2), (3), (4) and (5) may be attributed to carbon contamination whereas the lower value for (7) may be due to the formation of volatile sulfide species at high temperatures, thereby causing a further loss in the percentage weight of the residue as reported earlier in literature (Akhtar *et al.*, 2010; Akhtar *et al.*, 2011; Mlowe *et al.*, 2015). The good agreement between the calculated expected weights of PbS from the structures of the complexes at 100% conversion to the experimentally determined residue weights indicate that the complexes could be used as precursors for the syntheses of PbS thin films and nanoparticles under inert atmosphere.

4.4 Characterization of PbS thin films

4.4.1 Powder XRD of PbS thin films

The p-XRD patterns of each of the PbS thin films obtained from heating the coated glass slides from complex (1), (2), (3), (4), (5) and (7) showed diffraction peaks at 2 theta values of 25.96°, 30.08°, 43.06°, 50.98°, 53.41°, 62.54°, 68.88°, 70.97°, 78.92° and 84.80°. These were indexed

to the (111), (200), (220), (311), (222), (400), (331), (420), (422) and (511) planes of a face centred cubic structure of PbS (ICDD 00-003-0614) respectively. All the PbS thin films had a preferred orientation along the (200) plane. The cubic phase is consistent with earlier reports on the syntheses of PbS from *bis*(dialkyldithiocarbonato) lead (II) SSPs using techniques such as CVD and spin coating (Akhtar *et al.*, 2011; Clark *et al.*, 2011; Lewis *et al.*, 2015). The highly intense peaks suggest that the as-synthesized PbS thin films were highly crystalline as reported earlier in literature (Barote *et al.*, 2011; Kumar *et al.*, 2009; Obaid *et al.*, 2013; Qiu *et al.*, 2011). One of the major factors that affect the growth of nanomaterials is temperature, therefore the coated thin films were heated at different temperatures to investigate the effect of temperature on the properties of PbS crystallites. This study was to investigate the effect of temperature on properties such as shape and size of the PbS nanomaterials at constant time. At 125 °C, the pXRD pattern of PbS obtained from complex (1) showed the presence of additional peaks, which did not match to any PbS phase (Figure 4.3). These additional peaks may have resulted from the incomplete decomposition of the precursor since the melting point of the complex is 125 °C. However, increasing the temperature to 150 °C resulted in the complete decomposition of the complex to yield a pure cubic PbS phase. A further increase in the decomposition temperature up to 300 °C, resulted in an increase in intensity of the PbS peaks.

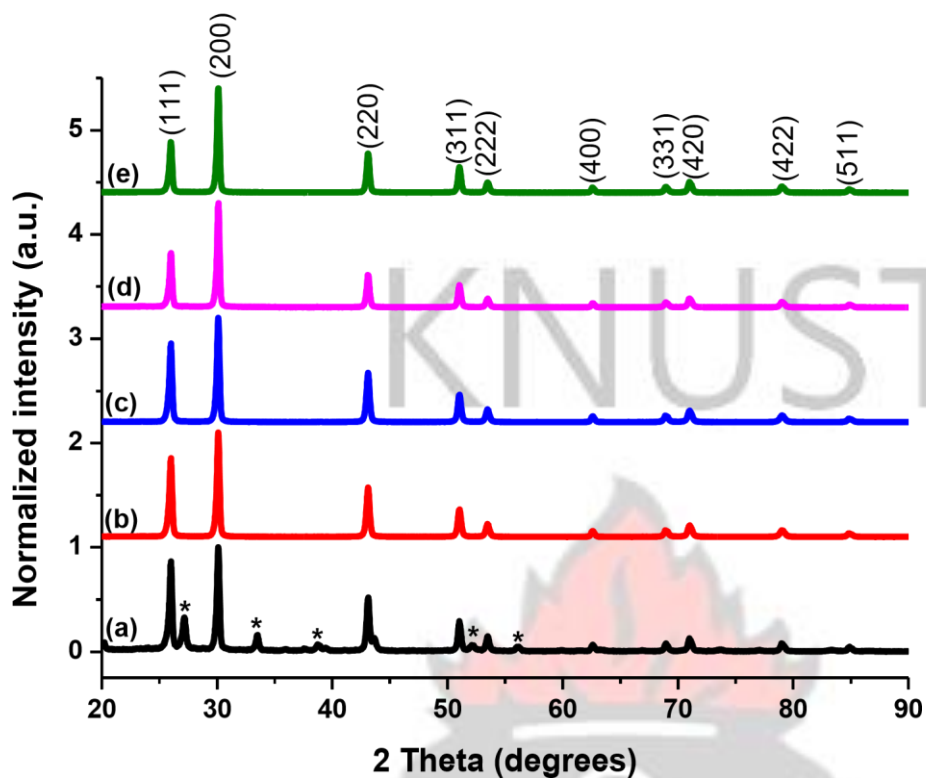


Figure 4.3 p-XRD pattern of PbS thin films obtained from heating complex (**1**) at (a) 125, (b) 150, (c) 200, (d) 250 and (e) 300 °C (* additional peaks)

Clark and co-workers had earlier deposited PbS thin film from complex (**1**) at 350 °C using AACVD technique (Clark *et al.*, 2011). However, from the present study, the spin coating method which was used has proved to be an efficient technique for the deposition of PbS thin films from (**1**) at a relatively lower temperature of 150 °C as compared to the 350 °C reported using AACVD (Clark *et al.*, 2011).

A report of an earlier study by McNaughter and Saah *et al.*, (2016) on the formation of PbS nanoparticles from complex (**1**) using the melt method, also produced additional peaks at 125 °C, however, a clean spectrum was observed at 150 °C which is consistent with the current result obtained using the spin coating method. Other metal sulfide thin films have been synthesized using ethyl xanthate as ligand and these include cadmium sulfide (Onwudiwe *et al.*, 2014), zinc sulfide (Todescato *et al.*, 2012), europium sulfide (Mirkovic *et al.*, 2005),

bismuth sulfide (Kaltenhauser *et al.*, 2013), copper indium sulfide (Fradler *et al.*, 2014) and copper antimony sulfide (Rath *et al.*, 2015).

Heating of the coated slide from complex (2) yielded a pure cubic PbS phase at 125 °C without any impurities from the precursor or the substrate (Figure 4.4). A further increase in temperature up to 300 °C caused no change in the phase of the PbS thin films as observed in complex (1). However, an increase in the intensity of the peaks was observed implying that the crystallinity of the thin films was improved at higher temperatures. From this study, 125 °C is a suitable temperature for the deposition of PbS thin films from complex (2) using the spin coated method.

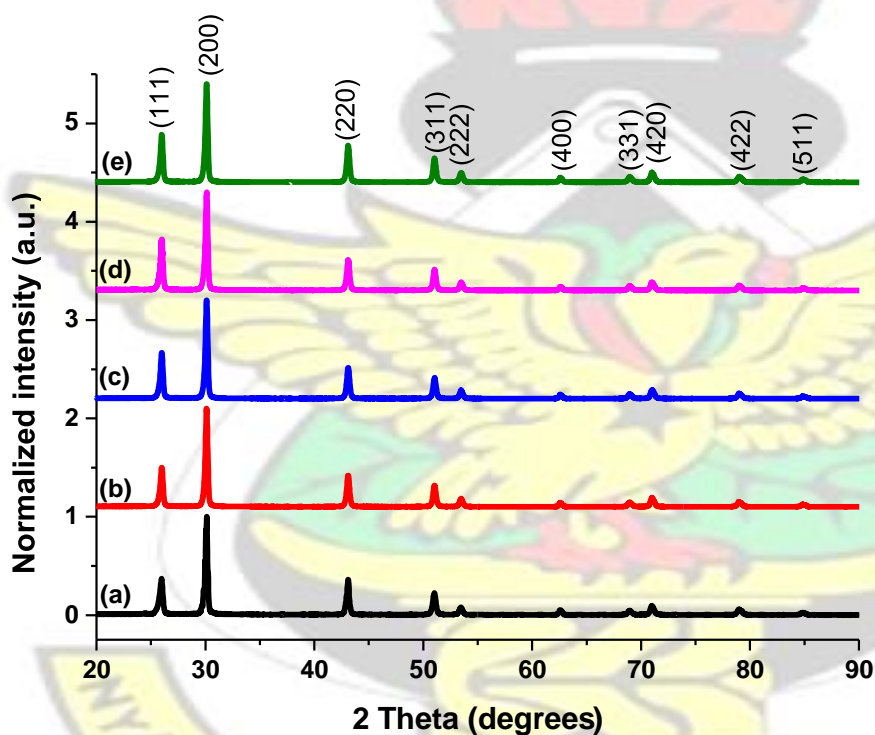


Figure 4.4 p-XRD pattern of PbS thin films obtained from heating complex (2) at (a) 125, (b) 150, (c) 200, (d) 250 and (e) 300 °C

The coated slides from complex (3) yielded a pure PbS phase at all the heating temperatures used in the experiment (125-300 °C) (Figure 4.5). Earlier studies on the deposition of PbS from complex (3) have been reported by the O'Brien's group. For example, Akhtar and co-workers (2011) have reported the deposition of PbS thin films on plastic substrate from complex (3) at

150 °C using AACVD method. Furthermore, *insitu* syntheses of PbS from complex (3) in a polystyrene matrix yielded a pure phase at 100 °C at a heating time of 120 minutes (Lewis *et al.*, 2015). The relatively low heating temperature (100 °C) as compared to this study (125 °C) was as a result of melting point depression experienced by mixing the complex and polystyrene and the longer reaction time. Lastly, McNaughter and Saah *et al.*, (2016) have synthesized PbS nanoparticles from complex (3) using melt reactions to yield a pure PbS phase at 150 °C.

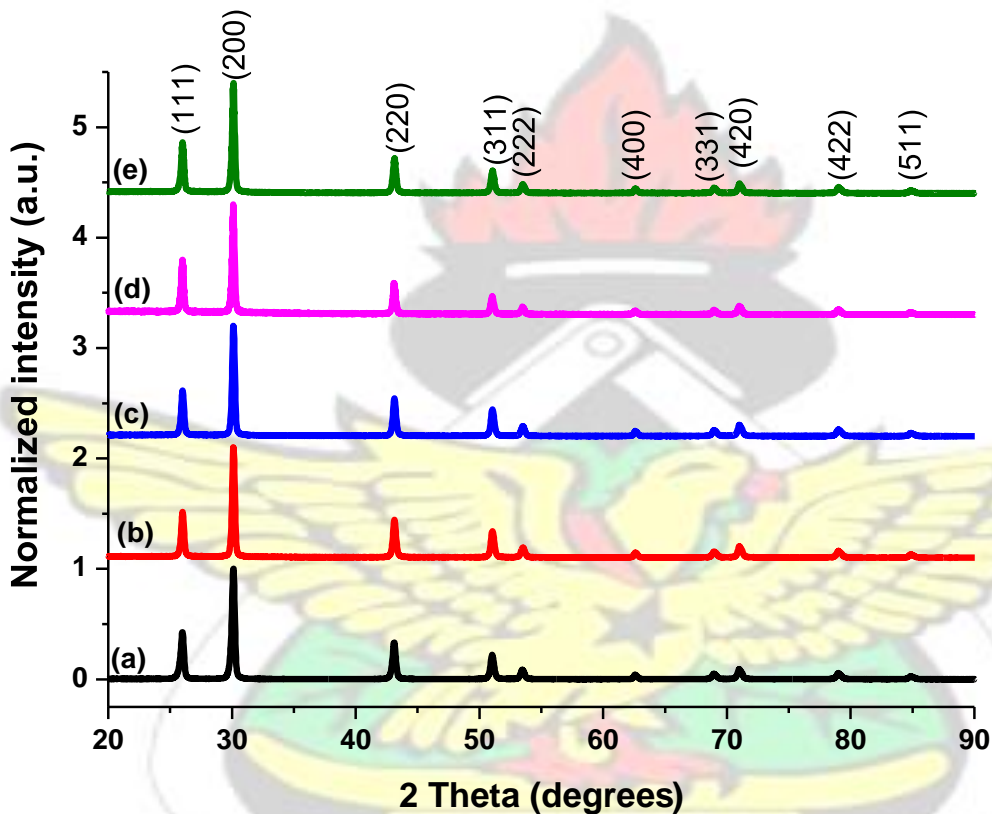


Figure 4.5 p-XRD pattern of PbS thin films obtained from heating complex (3) at (a) 125, (b) 150, (c) 200, (d) 250 and (e) 300 °C

Thin films heated from complex (4) produced pure cubic PbS phase with no peaks of impurities at all the temperature used from 125-300 °C (Figure 4.6). This showed that the temperature and time used for this experiment were right for the deposition of PbS thin films from complex (4) using the spin coating technique. The (200) plane was identified as the most preferred

orientation as seen earlier from literature (Lewis *et al.*, 2015; McNaughter and Saah *et al.*, 2016).

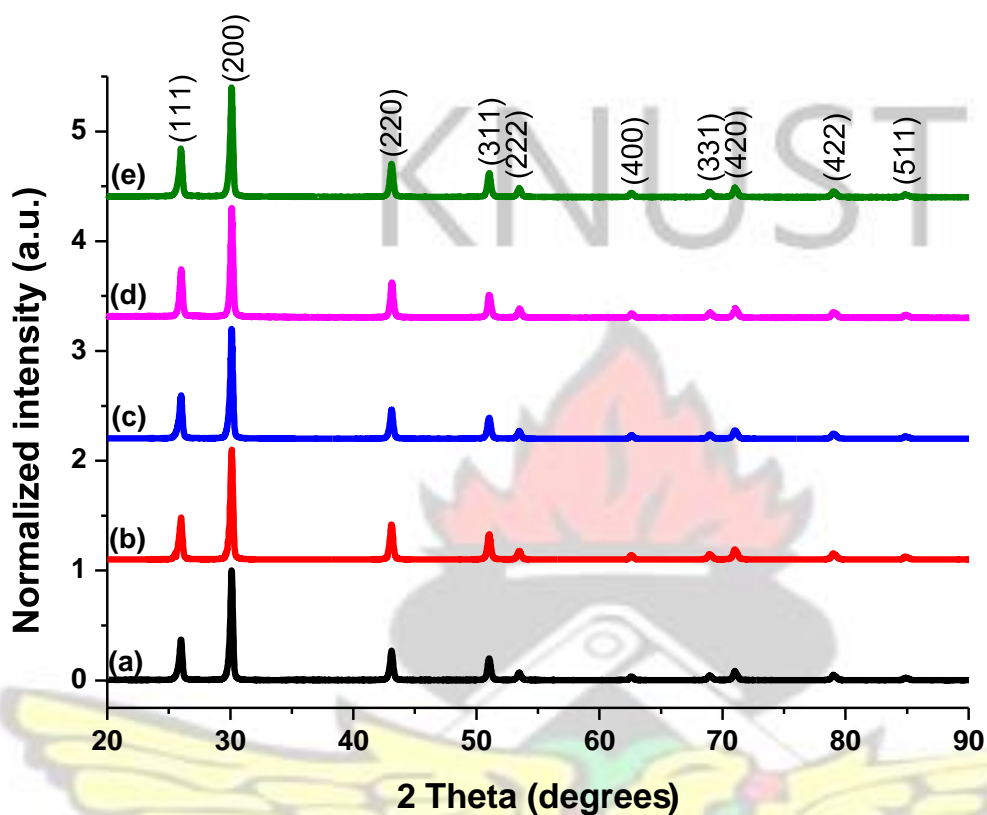


Figure 4.6 p-XRD pattern of PbS thin films obtained from heating complex (4) at (a) 125, (b) 150, (c) 200, (d) 250 and (e) 300 °C

The p-XRD pattern of PbS thin films obtained from complex (5) showed a relatively high intense peak for (111) plane although the (200) plane was the most intense (Figure 4.7). The relatively high intense (111) plane suggests the formation of some 1 dimensional structures as reported by Wang *et al.*, (2008). A pure PbS phase was observed at all the heating temperatures and times used. The peaks were however, broader as compared to those from complexes (1) to (4). This suggests relatively smaller dimensions of the nanomaterials which may have been as a result of improved self-capping activity with increasing alkyl chain length of the lead xanthate

SSPs. Similar trend was reported for the *insitu* decomposition of complex (5) in polystyrene matrix (Lewis *et al.*, 2015).

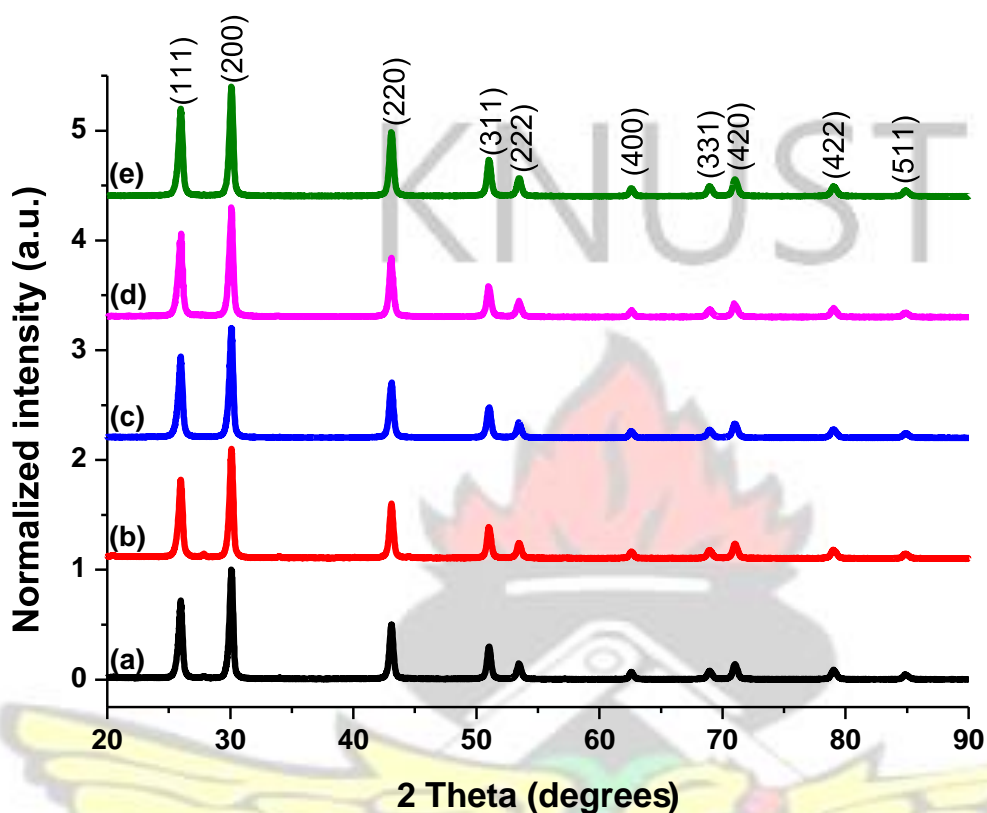


Figure 4.7 p-XRD pattern of PbS thin films obtained from heating complex (5) at (a) 125, (b) 150, (c) 200, (d) 250 and (e) 300 °C

The presence of broad diffraction peaks from the p-XRD pattern of PbS thin films obtained from heating coated glass slides with complex (7) indicates that the as-synthesized PbS nanomaterials had smaller sizes resulting from the relatively long alkyl chain in the precursor (Figure 4.8) (Akhtar *et al.*, 2010). The peaks became narrower as the temperature increased from 125 to 300 °C indicating grain growth. Also, a relatively high intense (111) peak was observed, similar to the pattern obtained for (5) although the (200) plane was the most intense in both cases. Furthermore, as the alkyl chain increases, the bond between the ligand and the metal weakens and therefore requires a relatively lower temperature to break as compared to lower alkyl chain metal dithiocarbonate complexes (Sharma, 1986).

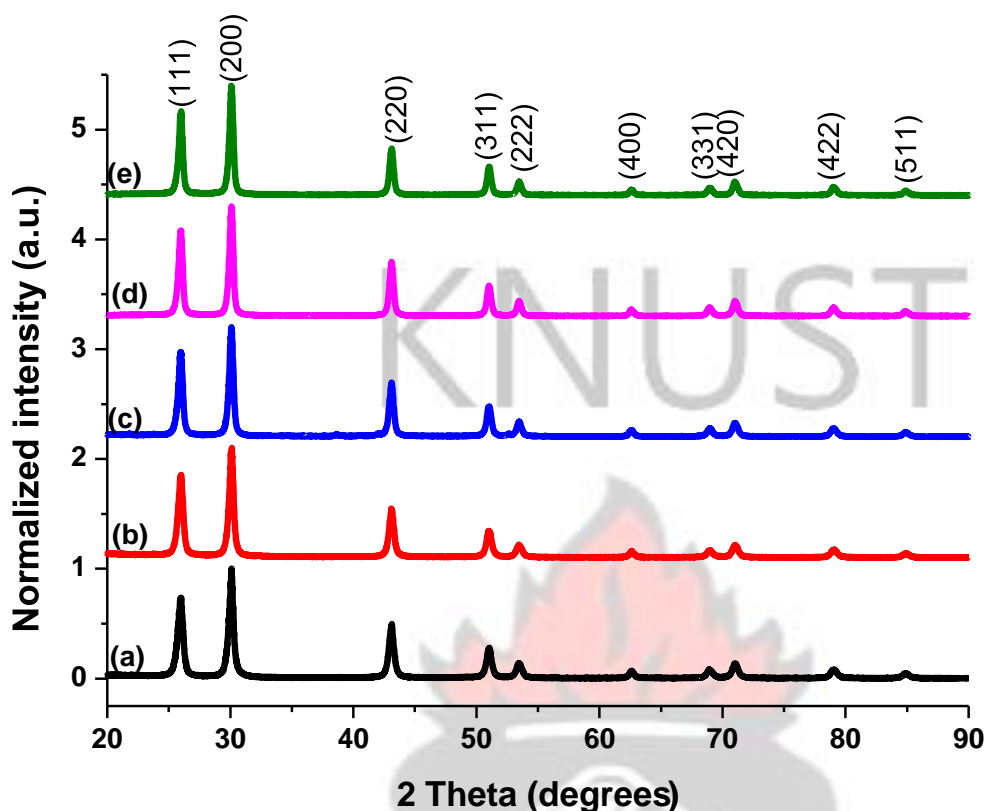


Figure 4.8 p-XRD pattern of PbS thin films obtained from heating complex (7) at (a) 125, (b) 150, (c) 200, (d) 250 and (e) 300 °C

The crystallite sizes were estimated by applying the Scherrer equation as given in equation 3.1. The calculated crystallite sizes of the nanomaterials increased gradually with increasing heating temperature for the coated slides. For a particular precursor, increasing the temperature caused an increase in the crystallite sizes. For instance, the crystallite sizes for PbS thin films deposited from complex (1) and heated at 150, 200, 250 and 300 °C were 31.63, 31.74, 33.45 and 35.87 nm respectively as seen in Figure 4.9. This confirms that the nanomaterials have high surface energy and tend to grow into bigger crystals at higher temperatures. This trend was observed in all the lead dithiocarbonate complexes used for this study. Also, an increase in alkyl group in the complexes caused a corresponding increase in their self-capping activities as reported earlier by Lewis *et al.*, (2015). Hence the broader peaks observed in the p-XRD pattern of (7) as compared to the other precursors of shorter alkyl chains such as complex (1). At a constant

temperature of 150 °C, the calculated crystallite size decreased from 31.63 to 19.69 nm as the alkyl chain in the starting precursor increased from ethyl to dodecyl (Figure 4.9).

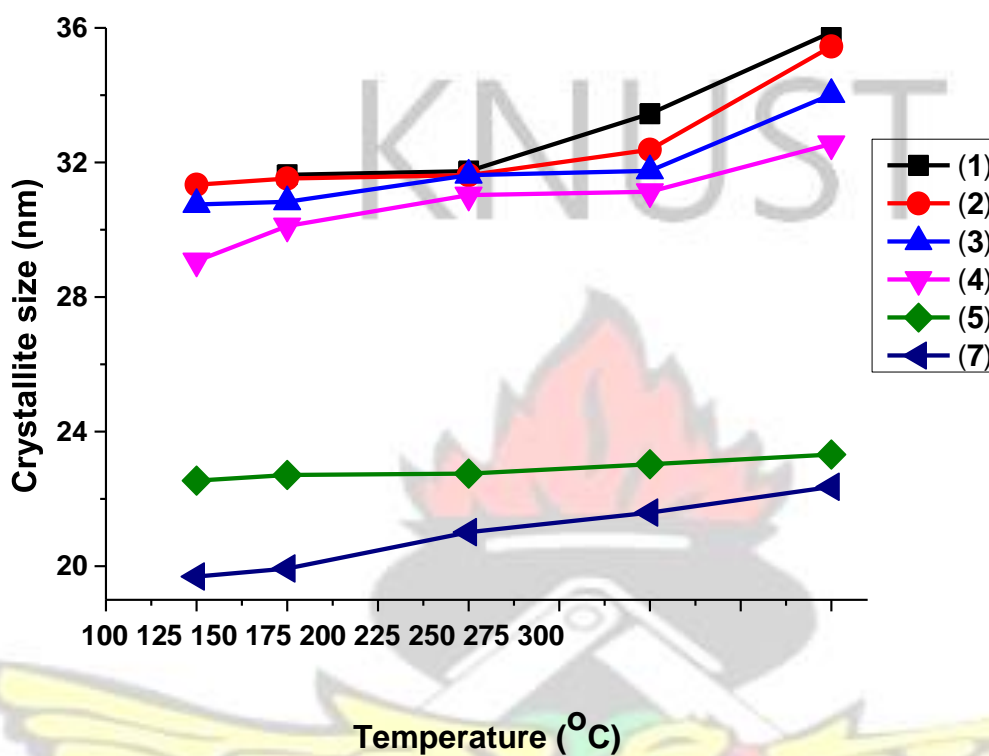


Figure 4.9 A plot of crystallite sizes against heating temperature of the complexes

The dislocation density (δ) which represents the number of lattice imperfections or defects in the material were also calculated using equation 3.2. There was a decreases in the number of defect as the crystallite sizes increased (Rajashree and Balu, 2016). This may be due to a decrease in the occurrence of grain boundaries as the crystallite size increases with temperature (Begum *et al.*, 2012; Preetha and Remadevi, 2014; Srivastav *et al.*, 2015). The dislocation density was calculated using equation 3.2. Generally, the smaller the crystallite size, the higher the dislocation density and hence the imperfections in the sample. PbS crystals obtained from complex (7) showed higher dislocation density as compared to that from complex (1). This is due to the smaller crystallite sizes in the PbS nanomaterials from complex (7) (Figure 4.10).

Similar trend of decreasing dislocation density with increasing crystallite size have been reported for PbS thin films (Hussain *et al.*, 2013; Kumar *et al.*, 2014; Puiso *et al.*, 2003).

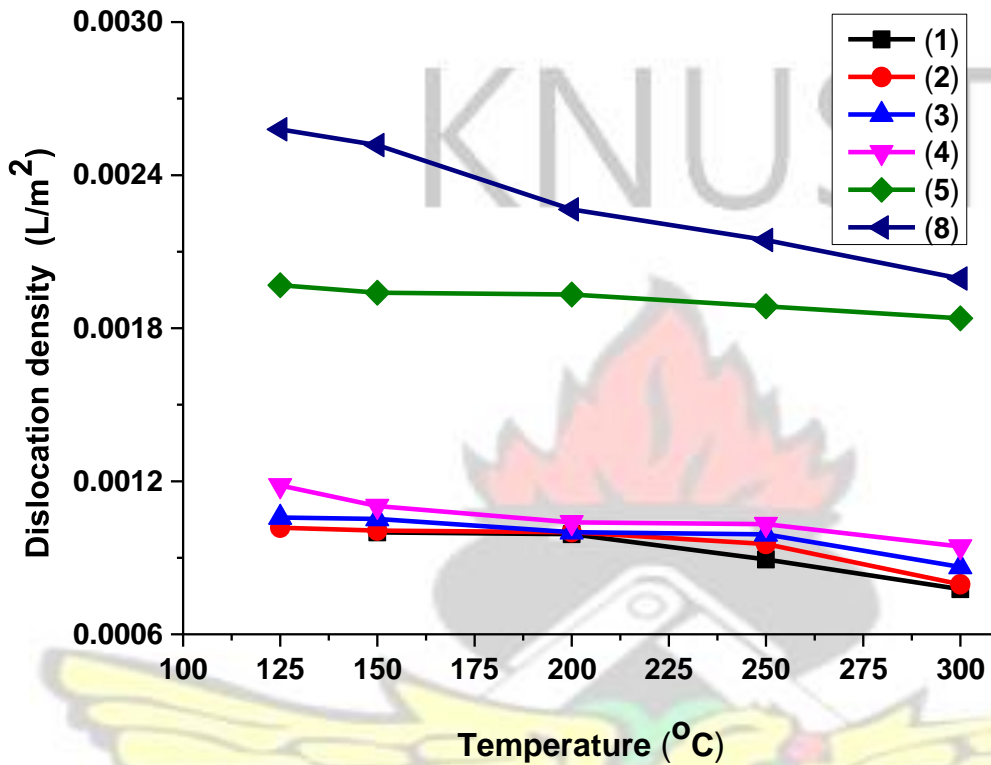


Figure 4.10 A plot of dislocation density against heating temperatures of the coated glass slides

Lattice constant “a” refers to a measured length that defines the shape of the unit cell of a crystal lattice (Raju and Srivastava, 2010). It is primarily determined from the p-XRD pattern. The lattice constant for a cubic phase was calculated using equation 3.3 (Raju and Srivastava, 2010). As seen from Figure 4.11, the average lattice constants for PbS obtained from complexes (1-7) at 250 °C were similar to that of bulk PbS which is 5.9362 Å (Boadi *et al.*, 2012). At a particular temperature of 250 °C, there was a gradual decrease in lattice constant as the alkyl chain length increased from ethyl to dodecyl.

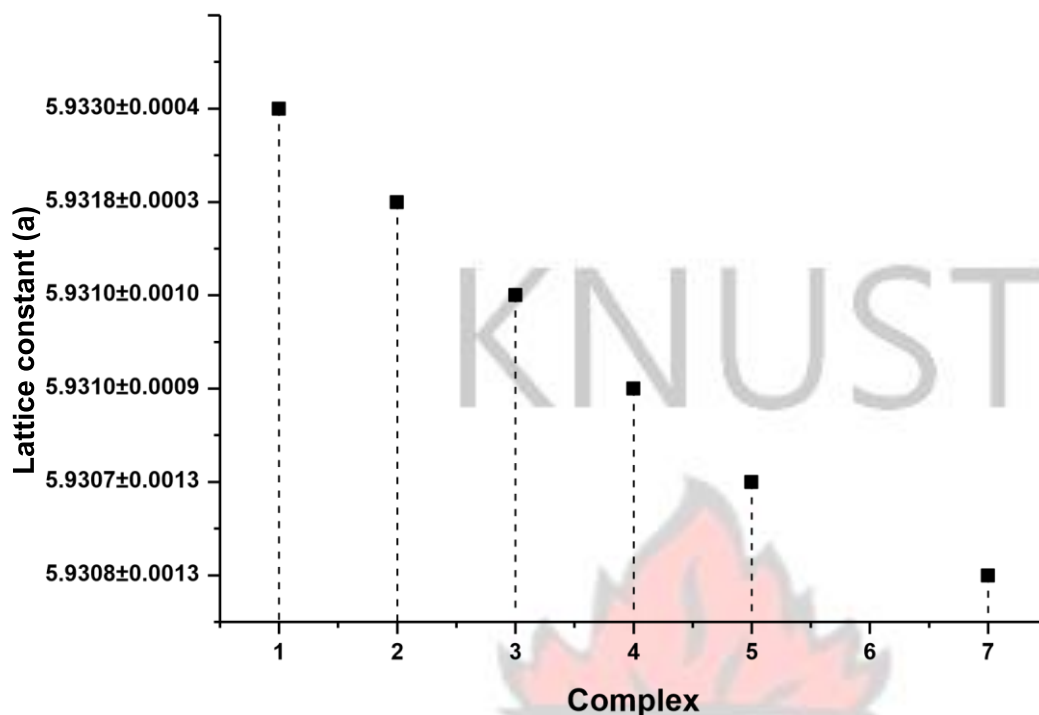
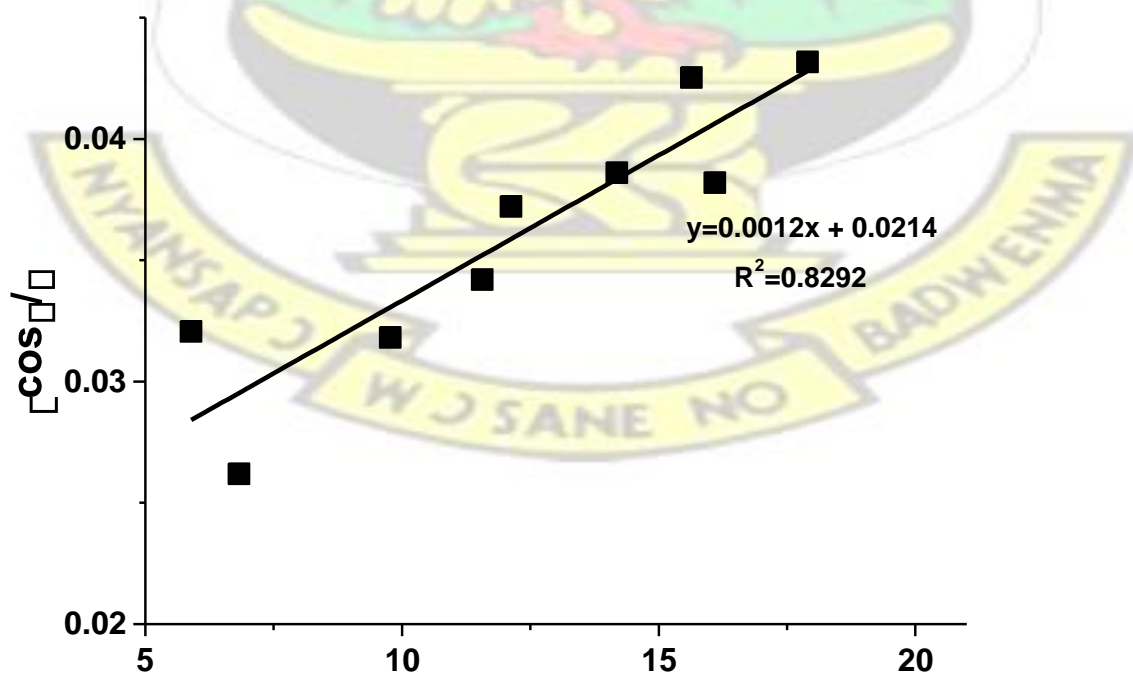


Figure 4.11 Effect of alkyl chain length on the lattice constant “a” of PbS thin films at 250 °C

A plot of $\beta \cos \theta / \lambda$ against $4 \sin \theta / \lambda$, which is the Williamson-Hall plot, gives a linear plot with microstrain as the slope and particle size as the inverse of the intercept (Kumar *et al.*, 2014).

This is another way of calculating the crystallite size from p-XRD data. A typical Williamson-Hall plot for PbS obtained from complex (3) at 250 °C is shown below (Figure 4.12).



4sin θ / λ

Figure 4.12 Williamson-Hall plot for PbS thin films obtained from complex (3) at 250 °C.

In all cases, the calculated sizes from the W-H plot were greater than the crystallite sizes (Table 4.3). This is because the crystallite sizes were calculated along the preferred orientation (200 plane) whereas the size obtained from the W-H plot gave the average size along all the planes from the p-XRD pattern. A variation (14.9 – 17.6 nm) was observed for the sizes obtained from the lower alkyl chain dithiocarbonates (complexes (1), (2) and (3)). This may be due to the growth of larger crystallites along other planes aside the most preferred orientation. However, PbS thin films from higher alkyl chain lead dithiocarbonates (complex (4), (5) and (7)) showed similar values for the sizes obtained from using both Scherrer equation and the W-H plots. This relates to the uniformity of the sizes along all the planes in the p-XRD patterns. Similar variation between the sizes calculated from the W-H plot and Scherrer equation exist in literature (Choudhury and Sarma, 2009; Kumar *et al.*, 2014; Yogamalar *et al.*, 2009). In both cases, a decrease in size of the PbS nanomaterials with increasing alkyl chain in the starting material was observed due to the self-capping activity of the SSPs.

Table 4.3 Effect of alkyl chain length on the sizes of PbS nanomaterials determined from the p-XRD profile

PbS from complex at 250 °C	Size from W-H plot (nm)	Crystallite size (nm)
(1)	51.09	33.45
(2)	49.02	32.38
(3)	46.73	31.75
(4)	34.84	31.13
(5)	25.97	23.03

For a particular starting material (eg. complex (7)), the effect of temperature on the sizes calculated from the p-XRD data were also analysed. From the sizes calculated from the W-H plots and Scherrer equation, there was an increase in size with increasing heating temperature from 125 to 300 °C (Table 4.4). This observation confirms the narrowing of the peaks of the p-XRD pattern as the temperature increased.

Table 4.4 Effect of temperature on the sizes of PbS nanomaterials determined from the p-XRD profile

PbS from complex (7) at	Size from W-H plot (nm)	Crystallite size (nm)
125 °C	20.83	19.69
150 °C	21.37	19.93
200 °C	22.79	21.01
250 °C	23.09	21.59
300 °C	24.88	22.36

Strain, which is the relative change in shape or size of a material due to an externally applied force, was also determined using the slope of the W-H plot (Gayner and Kar, 2015). From the plot, a positive slope was observed for all the PbS thin films (Figure 4.12), signifying that tensile strain was dominant in all the thin films as observed earlier by Bhatt *et al.*, (2014) and Mozafari *et al.*, (2012). The strain in thin films are dependent on the sizes. Generally, the magnitude of the strain decreases with increasing size indicating that strain is a function of size. From Table 4.5, there was a decrease in strain with increasing deposition temperature. This is so because at higher a temperature, there is an increase in crystallite sizes and thereby a reduction in force per unit area between grains, which consequently paved the way for strain relaxation (Remadevi and Preetha, 2012). This strain relaxation favours grain growth and hence

better crystallinity of the nanomaterials (Kumar *et al.*, 2014; Mehmood *et al.*, 2010; Shyju *et al.*, 2012).

Table 4.5 Effect of temperature on the strain of PbS nanomaterials determined from W-H plots

PbS from complex (7) at	Strain from W-H plot
125 °C	0.00080
150 °C	0.00070
200 °C	0.00060
250 °C	0.00048
300 °C	0.00040

4.4.2 Scanning electron microscope (SEM) images of PbS thin films

SEM images of PbS obtained from heating coated glass slides from complex (1) at 150 °C showed a densely packed cubic morphology. The sizes of the cubes increased with an increase in heating temperature. Almost uniformly sized cubes were obtained at the lower heating temperatures. However, at 300 °C, there was a wide variation in the sizes of the cubes (Figure 4.13). This may have resulted from agglomeration of some of the crystallites. PbS cubes with an average size of 158 ± 11 , 178 ± 8 , 207 ± 11 and 253 ± 25 nm were obtained for coated glass slides heated at 150, 200, 250 and 300 °C respectively. The thin film obtained at 125 °C was not analysed because it did not give a pure PbS phase. Clark and co-workers (2011), have earlier reported on the synthesis of PbS cubes with size of about 300 nm from complex (1) using AACVD at 350 °C. The smaller sizes obtained from this experiment at relatively low temperatures make the spin coating technique a viable approach for the deposition of PbS thin films. At the nanometer regime, most of the material properties are size dependent and hence the smaller the better. Melt reaction involving complex (1) at 150 °C revealed the formation of cubes with side length of 156 ± 6 nm and has been reported (McNaughter and Saah *et al.*, 2016).

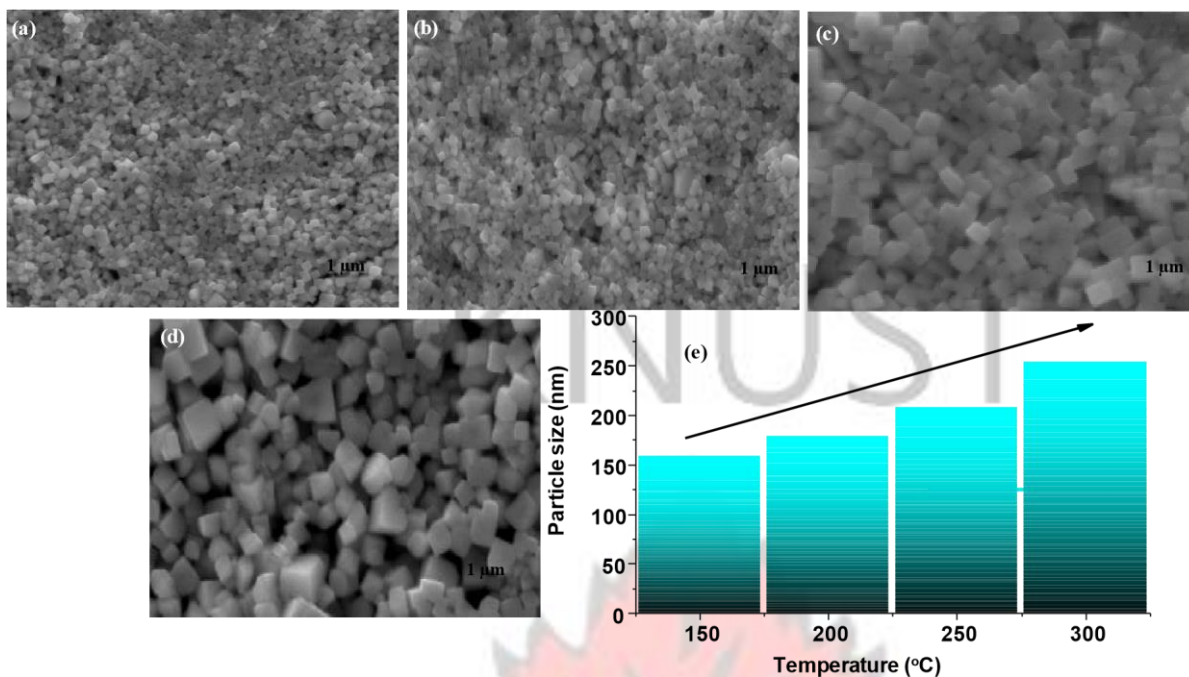


Figure 4.13 SEM images of PbS obtained from complex (1) at 20000x magnification by heating coated films at (a) 150, (b) 200, (c) 250, (d) 300 °C and (e) effect of temperature on size

SEM images of thin films deposited from (2) also gave closely packed uniformly sized cubes at all temperatures used in this research (Figure 4.14). The cubes were characterized by their well-defined edges at all temperatures used for the experiment. Particle sizes of 95 ± 5 , 103 ± 8 , 109 ± 7 , 115 ± 6 and 124 ± 9 nm were obtained at temperatures of 125, 150, 200, 250 and 300 °C respectively. The effect of temperature on the sizes and morphology of the nanomaterials formed was minimal, further confirming their p-XRD pattern which showed no significant change as the temperature was increased from 125 to 300 °C. The relatively smaller sizes obtained as compared to those from complex (1) is due to the better self-capping property of the propyl group as compared to the ethyl derivative in the starting precursor.

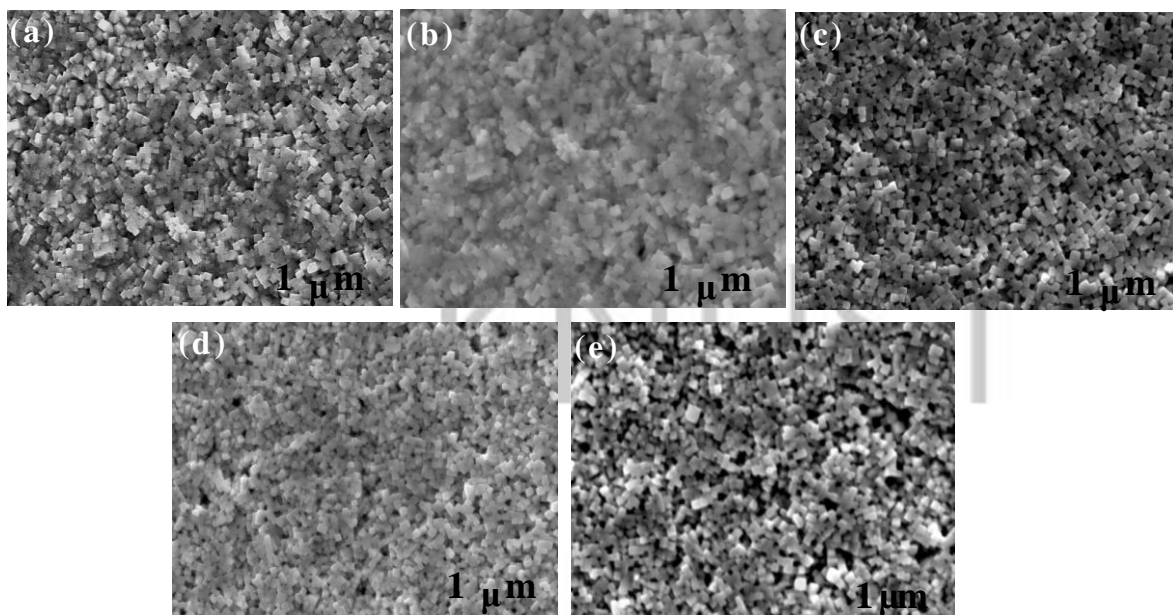


Figure 4.14 SEM images of PbS obtained from complex (2) at 20000x magnification by heating coated films at (a) 125, (b) 150, (c) 200, (d) 250 and (e) 300 °C

Complex (3), which is the butyl derivative of the lead dithiocarbonate precursor also gave closely packed uniformly sized cubes. The cubes had sizes of 62 ± 3 , 69 ± 5 , 74 ± 4 , 77 ± 6 and 80 ± 6 nm at 125, 150, 200, 250 and 300 °C heating temperatures respectively. The smaller particle sizes show an improved self-capping activity with increasing alkyl chain in the starting precursor as compared to the sizes obtained from complexes (1) and (2). Deposition of PbS thin films from complex (3) at 170 °C using AACVD by Akhtar *et al.*, (2010) yielded large non-uniform cubes with average dimensions of about 0.2 μm. By comparison, the spin coating method yielded a uniform PbS thin films at relatively low temperatures as compared to the temperatures reported in literature using CVD techniques. Furthermore, the spin coated slides showed well coverage of the substrate, which is an advantage of the deposition method (Figure 4.15).

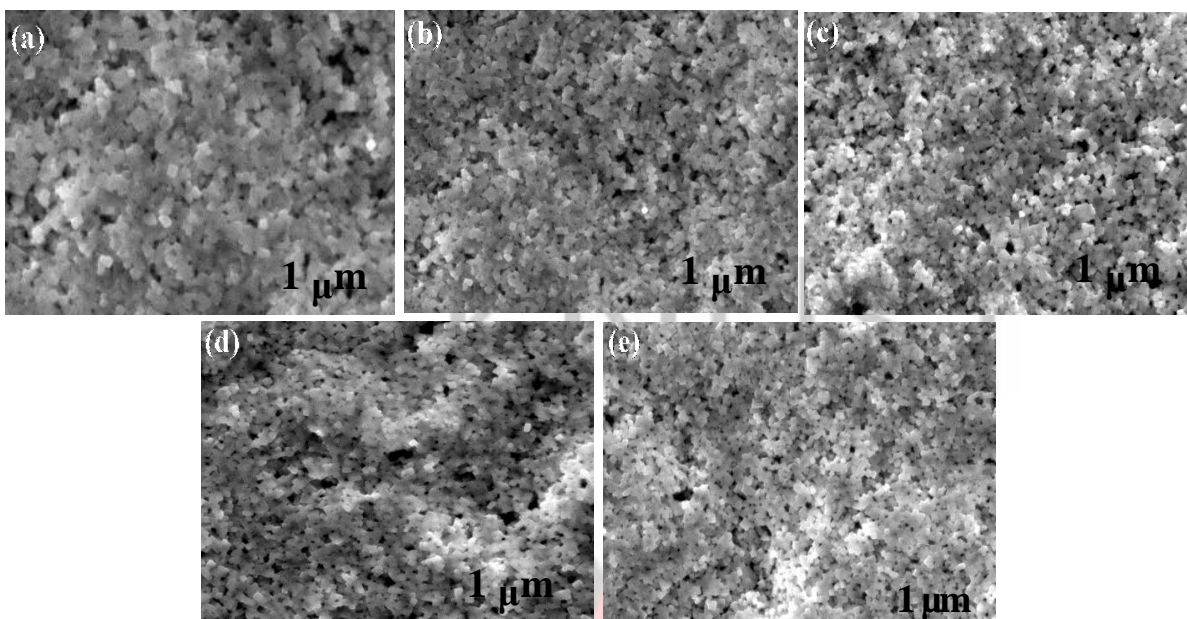


Figure 4.15 SEM images of PbS obtained from complex (3) at 20000x magnification by heating coated films at (a) 125, (b) 150, (c) 200, (d) 250 and (e) 300 °C

The SEM image of the hexyl derivative decomposed at 125 °C showed unresolved morphology although the p-XRD pattern corresponded to a pure PbS phase (Figure 4.16a). However, an increase in the temperature to 150 °C revealed a uniformly sized well-defined cubic morphology with distinct edges. Cubes with side length of 55 ± 3 , 62 ± 4 , 69 ± 5 and 75 ± 5 nm were obtained at 150, 200, 250 and 300 °C respectively.

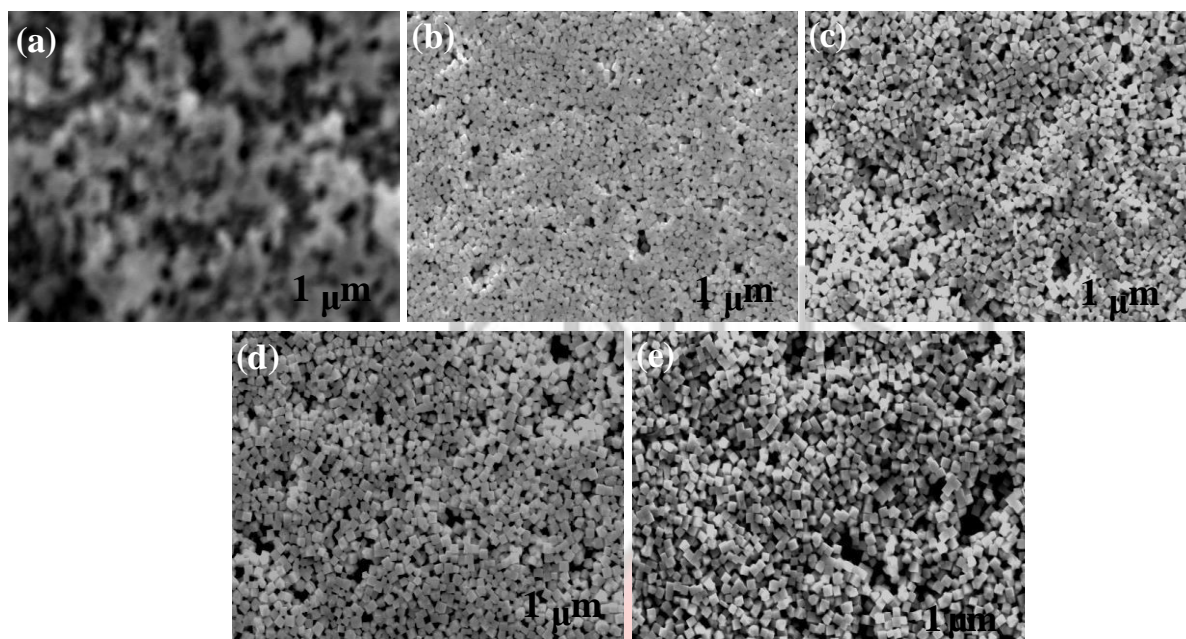


Figure 4.16 SEM images of PbS obtained from complex (4) at 20000x magnification by heating coated films at (a) 125, (b) 150, (c) 200, (d) 250 and (e) 300 °C

The SEM image of PbS thin film from complex (5) heated at 125 °C revealed an unresolved morphology. An increase in temperature to 150 °C resulted in the formation of a lumpy material which had no distinct shape and size. At 200 and 250 °C, a growth towards cubes with few rods were observed. However, at 300 °C, it was observed that the growth towards a rod with a cube at the tip had developed. The cubes had a side length of 54 ± 4 nm whereas the rod had a diameter of 35 nm. From the morphological studies, there was a great effect of temperature on the shapes of the PbS nanomaterials from 125-300 °C (Figure 4.17). From the earlier SEM images from complexes (1-4), the choice of starting material has a profound effect on the morphology of the PbS nanomaterials formed. This report throws more light on the anisotropic growth of PbS nanomaterials. An earlier report on the decomposition of complex (5) in polystyrene matrix at 275 °C also revealed the formation of rods with cubes at the tip as observed by Lewis *et al.*, (2015).

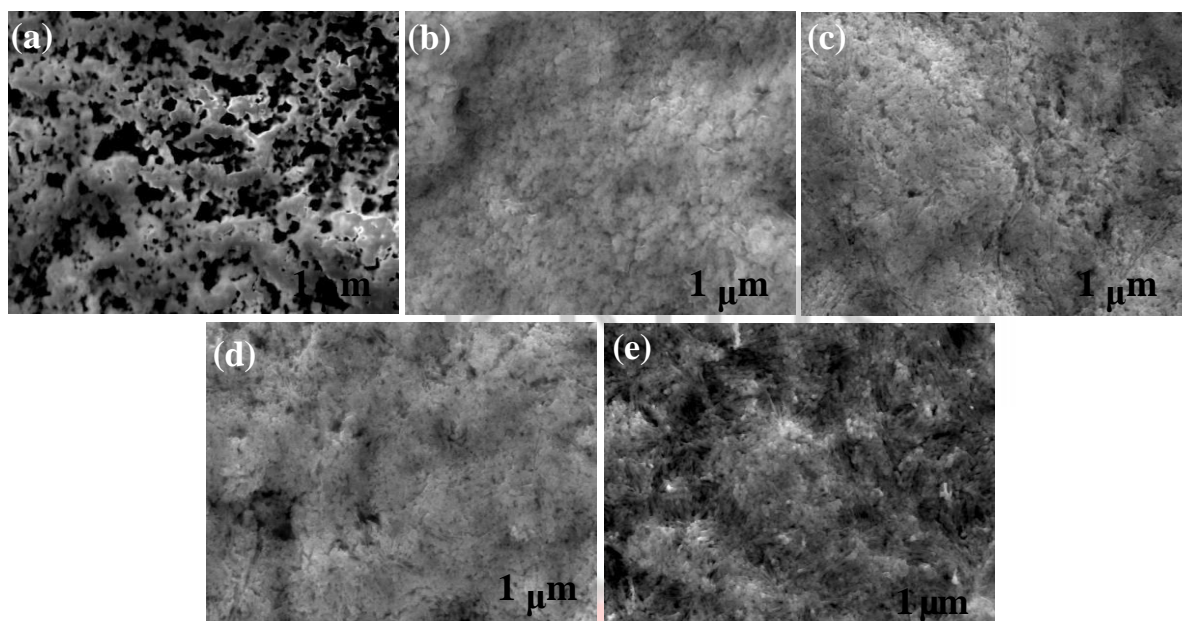


Figure 4.17 SEM images of PbS obtained from complex (5) at 20000x magnification by heating coated films at (a) 125, (b) 150, (c) 200, (d) 250 and (e) 300 °C

At temperatures below 200 °C, the morphologies of the PbS nanomaterials from complex (7) were not fully resolved making it difficult to identify the distinct shapes and estimate the particle sizes. However, at 200 °C, a rod-like growth with cubes arranged at regular intervals were observed. The rod was about 500 nm long and the diameter of the cubes were about 30 nm (Figure 4.18). The smaller sizes were as a result of efficient self-capping activity of the dodecyl chain in the starting precursor. Such unique morphology for PbS has not been reported in literature. The side length of the adhering cubes were 31 ± 3 , 35 ± 4 , and 40 ± 4 nm for thin films heated at 200, 250 and 300 °C respectively. The smaller particle sizes were as a result of the enhanced self-capping effect of the dodecyl chain in the starting precursor as compared to those of the lower alkyl chains for complexes (1) to (5).

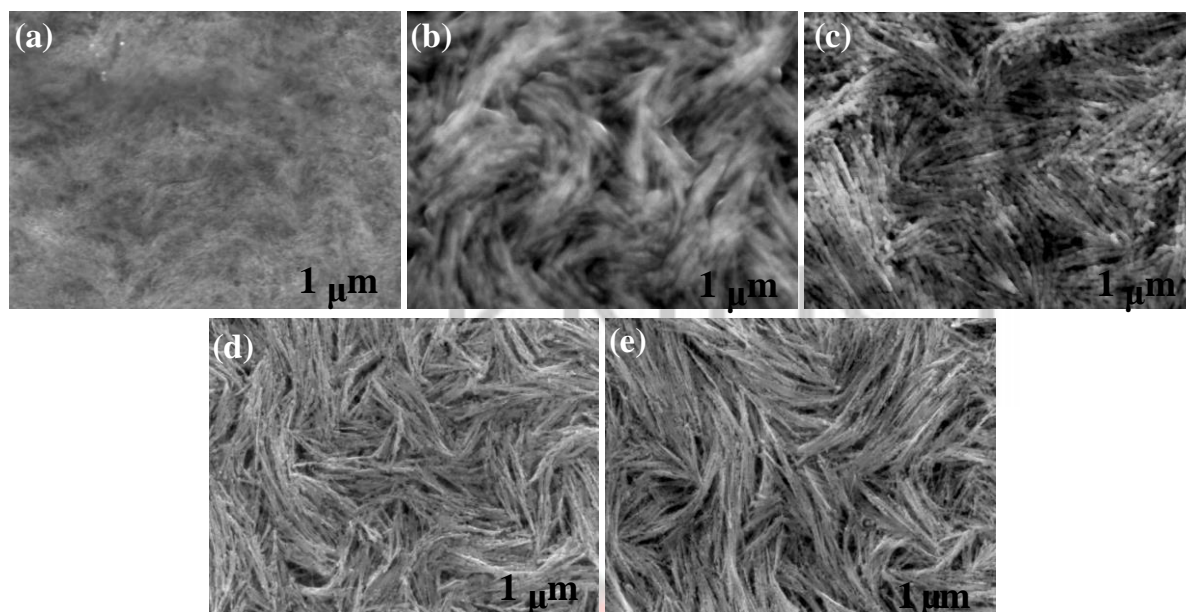


Figure 4.18 SEM images of PbS obtained from complex (7) at 20000x magnification by heating coated films at (a) 125, (b) 150, (c) 200, (d) 250 and (e) 300 °C

4.4.3 Energy dispersive X-ray (EDX) analyses of PbS thin films

EDX analyses of the PbS thin films from complexes (1), (2), (3), (4), (5) and (7) revealed emissions exclusively due to lead and sulfur atoms within the detection limits of the instrument, further providing evidence for the purity of the samples (Figure 4.19). The ratio of Pb:S was approximately equal to 1:1 atomic ratios. However, at a higher heating temperature (300 °C), slightly lead rich thin films were obtained. For instance, quantifying the EDX spectrum of PbS deposited from complex (1) at 300 °C gave 54.05% of Pb and 45.95 % of S as the atomic percentages. This observation may have resulted in the loss of some volatile sulfides at the relatively high decomposition process temperature as observed by Barote *et al.*, (2011). Earlier reports on the EDX analyses of PbS from dithiocarbonates gave similar atomic percentages for Pb and S atoms (Clark *et al.*, 2011; McNaughten and Saah, *et al.*, 2016).

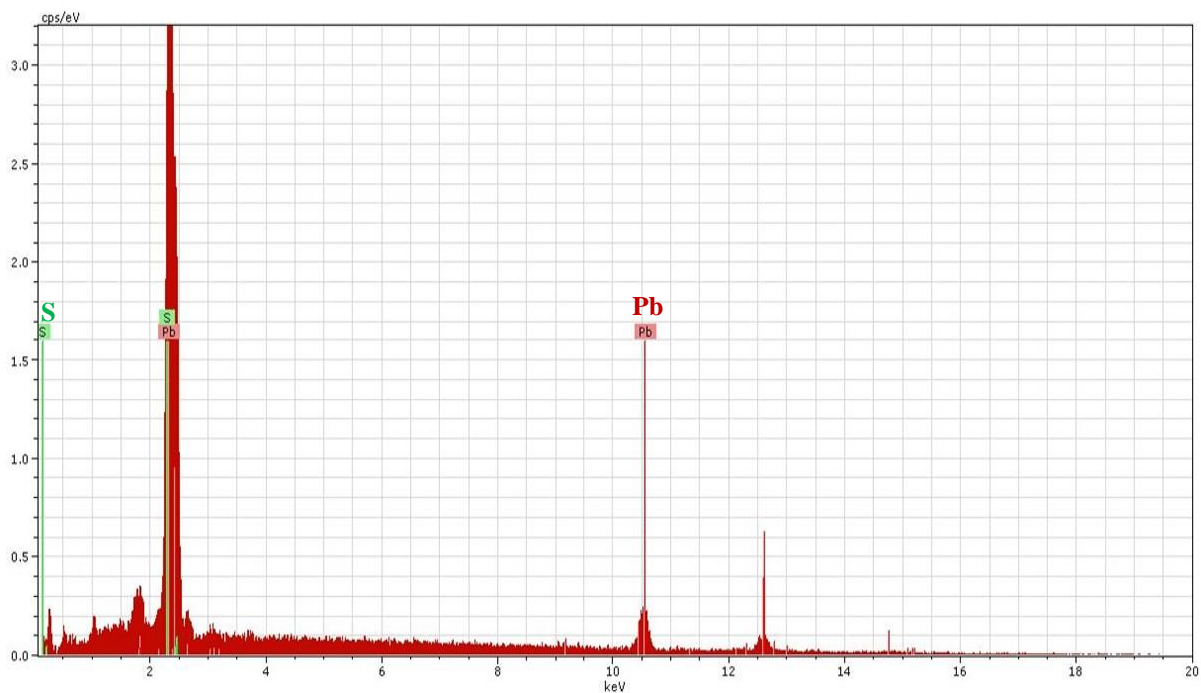
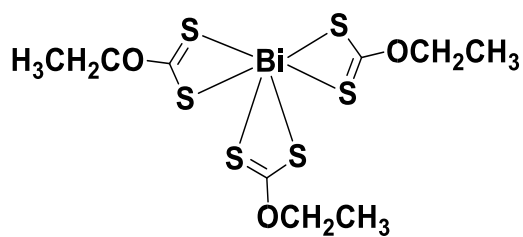


Figure 4.19 Representative EDX spectrum for PbS thin films

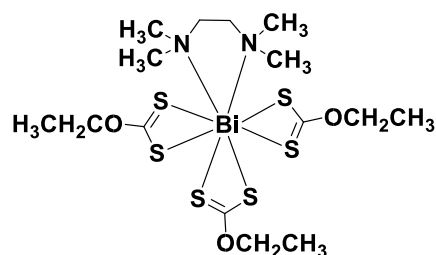
4.5 Syntheses of bismuth ethyl xanthate and its N-adduct complexes

Bismuth ethyl xanthate (**9**) and its N-adducts (TMEDA (**10**), triethylamine (**11**), 1, 10 phenanthroline (**12**) and pyridine (**13**)) have been synthesized and characterized. The complexes were isolated in high yields (> 80 %) as yellow from acetone solution of the crude precipitate. There was no trend of the effect of adduct on the yield of the pure complexes.

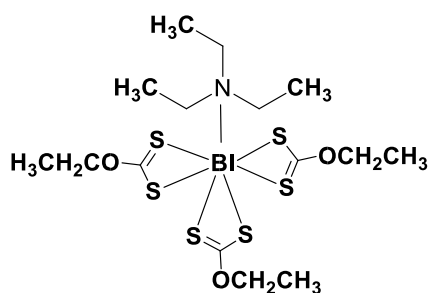
The good solubility of the complexes in common organic solvents such as acetone and chloroform makes the spin coating method followed by heating a viable option for the deposition of Bi_2S_3 thin films from the complexes at a relatively low cost.



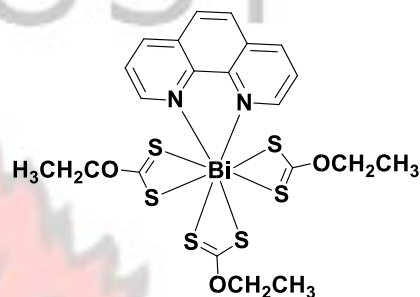
Bismuth ethyl xanthate (9)



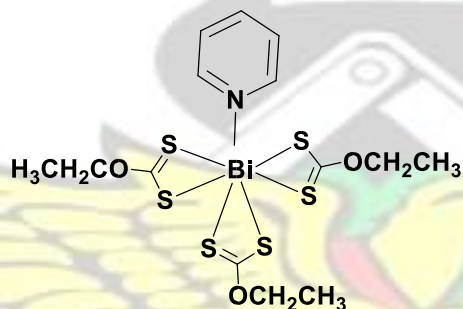
TMEDA adduct of bismuth ethyl xanthate (10)



Triethylamine adduct of bismuth ethyl xanthate (11)



1,10 Phenanthroline adduct of bismuth ethyl xanthate (12)



Pyridine adduct of bismuth ethyl xanthate (13)

bismuth ethyl xanthate (12)

Figure 4.20 Structure of bismuth ethyl xanthate complex and its adducts

4.6 Characterization of bismuth ethyl xanthate and its N-adduct complexes

Micro elemental analyses of all five complexes gave calculated elemental compositions which were within 0.2% of the experimentally determined percentages, thus, confirming that the complexes were of high purity.

Vibrational spectra are unique physical properties and characteristic of a particular molecule.

It can therefore be used as a fingerprint in determining the functional groups present in a

molecule and hence for identification of molecules (Coates and Ed, 2000). The infrared spectra of bismuth ethyl xanthate and its adducts have been extensively reported in literature (Kaltenhauser *et al.*, 2013; Koh *et al.*, 2003; Shankaranarayana and Patel, 1961). Common functionalities that run through all five complexes ((**9**) to (**13**)) include the C–S bond in the C–O bonds which occur around 1020 and 1105 cm^{-1} respectively. Complexes (**10**) to (**13**) exhibited a $\nu_{(\text{C-N})}$ between 1274 and 1282 cm^{-1} which was not seen in the bismuth ethyl xanthate complex.

Mass spectrometric analyses were undertaken on the complexes using positive and negative electro spray ionisation (ESI) which is a ‘soft’ ionization technique in accordance with literature (Barreca *et al.*, 2005, Holcapek *et al.*, 1999, Nair *et al.*, 2002). Mass spectra analyses of the bismuth ethyl xanthate showed a base peak with m/z of 451 which corresponds to the fragment remaining after the release of one ethyl xanthate ligand from the complex. The molecular ion peak which occurred at m/z of 594 was as a result of the addition of sodium atom to the molecular mass of the complex $[(\text{C}_2\text{H}_5\text{OCS}_2)_3\text{Bi} = 571 \text{ g/mol}]$. Complexes (**10**) to (**13**) showed base peaks which correspond to the release of the nitrogen adducts at m/z of 117, 102, 181 and 80 respectively. In all cases, the weakly bound adducts had effects on the coordination of the bismuth metal in the complexes. Both complexes (**10**) and (**12**) showed a coordination of +8 whereas complexes (**11**) and (**13**) showed +7. Molecular ion peaks were observed at 689 ($\text{C}_{15}\text{H}_{31}\text{O}_3\text{S}_6\text{N}_2\text{Bi} = 688 \text{ g/mol}$), 674 ($\text{C}_{15}\text{H}_{30}\text{O}_3\text{S}_6\text{NBi} = 673 \text{ g/mol}$), 755 ($\text{C}_{21}\text{H}_{23}\text{O}_3\text{S}_6 \text{N}_2\text{Bi} = 754 \text{ g/mol}$) and 675 ($\text{C}_{14}\text{H}_{20}\text{O}_3\text{S}_6\text{NBi} = 651 \text{ g/mol}$) for complexes (**10**) to (**13**) respectively. With the exception of the pyridine adduct (complex **13**) which showed the attachment of a sodium atom to the molecular ion peak, the other complexes showed the attachment of a hydrogen atom. All these atoms were used in the bombarding process when adopting the ESI positive technique (Barreca *et al.*, 2005; Fenn *et al.*, 1989).

^1H NMR analyses on these complexes confirmed the hydrogen environments in all five complexes.

4.6.1 Crystal structure of complexes (9) and (12)

The molecular structure of complexes (9) and (12) are shown in Figures 4.21 and 4.22 and selected geometric parameters are collected in Table 4.6 below. Both complexes exhibit a triclinic crystal system with a P-1 space group. The bismuth atom in complex (9) is coordinated to three chelating ethyl xanthate ligands through the two sulfur atoms from each xanthate ligand defining the vertices of a triangular prism. This makes the bismuth atom have a coordination of +6. The complex adopts a trigonal prismatic geometry. The bismuth atom in complex (12) is coordinated to 8 atoms. Six of these atoms are from the 6 sulfur atoms from the three xanthate ligands and the others from the two nitrogen atoms in the 1, 10 phenanthroline. The complex adopts a tetrahedron.

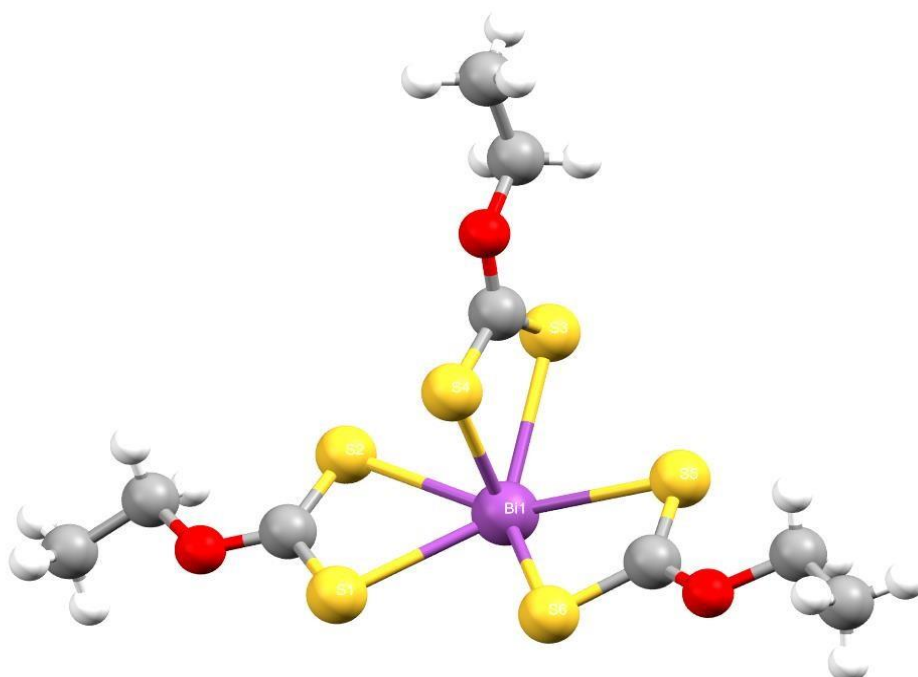


Figure 4.21 X-ray crystal structure of $\text{C}_9\text{H}_{15}\text{BiO}_3\text{S}_6$

Table 4.6 Single crystal data for complexes (9) and (12)

	Complex (9)	Complex (12)
Chem formula	C ₉ H ₁₅ BiO ₃ S ₆	C ₂₁ H ₂₃ BiN ₂ O ₃ S ₆
Formula wt	572.55	752.75
Cryst syst	Triclinic	Triclinic
Space group	P -1	P -1
a(Å)	10.5314(4)	10.6984(4)
b(Å)	11.8403(5)	11.1106(4)
c(Å)	14.0780(6)	11.1601(5)
α(deg)	92.382(3)	95.781(3)
β(deg)	90.575(3)	91.409(4)
γ(deg)	100.200(3)	91.081(3)
V(Å ³)	1725.95(12)	1319.10(9)
Z	2	2
D _{calcd} (g cm ⁻³)	2.203	1.895
μ(Mo Kα) (mm ⁻¹)	10.939	7.184
R1 (I>2σ(I)) ^b	0.0255(5536)	0.0301(4589)
wR2 (all data)	0.0573(6336)	0.0743(4778)
GOF on F ²	1.019	1.032

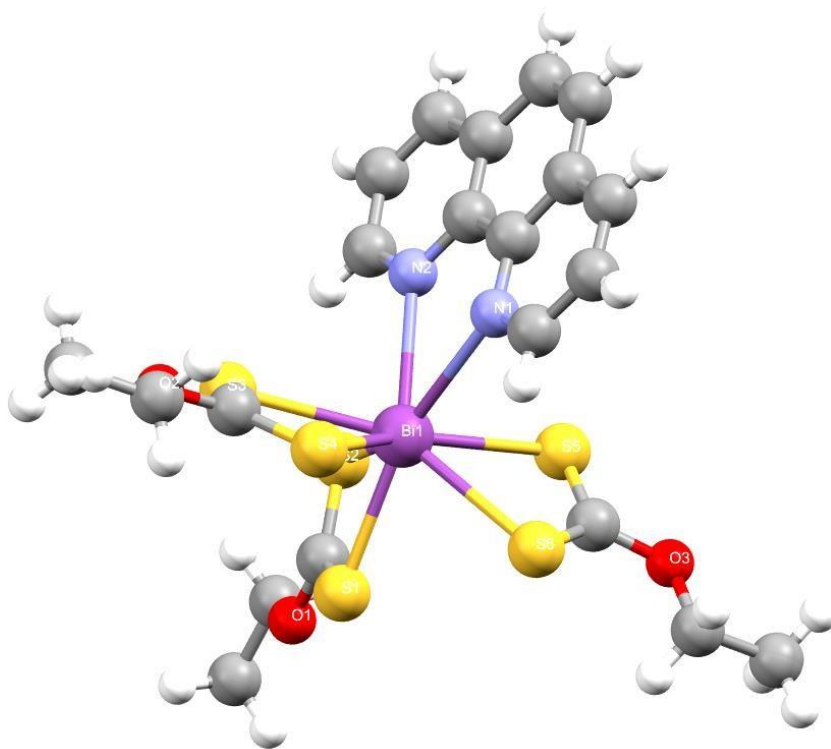


Figure 4.22 X-ray crystal structure of $C_{21}H_{23}BiN_2O_3S_6$

4.7 Characterization of Bi_2S_3 thin films

4.7.1 P-XRD characterization of the Bi_2S_3 thin films

The p-XRD patterns of the Bi_2S_3 thin films were indexed to an orthorhombic Bi_2S_3 phase with ICDD: 00-017-0320, which is by far the widely reported phase of Bi_2S_3 (Tian *et al.*, 2008; Wu *et al.*, 2010; Yang *et al.*, 2017). Diffraction peaks observed at 2 theta values of 15.8° , 17.6° , 22.8° , 26.2° , 28.5° , 31.8° , 33.1° , 35.6° , 36.6° , 46.6° , 52.8° , 59.3° , 62.7° , 66.4° , 66.6° , 66.9° , 67.5° and 67.6° were assigned to the (020), (120), (220), (130), (211), (221), (301), (240), (231), (431), (351), (242), (152), (522), (180), (470), (352) and (870) planes in the pure orthorhombic phase of Bi_2S_3 respectively. There were no deviations in the relative peak intensities as compared to the standard pattern. From the spectra, all the peaks were indexed, indicating that no impurities such as oxides or metals or other phases of Bi_2S_3 were detected, suggesting that the as-deposited thin films were pure products (Figure 4.23). The most intense peak was the

(301) plane which is the preferred orientation. The sharpness of the diffraction peaks gave an information about the good crystallinity of Bi_2S_3 thin films.

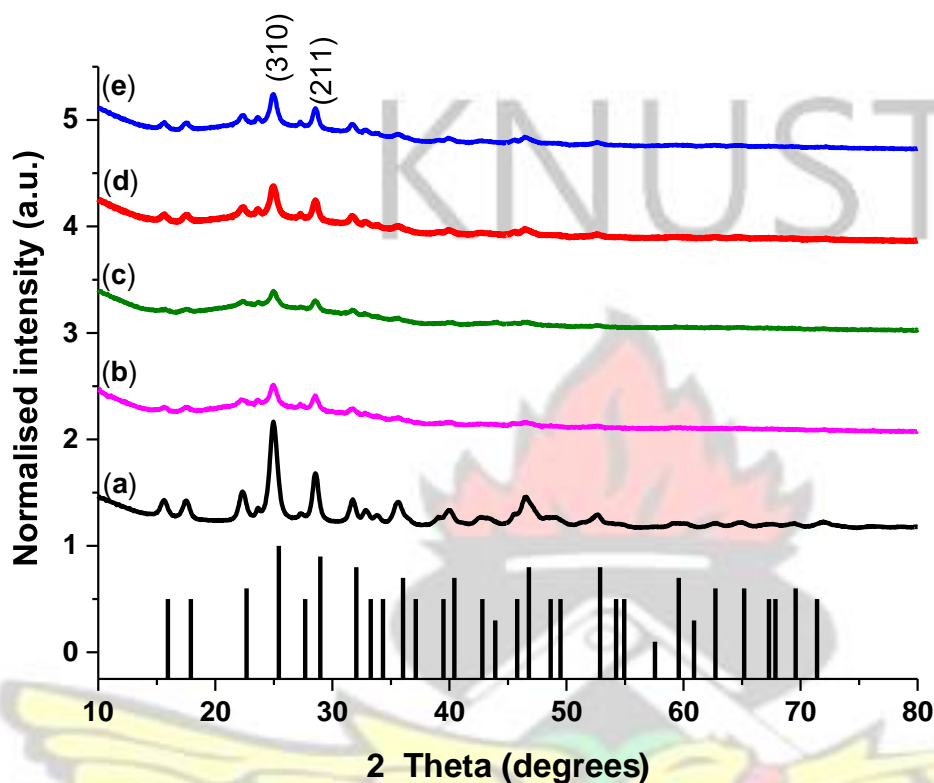


Figure 4.23 p-XRD pattern of Bi_2S_3 thin film from complex (a) (9) (b) (10) (c) (11) (d) (12) and (e) (13)

The p-XRD patterns were in agreement with reported literature for Bi_2S_3 using multiple source starting materials (Arumugam *et al.*, 2017; Dutta *et al.*, 2014; Song *et al.*, 2016). Earlier reports on the deposition of Bi_2S_3 thin film from bismuth diethyldithiocarbamate at a water-toluene interface showed a p-XRD pattern which was also indexed to an orthorhombic Bi_2S_3 (Fan *et al.*, 2008a). A recent report by the Revaprasadu group on the syntheses of Bi_2S_3 using of bismuth piperidine dithiocarbamate complex gave similar p-XRD patterns (Kun *et al.*, 2016).

Table 4.7 Structural parameters of Bi_2S_3 thin films

Bi ₂ S ₃ from complex	Crystallite size (nm)	Size from W-H plot (nm)	Strain (Lm ⁻²)	Lattice parameter (Å)		
				a	B	C
(9)	5.9	11.14	0.0353	11.13	11.27	3.97
(10)	4.4	4.70	0.0038	11.12	11.26	3.97
(11)	1.8	2.60	0.0015	11.11	11.24	3.96
(12)	1.6	1.67	0.0011	11.11	11.24	3.96
(13)	2.3	2.81	0.0052	11.11	11.23	3.94

The positive values for the calculated strain in the Bi₂S₃ thin films all signify the dominance of tensile strain. From literature, there is dominance of tensile strain in most thin films (Ali and Saleh, 2014; Bhatt *et al.*, 2014; Preetha and Remadevi, 2014). The lattice parameters calculated from equation 3.4 were close to the values of bulk Bi₂S₃ which were a=11.14, b=11.30 and c=3.98 (Bhatt *et al.*, 2014).

4.7.2 Scanning electron microscopic analyses of the Bi₂S₃ thin films

Morphological analyses of the Bi₂S₃ thin films show varying images depending on the nitrogen source used as adduct (Figure 4.24). The Bi₂S₃ thin films from heating spin coated slide of complex (9) showed the formation of uniformly sized monodispersed nanowires which were vertically oriented. The width of the nanowires was about 100 nm and an ultra long length of about one micron. The aspect ratio was estimated to be 10. Bao *et al.*, (2008) have earlier reported similar Bi₂S₃ nanowires by the hydrothermal reaction between ethylenediaminetetraacetic acid disodium salt, bismuth nitrate pentahydrate and mercaptosuccinic acid.

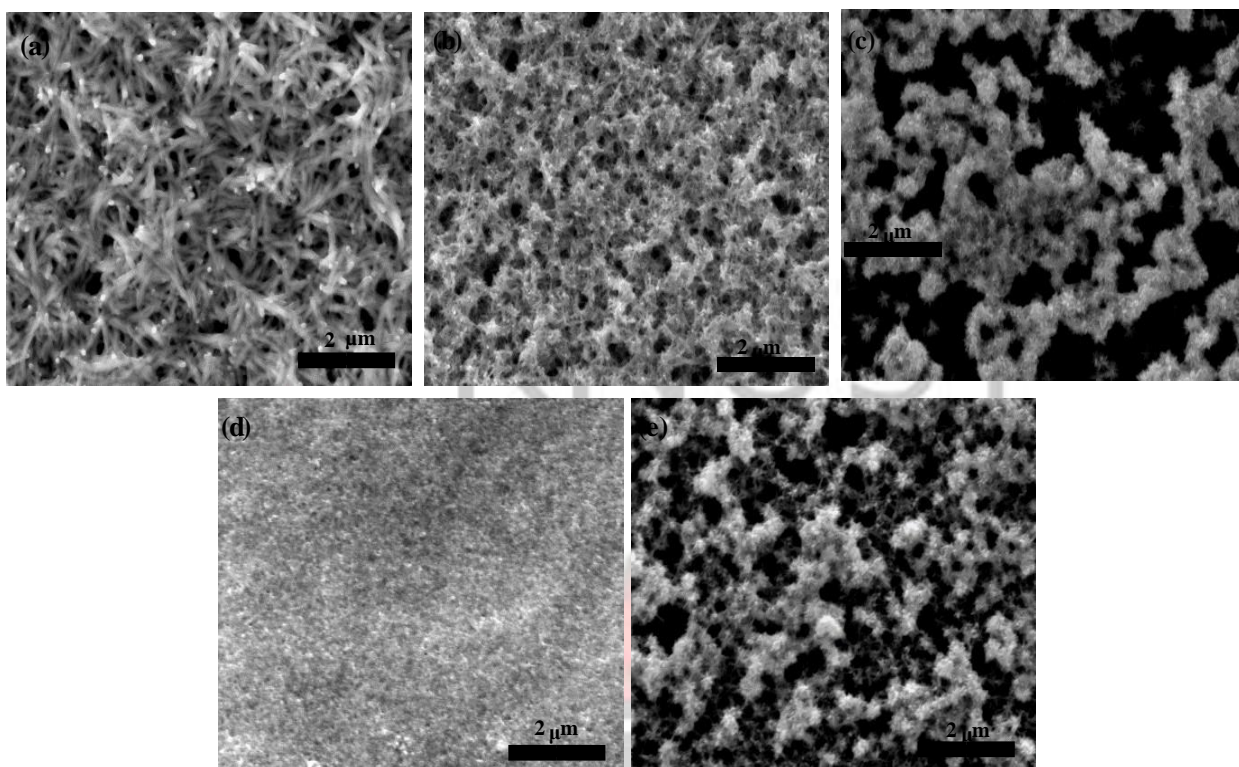


Figure 4.24 SEM images of Bi_2S_3 thin film from complex (a) (9), (b) (10), (c) (11) (d) (12) and (e) (13)

The Bi_2S_3 thin films from complex (10) also showed the growth of nanowires. The width of the Bi_2S_3 nanowires were 85 nm and length of about 450 nm. Each of these wires also had an aspect ratio of 5. The Bi_2S_3 nanowires from complexes (9) and (10), showed uniform coverage of the substrate. The Bi_2S_3 thin films from complexes (11) and (13) showed the formation of uniformly sized nanorods which were joined together into clusters to form nanoflowers. The rods had a width of about 50 nm and length of about 150 nm. The growth towards 1 dimensional morphology in Bi_2S_3 nanoparticles and thin films is due to the weak van der Waals interactions linking the Bi_2S_3 units. This forms infinite chains parallel to the c-axis, thus the preferential growth along the [301] direction as reported by Yang *et al.*, 2017. These clusters stretch across the entire surface of the glass substrate. The major difference between the clusters were that, a much denser cluster was seen on the entire substrate surface of the Bi_2S_3 from complex (11) as

compared to the clusters from complex (13). Similar aggregation of smaller rods have been reported for Bi₂S₃ deposited from bismuth diethyldithiocarbamate SSP at a water-toluene interface at 80 °C (Fan *et al.*, 2008a). Uniformly sized nanodots were formed from decomposing the spin coated slide from complex (12) at 200 °C. Similar, Bi₂S₃ nanodots with diameters 8 nm have earlier been reported from bismuth chloride and thioacetamide using hot injection technique (Wu *et al.*, 2010).

4.7.3 Energy dispersive X-ray analyses of the Bi₂S₃ thin films

Despite the dependence of the morphology on the adduct, qualitative EDX analysis detected bismuth and sulfur as the only elements present other than the constituent elements in the glass substrates within the detection limit of the instrument. The strong silicon peaks observed at 1.74 keV was as a result of emission from the glass substrate due to the relatively thin Bi₂S₃ deposit. Other low intensed peaks observed at 0.28, 0.53, 1.04, 1.25 and 1.49 keV were as a result of carbon, oxygen, sodium, magnesium and aluminium from the glass substrate. In all the five Bi₂S₃ thin films, the atomic percentages for Bi and S match closely to 40.0 and 60.0% for Bi and S in Bi₂S₃ as shown in Table 4.8.

Table 4.8 EDX analyses of Bi₂S₃ thin films

Bi ₂ S ₃ from complex	% Bi	% S
(9)	40.10	59.90
(10)	40.09	59.91
(11)	39.23	60.72
(12)	41.91	58.09
(13)	37.93	62.07

CHAPTER 5

RESULTS AND DISCUSSIONS ON THE SYNTHESIS AND CHARACTERIZATION OF TERNARY LEAD CHALCOGENIDES AND BISMUTH DOPED LEAD SULFIDE THIN FILMS AND NANOPARTICLES

5.1 Summary of results for ternary $\text{PbS}_x\text{Se}_{(1-x)}$ and Bi doped PbS nanomaterials

Ternary $\text{PbS}_x\text{Se}_{(1-x)}$ thin films have been deposited from heating a mixture of complexes (7) and (15) whereas complexes (15) and (17) have been used to synthesize $\text{PbS}_x\text{Se}_{(1-x)}$ nanoparticles. Complexes (19) and (20) have also been mixed to synthesize Bi doped PbS ternary nanoparticles. The effect of the dopant concentrations on the properties of the ternary alloys were investigated using techniques such as XRD, SEM, TEM, EDX and ICP.

5.2 Syntheses of complexes (7) and (15)

Complexes (7) and (15) were obtained as solids with complex (7) being brown and (15) being yellow. To the best of our knowledge, there has not been any report on the syntheses and characterization of complex (7) in literature. However, the few reports on the syntheses and characterization of complex (15) did not state the colour of the complex. For example, Akhtar *et al.*, (2012a) synthesized complex (15) but did not report its colour. The complexes were stable and easy to handle. The complexes were obtained in high yields (> 80%) after recrystallization. The chemical structures of the molecular complexes used as single source precursors for the deposition of PbS, PbSe and $\text{PbS}_x\text{Se}_{(1-x)}$ thin films in this study are shown in Figure 5.1.

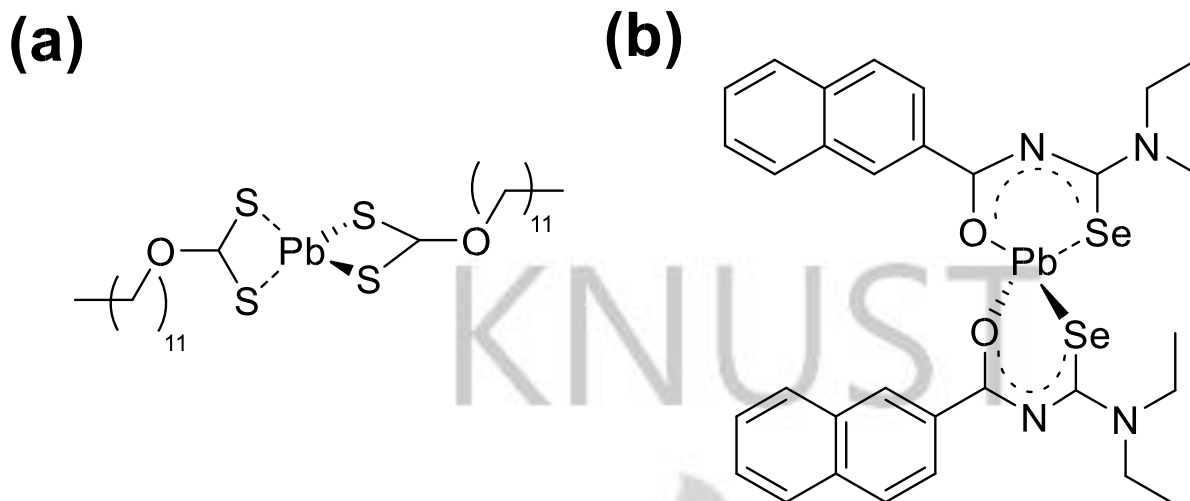


Figure 5.1 Structures of the single source precursors used (a) *bis*(didodecyldithiocarbonate)lead(II) (**7**) and (b) *bis*(*N,N*-diethyl-*N'* naphthylselenoureato)lead (II) (**15**)

5.3 Characterization of complexes (**7**) and (**15**)

The experimental elemental analyses (%) for both complexes were found to be within 0.5 % of the calculated values, and the correct exact masses were observed by electrospray mass spectrometry which confirmed that the synthesized complexes were pure and agreed with the proposed stoichiometric formulae. Since the groups around the Pb in both complexes were symmetrical, only one half of the complex was considered for interpreting the ^1H NMR spectra. ^1H and ^{77}Se NMR (for complex (**15**)) spectra confirmed the requisite number of proton and selenium environments in all cases and the expected J couplings were also observed in the ^1H NMR spectra.

In order to further characterize the structure of the complexes, mass spectrometric analyses were undertaken using positive and negative Electro Spray Ionisation (ESI) which is a ‘soft’ ionization technique. The m/z of complexes (**7**) and (**15**) were observed 754 and 873 respectively. There was a sodium atom attached to the molecular ion peak of complex (**7**) which

is due to the use of sodium atom in bombarding the complex during the analyses (Fenn *et al.*, 1989).

Thermogravimetric analyses (TGA) of the complexes, were performed to determine their thermal decomposition profiles. The *bis*(didodecyldithiocarbonate) lead (II) complex (**7**) decomposed in two steps to a plateau which is indicative of the formation of a residue with a constant weight (Figure 5.2). The first step began at 91.4 °C and completed at 193.9 °C with a 23.7 % weight loss corresponding to the loss of one dodecyl alkyl chain (23.2 %). The second step started at 198.7 °C and was completed at 326.9 °C with a maximum weight loss of 46.9 %, resulting in a residue amounting to 29.4 % of the initial weight. This value is lower than 32.8 % calculated for 100 % conversion of complex (**7**) to PbS. This may have been caused by some evaporation or sublimation of sulfur from the complex at high temperatures. The lead selenoureato complex (**15**) decomposed in four steps to give a residual weight of 37.8 %, which is higher than the expected value of 32.8 % for PbSe (Figure 5.2). This could be due to some carbon contamination because of its relative bulkiness as reported by Akhtar *et al.*, (2012a). Generally, selenourea complexes have been known to exhibit multiple decomposition steps. For example, *bis*[*N, N*-diisobutyl-*N'*-(4 nitrobenzoyl)selenoureaato]lead (II) complex have been reported to decompose in multiple steps (Akhtar *et al.*, 2011).

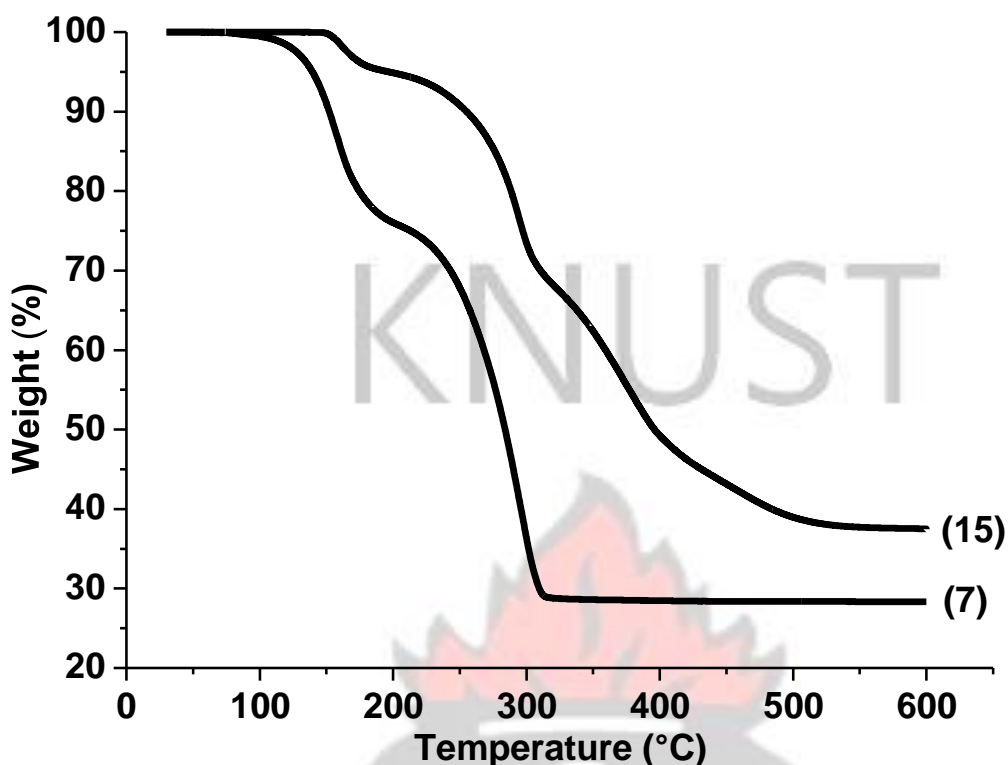


Figure 5.2 Thermogravimetric analyses (TGA) profile of complexes (7) and (15)

5.4 Characterization of $\text{PbS}_x\text{Se}_{(1-x)}$ thin films

5.4.1 p-XRD analyses of $\text{PbS}_x\text{Se}_{(1-x)}$ thin films

The p-XRD patterns of the as-deposited PbS and PbSe thin films from complexes (7) and (15) after heating at temperatures ranging from 250–400 °C were consistent with the face-centred cubic (halite) structure of PbS (ICDD 00-005-0592) and PbSe (ICDD 01-077-0245) (Figure 5.3) respectively. Preferred growth along (200) plane was observed in all cases of the thin films as reported earlier by Akhtar *et al.*, (2010). The cubic phase is consistent with earlier reports on the syntheses of PbS from lead alkyl xanthate SSPs using techniques such as CVD and spin coating (Akhtar *et al.*, 2012a; Clark *et al.*, 2011; Lewis *et al.*, 2015). The highly intense peaks suggest that the as-deposited PbS and PbSe thin films were highly crystalline (Barote *et al.*, 2011; Kumar *et al.*, 2009; Obaid *et al.*, 2013; Qiu *et al.*, 2011). The peaks of the PbS thin films

were broader as compared to the peaks of the PbSe thin films, suggesting smaller crystallite sizes for the PbS nanomaterials as compared to the PbSe as observed earlier by Lewis *et al.*, (2015).

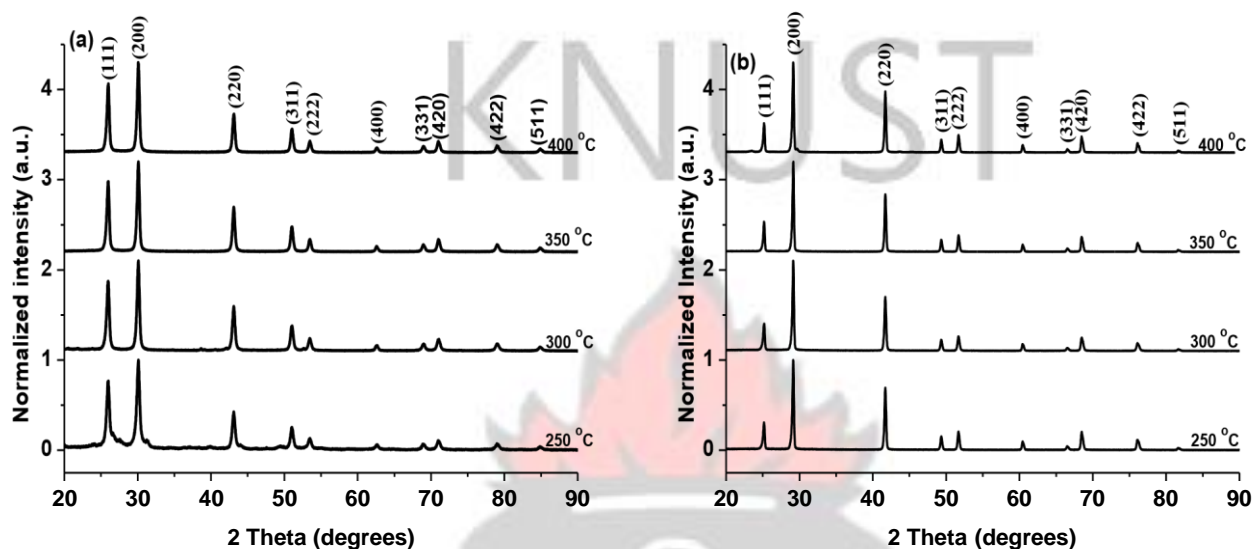


Figure 5.3 Powder XRD patterns of (a) PbS and (b) PbSe thin films deposited by spin coating of complexes (7) and (15) respectively following heating for 30 minutes at different temperatures as indicated

The crystallite sizes calculated using equation 3.1 for the particles along the (200) plane of the PbS thin films were 17.4, 21.6, 22.4 and 22.8 nm for 250, 300, 350 and 400 °C respectively.

An increase in temperature led to larger crystallites in the thin films as similarly observed by Codato *et al.*, (2011). There was a similar variation in the PbSe growth with critical dimensions ranging from 33.7 to 35.5 nm. As seen from Table 5.1, the calculated lattice constant (a) using equation 3.3 compared closely to the literature values of 5.936 Å and 6.127 Å for bulk PbS and PbSe respectively (Boadi *et al.*, 2012; Lewis *et al.*, 2015).

Table 5.1 Effect of temperature on the lattice constant of as-deposited PbSe and PbS thin films

Temperature (°C)	Lattice constant (Å) of PbSe	Lattice constant (Å) of PbS
------------------	------------------------------	-----------------------------

250	6.1257	5.9358
300	6.1260	5.9362
350	6.1266	5.9366
400	6.1269	5.9370

The p-XRD patterns of the as-deposited $\text{PbS}_x\text{Se}_{(1-x)}$ thin films varied with the composition of the precursor mixture (Figure 5.4). The p-XRD pattern of $\text{PbS}_x\text{Se}_{(1-x)}$ thin films exhibited the same general pattern of cubic reflections as observed for the parent PbS and PbSe compounds. The $\text{PbS}_x\text{Se}_{(1-x)}$ alloys exhibit linearity in the incorporation of the selenium in the thin films as compared to the mole fraction present in the original precursor solution (Akhtar *et al.*, 2011; Monshi *et al.*, 2012; Smith *et al.*, 2011). However, at a selenium mole fraction greater than 0.5, the p-XRD pattern matched closely to a pure PbSe phase. From the p-XRD pattern, it was also observed that there was not 100% incorporation of selenium into the PbS crystal lattice. This might be due to the difference in the thermodynamic stability of the two chalcogens. The selenium which has a bigger atomic size is preferred over the sulfur. As an illustration, at a selenium mole fraction of 0.3 in the coating mixture, the alloy formed had a p-XRD pattern that was exactly in-between the matching lines of the two parent binaries. This spectrum also matched to the standard pattern of $\text{PbS}_{0.5}\text{Se}_{0.5}$ ternary alloy.

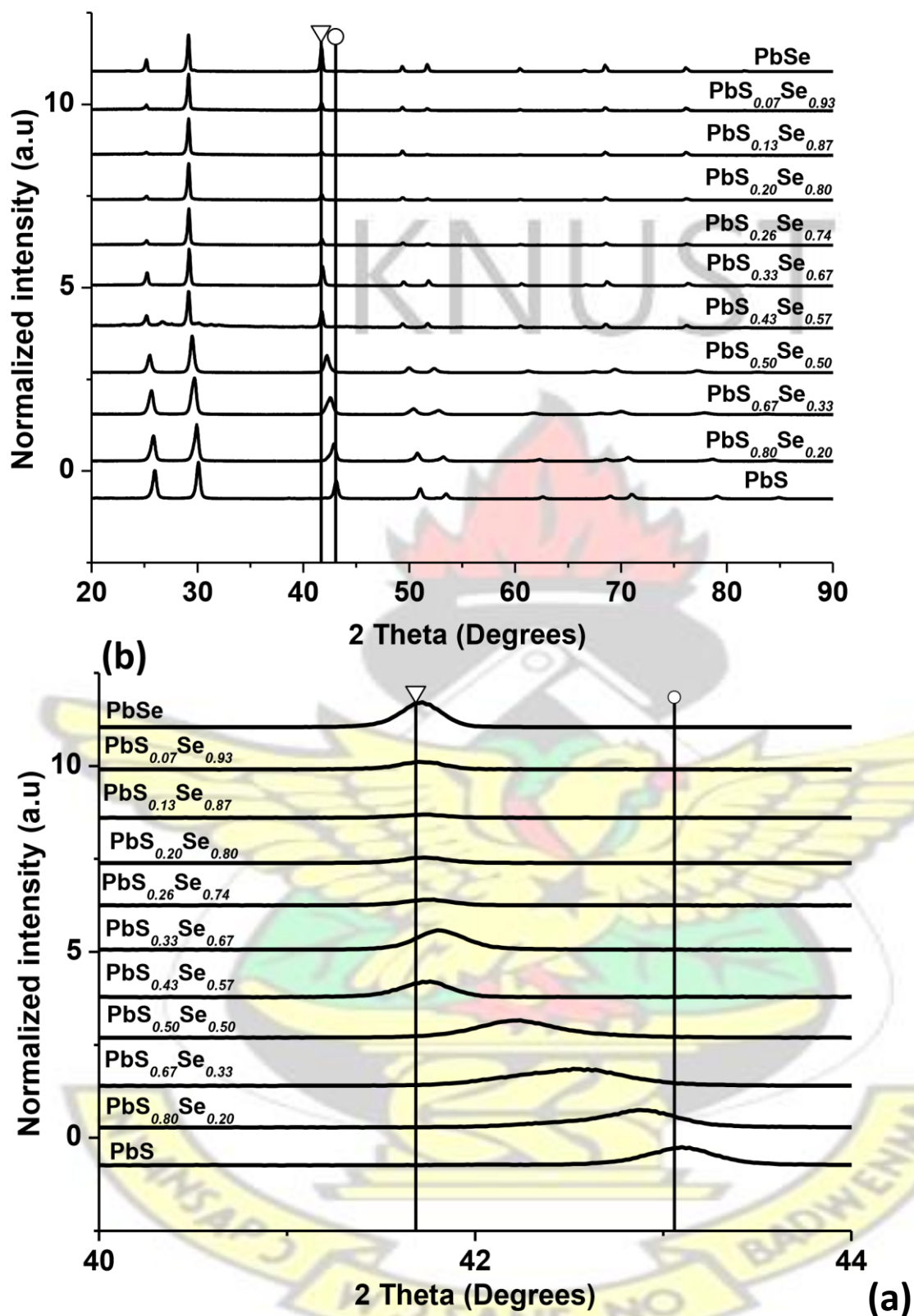


Figure 5.4 (a) p-XRD patterns of $\text{PbS}_x\text{Se}_{1-x}$ obtained by spin coating mixtures of complexes (7) and (15) following heating for 30 minutes at 250 °C and (b) expanded form of (a) along the (220) plain with corresponding (triangle) PbSe and (circle) PbS

Generally, increasing the mole fraction of selenium in the feed precursor caused a gradual shift of the diffraction angle of the p-XRD pattern to lower 2 theta values. To illustrate this, the (200) reflection of PbS was at 30.1° which moved to 29.5° for PbS_{0.5}Se_{0.5} and settled at 29.1° for PbSe. This confirms the formation of a single ternary PbS_xSe_(1-x) alloy rather than mixed phases of PbS and PbSe.

Similar shift in p-XRD pattern in ternary PbS_xSe_(1-x) to lower 2 theta values as the selenium content increased have been reported earlier using elemental sulfur and selenium as the chalcogen sources (Gao *et al.*, 2013; Kumar *et al.*, 2010; Shao *et al.*, 2014). The only report on the use of SSPs for the synthesis of PbS_xSe_(1-x) nanowires using solution-liquid-solution growth technique is on the use of lead(II)diethyldithiocarbamate and lead(II)imido *bis*(selenodiisopropylphosphinate) by Onicha *et al.*, (2012). A similar shift from a PbS to PbSe phase was observed as the ratio of the lead(II)imido *bis*(selenodiisopropylphosphinate) complex was increased from 0 to 1. All these reports point to the fact that different chalcogen sources can be used in the syntheses of high quality PbS_xSe_(1-x) nanoparticles and thin films. However, other factors such as toxicity and cost have a great influence on the choice of starting material.

The effect of temperature on the microstrain in the as-deposited thin films were also determined by equation 3.5 which represents the slope of the W-H plot.

Table 5.2 Effect of temperature on the strain in PbSe and PbS thin films

Temperature (°C)	Strain for PbSe	Strain for PbS
250	0.0011	0.0005
300	0.0010	0.0004
350	0.0009	0.0004
400	0.0007	0.0003

From the Table 5.2, the calculated positive values for both PbS and PbSe thin films signify that tensile strain was dominant in all the thin films as reported earlier by Mozafari *et al.*, (2012). The strain in thin films also depend on size. Generally, the magnitude of the strain decreased with increasing size indicating that strain is a function of size (Table 5.2). This is because at higher temperature, there is an increase in crystallite sizes and thereby a reduction in force per unit area between grains and consequently strain relaxation (Remadevi and Preetha, 2012).

The effect of selenium concentration on the crystallite sizes were also calculated using equation 3.1. Generally, there was an increase in crystallite sizes as the concentration of selenium in the coating mixture increased from 0 to 1 (Table 5.3). This is due to the larger crystallite sizes of the PbSe as compared to the PbS and therefore affect the sizes of the alloy at high concentrations. However, the smallest crystallites were formed at a 0.3 mole fractions of selenium which deviates from the general trend.

Table 5.3 Effect of selenium mole fraction of on crystallite sizes and dislocation density of $PbS_xSe_{(1-x)}$ thin film

Mole fraction of complex (15) in coating mixture	Crystallite sizes (nm)	Dislocation density (L/m^2)
0	17.4	0.003303
0.1	18.8	0.002829
0.2	15.2	0.004328
0.3	14.7	0.004628
0.4	26.1	0.001468
0.5	26.1	0.001468
0.6	30.8	0.001054
0.7	32.1	0.000970
0.8	31.3	0.001021
0.9	31.9	0.000983
1	33.7	0.000881

In crystalline materials, the dislocation density (δ) decreases with increasing crystallite size (Begum *et al.*, 2012). According to Preetha and Remadevi, (2014), they proposed that this is

due to a decrease in the occurrence of grain boundaries because of an increase in the crystallite size of the film with increasing temperature. In order to ascertain the validity of the above statement, the dislocation density (δ) was calculated using equation 3.2.

From Table 5.3, there was a gradual decrease in dislocation density as the mole fraction of the Se increased. This is due to the bigger atomic radius of selenium which has a strong effect on structural parameters with increased Se content which confirms the earlier statement by Preetha and Remadevi, (2014). There was also a dominance of tensile stress in all the $PbS_xSe_{(1-x)}$ thin films (Table 5.4).

Table 5.4 Effect of the mole fraction of complex (15) on the strain of $PbS_xSe_{(1-x)}$ thin films

Mole fraction complex of (15) in coating mixture	Strain (L/m^2)
0	0.00048
0.1	0.00017
0.2	0.00022
0.3	0.00020
0.4	0.00019
0.5	0.00011
0.6	0.00013
0.7	0.00080
0.8	0.00080
0.9	0.00013
1	0.00070

The lattice constant 'a' of the alloys were estimated from the p-XRD data using equation 3.3. A plot of lattice constant against mole fraction of selenium in the coating mixture showed that the lattice constants increased linearly and monotonically, only reaching a plateau when the

mole fraction of selenium in the coating mixture was above 0.5 (Figure 5.5). The linear behaviour observed was as a result of all the selenium in the coating mixture being incorporated into the $\text{PbS}_x\text{Se}_{(1-x)}$ thin films (at selenium feed ratio ≤ 0.5). This confirms that unit cell parameters vary linearly with composition for a continuous substitutional solid as proposed earlier in literature (Akhtar *et al.*, 2011; Monshi *et al.*, 2012; Thomson *et al.*, 2012). This observation is consistent with the p-XRD pattern which shows a gradual shift from the PbS standard pattern to a PbSe as the mole fraction of selenium increase from 0 to 0.5 and matching to a PbSe phase when the mole fraction of selenium in the coating mixture was above 0.5.

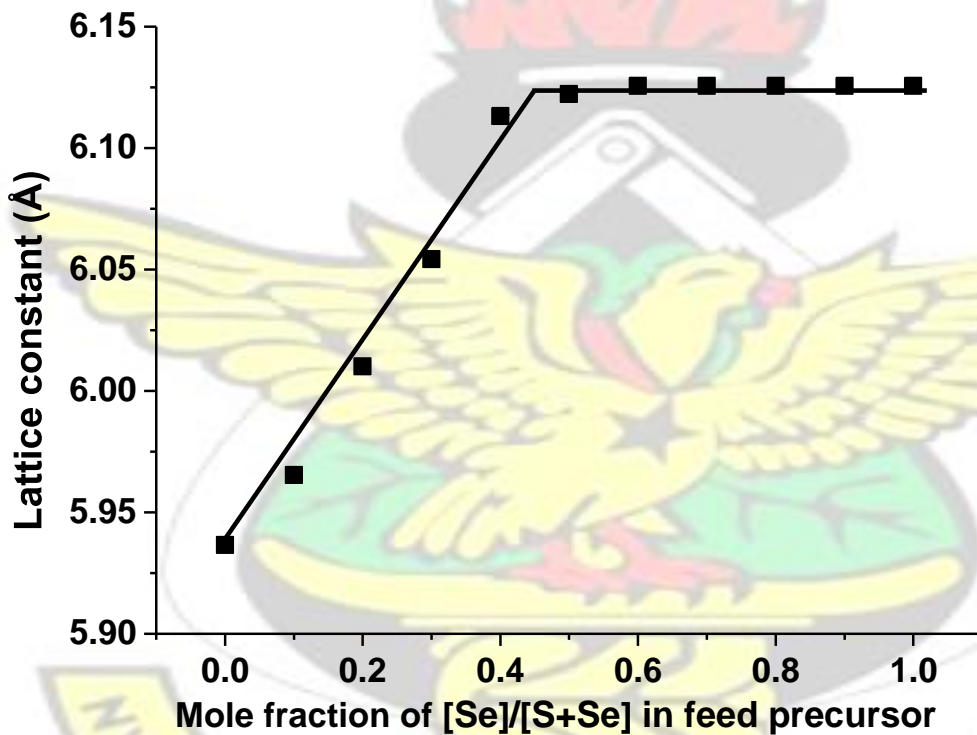


Figure 5.5 Relation between the cubic lattice constant 'a' to the ratio of [Se]/[S+Se] in the coating mixture used for spin coating.

5.4.2 Scanning electron microscopy images of $\text{PbS}_x\text{Se}_{(1-x)}$ thin films

In order to investigate the morphologies of the as-deposited $\text{PbS}_x\text{Se}_{(1-x)}$ thin films, scanning electron microscopy analyses were performed using a secondary electron detector. It is well

known that surface properties of thin films influence their optostructural and electrical properties and is important factor regarding application of the materials. Thus, it was very important to investigate surface morphology of the thin films. The PbS thin films showed a closely packed network of fibrous structures, each covered with adhering cubes. The fibrous structures were *ca.* 500 nm in length and 25 nm in width. The side lengths of the cubic crystallites were 34 ± 4 , 44 ± 3 , 47 ± 5 and 50 ± 4 nm, showing an increase with increasing deposition temperature from 250, 300, 350 and 400 °C respectively (Figure 5.6).

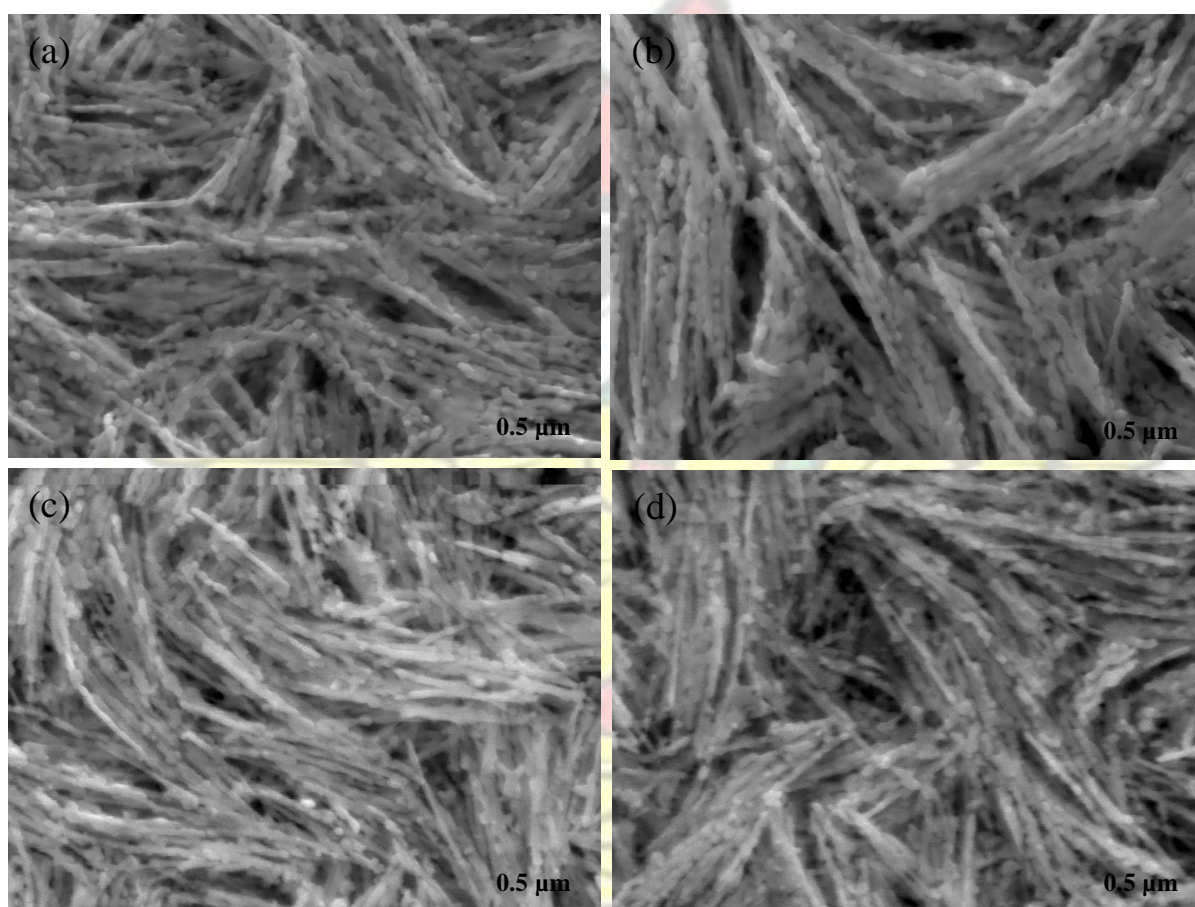


Figure 5.6 SEM images of PbS nanoparticles deposited on glass substrate obtained from decomposition of complex (7) at (a) 250, (b) 300, (c) 350 and (d) 400 °C.

The crystallite sizes from p-XRD calculated using equation 3.1 were between 17.4-22.4 nm. These were multiples of the particle sizes obtained from the SEM implying that the particles and elongated features were polycrystalline as postulated earlier by Monshi and coworkers (2012). Although PbS has been known to give anisotropic growth with common morphologies

such as cubes (McNaughter and Saah *et al.*, 2016), spheres (Jin *et al.*, 2012), stars (Ma *et al.*, 2004), rods (Nyamen *et al.*, 2012), wires (Onicha *et al.*, 2012) and rod with a cube at the tip (Lewis *et al.*, 2015), there is no report on such unique elongated structure with cubes at equal lengths along the entire length for PbS nanocrystals.

PbSe thin films showed the growth of cubes with well-defined edges at 250 °C although the substrate was poorly covered. A further increase in temperature to 350 °C also showed the growth of well-defined cubes with improved substrate coverage. Few of the cubes lost their edges at 400 °C due to agglomeration at high processing temperature (Figure 5.7). At these high temperatures, the nanoparticles have higher surface energy and therefore have the ability to collide to form bigger particles (Chen *et al.*, 2010). Several researchers have reported cubic morphology for PbSe nanomaterials (Boadi *et al.*, 2016; Cui *et al.*, 2012) although other morphologies such as octahedron (Chang *et al.*, 2010), dendrites (Cao *et al.*, 2011), rods (Chen *et al.*, 2001) and tubes (Shi *et al.*, 2010) have also been seen. The estimated particle sizes from the SEM using ImageJ software were 322 ± 19 , 403 ± 10 , 437 ± 16 and 441 ± 17 nm at temperatures of 250, 300, 350 and 400 °C respectively. The Scherrer sizes were multiples of the particle sizes implying that several smaller crystallites agglomerated to form the particles.

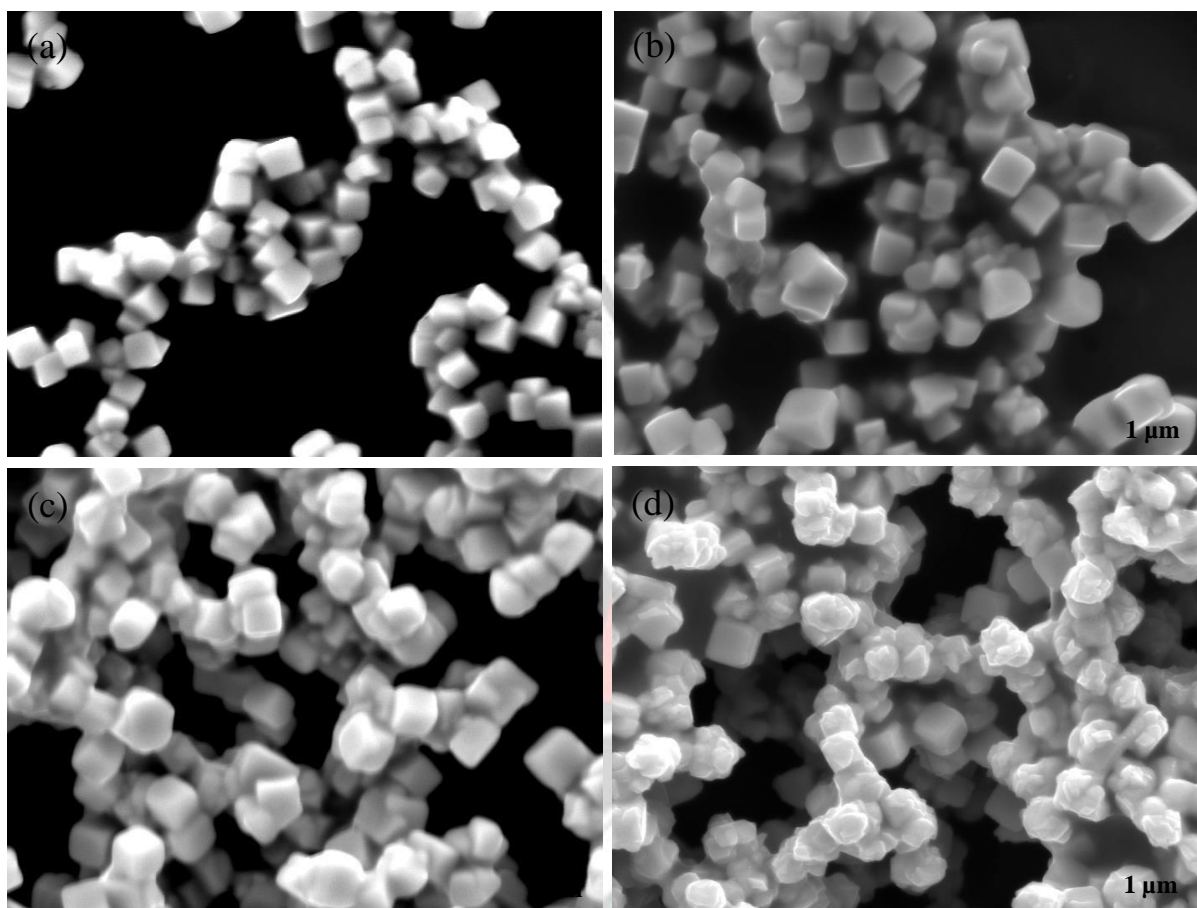


Figure 5.7 SEM images of PbSe nanoparticles deposited on glass substrate obtained from decomposition of complex **(15)** at (a) 250, (b) 300, (c) 350 and (d) 400 °C.

The morphology of the ternary $\text{PbS}_x\text{Se}_{(1-x)}$ thin films showed varying shapes depending on the mole fraction of the selenium in the coating mixture (Figure 5.8). At a selenium mole fraction of 0.1 and 0.2, the $\text{PbS}_x\text{Se}_{(1-x)}$ thin films produced were predominantly rods with few cubes. The rods may have been formed from the breakdown of the fibrous structures in the PbS thin films. A close packed mixed morphology of cubes and few rods were observed in the morphology of the thin films containing 0.3 mole fraction of selenium. From the p-XRD pattern, $\text{PbS}_{0.5}\text{Se}_{0.5}$ thin films were formed at this ratio. A close packed mixed morphology of cubes and few rods were observed. A further increase in the selenium mole fraction (complex

(15)), resulted in the formation of cubes although the dimensions were smaller than that of the PbSe films. These thin films had a better substrate coverage as compared to that of the PbSe thin film.

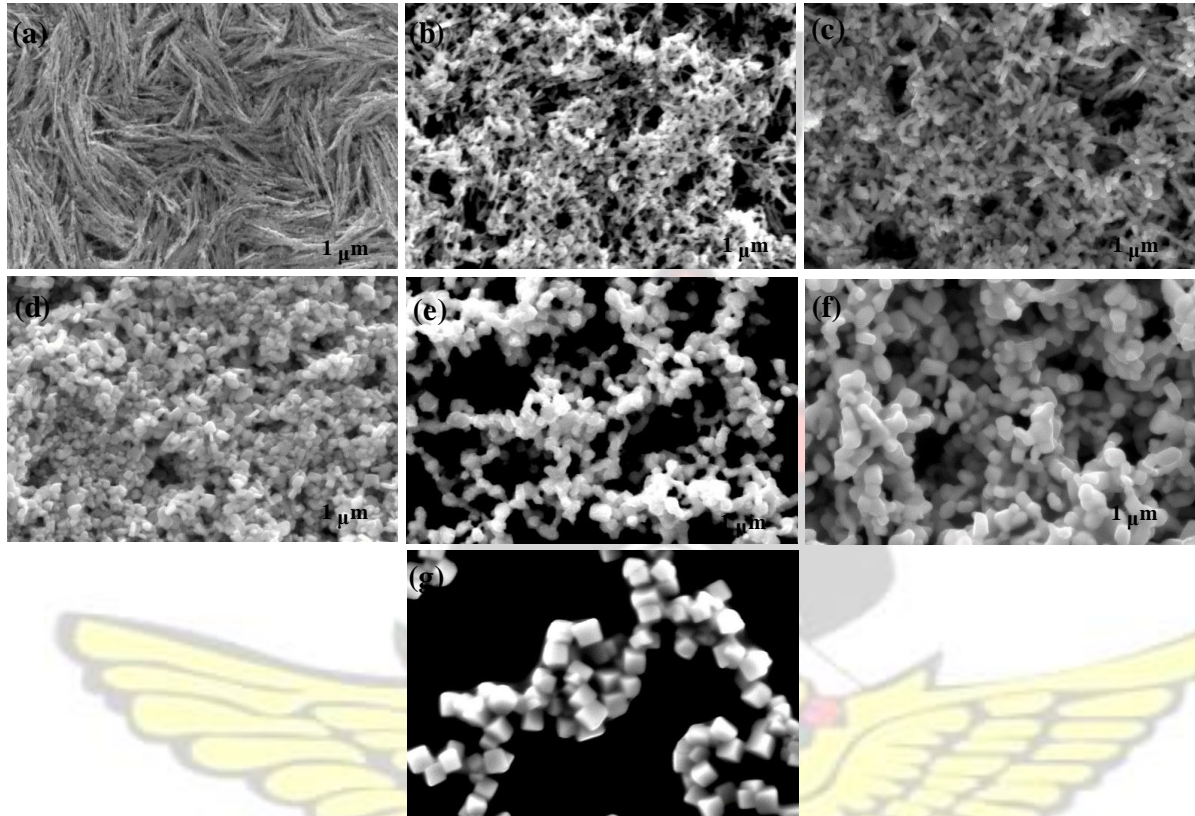


Figure 5.8 SEM images of $\text{PbS}_x\text{Se}_{(1-x)}$ thin films obtained from mixing complexes (7):(15) at (a) 1:0, (b) 0.9:0.1, (c) 0.8:0.2, (d) 0.7:0.3, (e) 0.6:0.4, (f) 0.5:0.5 and (g) 0:1

5.4.3 Energy dispersive X-ray spectroscopy analyses of $\text{PbS}_x\text{Se}_{(1-x)}$ thin films

Elemental composition of the $\text{PbS}_x\text{Se}_{(1-x)}$ thin films were analysed using energy dispersive X-ray spectroscopy (EDX). The EDX analyses of PbS and PbSe thin films showed only peaks characteristic of Pb, S or Se atoms. Quantifying the spectra showed approximately 1:1 atomic ratios for Pb:S and Pb:Se. The alloys showed peaks characteristic of Pb, S and Se (Figure 5.9).

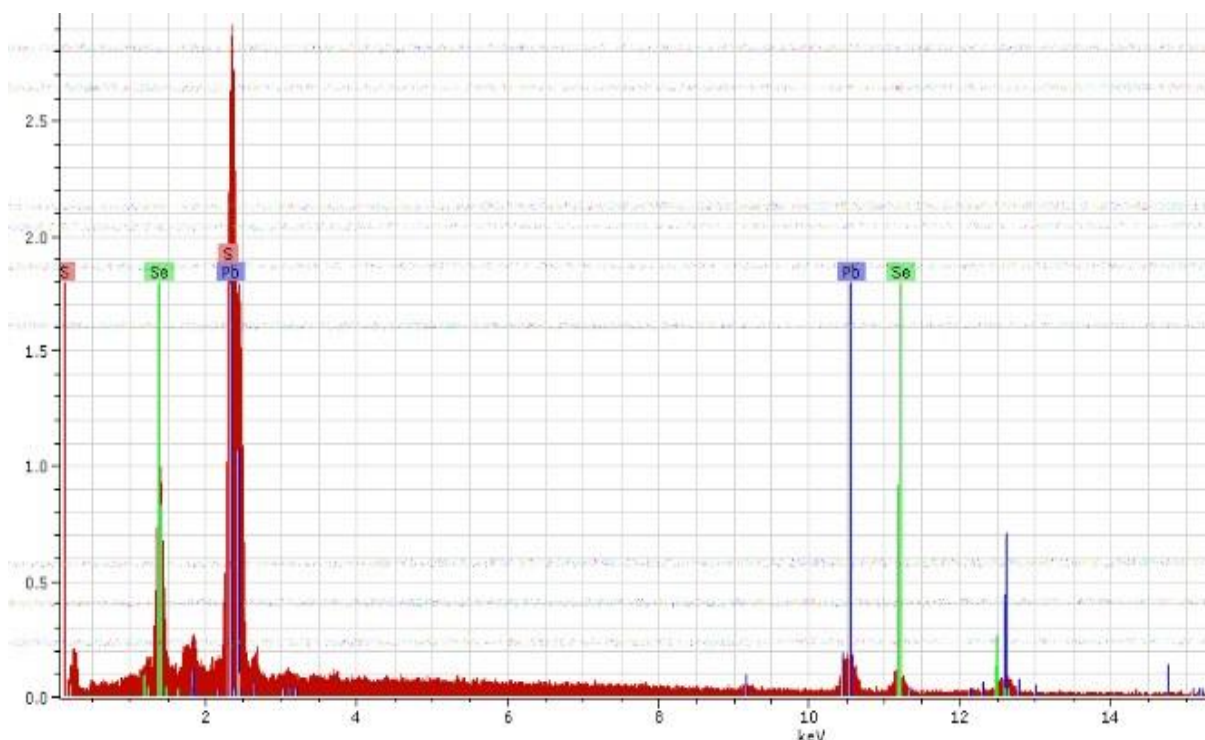


Figure 5.9 Representative EDX spectrum of $\text{PbS}_x\text{Se}_{(1-x)}$ thin film prepared at 250 °C

All the thin films were lead rich, but the relative sulfur content decreased linearly as the ratio of complex (15) in the coating mixture increased. At a selenium mole fraction of 0.3 in the feed precursor, the %S content increased sharply and the formation of the alloy, $\text{PbS}_{0.5}\text{Se}_{0.5}$ was observed. The p-XRD pattern also confirmed the formation of a ternary alloy with the peaks shifting between those of pure PbS and PbSe. After the addition of 0.5 mole fraction of complex (15), there was virtually only selenium and lead with little amount of sulfur (3%) as quantified by the EDX (Figure 5.10). This correlates with the p-XRD pattern matching closely to PbSe at these mole fractions.

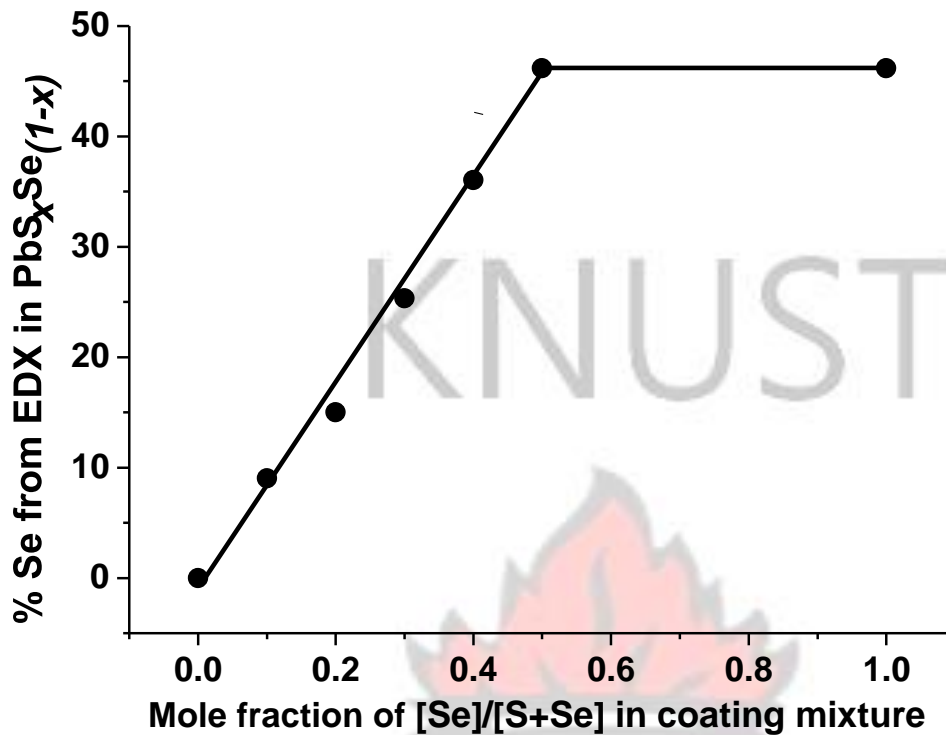


Figure 5.10 Percentage Se quantified from EDX as a function of mole fraction of Se in coating mixture

5.4.4 Optical studies of $PbS_xSe_{(1-x)}$ thin films

Optical properties of ternary $PbS_xSe_{(1-x)}$ are important from the point of view of its widespread application in photovoltaic and optoelectronic devices. The absorption spectra of the thin films were measured in the NIR region from 1000 to 2500 nm.

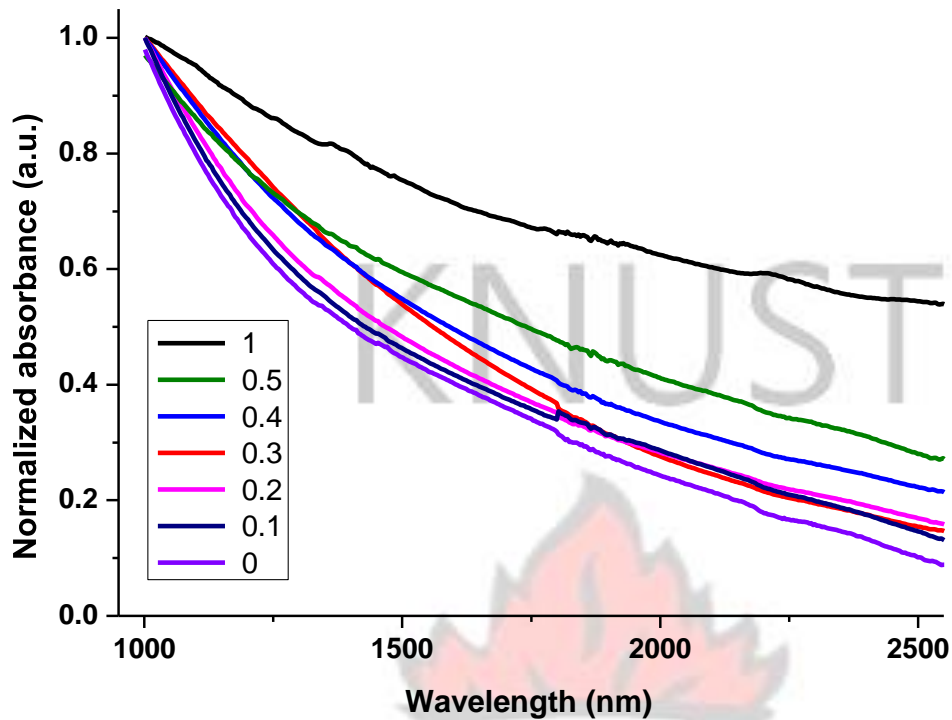


Figure 5.11 Nir absorption spectra of $PbS_xSe_{(1-x)}$ thin films obtained at mole fraction of complex (15) in coating mixture at 0, 0.1, 0.2, 0.3, 0.4, 0.5 and 1

There are many reports on the measurements and calculation of band gaps for lead chalcogenides (Anila *et al.*, 2012; Barote *et al.*, 2011; Begum *et al.*, 2012; El-Shazly *et al.*, 2011; Göde *et al.*, 2014; Kumar *et al.*, 2005; Mulik *et al.*, 2010; Obaid *et al.*, 2012; Pawar *et al.*, 2011; Preetha and Remadevi, 2013; Sadovnikov and Gusev, 2013; Valenzuela-Jáuregui *et al.*, 2003; Vijayaprasath *et al.*, 2015; Zaman *et al.*, 2010). There is a good consensus that the bulk band gaps for pure PbS and PbSe lie at 0.41 and 0.27 eV respectively (Zaman *et al.*, 2010). The band gaps of these materials as films, and especially as the sulfides have been measured on many occasions (Anila *et al.*, 2012; Barote *et al.*, 2011; Begum *et al.*, 2012; El-Shazly *et al.*, 2011; Göde *et al.*, 2014; Kumar *et al.*, 2005; Mulik *et al.*, 2010; Obaid *et al.*, 2012; Pawar *et al.*, 2011; Preetha and Remadevi, 2013; Sadovnikov and Gusev, 2013; Valenzuela-Jáuregui *et al.*, 2003; Vijayaprasath *et al.*, 2015; Zaman *et al.*, 2010). Both PbS and PbSe are known to be direct band gap semiconductors and hence a plot of ahv^2 against hv is expected to show a

linear portion that corresponds to the energy of the optical band gap when extrapolated to the $h\nu$ axis.

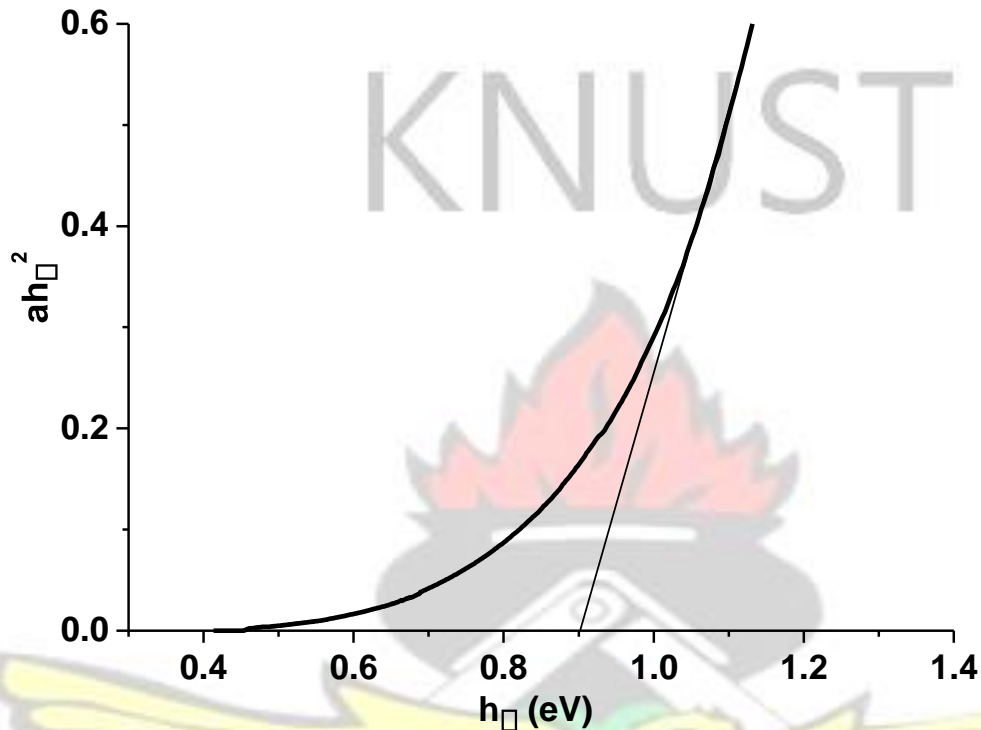


Figure 5.12 Representative Tauc plot of $\text{PbS}_x\text{Se}_{(1-x)}$ thin film prepared at 250 °C

In line with other works, this study leads to values in the range of 0.73 to 1.03 eV for the parent binary PbSe and PbS respectively. The estimated band gap values obtained from the Tauc plots of the $\text{PbS}_x\text{Se}_{(1-x)}$ thin films decreased from 1.03 eV for the PbS to 0.908 eV at 0.5 mole fraction of selenium addition. Both theoretical and experimental determination of the dependence of band gap values on composition of $\text{PbS}_x\text{Se}_{(1-x)}$ have been reported to show a linear relationship between the band gap energy of thin films and the composition (Akhtar *et al.*, 2011; Lifshitz *et al.*, 2006).

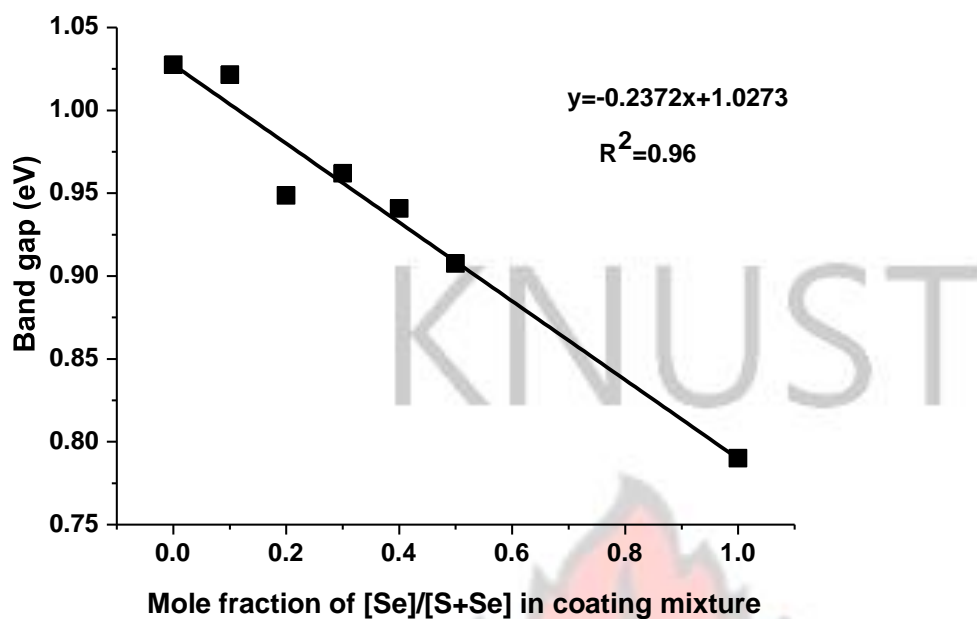


Figure 5.13 A linear plot band gap against mole fraction of Se/S+Se in coating mixture

5.5 Characterization of complexes (15) and (17)

The difference between the experimental and calculated elemental percentages for the complexes were found to be within 0.2% of each other thus confirming the purity of the complexes. The hydrogen environment, *J* coupling and molecular ion peak further confirmed the proposed structures of the complexes (Figure 5.14).

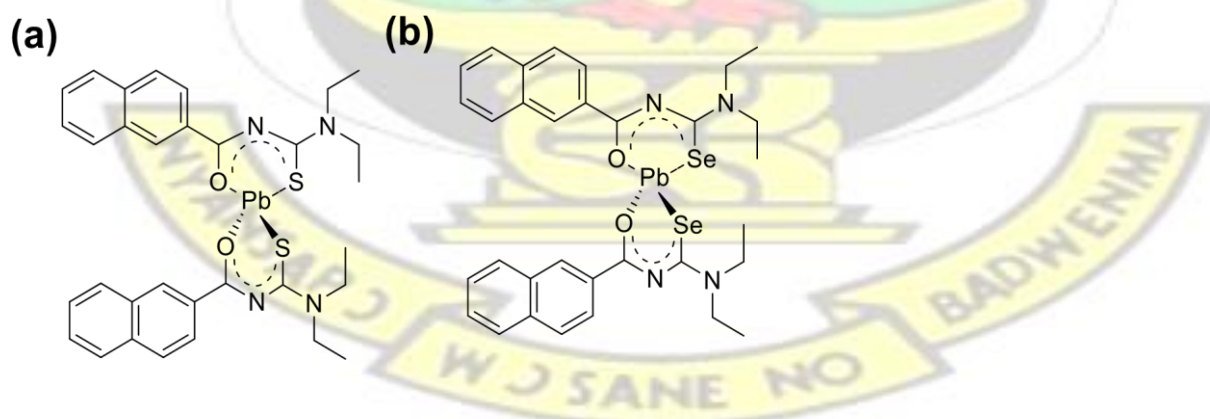


Figure 5.14 The chemical structures of complexes (a) *bis*(*N, N*-diethyl-*N'* naphthoylthioureato)lead(II) (17) and (b) *bis*(*N, N*-diethyl-*N'* naphthoylselenoureato)lead (II) (15)

5.5.1 Thermal properties of complexes (15) and (17)

Thermal properties of the complexes were assessed by thermogravimetric analyses (TGA) under nitrogen at a heating rate of $10\text{ }^{\circ}\text{C min}^{-1}$ from 30–600 $^{\circ}\text{C}$. The TGA of the complexes showed multiple decomposition steps (Figure 5.15).

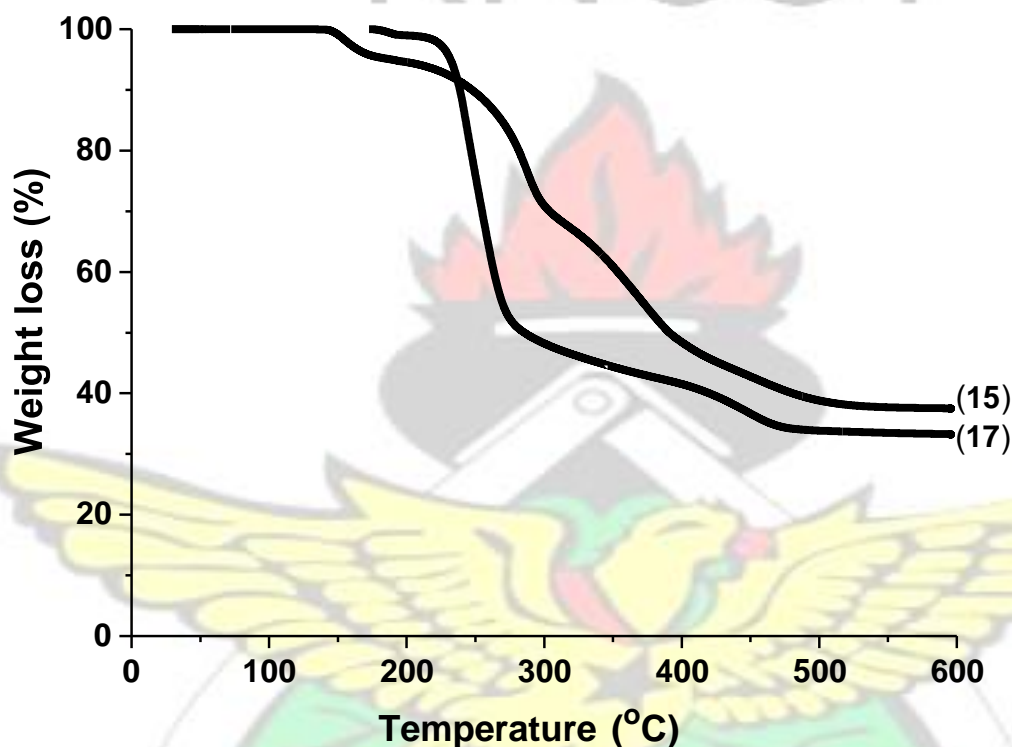


Figure 5.15 Thermogravimetric analysis (TGA) of complex (15) and (17) at a heating rate of $10\text{ }^{\circ}\text{C min}^{-1}$ under nitrogen.

The first decomposition step for complex (17) began at $175.7\text{ }^{\circ}\text{C}$ and completed at $203.9\text{ }^{\circ}\text{C}$. This step represents the release of one of the two ethyl groups around a diethyl amine group in the structure with a weight loss of 5%. The second step started at $212.4\text{ }^{\circ}\text{C}$ and completed at $386.6\text{ }^{\circ}\text{C}$ with a weight loss of 56.5% representing the release of the two naphthoyl groups. This is directly followed by the last stage ranging from 395.5 to $495.7\text{ }^{\circ}\text{C}$ resulting in a residue amounting to 33.7% of its initial weight. The value matches closely to the expected weight of

PbS (32.1 %) from complex (17) with 100% conversion. Complex (15) on the other hand decomposed in four steps to yield a stable residue at 594.6 °C with a weight of 37.8 % of its initial weight as compared to 32.8 % from theoretical calculations. The first step which occurred between 41.7 and 190.1 °C, could be due to the loss of the two ethyl groups around one of the two diethyl groups. The second step was as a result of the decomposition of naphthoyl group in one of the ligands. The third step which started from 300.2 and ended at 393.6 °C was followed immediately by the fourth step. The higher experimentally determined weight of the residues may have resulted from carbon contamination from the bulky organic moiety of the complexes as suggested by Chen *et al.*, (2010).

5.6 Characterization of $\text{PbS}_x\text{Se}_{(1-x)}$ nanoparticles

5.6.1 Powder-X ray diffraction patterns of $\text{PbS}_x\text{Se}_{(1-x)}$ nanoparticles

Powder-X ray patterns of the as-synthesized PbS and PbSe nanoparticles were indexed to a face centred cubic (halite) structure with the (200) plane as the most preferred orientation. The strong diffraction peaks confirmed the good crystallization of the as-synthesized nanoparticles (Chen *et al.*, 2010). The PbS nanoparticles exhibited peaks at 25.96°, 30.08°, 43.06°, 50.98°, 53.41°, 62.54°, 68.88°, 70.97° and 78.92° which are indexed to the (111), (200), (220), (311), (222), (400), (331), (420) and (422) planes of a cubic PbS (ICDD 00 003 0614). Also peaks at 25.17°, 29.14°, 41.69°, 49.33°, 51.66°, 60.42°, 66.50°, 68.48° and 76.08° were also indexed to the (111), (200), (220), (311), (222), (400), (331), (420) and (422) planes of a cubic PbSe (ICDD 00 002 0588). The positions and relative intensities of the PbS and PbSe reflections agreed well with their ICDD database.

The p-XRD patterns of the ternary-alloyed nanoparticles at all compositions corresponded to the halite structure with characteristic reflections similar to the parent binaries. The 2 theta

values of the alloys fall between the values for PbS and PbSe. The alloys further exhibited significant diffraction angle shift as the [Se] content changed from 0 to 1. To illustrate this, the (220) reflection of PbS was at 43.06° which moves to 42.01° for $\text{PbS}_{0.5}\text{Se}_{0.5}$ and settles at 41.69° for PbSe. This provides strong evidence for the formation of a homogenous ternary $\text{PbS}_x\text{Se}_{(1-x)}$ solid solution rather than simply mixed phases of pure PbSe and PbS as reported in literature (Onicha *et al.*, 2012; Safrani and Golan, 2015; Song *et al.*, 2016). Otherwise diffraction patterns of PbSe and PbS would have been detected in the p-XRD pattern of the ternary $\text{PbS}_x\text{Se}_{(1-x)}$.

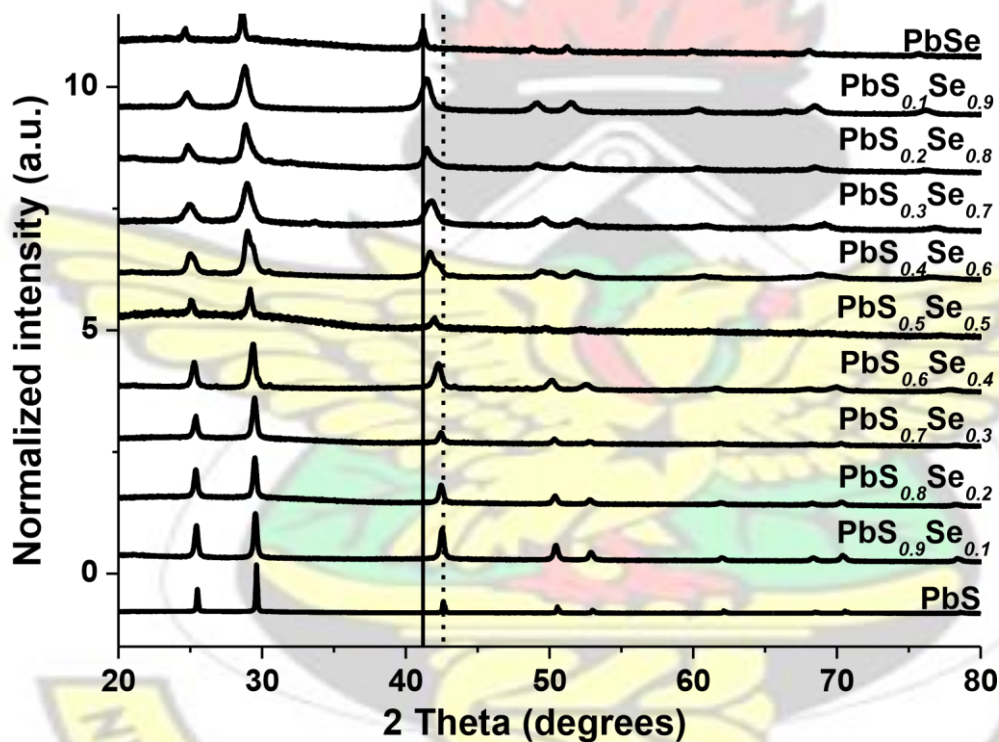


Figure 5.16 p-XRD patterns of $\text{PbS}_x\text{Se}_{(1-x)}$ nanoparticles synthesized at 200°C with standard matching lines of PbS (dash) and PbSe (line).

Similar shift in 2 theta values for $\text{PbS}_x\text{Se}_{(1-x)}$ nanoparticles to lower values with the incorporation of selenium as compared to PbS have been reported by Gao *et al.*, (2013); Guchhait *et al.*, (2011); Onicha *et al.*, (2012).

Other reports on the colloidal syntheses of ternary $\text{PbS}_x\text{Se}_{(1-x)}$ nanoparticles all showed a gradual incorporation of selenium at all the mole fractions used from 0 to 1 (Akhtar *et al.*, 2011; Gao *et al.*, 2013). However, this trend looks different from that observed in $\text{PbS}_x\text{Se}_{(1-x)}$ thin films (Figure 5.4). It seems that the sulfur is first consumed and therefore being deficient in the lattice of the final product or at the high processing temperature (250 °C), part of the sulfur atoms volatilised and was carried away by the carrier gas used in the heating process of the coated slides. This suggests a good incorporation of selenium into PbS lattice using a colloidal approach at relatively low temperatures. The mechanism of the alloying involves the dissociation of the Pb-Se bond followed by the diffusion of the Se atom in the PbS lattice structure. Selenium has an important role depending upon concentration when incorporated into the lattice of PbS, it has a strong tendency of fitting into PbS lattice because of the bigger ionic radius.

Generally, the calculated crystallite sizes which represent the crystallite sizes of the nanomaterials increased gradually with increasing value of the mole fraction of complex (15) in the injection mixture. The calculated crystallite sizes for PbS and PbSe nanoparticles were 7.69 to 12.55 nm respectively. The crystallite size increased linearly from 7.69 to 12.55 nm as the mole fraction of (15) in the injection mixture changed from 0 to 1 at an increment of 0.1. This may be due to the bigger crystallite size of the PbSe as compared to the crystallite size of the PbS.

Dislocation density which represents imperfections in a crystal, increases with a corresponding decrease in the crystallite size. This is due to the bigger atomic radius of selenium which has a strong effect on structural parameters with increased Se content (Bagade *et al.*, 2015). From the Figure 5.17, there was a gradual decrease in imperfections as the ratio of selenium increased from 0 to 1.

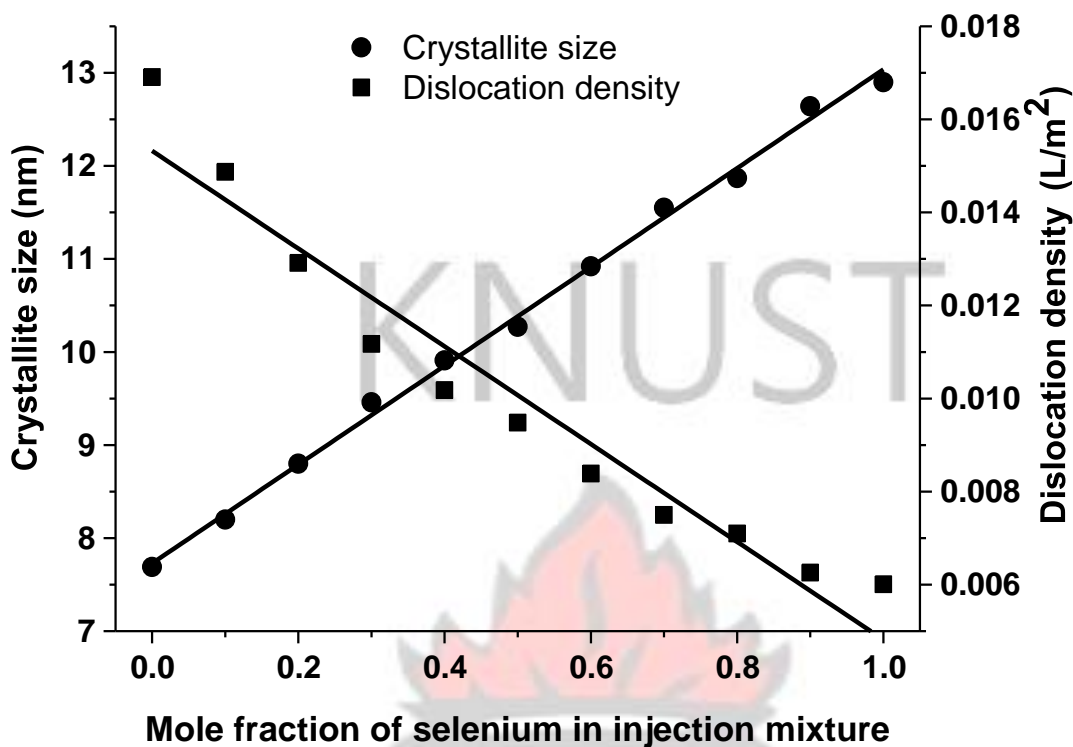


Figure 5.17 Effect of selenium mole fraction of on crystallite size (left y-axis, circle) and dislocation density (right y-axis, square) of $\text{PbS}_x\text{Se}_{(1-x)}$ nanoparticles

The lattice constants of PbS and PbSe which were 5.9888 and 6.1873 Å respectively are similar to the 5.9362 and 6.1282 for their respective bulk materials (Onicha *et al.*, 2012). The influence of the [Se] content in the injection mixture on the lattice constants of the $\text{PbS}_x\text{Se}_{(1-x)}$ nanoparticles formed is presented in Figure 5.18. There is a linear increase in the lattice constant as the [Se] in the injection mixture increased. This linear increase confirms that unit cell parameters vary linearly with composition for a continuous substitutional solid (Çapan *et al.*, 2010). The observed linearity further confirms the gradual shift from PbS to PbSe phase as the [Se] content in the injection mixture increases from 0 to 1. Similar linear behaviour has been reported for $\text{PbS}_x\text{Se}_{(1-x)}$ nanostructures synthesized by reacting lead oleate with triphenylphosphine selenide and dibenzyl disulfide in dibenzylamine with addition of oleic acid at 260 °C (Shao *et al.*, 2014).

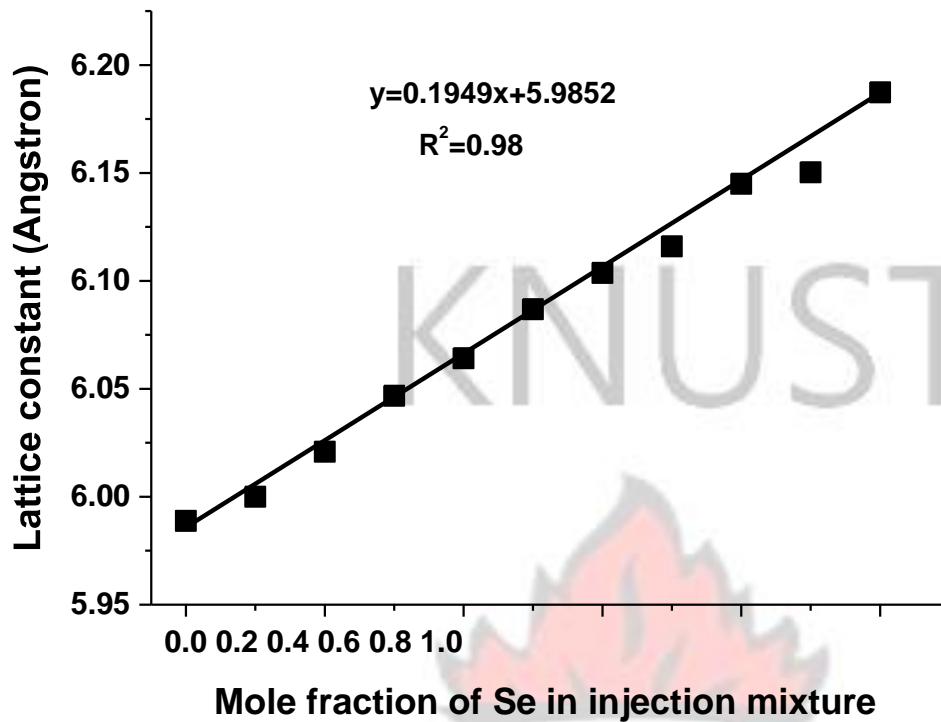


Figure 5.18 Relationship between the cubic lattice constant “a” to the ratio of [Se]/[S+Se] in the injection mixture.

5.6.2 Transmission electron microscopy (TEM) images of $\text{PbS}_x\text{Se}_{(1-x)}$ nanoparticles

Transmission electron microscopy (TEM) was employed to obtain greater insight into the nanostructure of the materials. TEM images of the as-synthesized nanoparticles showed cubic morphologies.

TEM images of the as-synthesized nanoparticles showed a nearly even distribution of cubes on the grid further confirming the p-XRD patterns. The PbS nanoparticles showed a nearly uniform sized cubes with side length of *ca.* 14.6 ± 1.2 nm whereas PbSe nanoparticles showed sizes of *ca.* 26.9 ± 6.9 nm. The sizes of the nanoparticles were below their respective Bohr exciton radii (PbS = 18 nm and PbSe = 48 nm), therefore, there is a great tendency for quantum confinement which is exhibited in the optical properties of the $\text{PbS}_x\text{Se}_{(1-x)}$ nanoparticles. Although the alloy also exhibited a cubic morphology just as the parent binaries, there was a

significant change in size with the incorporation of the selenium atoms. The alloy had sizes that ranged in between that of the parent binaries depending on the composition of the injecting mixture. That is, the side length of the cubes increased as the mole fraction of complex **(15)** in the injection mixture increased. The hot injection technique has been reported to produce smaller particle sizes. For instance, monodispersed $\text{PbS}_x\text{Se}_{(1-x)}$ nanocrystals with particles sizes *ca.* 5 nm have been synthesized by reacting TMS, TMS₂Se and PbO at 130 °C (Akhtar *et al.*, 2011). Further, lead chloride salt, elemental S and Se dissolved in oleylamine has been employed as starting materials for the synthesis of spherical $\text{PbS}_x\text{Se}_{(1-x)}$ nanocrystals with an average size of 10 nm (Gao *et al.*, 2013). The growth of $\text{PbS}_x\text{Se}_{(1-x)}$ wires with diameters of 9 nm have been reported using lead(II) diethyldithiocarbamate and lead(II) imido(bis(selenodiisopropylphosphinate)) as starting precursors at temperatures ranging from 210 to 230 °C (Onicha *et al.*, 2012). The syntheses of hexapod-like ternary $\text{PbSe}_x\text{S}_{1-x}$ nanostructures based on the reactions of lead (II) acetate with triphenylphosphine selenide and dibenzyl disulfide in oleylamine has been reported (Shao *et al.*, 2014). The difference in morphology in the $\text{PbS}_x\text{Se}_{(1-x)}$ nanoparticles (Figure 5.19) as compared to the $\text{PbS}_x\text{Se}_{(1-x)}$ thin films (Figure 5.8) may be primarily due to the difference in starting precursors. The successful growth of ternary $\text{PbS}_x\text{Se}_{(1-x)}$ nanocubes from a mixture of complexes **(15)** and **(17)** demonstrate that ureas as a class of SSPs are efficient starting materials in the syntheses of compositionally complex systems.

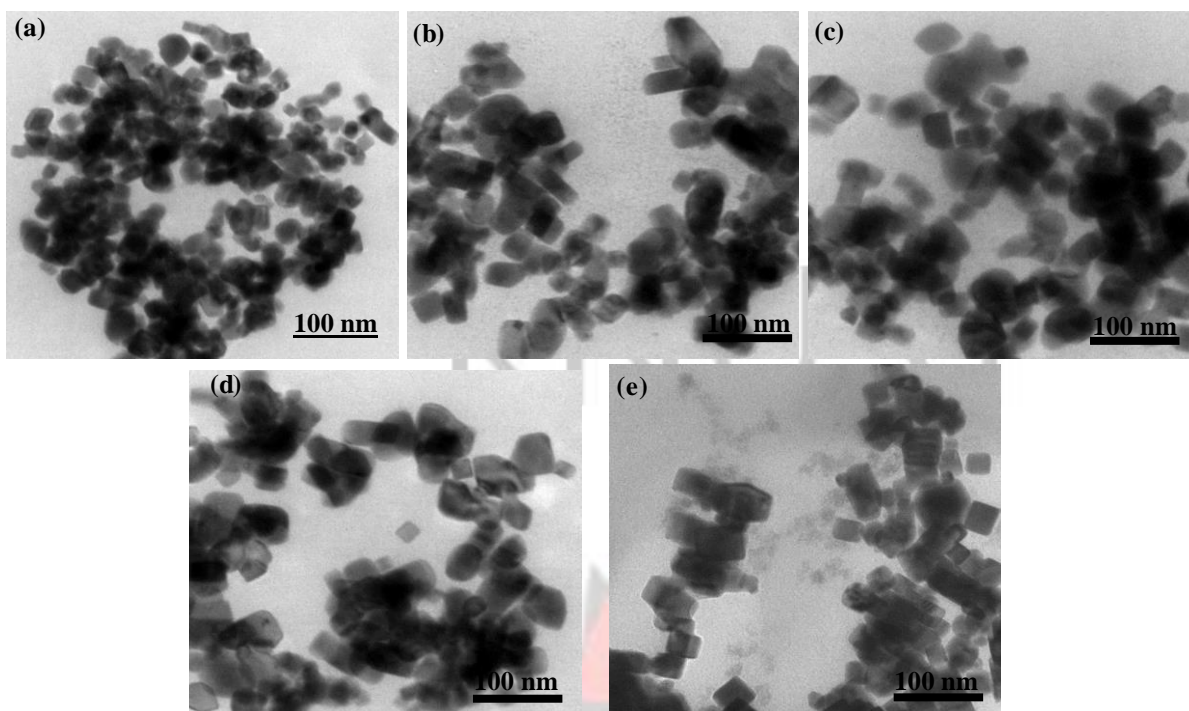


Figure 5.19 TEM images of $\text{PbS}_x\text{Se}_{(1-x)}$ obtained at x values of (a) 0, (b) 0.3, (c) 0.5, (d) 0.8, (e) 1.

5.6.3 Energy dispersive X-ray (EDX) analyses of the $\text{PbS}_x\text{Se}_{(1-x)}$ nanoparticles

Energy dispersive X-ray (EDX) analyses were performed to confirm the elemental composition of the as-synthesized nanoparticles. Energy dispersive X-ray analyses of the nanoparticles revealed emission exclusively due to lead, sulfur, selenium and gold within the detection limits of the equipment. The gold was as a result of the gold coating prior to the analyses to prevent charging of the nanoparticles. All the ternary nanoparticles were lead rich, which confirms earlier report by other investigators (Onicha *et al.*, 2012; Shao *et al.*, 2014; Smith *et al.*, 2011). The relative sulfur content increased linearly as the ratio of complex (15) in the injection mixtures decreased. At a complex (15) mole fraction of 0.5 in the injecting mixture, the % S and % Se content were 29.9 and 27.3 respectively and the formation of the alloy, $\text{PbS}_{0.5}\text{Se}_{0.5}$ was observed (Figure 5.20). The p-XRD pattern also confirmed the formation of a ternary alloy with the peaks shifting between those of pure PbS and PbSe (Figure 5.16).

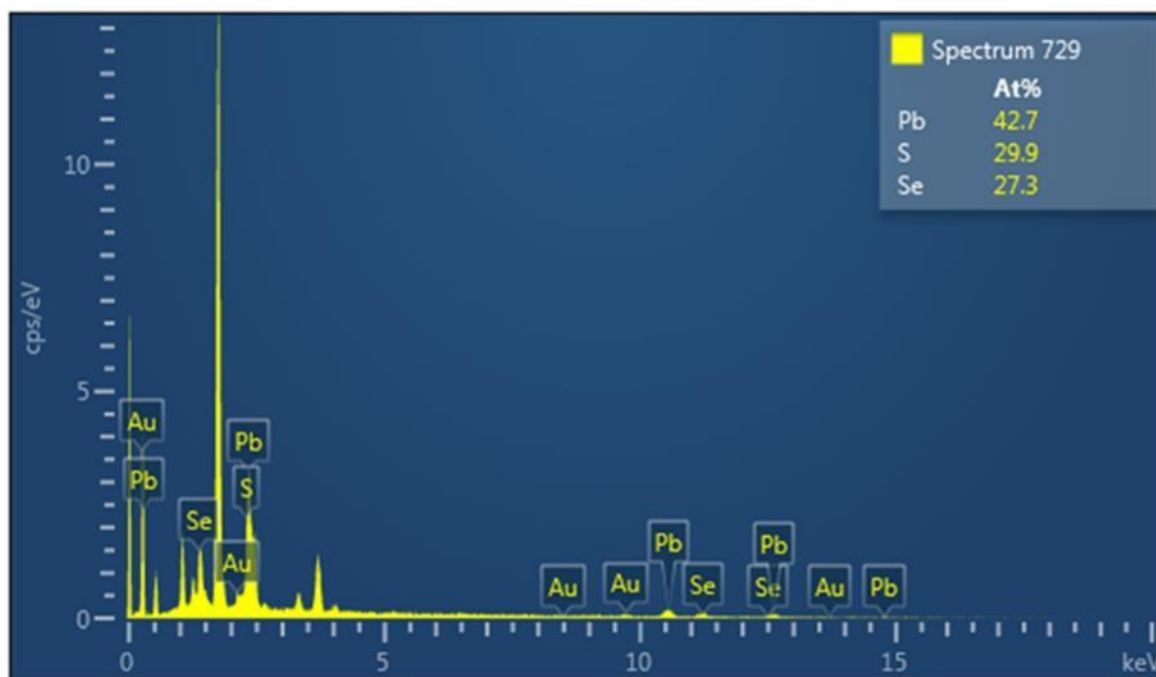


Figure 5.20 EDX spectrum for PbS_{0.5}Se_{0.5} nanoparticles

5.6.4 Optical properties of the PbS_xSe_(1-x) nanoparticles

As the sizes of nanoparticles were below their respective Bohr exciton radii (PbS = 18 nm and PbSe = 48 nm), there is a great tendency for quantum confinement which is exhibited in the optical properties of the nanoparticles. PbS, PbSe and their ternary alloys are direct band gap semiconductors and hence a plot of ahv^2 against hv is expected to show a linear portion that corresponds to the energy of the optical band gap when extrapolated to the hv axis. The estimated optical band gaps for PbS and PbSe were 0.95 and 0.75 eV respectively. These band gaps have been blue shifted from their bulk values of 0.41 and 0.21 eV of PbS and PbSe respectively. The estimated optical band gaps for the alloy were 0.91, 0.84, 0.81 eV for PbS_{0.8}Se_{0.2}, PbS_{0.5}Se_{0.5}, PbS_{0.3}Se_{0.7} respectively. These values were in between the optical band gap values for the parent binary materials. The band gap values shifted linearly towards the band gap of PbSe as the Se content in the alloy increase from 0 to 1. Similar trends in band gap

have been reported for ternary alloys in literature by Siddique *et al.*, (2014) using CBD technique and Akhtar *et al.*, (2011) using hot injection.

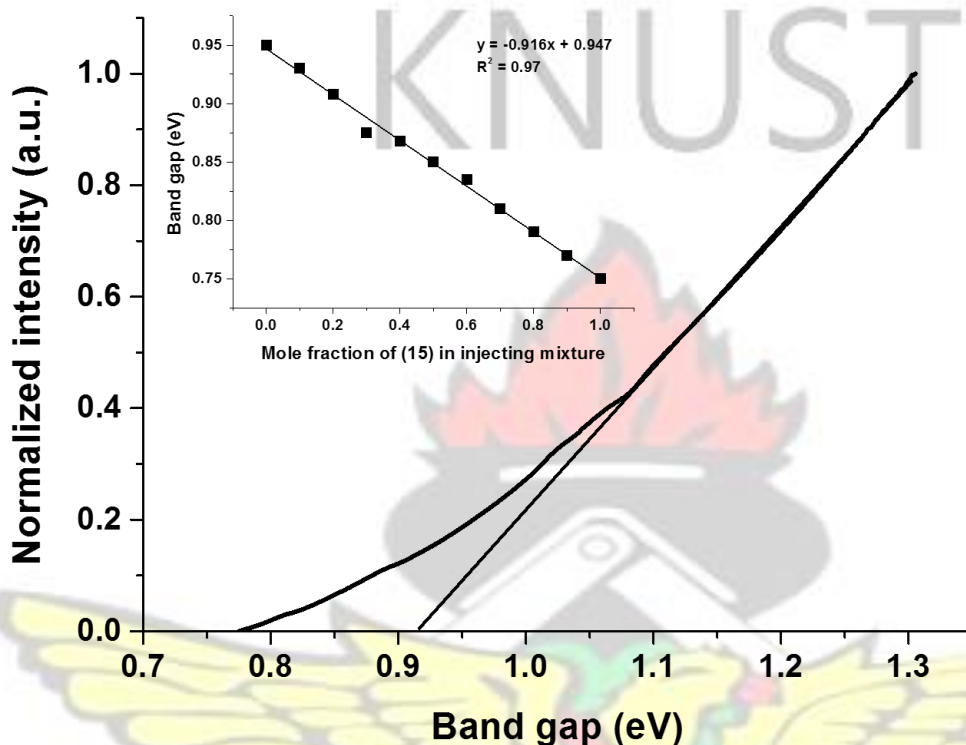


Figure 5.21 (a) Representative Tauc plot of $\text{PbS}_x\text{Se}_{(1-x)}$ nanoparticles and (inset) effect of mole fraction of complex (15) in the injecting mixture on the band gap of the nanoparticles

5.7 Syntheses of sodium, lead and bismuth piperidine dithiocarbamate complexes

The use of water as a solvent for the synthesis of the ligand and complexes make the overall synthetic process environmentally safe. Water as a reaction medium has been reported to give high yields as compared to other organic solvents such as methanol, chloroform and hexane (Halimehjani *et al.*, 2010). The atom economy of a reaction, which is defined as the ratio of molecular mass of desired product to the molecular mass of reactants, was also calculated.

Atom economy for the syntheses were 100, 92 and 90% for the sodium, bismuth and lead piperidine dithiocarbamate complexes. The high atom economy of the synthesis makes this approach an environmentally viable pathway for the syntheses of the complexes (Lewis *et al.*, 2015). The precursors were air stable, easy to synthesize and soluble in organic solvents such as chloroform and dichloromethane. All these properties are advantages of SSPs over the multiple source routes (Boadi *et al.*, 2012).

5.8 Characterization of sodium, lead and bismuth piperidine dithiocarbamate complexes

The purity of the ligand and complexes were determined using the micro elemental analyzer. The experimentally determined elemental percentages were similar to the calculated values for the proposed structures. This confirmed the purity of the complexes.

5.8.1 TGA of metal piperidine dithiocarbamate ligand and complexes

The sodium piperidine dithiocarbamate (**18**) decomposed in two steps at 100 and 343 °C to yield a residue of 22.9%. The expected % weight of NaS was 27.3%. The first step with a weight loss of 17.8% was the release of the water molecule bound to the ligand which occurred at 100 °C. The second decomposition step which yielded 59.3% was as a result of the breakdown of C₆H₁₀NS attached to the NaS (Figure 5.22). Complex (**19**) decomposed in a single step to produce a stable residue at 326 °C. The theoretical percentage of PbS from the molecular formula of the complex at 100% conversion was calculated to be 47.6% which was close to the experimentally determined percentages of 47.3%. Nyamen *et al.*, (2014) have also reported a one-step decomposition thermograph for this same complex. The bismuth derivative, complex (**20**), however, decomposed in two steps at 280 and 495 °C. The first step corresponded to the decomposition of three of the piperidyl dithiocarbamate ligands (51.1%)

attached to the Bi. The second step at 495 °C represents the breakdown of other component attached to the complex leading the formation of BiS_{1.5} (43.5%) compared to a calculated value of 37.3 %. Similar thermograph for the decomposition of bismuth piperidine dithiocarbamate complex have been reported recently in literature (Kun *et al.*, 2016).

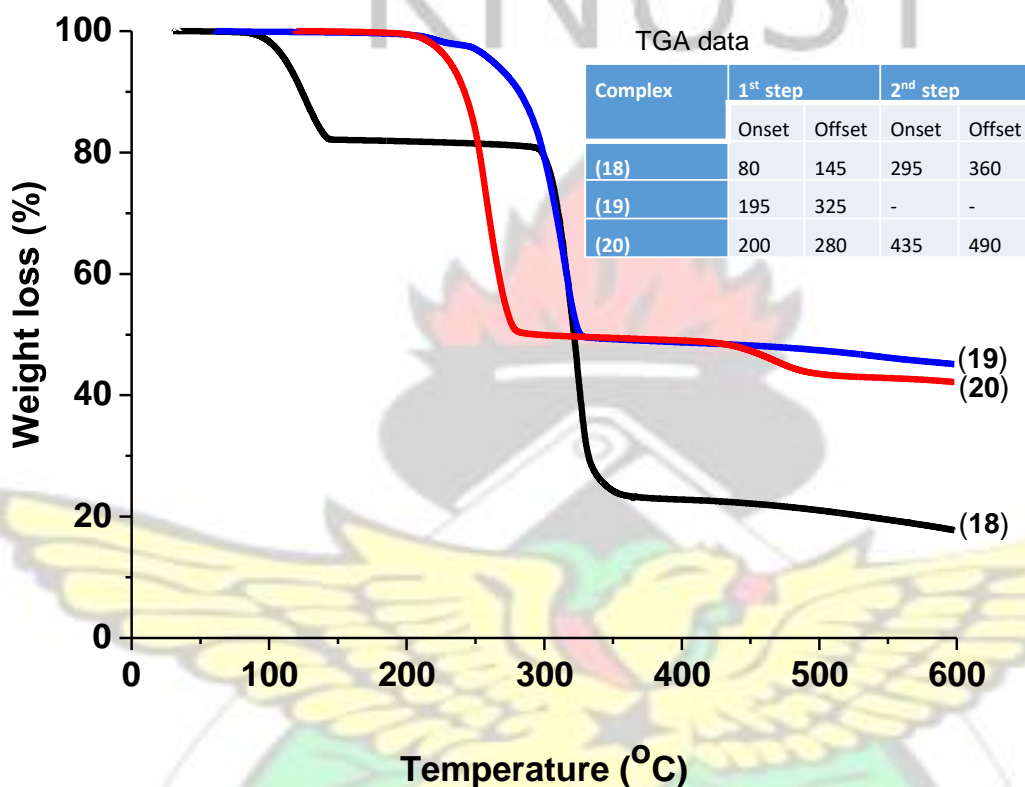


Figure 5.22 TGA thermograms of ligand and complexes, (inset) TGA data

5.8.2 Fourier transform infrared spectra of metal piperidine dithiocarbamate complexes

Infrared spectrum of the sodium piperidine dithiocarbamate ligand (complex (18)) showed strong peaks around 3335 cm⁻¹ due to $\nu(\text{O-H})$ vibrations of water molecules bound to the sodium dithiocarbamate ligand. This O-H peak was completely absent in all the complexes, indicating the complete loss of the water molecules as a result of the coordination to the metal ions. The loss of OH bond in piperidine dithiocarbamate complexes of bismuth (Kun *et al.*,

2016), praseodymium (Pitchaimani *et al.*, 2015) and lead (Nyamen *et al.*, 2012) have been reported. The $\nu(\text{C}=\text{N})$ of the ligand (18) was observed at 1421 cm^{-1} whereas those of the complexes were 1443 and 1450 cm^{-1} for Bi and Pb respectively. The shift to higher energy in the complexes were as a result of increase in the double bond character upon coordination to the metal center (Ajibade *et al.*, 2011). Peaks ranging from 2932 - 2938 and 2840 - 2844 cm^{-1} were associated to $\nu(\text{C}-\text{H})$ anti-symmetric and symmetric stretches respectively. Other C-H stretches such as scissoring and bending occurred around 1460 and 1420 cm^{-1} . Peaks observed at 1221 to 1233 cm^{-1} were associated with C-N stretches. The C-S stretches ranged from 1002 to 1008 cm^{-1} . Similar wavenumbers have been reported by the Revaprasadu group for Na, Bi and Pb piperidine complexes (Kun *et al.*, 2016; Nyamen *et al.*, 2012).

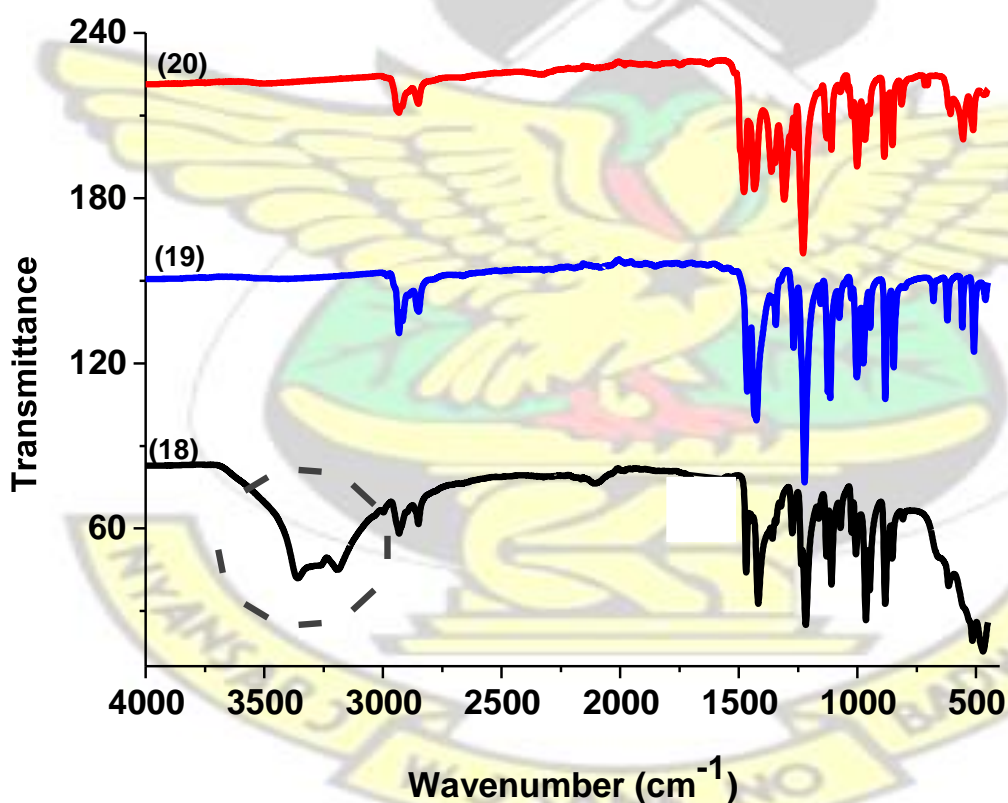


Figure 5.23 IR spectra of complexes (18), (19) and (20)

5.9 Characterization of Bi doped PbS nanoparticles

5.9.1 Powder X-ray diffraction (p-XRD) of Bi doped PbS nanoparticles

Powder X-ray diffraction (p-XRD) patterns of the Bi_2S_3 nanoparticles grown at 200 °C in oleylamine were indexed to an orthorhombic phase of Bi_2S_3 with ICDD: 00-002-0391. Diffraction peaks observed at 2 theta values of 15.8°, 17.6°, 22.8°, 26.2°, 28.5°, 31.8°, 33.1°, 35.6°, 36.6°, 46.6°, 52.8°, 59.3°, 62.7° and 66.4° can be assigned to the (020), (120), (220), (130), (211), (221), (301), (240), (231), (431), (351), (242), (152) and (522) planes respectively, in the pure orthorhombic phase of Bi_2S_3 . The (301) plane was identified as the most preferred orientation in the p-XRD pattern. The detection of no additional peaks in the pattern, indicates the high purity of the as-synthesized nanoparticles (Bao *et al.*, 2007). The crystallinity of the samples were confirmed by the high intensity of the diffraction peaks. The p-XRD pattern was in agreement with reported literature for Bi_2S_3 using both single and multiple source starting materials (Abd-Elkader and Deraz, 2014; Tian *et al.*, 2008; Zhang *et al.*, 2011). A recent report by the Revaprasadu group on the syntheses of Bi_2S_3 nanoparticles using catena-(μ -nitrateO,O')bis(piperidinedithiocarbamate)bismuth(III) complex gave similar p-XRD patterns (Kun *et al.*, 2016). The p-XRD patterns of the PbS nanoparticles synthesized using the same conditions were indexed to a face centered cubic structure. Diffraction peaks at 2 theta values of 25.96°, 30.07°, 43.05°, 50.97°, 53.41° and 62.53° corresponding to the (111), (200), (220), (311), (222) and (400) planes of cubic PbS respectively. From the diffraction patterns, the (200) plane was the most preferred orientation. There was no evidence of extra peaks from impurities, undecomposed precursor or by-product, thus, making the reaction conditions suitable for the syntheses of PbS from lead piperidine dithiocarbamates.

The p-XRD pattern of the alloys showed diffraction peaks at different 2 theta values based on the composition of the injection mixture used. As seen from the p-XRD pattern, up to 60% Bi doping, the overall spectra had the general PbS reflection (Figure 5.24). Compared to the pXRD

pattern of the pure PbS nanoparticles, the peaks broadened with the % Bi doping from 10 to 60. This observation favours the decrease in their crystallite size as compared to the PbS nanoparticles.

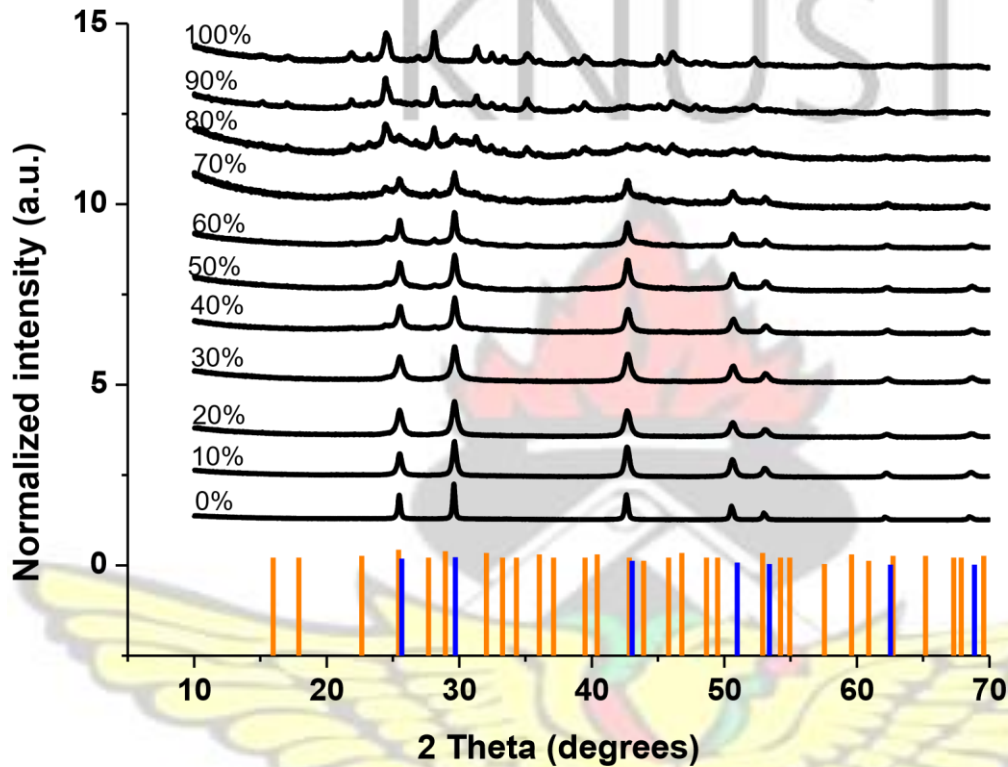


Figure 5.24 p-XRD pattern of PbS, Bi_2S_3 and Bi doped PbS nanoparticles with (orange) Bi_2S_3 pattern and (blue) PbS pattern

Similar observations have been made in the p-XRD pattern of up to 4 % iron doped PbS nanoparticles by Balu *et al.*, (2017), 15% aluminium doped PbS by Suganya *et al.*, (2016) and 5% calcium doped PbS thin films by Yücel and Yücel, (2017). The intensity of the planes remained constant signifying that there were no defects in the crystal lattice of the PbS with the incorporation of the Bi ions up to 60% (Balu *et al.*, 2017). There were no extra peaks from the Bi ions in the p-XRD spectra further confirming the substitution of Bi^{3+} ions into the regular sites of Pb^{2+} ions or complete incorporation of the Bi atoms into the PbS crystal lattice as reported by Yücel and Yücel, (2017). There was also a small shift in the Bragg angle to higher

2 theta values with the incorporation of the Bi atom. This shift in the Bragg angle can be associated with lattice strain due to structural differences between the Bi ions and PbS, further confirming the successful incorporation of the bismuth into the PbS crystal lattice. The effect in the 2 theta shift is minimal as compared to those reported for the incorporation of strontium (Yücel and Yücel, 2016), copper (Touati *et al.*, 2016) into the crystal lattice of PbS thin films. It was also observed that up to 60% Bi doping, the p-XRD spectra had a strong (200) plane which is consistent with the results reported for both metal doped and undoped PbS (Du *et al.*, 2017; Rajashree *et al.*, 2016; Suganya *et al.*, 2016). However, at Bi doping between 70 and 80% a mixture of PbS and Bi₂S₃ patterns were observed. This may be due to the excess Bi ions within the crystal lattice of PbS. No such high dopant concentration have been reported. A further increase to 90% Bi doping produced a p-XRD pattern which matched closely to an orthorhombic Bi₂S₃ phase.

From Figure 5.25, the crystallite sizes decreased gradually as the % Bi doping increased presupposing that the Bi had smaller dimensions as compared to the PbS nanoparticles. Literature reports that the crystallite size of PbS nanoparticles decrease with increasing dopant concentration (Balu *et al.*, 2017; Rajashree *et al.*, 2016; Yücel and Yücel, 2017). This decrease in crystallite size may be attributed to the distortion induced in the PbS lattice due to the ionic radii mismatch between the dopant and host ions which prevent grain growth (Suganya *et al.*, 2016).

There was a gradual increase in the dislocation density as the % Bi doping increase from 0 to 100%. This is as a result of the decreasing crystallite size and hence the increasing imperfections (Begum *et al.*, 2012).

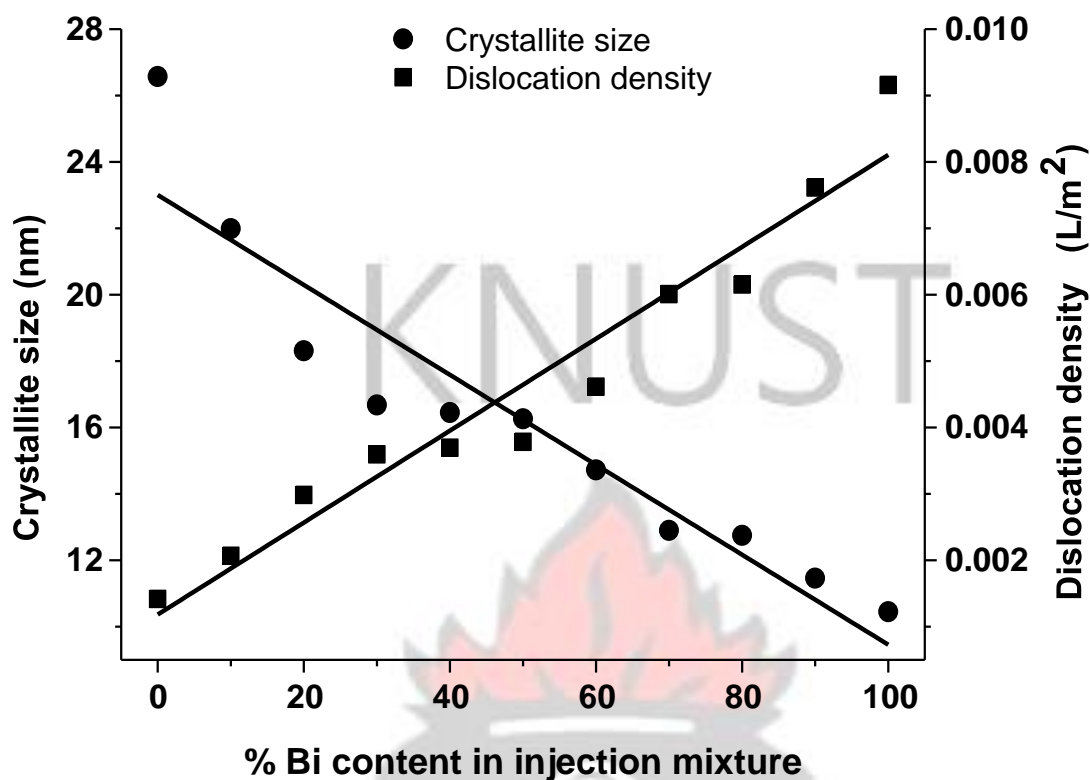


Figure 5.25 Effect of % bismuth content in the injection mixture on Scherrer size (circles) and dislocation density (squares) of PbS nanoparticles

The lattice parameters for the samples are presented in table 5.5 below. Up to 60% Bi doping, the p-XRD patterns corresponded to a cubic phase. For such a phase, the lattice parameters ‘a’, were calculated using equation 3.3. There was a gradual decrease in lattice constant as the % Bi doping increased from 10 to 60. This might be due to the substitution of large sized Pb^{2+} ions by smaller Bi^{3+} ions as reported elsewhere in literature (Suganya *et al.*, 2016). The p-XRD patterns for the 70 and 80% Bi doping showed a mixed phase therefore making it difficult to calculate the lattice constants. At 90% Bi doping, the p-XRD pattern was similar to a pure orthorhombic phase hence lattice parameters were calculated using equation 3.4.

Table 5.5 Effect of %Bi doping on lattice constant

% Bi content in injection mixture	Lattice constant ‘a’ (Å)
-----------------------------------	--------------------------

0	6.057712
10	5.971942
20	5.969228
30	5.965962
40	5.964030
50	5.963751
60	5.962146

At 90% Bi doping, the lattice parameters given as a, b and c were 11.102838, 11.253814 and 3.942346 Å whereas the pure Bi₂S₃ had 11.102981, 11.264792 and 3.951003 Å as the lattice parameters. These values are comparable to the literature values of bulk Bi₂S₃ which are a=11.14, b=11.30 and c=3.98 Å (Fan *et al.*, 2008a).

5.9.2 Transmission electron microscopy images of Bi doped PbS nanoparticles

The morphology of the as-synthesized nanoparticles were investigated with the TEM. TEM images of the PbS nanoparticles showed predominantly cubes with sizes ranging from 10 to 30 nm (Figure 5.26). Earlier report on the use lead piperidine dithiocarbamate in oleylamine at 230 °C using hot injection method, gave cubic morphology with an average diameter of 24.53 nm (Nyamen *et al.*, 2012).

The rapid growth of Bi₂S₃ along the (301) plane in the p-XRD has been reported to give rise to the growth towards 1-dimensional nanorods, which is an inherent property due Bi-S chain type structure (Tian *et al.*, 2008). Several researchers have reported on the formation of Bi₂S₃ rods (Lui *et al.*, 2015; Tian *et al.*, 2008; Zhang *et al.*, 2011).

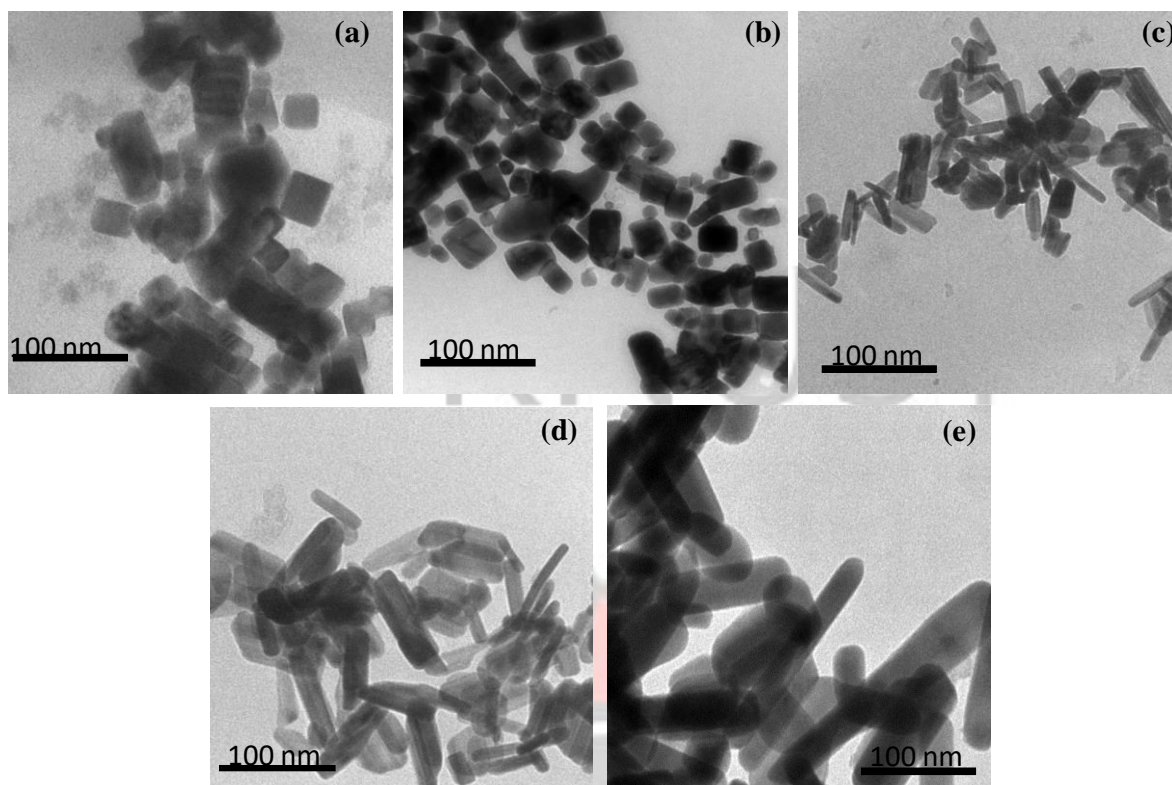


Figure 5.26 TEM images of Bi doped PbS nanoparticles at %Bi doping of (a) 0, (b) 50, (c) 80, (d) 90, (e) 100

The morphology of the Bi doped PbS revealed a mixture of cubes and rods depending on the composition of the injection mixture. Generally, the quantity of rods increased with increasing Bi content in the injection mixture (Figure 5.26). Addition of 50% of Bi showed predominantly cubic morphology further confirming the p-XRD pattern that matched to an overall PbS pattern at this doping percentage. However, a mixture of cubes and rods were observed at 80% Bi doping into the PbS nanoparticles as seen from the p-XRD pattern as a mixture of cubic and orthorhombic phases. Only rods were observed in the TEM image at 90% Bi doping. This confirmed the p-XRD pattern which was similar to that of the pure Bi_2S_3 nanoparticles. The Bi_2S_3 consisted of rods with average dimensions of 20 nm in diameter and 80 nm in length.

Aspect ratio is defined as the surface to volume ratio (Padilha *et al.*, 2013). The calculated aspect ratio from the TEM image of Bi_2S_3 was 4. Higher aspect ratio corresponds to higher

surface energies and therefore the tendency for agglomeration (Nyamen *et al.*, 2011; Ramasamy *et al.*, 2013b).

5.9.3 Energy dispersive X-ray spectroscopy of Bi doped PbS nanoparticles

EDX analyses of the nanoparticles produced signals from Pb or/and Bi and S atoms within the detection limit of the instrument, further confirming the purity of the as-synthesized ternary nanoparticles.

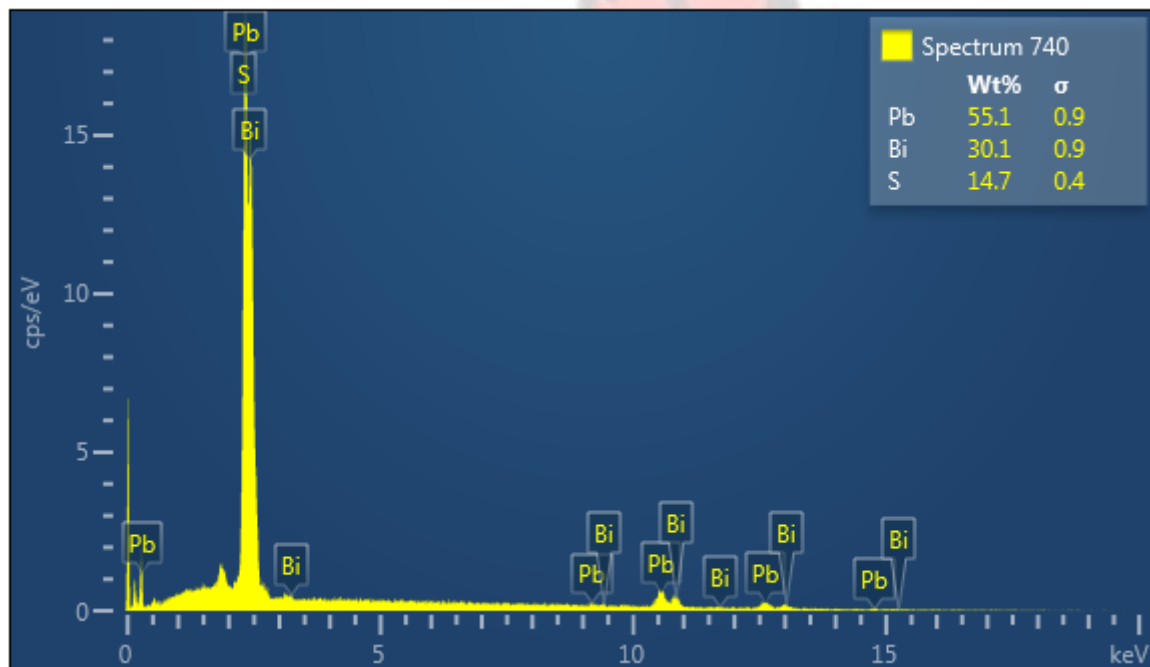


Figure 5.27 Representative EDX spectrum of Bi doped PbS nanoparticles

Quantifying the EDX spectrum gave weight percent of 55.11, 30.1 and 14.7 for Pb, Bi and S respectively. Converting these values to atomic percentages gave 30.6, 16.6 and 54.7 for Pb, Bi and S respectively, indicating that a slightly sulfur rich alloy was formed.

5.9.4 Inductively coupled plasma analyses of Bi doped PbS nanoparticles

The exact dopant content in the nanoparticles grown using hot injection was quantified using inductively coupled plasma optical emission spectrometry (ICP-OES). The Bi³⁺ content measured by ICP indicates successful incorporation of the Bi ions during the syntheses followed by the substitution into the PbS crystal lattice. As seen from Table 5.6, there was not 100% incorporation of the Bi ions into the PbS lattice.

Table 5.6 Percentage incorporation of Bi into the PbS crystal lattice

% Bi content in injection mixture	% Bi incorporated into the PbS crystal lattice
0	0
10	3.86
20	9.85
30	12.81
40	15.75
50	20.51
60	26.72
70	31.23
80	36.59
90	37.59
100	38.59

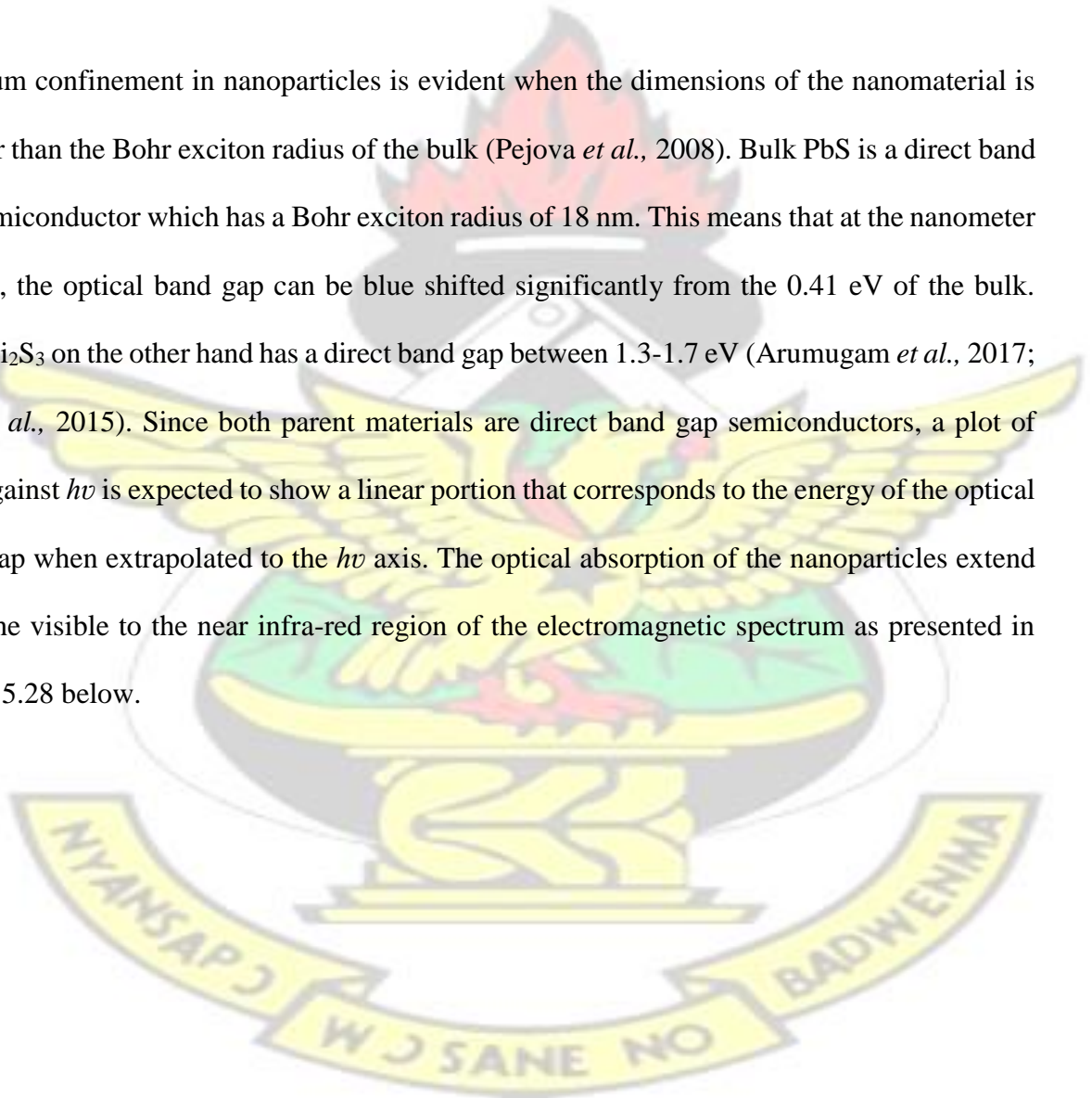
Deviation between the injection and alloy ratios of Pb:Bi can be attributed to a favoured incorporation of Bi in the PbS structure i.e. cation exchange reactions during the nanoparticle formation and growth, or/and formation of Pb²⁺ vacancies upon Bi³⁺ incorporation in the nanoparticle structure as a charge compensation mechanism (Papagiorgis *et al.*, 2016). There was approximately, 40% incorporation of the Bi ions into the PbS crystal lattice which confirms earlier research by Papagiorgis and co-workers (2017). Stavrinadis *et al.*, (2013) have also

reported on the successful incorporation of about 40% Bi doping into PbS quantum dots using colloidal method. However, the growth of Bi doped PbS thin films using an in situ solution processed method revealed the incorporation of about 30% Bi ions into the PbS lattice (Abdelhady *et al.*, 2016).

KNUST

5.9.5 Optical properties of Bi doped PbS nanoparticles

Quantum confinement in nanoparticles is evident when the dimensions of the nanomaterial is smaller than the Bohr exciton radius of the bulk (Pejova *et al.*, 2008). Bulk PbS is a direct band gap semiconductor which has a Bohr exciton radius of 18 nm. This means that at the nanometer regime, the optical band gap can be blue shifted significantly from the 0.41 eV of the bulk. Bulk Bi₂S₃ on the other hand has a direct band gap between 1.3-1.7 eV (Arumugam *et al.*, 2017; Han *et al.*, 2015). Since both parent materials are direct band gap semiconductors, a plot of ahv^2 against hv is expected to show a linear portion that corresponds to the energy of the optical band gap when extrapolated to the hv axis. The optical absorption of the nanoparticles extend from the visible to the near infra-red region of the electromagnetic spectrum as presented in Figure 5.28 below.



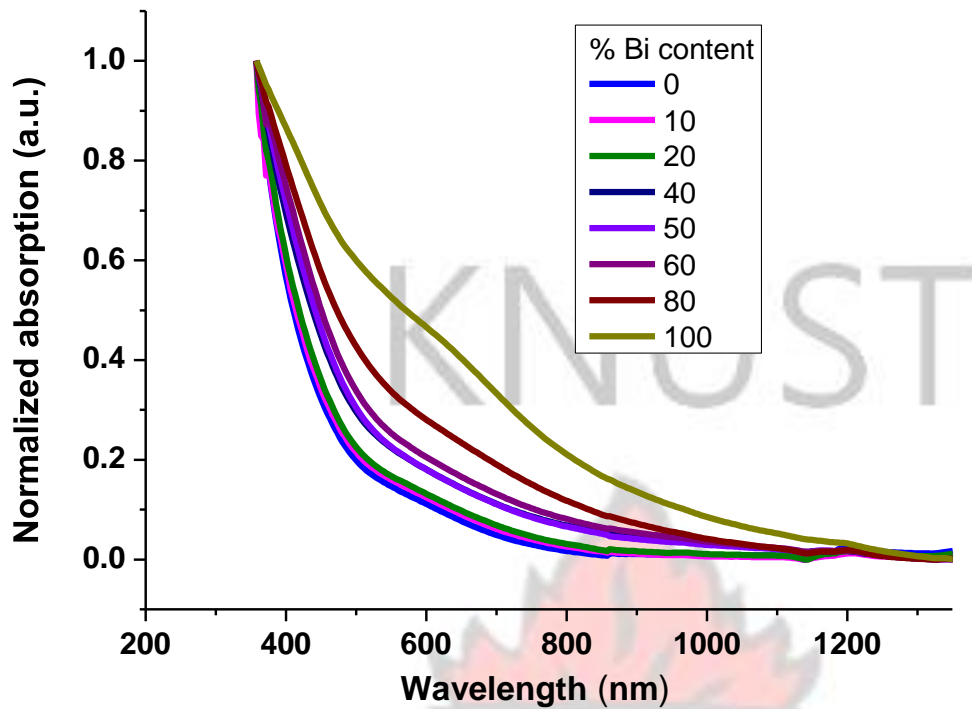


Figure 5.28 Absorption spectra of Bi doped PbS nanoparticles

The estimated optical band gap for the PbS nanoparticles was 0.72 eV which has been blue shifted from the bulk band gap of 0.41 eV. This blue shift is as a result of the relatively small size of the nanoparticles (Figure 5.26). The optical band gaps of the Bi₂S₃ nanoparticles were estimated to be 1.94 eV, also indicating a blue shift from its bulk value which lies between 1.3 to 1.7 eV. Earlier research on Bi₂S₃ with similar dimensions have estimated band gaps of 1.82 and 1.87 eV by Arumugan *et al.*, (2017) and Han *et al.*, (2015) respectively.

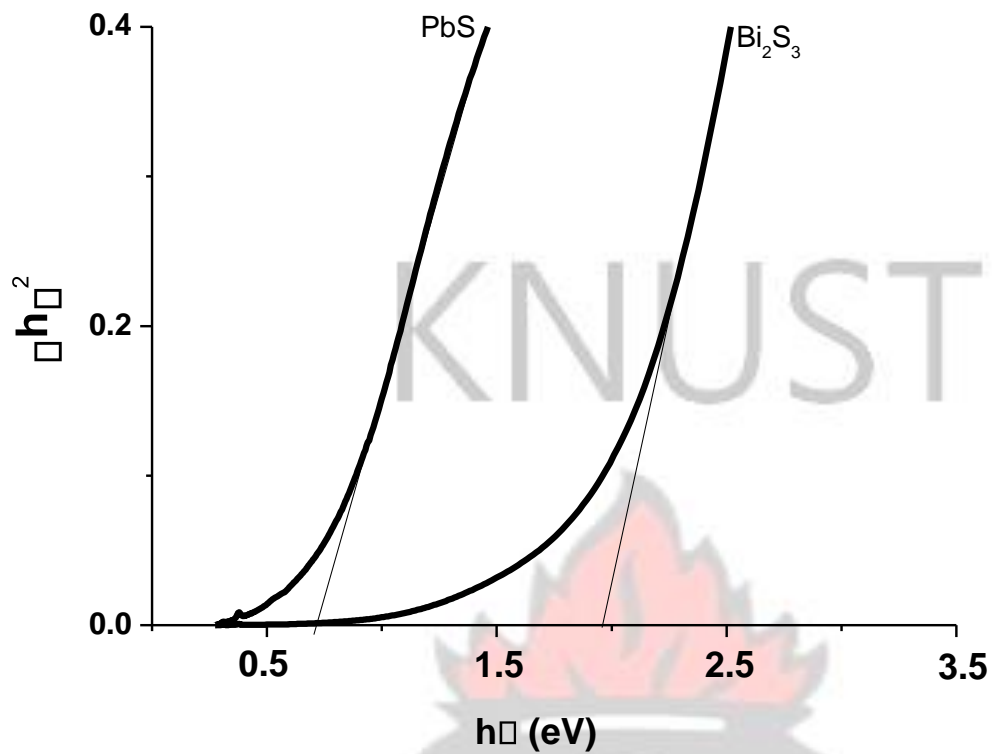


Figure 5.29 Representative Tauc plots of PbS and Bi₂S₃ nanoparticles

The alloy exhibited an increase in band gap from that of the binary PbS based on the incorporation of Bi ions (Figure 5.30). This linearity confirms that unit cell parameters vary linearly with composition for a continuous substitutional solid (Çapan *et al.*, 2010). At 80 and 90% Bi doping, the estimated band gaps were 1.53 and 1.69 eV respectively. It has been reported that nickel doped PbS nanoparticles also showed blue shifting in the band gap values with increasing nickel dopant concentration from 2.45 to 2.67 eV (Kumar *et al.*, 2015).

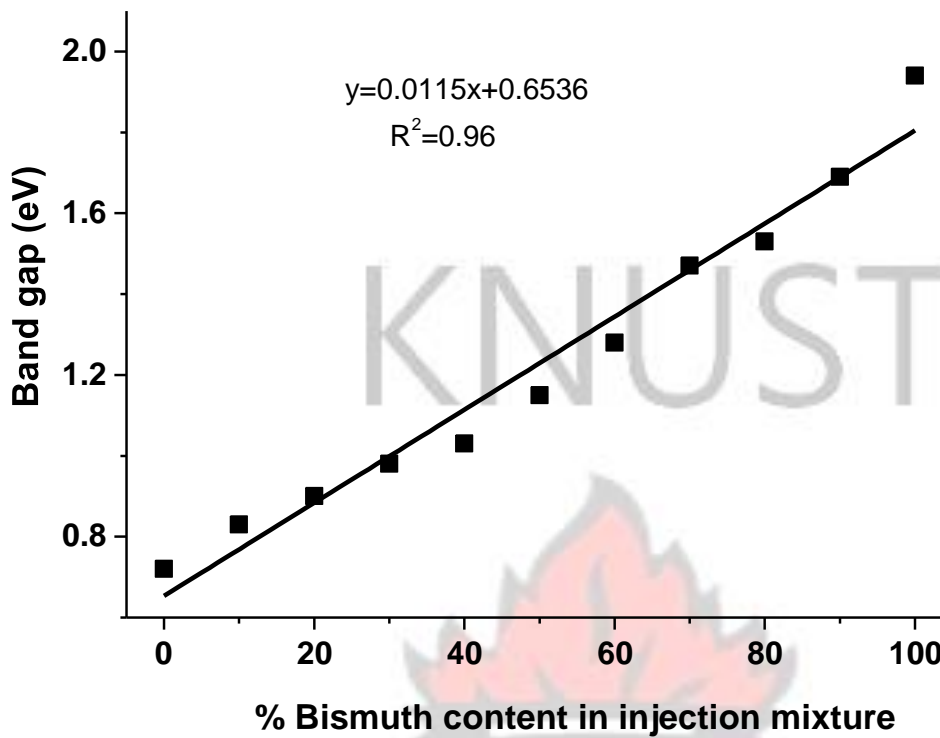
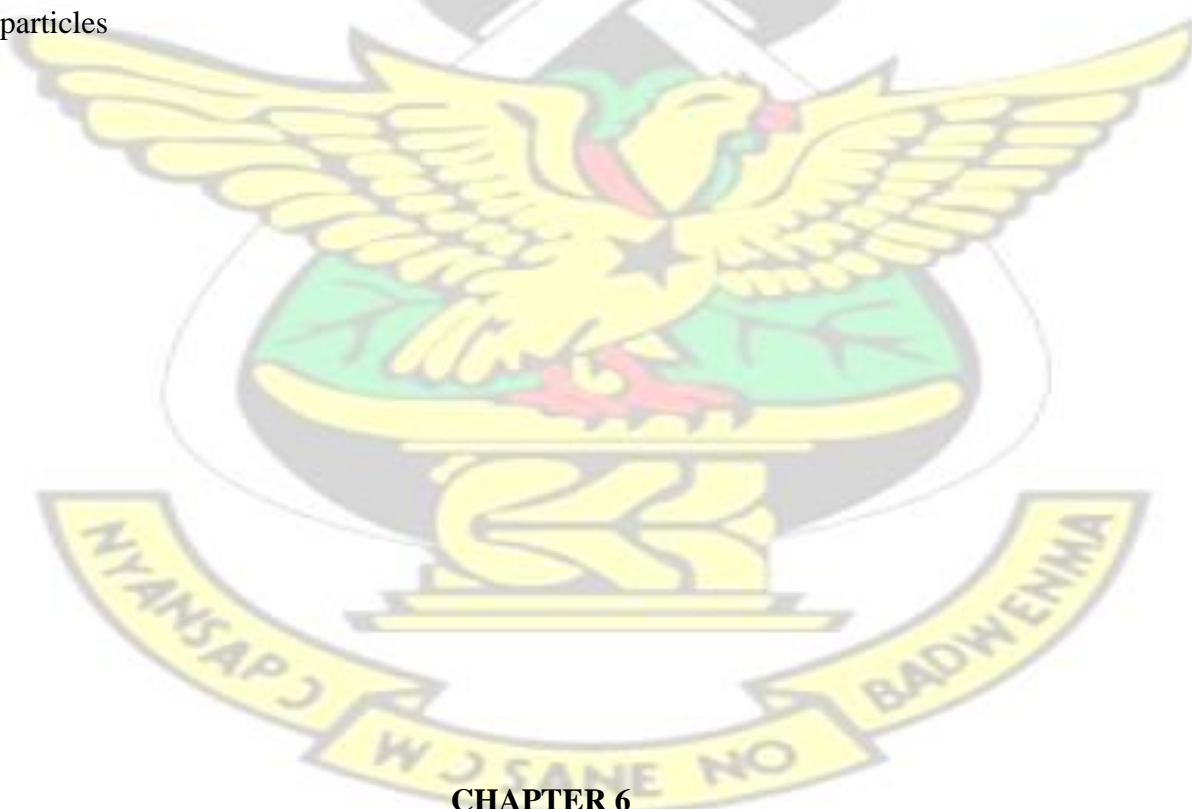


Figure 5.30 Effect of % Bi content in injection mixture on the band gap of Bi doped PbS nanoparticles



CHAPTER 6

CONCLUSIONS AND RECOMMENDATIONS

6.1 Conclusions

Different single source precursors namely lead alkyl xanthates [ethyl (1), propyl (2), butyl (3), hexyl (4), octyl (5) and dodecyl (7)], bismuth ethyl xanthate (9) and its nitrogen adducts [TMEDA (10), triethylamine (11), 1, 10 phenanthroline (12), pyridine (13)], ureas [*bis*(*N*, *N*-diethyl- *N'*-naphthoylselenoureato) lead(II) (15) and *bis*(*N*, *N*-diethyl- *N'*-naphthoylthioureato) lead(II) (17)] and metal piperidine dithiocarbamates [lead (19) and bismuth (20)] have been synthesized. Characterization of these complexes using micro elemental analyses, nuclear magnetic resonance, infrared spectroscopy and thermogravimetric analyses all confirmed the purity of the complexes and their suitability for use as starting materials for the syntheses of their respective metal chalcogenides.

The effect of alkyl chain on the properties of PbS thin films synthesized from complexes (1) to (7) above have been studied. SEM showed the formation of nanocubes for PbS from complexes (1) to (4) with side length that decreased with increasing alkyl chain length in the starting precursor. For a particular precursor, an increase in temperature was found to cause agglomeration in the nanocubes and hence an increase in size. The PbS from the octyl derivative, (complex (5)) resulted in the formation of a rod with a cube at the tip whereas those from complex (7) produced a fibrous structure with cubes arranged along its entire length. The choice of alkyl chain caused a significant effect on the dimensions of the cubes formed with the ethyl derivative having the largest dimensions.

Complexes (9) to (13) showed anisotropic growth of Bi₂S₃ thin films. From their SEM images, the choice of the type of nitrogen adduct had a great effect on the properties of the thin films deposited when subjected to the same reaction conditions. Bi₂S₃ structures ranging from wires (TMEDA adduct) to cluster of rods (triethylamine and pyridine) to dots (1, 10 phenanthroline adduct) were seen from the SEM images.

Complexes (7) and (15), and complexes (15) and (17) were combined in the syntheses of $\text{PbS}_x\text{Se}_{(1-x)}$ thin films and nanoparticles respectively. There was a gradual shift in the 2 theta values from PbS to lower values of PbSe as the mole fraction of selenium in the precursor mixture increased from 0 to 1. EDX analyses further confirmed the formation of the ternary $\text{PbS}_x\text{Se}_{(1-x)}$ at different values of x . A mixture of complexes (19) and (20) confirmed the formation of Bi doped PbS nanoparticles using hot injection method. From the p-XRD patterns, there was a change from cubic to an orthorhombic phase as the percentage of complex (20) in the injection mixture increased over 80%. A change from a cubic to a rod-like morphology was seen from the TEM analyses. In all the nanomaterials, the optical band gaps were blue shifted from their bulk materials.

The key findings from this study are:

- (a) Anisotropic growth of PbS nanomaterials have been demonstrated through the choice of alkyl chain length in lead xanthate SSPs from cubes to a rods.
- (b) Single crystal structures of bismuth ethyl xanthate and its 1, 10 phenanthroline adduct have been determined to have trigonal prismatic and tetrahedron geometries respectively.
- (c) The effect of N-adduct on the morphology of Bi_2S_3 thin films have been shown to change from wires (TMEDA) to clusters of rods (triethylamine and pyridine) to dots (1, 10 phenanthroline).
- (d) Selenourea (15) has been used as a dopant to xanthate (7) and thiourea (17) to synthesize $\text{PbS}_x\text{Se}_{(1-x)}$ thin films and nanoparticles respectively with rodlike and cubic morphologies.
- (e) Band gap of PbS nanoparticles from lead piperidine dithiocarbamate (19) has been widely tuned from 0.72 to 1.69 eV by changing the concentration of bismuth piperidine dithiocarbamate (20) used as dopant.

6.2 Recommendations

Further work should be done on:

- (a) the morphology of the PbS thin films using TEM.
- (b) magnetic properties of the Bi doped PbS nanoparticles should also be carried out.
- (c) in terms of the xanthate SSPs, longer alkyl chain length such as hexadecyl and octadecyl should be investigated to know their effect on the shape and size on the nanomaterials formed.
- (d) since the alloyed nanoparticles and thin films showed improved properties as compared to their parent binaries, further investigations on the use of these nanoparticles in the fabrication of solar cells should be exploited.

REFERENCES

- Abbas, M.M., Shehab, A.A.-M., Hassan, N.-A. and Al-Samuraee, A.-K. (2011), “Effect of temperature and deposition time on the optical properties of chemically deposited nanostructure PbS thin films”, *Thin Solid Films*, Vol. 519 No. 15, pp. 4917–4922.

- Abd-Elkader, O.H. and Deraz, N.M. (2014), “Structural and optical properties of nanoscale galinobisuitite thin films.”, *International Journal of Molecular Sciences*, Vol. 15 No. 2, pp. 1842–1851.
- Abdelhady, A.L., Afzaal, M., Malik, M.A. and O’Brien, P. (2011), “Flow reactor synthesis of CdSe, CdS, CdSe/CdS and CdSeS nanoparticles from single molecular precursors”, *Journal of Materials Chemistry*, Vol. 21, pp. 18768–18775.
- Abdelhady, A.L., Malik, M.A. and O’Brien, P. (2014), “Colloidal synthesis of ZnS, CdS and $Zn_xCd_{1-x}S$ nanoparticles from zinc and cadmium thiobiuret complexes”, *Journal of Inorganic and Organometallic Polymers and Materials*, Vol. 24 No. 1, pp. 226–240.
- Abdelhady, A.L., Ramasamy, K., Malik, M.A. and O’Brien, P. (2013), “Very narrow In_2S_3 nanorods and nanowires from a single source precursor”, *Materials Letters*, Vol. 99, pp. 138–141.
- Abdelhady, A.L., Ramasamy, K., Malik, M.A., O’Brien, P., Haigh, J.S. and Raftery, J. (2011), “New routes to copper sulfide nanostructures and thin films”, *Journal of Materials Chemistry*, Vol. 21, pp. 17888–17895.
- Abdelhady, A.L., Saidaminov, M.I., Murali, B., Adinol, V., Voznyy, O., Katsiev, K. and Alarousu, E. (2016), “Heterovalent dopant incorporation for bandgap and type engineering of perovskite crystals”, *The Journal of Physical Chemistry Letters*, Vol. 7, pp. 295–301.
- Abdelhady, L.A., Malik, M.A., O’Brien, P. and Tuna, F. (2012), “Nickel and iron sulfide nanoparticles from thiobiurets”, *The Journal of Physical Chemistry C*, Vol. 116, pp. 2253–2259.
- Abdulwahab, K., Malik, M.A., O’Brien, P., Govender, K., Muryn, C.A., Timco, G.A. and Tuna, F. (2013), “Synthesis of monodispersed magnetite nanoparticles from iron pivalate clusters”, *Dalton Transactions*, Vol. 42, pp. 196–206.
- Abe, K., Hanada, T., Yoshida, Y., Tanigaki, N., Takiguchi, H., Nagasawa, H. and Nakamoto, M. (1998), “Two-dimensional array of silver nanoparticles”, *Thin Solid Films*, Vol. 327–329, pp. 524–527.
- Abel, K.A., Qiao, H., Young, J.F. and van Veggel, F.C.J.M. (2010), “Four-fold enhancement of the activation energy for nonradiative decay of excitons in PbSe/CdSe core/shell versus PbSe colloidal quantum dots”, *The Journal of Physical Chemistry Letters*, Vol. 1 No. 15, pp. 2334–2338.
- Aeberhard, U., Vaxenburg, R., Lifshitz, E. and Tomić, S. (2012), “Fluorescence of colloidal PbSe/PbS QDs in NIR luminescent solar concentrators”, *Physical Chemistry Chemical Physics*, Vol. 14, pp. 16223–16228.
- Aernouts, T., Vanlaeke, P., Geens, W., Poortmans, J., Heremans, P., Borghs, S. and Mertens, R. (2004), “Printable anodes for flexible organic solar cell modules”, *Thin Solid Films*, Vol. 451–452, pp. 22–25. Aerts, M., Sandeep, C.S.S., Gao, Y., Savenije, T.J., Schins, J.M., Houtepen, A.J. and Kinge, S.

- (2011), “Free charges produced by carrier multiplication in strongly coupled PbSe quantum dot films”, *Nano Letters*, Vol. 11, pp. 4485–4489. Aerts, M., Spoor, F.C.M., Grozema, F.C., Houtepen, A.J., Schins, J.M. and Siebbeles, L.D.A.
- (2013), “Cooling and Auger recombination of charges in PbSe nanorods: crossover from cubic to bimolecular decay”, *Nano Letters*, Vol. 13, pp. 4380–4386.
- Afzaal, M., Ahmad, K. and O’Brien, P. (2012), “Probing the growth mechanism of selfcatalytic lead selenide wires”, *Journal of Materials Chemistry*, Vol. 22, pp. 12731–12735.
- Afzaal, M., Ellwood, K., Pickett, N.L., O’Brien, P., Raftery, J. and Waters, J. (2004), “Growth of lead chalcogenide thin films using single-source precursors.”, *Journal of Materials Chemistry*, Vol. 14 No. 8, pp. 1310–1315.
- Afzaal, M. and O’Brien, P. (2006), “Recent developments in II-VI and III-VI semiconductors and their applications in solar cells”, *Journal of Materials Chemistry*, Vol. 16 No. 17, pp. 1597-1602.
- Ahmad, K., Afzaal, M., O’Brien, P., Hua, G. and Woollins, J.D. (2010), “Morphological Evolution of PbSe crystals via the CVD route”, *Chemistry of Materials*, Vol. 22 No. 16, pp. 4619–4624.
- Ahmad, S. and Isab, A.A. (2003), “Mixed ligand gold (I) complexes with phosphines and selenourea”, *Transition Metal Chemistry*, Vol. 28, pp. 540–543.
- Ajibade, P.A., Onwudiwe, D.C. and Moloto, M.J. (2011), “Synthesis of hexadecylamine capped nanoparticles using group 12 complexes of N-alkyl-N-phenyl dithiocarbamate as single-source precursors”, *Polyhedron*, Vol. 30, pp. 246–252.
- Akhtar, J., Afzaal, M., Banski, M., Podhorodecki, A., Syperek, M., Misiewicz, J. and Bangert, U. (2011), “Controlled synthesis of tuned bandgap nanodimensional alloys of $\text{PbS}_x\text{Se}_{1-x}$ ”, *Journal of the American Chemical Society*, Vol. 133, pp. 5602–5609.
- Akhtar, J., Afzaal, M., Vincent, M.A., Burton, N.A., Hillier, I.H. and O’Brien, P. (2011), “Low temperature CVD growth of PbS films on plastic substrates”, *Chemical Communications*, Vol. 47, pp. 1991–1993.
- Akhtar, J., Afzaal, M., Vincent, M.A., Burton, N.A., Raftery, J., Hillier, I.H. and O’Brien, P. (2011), “Understanding the decomposition pathways of mixed sulfur/selenium lead phosphinato complexes explaining the formation of lead selenide”, *The Journal of Physical Chemistry C*, Vol. 115, pp. 16904–16909.
- Akhtar, J., Akhtar, M., Malik, M.A., O’Brien, P. and Raftery, J. (2012a), “A single-source precursor route to unusual PbSe nanostructures by a solution–liquid–solid method”, *Journal of the American Chemical Society*, Vol. 134, pp. 2485–2487.
- Akhtar, J., Malik, M.A., O’Brien, P. and Helliwell, M. (2010), “Controlled synthesis of PbS nanoparticles and the deposition of thin films by aerosol-assisted chemical vapour deposition (AACVD)”, *Journal of Materials Chemistry*, Vol. 20, pp. 6116–6124.
- Akhtar, J., Malik, M.A., O’Brien, P., Wijayantha, K.G.U., Dharmadasa, R., Hardman, S.J.O. and Graham, D.M. (2010), “A greener route to photoelectrochemically active PbS nanoparticles”, *Journal of Materials Chemistry*, Vol. 20, pp. 2336–2344.

- Akhtar, J., Malik, M.A., Stubbs, S.K., O'Brien, P., Helliwell, M. and Binks, D.J. (2011), "Morphology tailored synthesis of PbSe nanocrystals and thin films from bis[N,N-diisobutyl-N'-(4 nitrobenzoyl)selenoureato]lead(II)", *European Journal of Inorganic Chemistry*, pp. 2984–2990.
- Al-Dulaimi, N., Lewis, D.J., Zhong, L., Azad, M. and O'Brien, P. (2016), "Chemical vapour deposition of rhenium disulfide and rhenium-doped molybdenum disulfide thin films using single-source precursors", *Journal of Materials Chemistry C*, Vol. 4, pp. 2312–2318.
- Al-Ghamdi, A.A., Al-Heniti, S. and Khan, S.A. (2013), "Structural, optical and electrical characterization of Ag doped lead chalcogenide (PbSe) thin films", *Journal of Luminescence*, Vol. 135, pp. 295–300.
- Al-Juaid, F., Merazga, A., Al-Baradi, A. and Abdel-Wahab, F. (2013), "Effect of sol-gel ZnO spin-coating on the performance of TiO₂-based dye-sensitized solar cell", *Solid State Electronics*, Vol. 87, pp. 98–103.
- Al-shakban, M., Xie, Z., Savjani, N., Malik, M.A. and O'Brien, P. (2016), "A facile method for the production of SnS thin films from melt reactions", *Journal of Materials Science*, Vol. 51, pp. 6166–6172.
- Alam, F., Kumar, N. and Dutta, V. (2015), "A simple route for making surfactant free lead sulfide (PbS) quantum dots", *Materials Research Bulletin*, Vol. 65, pp. 89–93.
- Alam, N., Hill, M.S., Kociok-Ko, G., Zeller, M., Mazhar, M. and Molloy, K.C. (2008), "Pyridine adducts of nickel (II) xanthates as single-source precursors for the aerosol-assisted chemical vapor deposition of nickel sulfide", *Chemistry of Materials*, Vol. 20, pp. 6157–6162.
- Ali, A., Khan, A., Ali, A. and Ahmad, M. (2017), "Pressure-sensitive properties of carbon nanotubes/bismuth sulfide composite materials", *Nanomaterials and Nanotechnology*, Vol. 7, pp. 1–9.
- Ali, H.M. and Saleh, S.A. (2014), "Growth and opto-electro-structural properties of nanocrystalline PbSe thin films", *Thin Solid Films*, Vol. 556, pp. 552–559.
- Altiocka, B., Baykul, M.C. and Altiocka, M.R. (2013), "Some physical effects of reaction rate on PbS thin films obtained by chemical bath deposition", *Journal of Crystal Growth*, Vol. 384, pp. 50–54.
- An, J.M., Franceschetti, A., Dudy, S. V and Zunger, A. (2006), "The peculiar electronic structure of PbSe quantum dots", *Nano Letters*, Vol. 6 No. 12, pp. 2728–2735.
- Ananthakumar, S., Ramkumar, J. and Babu, S.M. (2014), "Synthesis of thiol modified CdSe nanoparticles/P3HT blends for hybrid solar cell structures", *Materials Science in Semiconductor Processing*, Vol. 22, pp. 44–49.
- Andreev, A. and Lipovski, A.A. (1999), "Effect of anisotropy of band structure on optical gain in spherical quantum dots based on PbS and PbSe", *Semiconductors*, Vol. 33 No. 12, pp. 1304–1308.

- Angmo, D., Hösel, M. and Krebs, F.C. (2012), “All solution processing of ITO-free organic solar cell modules directly on barrier foil”, *Solar Energy Materials and Solar Cells*, Vol. 107, pp. 329–336.
- Anila, E.I., Saji, K.J. and Sajeev, U.S. (2012), “Synthesis of corrugated structured n type Pbs thin film”, *Key Engineering Materials*, Vol. 500, pp. 118–122.
- Anthony, S.P., Cho, W.J., Lee, J.I. and Kim, J.K. (2009), “Synthesis of lead chalcogenide nanoparticles in block copolymer micelles: investigation of optical properties and fabrication of 2-D arrays of nanoparticles”, *Journal of Materials Chemistry*, Vol. 19, pp. 280–285.
- Anwar, S., Anwar, S. and Mishra, B.K. (2015), “Effect of bath temperature on PbSe thin films prepared by chemical synthesis”, *Materials Science in Semiconductor Processing*, Vol. 40, pp. 910–916.
- Aradia, T., Hornok, V. and D'Ekany, I. (2008), “Layered double hydroxides for ultrathin hybrid film preparation using layer-by-layer and spin coating methods”, *Colloids and Surfaces A: Physicochemical and Engineering Aspects*, Vol. 319, pp. 116–121.
- Argeri, M., Fraccarollo, A., Grassi, F., Marchese, L. and Cossi, M. (2011), “Density functional theory modeling of PbSe nanoclusters: effect of surface passivation on shape and composition”, *The Journal of Physical Chemistry C*, Vol. 115, pp. 11382–11389.
- Artem, A. V., Shagun, V.A., Gusarova, N.K., Liu, C.W., Liao, J.-H., Gatilov, Y. V. and Tro, B.A. (2014), “DFT study and dynamic NMR evidence for cis-trans conformational isomerism in square planar Ni (II) thioselenophosphinate, Ni(SeSPPH₂)₂”, *Journal of Organometallic Chemistry*, Vol. 768, pp. 151–156.
- Arumugam, J., Raj, A.D., Irudayaraj, A.A. and Pazhanivel, T. (2017), “Temperature based investigation on structure and optical properties of Bi₂S₃ nanoflowers by slvothermal approach”, *Mechanics, Materials Science and Engineering*, Vol. 9, pp. 1–8.
- Asunskis, D.J., Bolotin, I.L., Haley, J.E., Urbas, A. and Hanley, L. (2009), “Effects of surface chemistry on nonlinear absorption of PbS nanocrystals”, *Journal of Physical Chemistry C*, Vol. 113, pp. 19824–19829.
- Asunskis, D.J., Bolotin, I.L. and Hanley, L. (2008), “Nonlinear optical properties of PbS nanocrystals grown in polymer solutions”, *The Journal of Physical Chemistry C*, Vol. 112, pp. 9555–9558.
- Ayodhya, D. and Veerabhadram, G. (2017), “Investigation of structural, optical, catalytic, fluorescence studies of eco-friendly synthesized Bi₂S₃ nanostructures”, *Superlattices and Microstructures*, doi:10.1016/j.spmi.2016.12.027.
- Bag, B., Das, B. and Mishra, B.K. (2011), “Geometrical optimization of xanthate collectors with copper ions and their response to flotation”, *Minerals Engineering*, Vol. 24 No. 8, pp. 760–765.
- Bagade, C.S., Mali, S.S., Ghanwat, V.B., Khot, K. V., Patil, P.B., Kharade, S.D. and Mane, R.M. (2015), “A facile and low cost strategy to synthesize Cd_{1-x}Zn_xSe thin films for photoelectrochemical performance: effect of zinc content”, *RSC Advances*, Vol. 5 No. 69, pp. 55658–55668.

- Baik, C., Kim, D., Kang, M.-S., Song, K., Kang, S.O. and Ko, J. (2009), "Synthesis and photovoltaic properties of novel organic sensitizers containing indolo[1,2f]phenanthridine for solar cell", *Tetrahedron*, Vol. 65 No. 27, pp. 5302–5307.
- Bakar, S.A., Hussain, S.T. and Mazhar, M. (2012), "CdTiO₃ thin films from an octa-nuclear bimetallic single source precursor by aerosol assisted chemical vapor deposition (AACVD)", *New Journal of Chemistry*, Vol. 36, pp. 1844–1851.
- Balasubramanian, V. and Suriyanarayanan, N. (2013), "Preparation and characterization of novel single-crystalline PbBiS₂ thin films", *Materials Letters*, Vol. 91, pp. 362–364.
- Balu, A.R., Usharani, K., Prabha, D. and Nagarethinam, V.S. (2017), "Optical and magnetic properties of PbS thin films doped with Fe²⁺ ions", *Optik - International Journal for Light and Electron Optics*, doi:10.1016/j.ijleo.2017.01.010.
- Bao, H., Cui, X., Li, C.M., Gan, Y., Zhang, J. and Guo, J. (2007), "Photoswitchable semiconductor bismuth sulfide (Bi₂S₃) nanowires and their self-supported nanowire arrays", *Journal of Physical Chemistry C*, Vol. 111, pp. 12279–12283.
- Bao, H., Li, C.M., Cui, X., Gan, Y., Song, Q. and Guo, J. (2008), "Synthesis of a highly ordered single-crystalline Bi₂S₃ nanowire array and its metal/semiconductor/metal back-to-back Schottky diode", *Small*, Vol. 4 No. 8, pp. 1125–1129.
- Barote, M.A., Yadav, A.A., Chavan, T. V. and Masumdar, E.U. (2011), "Characterization and photoelectrochemical properties of chemical bath deposited n-PbS thin films", *Digest Journal of Nanomaterials and Biostructures*, Vol. 6 No. 3, pp. 979–990.
- Barreca, D., Gasparotto, A., Maragno, C., Seraglia, R., Tondello, E., Venzo, A. and Krishnan, V. (2005), "Cadmium O-alkylxanthates as CVD precursors of CdS: a chemical characterization", *Applied Organometallic Chemistry*, Vol. 19 No. 1, pp. 59–67.
- Barrios-Salgado, E., Nair, M.T.S., Nair, P.K. and Zingaro, R.A. (2011), "Chemically deposited thin films of PbSe as an absorber component in solar cell structures", *Thin Solid Films*, Vol. 519 No. 21, pp. 7432–7437.
- Begum, A., Hussain, A. and Rahman, A. (2012), "Effect of deposition temperature on the structural and optical properties of chemically prepared nanocrystalline lead selenide thin films", *Beilstein Journal of Nanotechnology*, Vol. 3, pp. 438–443.
- Belova, N.S. and Rempel, A.A. (2004), "PbS nanoparticles: synthesis and size determination by X-ray diffraction", *Inorganic Materials*, Vol. 40 No. 1, pp. 7–14.
- Bendt, G., Schiwon, R., Salamon, S., Landers, J., Hagemann, U., Limberg, C. and Wende, H. (2016), "Molecular design for tailoring a single-source precursor for bismuth ferrite", *Inorganic Chemistry*, doi. 10.1021/acs.inorgchem.6b0095.
- Benjamin, S.L., de Groot, C.H., Gurnani, C., Hector, A.L., Huang, R., Koukharenko, E. and Levason, W. (2014), "Controlling the nanostructure of bismuth telluride by selective chemical vapour deposition from a single source precursor", *Journal of Materials Chemistry A*, Vol. 2 No. 14, pp. 4865–4869.
- Bente, K.I. and Anton, R. (1995), "Crystal chemistry and thin film epitaxy of sulfides and BiSb-sulfosalts and their geological application", *Mineralogy and Petrology*, Vol. 53, pp. 209–228.

- Bera, S., Singh, S.B. and Ray, S.K. (2012), “Green route synthesis of high quality CdSe quantum dots for applications in light emitting devices”, *Journal of Solid State Chemistry*, Vol. 189, pp. 75–79.
- Bhardwaj, A., Srivastava, P. and Sehgal, H.K. (2007), “Chemically deposited PbSe nanoparticle films”, *Journal of The Electrochemical Society*, Vol. 154 No. 10, pp. 83–86.
- Bhat, S.V., Govindaraj, A. and Rao, C.N.R. (2011), “Hybrid solar cell based on P3HT – ZnO nanoparticle blend in the inverted device configuration”, *Solar Energy Materials and Solar Cells*, Vol. 95, pp. 2318–2321.
- Bhatt, S. V., Deshpande, M.P., Soni, B.H., Garg, N. and Chaki, S. (2014), “Chemical bath deposition of lead sulphide (PbS) thin film and their characterization”, *Solid State Phenomena*, Vol. 209, pp. 111–115.
- Bhawana, P. and Fulekar, M.H. (2012), “Nanotechnology: Remediation Technologies to clean up the Environmental pollutants”, *Research Journal of Chemical Sciences*, Vol. 2 No. 2, pp. 90–96.
- Bian, K., Richards, B.T., Yang, H., Bassett, W., Wise, F.W., Wang, Z. and Hanrath, T. (2014), “Optical properties of PbS nanocrystal quantum dots at ambient and elevated pressure”, *Physical Chemistry Chemical Physics*, Vol. 16, pp. 8515–8520.
- Boadi, N.O., Malik, M.A., O’Brien, P. and Awudza, J.A.M. (2012), “Single source molecular precursor routes to lead chalcogenides”, *Dalton Transactions*, Vol. 41 No. 35, pp. 10497–10506.
- Boadi, O.N., Mcnaughten, P.D., Helliwell, M., Malik, M.A., Awudza, J.A.M. and O’Brien, P. (2016), “The deposition of PbS and PbSe thin films from lead dichalcogenoimidophosphinates by AACVD”, *Inorganica Chimica Acta*, Vol. 453, pp. 439–442.
- Boercker, J.E., Clifton, E.M., Tischler, J.G., Foos, E.E., Zega, T.J., Twigg, M.E. and Stroud, R.M. (2011), “Size and temperature dependence of band-edge excitons in PbSe nanowires”, *The Journal of Physical Chemistry Letters*, Vol. 2, pp. 527–531.
- Bolanda, P., Foea, K., Gua, D., Baumgarta, H., Leeb, K., Namkoonga, G. and A. (2011), “Estimation of organic tandem solar cell power conversion efficiency via optical simulation methods”, *The Electrochemical Society Transactions*, Vol. 33 No. 17, pp. 199–205.
- Brumer, M., Sirota, M., Kigel, A., Sashchiuk, A., Galun, E., Burshtein, Z. and Lifshitz, E. (2006), “Nanocrystals of PbSe core, PbSe/PbS, and PbSe/PbSe_xS_{1-x} core-shell as saturable absorbers in passively Q-switched near-infrared lasers”, *Applied Optics*, Vol. 45 No. 28, pp. 7488–7497.
- Burmann, P., Zornoza, B., Téllez, C. and Coronas, J. (2014), “Mixed matrix membranes comprising MOFs and porous silicate fillers prepared via spin coating for gas separation”, *Chemical Engineering Science*, Vol. 107, pp. 66–75.
- Cant, D.J.H., Syres, K.L., Lunt, P.J.B., Radtke, H., Treacy, J., Thomas, P.J. and Lewis, E. A. (2015), “Surface properties of nanocrystalline PbS films deposited at the water-oil interface: a study of atmospheric aging.”, *Langmuir: The ACS Journal of Surfaces and Colloids*, Vol. 31 No. 4, pp. 1445–1453.

- Cao, H., Venkatasubramanian, R., Liu, C., Pierce, J., Yang, H., Zahid Hasan, M., and Wu, Y. (2012), “Topological insulator Bi₂Te₃ films synthesized by metal organic chemical vapor deposition”, *Applied Physics Letters*, Vol. 101 No. 16, pp. 162104–162104.
- Cao, H., Xiao, Y. and Liang, R. (2011), “Generation and superhydrophobicity of complex PbSe crystalline nanodendrites”, *CrystEngComm*, Vol. 13 No. 19, pp. 5688–5691.
- Çapan, R., Brzozowski, L., Barkhouse, D.A.R., Wang, X., Debnath, R., Wolowiec, R. and Palmiano, E. (2010), “Quantum dot photovoltaics in the extreme quantum confinement regime: the surface-chemical origins of exceptional air- and light-stability”, *Asenano*, Vol. 4 No. 2, pp. 869–878.
- Castro, J.R., Molloy, K.C., Liu, Y., Lai, C.S., Dong, Z., White, T.J. and Tiekink, E.R.T. (2008), “Formation of antimony sulfide powders and thin films from single-source antimony precursors”, *Journal of Materials Chemistry*, Vol. 18 No. 44, pp. 5399–5405.
- Chang, W.-S., Lin, Y.-F., Sarkar, B., Chang, Y.-M., Liu, L.-K. and Liu, C.W. (2010), “Synthesis and characterization of [Pb{Se₂P(OiPr)₂}₂]_n pseudo polymorphs: polymeric, single source precursor enabling preparation of shape-controlled lead selenide structures.”, *Dalton Transactions*, Vol. 39 No. 11, pp. 2821–2830.
- Chatterjee, D., Akash, R., Kamalnath, K., Ahmad, R., Singh, A.K. and Ravishankar, N. (2017), “Orientation selection during heterogeneous nucleation: implications for heterogeneous catalysis”, *Journal of the American Chemical Society*, doi.10.1021/acs.jpcc.7b02237.
- Cheek, G. and Mertens, R. (1983), “Metal- insulator- semiconductor silicon solar cells”, *Solar Cells*, Vol. 8, pp. 17–32.
- Chen, J., Wu, L.-M. and Chen, L. (2007), “Syntheses and characterizations of bismuth nanofilms and nanorhombuses by the structure-controlling solventless method.”, *Inorganic Chemistry*, Vol. 46 No. 2, pp. 586–591.
- Chen, L., Xing, H., Shen, Y., Bai, J. and Jiang, G. (2009), “Solid-state thermolysis of [MnO]₁₂ containing molecular clusters into novel MnO nano- and microparticles”, *Journal of Solid State Chemistry*, Vol. 182, pp. 1387–1395.
- Chen, M., Xie, Y., Lu, J., Zhu, Y. and Qian, Y. (2001), “A novel two-step radiation route to PbSe crystalline nanorods”, *Journal of Materials Chemistry*, Vol. 11 No. 2, pp. 518–520.
- Chen, S., Zhang, X., Hou, X., Zhou, Q. and Tan, W. (2010), “One-pot synthesis of hollow PbSe single-crystalline nanoboxes via gas bubble assisted ostwald ripening”, *Crystal Growth and Design*, Vol. 10, pp. 1257–1262.
- Chen, Z., Xie, C., Yang, F., Feng, L., Liang, X. and Xiang, W. (2014), “Controllable synthesis of colloidal CuInS₂ nanocrystals with tunable structures and its nonlinear optical properties”, *Journal of Alloys and Compounds*, Vol. 594, pp. 107–113.
- Chiang, M.-Y., Chang, S.-H., Chen, C.-Y., Yuan, F.-W. and Tuan, H.-Y. (2011), “Quaternary CuIn(S_{1-x}Se_x)₂ nanocrystals: facile heating-up synthesis, band gap tuning and gram-scale production”, *The Journal of Physical Chemistry C*, Vol. 115, pp. 1592–1599.
- Chivers, T., Ritch, J.S., Robertson, S.D., Konu, J. and Tuononen, H.M. (2010), “New insights into the chemistry of imidodiphosphinates from investigations of tellurium-centered systems”, *Accounts of Chemical Research*, Vol. 43 No. 8, pp. 1053–1062.

- Choi, H.M., Ji, I.A. and Bang, J.H. (2014), “Metal selenides as a new class of electrocatalysts for quantum dot- sensitized solar cells : A tale of $\text{Cu}_{1.8}\text{Se}$ and PbSe ”, *Applied Materials and Interfaces*, Vol. 6, pp. 2335–2343.
- Choi, I.H. and Park, H.J. (2014), “Pressure dependence of the photoluminescence from $\gamma\text{-In}_2\text{Se}_3$ thin films prepared using MOCVD with a single-source precursor”, *Journal of the Korean Physical Society*, Vol. 64 No. 9, pp. 1351–1355.
- Choi, J.-H., Oh, S.J., Lai, Y., Kim, D.K., Zhao, T., Fafarman, A.T. and Diroll, B.T. (2013), “In situ repair of high-performance, flexible nanocrystal electronics for large-area fabrication and operation in air”, *ACS Nano*, Vol. 7 No. 9, pp. 8275–8283.
- Chou, K.-S., Huang, K.-C. and Lee, H.-H. (2005), “Fabrication and sintering effect on the morphologies and conductivity of nano-Ag particle films by the spin coating method”, *Nanotechnology*, Vol. 16, pp. 779–784.
- Choudhury, N. and Sarma, B.K. (2009), “Structural characterization of lead sulfide thin films by means of X-ray line profile analysis”, *Bulletin of Material Science*, Vol. 32 No. 1, pp. 43–47.
- Christensen, S., Bindzus, N., Sist, M., Takata, M. and Iversen, B.B. (2016), “Structural disorder, anisotropic micro-strain and cation vacancies in thermo-electric lead chalcogenides.”, *Physical Chemistry Chemical Physics*, Vol. 18 No. 23, pp. 15874–15883.
- Chunggaze, M., Malik, M.A. and O’Brien, P. (1999), “Studies of the thermal decomposition of some diselenocarbamate complexes of cadmium or zinc: molecular design for the deposition of MSe films by CVD”, *Journal of Materials Chemistry*, Vol. 9, pp. 2433–2437.
- Clark, J.M., Kociok-Köhn, G., Harnett, N.J., Hill, M.S., Hill, R., Molloy, K.C. and Saponia, H. (2011), “Formation of PbS materials from lead xanthate precursors”, *Dalton Transactions*, Vol. 40 No. 26, pp. 6893–6900.
- Coates, J. and Ed, R.A.M. (2000), “Interpretation of infrared spectra , a practical approach”, pp. 10815–10837.
- Codato, S., Carta, G., Rossetto, G., Rizzi, G.A., Zanella, P. and Scardi, P. (1999), “MOCVD growth and characterization of ZrO_2 thin films obtained from unusual organo- zirconium precursors”, *Chemical Vapor Deposition*, Vol. 5 No. 4, pp. 159-200.
- Colson, P., Cloots, R. and Henrist, C. (2011), “Experimental design applied to spin coating of 2D colloidal crystal masks: a relevant method?”, *Langmuir*, Vol. 27, pp. 12800–12806.
- Conceicao, T.F., Scharnagl, N., Blawert, C., Dietzel, W. and Kainer, K.U. (2010), “Corrosion protection of magnesium alloy AZ31 sheets by spin coating process with poly (ether imide) [PEI]”, *Corrosion Science*, Vol. 52 No. 6, pp. 2066–2079.
- Corricelli, M., Enrichi, F., Altamura, D., Caro, L.D., Giannini, C., Falqui, A. and Agostiano, A. (2012), “Near infrared emission from monomodal and bimodal PbS nanocrystal superlattices”, *Journal of Physical Chemistry C*, Vol. 116, pp. 6143–6152.

- Cui, R., Gu, Y.-P., Zhang, Z.-L., Xie, Z.-X., Tian, Z.-Q. and Pang, D.-W. (2012), “Controllable synthesis of PbSe nanocubes in aqueous phase using a quasi-biosystem”, *Journal of Materials Chemistry*, Vol. 22, pp. 3713–3716.
- Cunningham, P.D., Boercker, J.E., Placencia, D. and Tischler, J.G. (2014), “Anisotropic absorption in PbSe nanorods”, *Ascnano*, Vol. 8 No. 1, pp. 581–590.
- Cupertino, D., Birdsall, D.J., Slawin, A.M.Z. and Woollins, J.D. (1999), “The preparation and coordination chemistry of $\text{Pr}_2\text{P}(\text{E})\text{NHP}(\text{E}')\text{iPr}_2(\text{E}, \text{E}'=\text{Se}; \text{E}=\text{Se}, \text{E}'=\text{S}; \text{E}=\text{S}, \text{E}'=\text{O}; \text{E}, \text{E}'=\text{O})$ ”, *Inorganica Chimica Acta*, Vol. 290, pp. 1–7.
- Cupertino, D., Keyte, R., Slawin, A.M.Z., Williams, D.J. and Woollins, J.D. (1996), “Preparation and single-crystal characterization of ‘ $\text{Pr}_2\text{P}(\text{S})\text{NHP}(\text{S})\text{Pr}_2$ ’ and homoleptic [$\text{Pr}_2\text{P}(\text{S})\text{NP}(\text{S})\text{Pr}_2$]- complexes of zinc, cadmium, and nickel”, *Inorganic Chemistry*, Vol. 35, pp. 2695–2697.
- Dai, Q., Zhang, Y., Wang, Y., Hu, M.Z., Zou, B., Wang, Y. and Yu, W.W. (2010), “Sizedependent temperature effects on PbSe nanocrystals”, *Langmuir: The ACS Journal of Surfaces and Colloids*, Vol. 26 No. 13, pp. 11435–11440.
- Davidovich, R.L., Stavila, V. and Whitmire, K.H. (2010), “Stereochemistry of lead(II) complexes containing sulfur and selenium donor atom ligands”, *Coordination Chemistry Reviews*, Vol. 254 No. 17–18, pp. 2193–2226.
- Demko, B.A. and Wasylishen, R.E. (2008a), “Comparing main group and transition-metal square-planar complexes of the diselenoimidodiphosphate anion: a solid-state NMR investigation of $\text{M}[\text{N}(\text{iPr}_2\text{PSe})_2]_2$ (M = Se, Te; Pd, Pt)”, *Inorganic Chemistry*, Vol. 47 No. 7, pp. 2786–2797.
- Demko, B.A. and Wasylishen, R.E. (2008b), “A solid-state NMR investigation of single-source precursors for group 12 metal selenides; $\text{M}[\text{N}(\text{iPr}_2\text{PSe})_2]_2$ (M = Zn, Cd, Hg)”, *Dalton Transactions*, Vol. 2, pp. 481–490.
- Dey, P., Paul, J., Bylsma, J., Karaiskaj, D., Luther, J.M., Beard, M.C. and Romero, A.H. (2013), “Origin of the temperature dependence of the band gap of PbS and PbSe quantum dots”, *Solid State Communications*, Vol. 165, pp. 49–54.
- Dharani, S., Mulmudi, K., Yantara, N., Thu, T., Park, N.G., Graetzel, M. and Mhaisalkar, S. (2014), “High efficiency electrospun TiO_2 nanofiber based hybrid organic–inorganic perovskite solar cell”, *Nanoscale*, pp. 1675–1679.
- Dilshad, M.K., Hameed, S., Haider, N., Afzal, A., Sportelli, M.C., Cioffid, N. and Malik, M.A. (2016), “Deposition of morphology-tailored PbS thin films by surfactant-enhanced aerosol assisted chemical vapor deposition”, *Materials Science in Semiconductor Processing*, Vol. 46, pp. 39–45.
- Dolatyari, M., Miri, S., Shekari, H., Bakhtiari, A. and Rostami, A. (2011), “Quantum dot and star like lead sulfide for infrared radiation detection”, *Optoelectronic Materials and Devices*, Vol. 8308, pp. 1–6.
- Le Donne, A., Dilda, M., Crippa, M., Acciarri, M. and Binetti, S. (2011), “Rare earth organic complexes as down-shifters to improve Si-based solar cell efficiency”, *Optical Materials*, Vol. 33 No. 7, pp. 1012–1014.

- Dowland, S., Lutz, T., Ward, A., King, S.P., Sudlow, A., Hill, M.S. and Molloy, K.C. (2011), "Direct growth of metal sulfide nanoparticle networks in solid-state polymer films for hybrid inorganic-organic solar cells", *Advanced Materials*, Vol. 23 No. 24, pp. 2739–2744.
- Du, X., Shi, R., Guo, Y., Wang, Y. and Yuan, Z. (2017), "Enhanced thermoelectric properties of $\text{Pb}_{1-x}\text{Bi}_x\text{S}$ prepared with hydrothermal synthesis and microwave sintering", *Dalton Transactions*, No. 7, pp. 1–5.
- Duan, H., Wang, D., Kurth, D.G. and Mohwald, H. (2004), "Directing self-assembly of nanoparticles at water/oil interfaces", *Angewandte Chemie*, Vol. 43, pp. 5639–5642.
- Duan, T., Lou, W., Wang, X. and Xue, Q. (2007), "Size-controlled synthesis of orderly organized cube-shaped lead sulfide nanocrystals via a solvothermal single-source precursor method", *Colloids and Surfaces A: Physicochemical and Engineering Aspects*, Vol. 310 No. 1–3, pp. 86–93.
- Dunbar, P.B., Haas, E.D. and Hernandez, M.C. (2010), "Laser interferometric calibration for real-time video color interpretation of thin fluid layers during spin coating", *Optics and Lasers in Engineering*, Vol. 48 No. 5, pp. 533–537.
- Dutta, A.K., Maji, S.K., Mitra, K., Sarkar, A., Saha, N., Ghosh, A.B. and Adhikary, B. (2014), "Single source precursor approach to the synthesis of Bi_2S_3 nanoparticles: a new amperometric hydrogen peroxide biosensor", *Sensors and Actuators B*, Vol. 192, pp. 578–585.
- Dutta, A.K., Maji, S.K., Srivastava, D.N., Mondal, A., Biswas, P., Paul, P. and Adhikary, B. (2012), "Synthesis of FeS and FeSe nanoparticles from a single source precursor: A Study of their photocatalytic activity, peroxidase-like behavior, and electrochemical sensing of H_2O_2 ", *Applied Materials and Interface*, Vol. 4, pp. 1919–1927.
- Ebnalwaled, A.A., EL-Raady, A.A.A. and Abo-Bakr, A.M. (2013), "On the effect of complexing agents on the structural and optical properties of CdS nanocrystals", *Chalcogenide Letters*, Vol. 10 No. 2, pp. 55–62.
- Ehsan, M.A., Ming, H.N., Misran, M., Arifin, Z., Tiekink, E.R.T., Safwan, A.P. and Ebadi, M. (2012), "Effect of AACVD processing parameters on the growth of greenockite (CdS) thin films using a single-source cadmium precursor", *Chemical Vapor Deposition*, Vol. 18, pp. 191–200.
- El-Shazly, E.A.A., Zedan, I.T. and Abd El-Rahman, K.F. (2011), "Determination and analysis of optical constants for thermally evaporated PbSe thin films", *Vacuum*, Vol. 86 No. 3, pp. 318–323.
- Emadi, H. and Salavati-Niasari, M. (2013), "Hydrothermal synthesis and characterization of lead sulfide nanocubes through simple hydrothermal method in the presence of [bis(salicylate) lead (II)] as a new precursor", *Superlattices and Microstructures*, Vol. 54, pp. 118–127.
- Embden, J. V., Chesman, A.S.R. and Jasieniak, J.J. (2015), "The heat-up synthesis of colloidal nanocrystals", *Chemistry of Materials*, Vol. 27, pp. 2246–2285.
- Fan, D., Afzaal, M., Mallik, M.A., Nguyen, C.Q., O'Brien, P. and Thomas, P.J. (2007), "Using coordination chemistry to develop new routes to semiconductor and other materials", *Coordination Chemistry Reviews*, Vol. 251, pp. 1878–1888.

- Fan, D., Thomas, P.J. and O'Brien, P. (2008a), "Synthesis and assembly of Bi₂S₃ nanoparticles at the water – toluene interface", *Chemical Physics Letters*, Vol. 465, pp. 110–114.
- Fan, D., Thomas, P.J. and O'Brien, P. (2008b), "Pyramidal lead sulfide crystallites with high energy {113} facets", *Journal of the American Chemical Society*, Vol. 130, pp. 10892–10894.
- Fenn, J.B., Mann, M., Meng, C.K., Wong, S.F. and Whitehouse, C.M. (1989), "Electrospray ionization for mass spectrometry of large biomolecules", *Journal of Physical Chemistry*, Vol. 246 No. 6, pp. 64–70.
- Ferne, M.J., Jensen, P. and Rubinsztein-dunlop, H. (2009), "Bistable switching between low and high absorbance states in oleate- capped PbS quantum dots", *Acs Nano*, Vol. 3 No. 9, pp. 2731–2739.
- Fierro, S. and Comninellis, C. (2010), "Kinetic study of formic acid oxidation on Ti/IrO₂ electrodes prepared using the spin coating deposition technique", *Electrochimica Acta*, Vol. 55, pp. 7067–7073.
- Foos, E.E., Zega, T.J., Tischler, J.G., Stroud, R.M. and Boercker, J.E. (2011), "Synthesis of PbSe nanowires: the impact of alkylphosphonic acid addition", *Journal of Materials Chemistry*, Vol. 21, pp. 2616–2623.
- Fradler, C., Rath, T., Dunst, S., Letofsky-Papst, I., Saf, R., Kunert, B. and Hofer, F. (2014), "Flexible polymer/copper indium sulfide hybrid solar cells and modules based on the metal xanthate route and low temperature annealing", *Solar Energy Materials and Solar Cells*, Vol. 124, pp. 117–125.
- Freitas, J.N., Gonçalves, A.S. and Nogueira, A.F. (2014), "A comprehensive review of the application of chalcogenide nanoparticles in polymer solar cells.", *Nanoscale*, Vol. 6, pp. 6371–6397.
- Fu, H., Luan, W. and Tu, S.-T. (2012), "A simple route for synthesis of PbSe nanocrystals: shape control by ligand and reaction time.", *Dalton Transactions*, Vol. 41 No. 39, pp. 12254–12258.
- Fu, H. and Tsang, S.-W. (2012), "Nanoscale infrared colloidal lead chalcogenide nanocrystals: synthesis, properties and photovoltaic applications", *Nanoscale*, Vol. 4, pp. 2187–2201.
- Fuentes-Martínez, J.P., Toledo-Martínez, I., Román-Bravo, P., García, P.G.Y., GodoyAlcántar, C., López-Cardoso, M. and Morales-Rojas, H. (2009), "Diorganotin(IV) dithiocarbamate complexes as chromogenic sensors of anion binding", *Polyhedron*, Vol. 28, pp. 3953–3966.
- Furlani, C., Cervone, E. and Camassei, F.D. (1968), "Transition metal N,N-diethyldiselenocarbamates", *Inorganic Chemistry*, Vol. 7 No. 2, pp. 265–268.
- Galagan, Y., Coenen, E.W.C., Abbel, R., van Lammeren, T.J., Sabik, S., Barink, M. and Meinders, E.R. (2013), "Photonic sintering of inkjet printed current collecting grids for organic solar cell applications", *Organic Electronics*, Vol. 14 No. 1, pp. 38–46.
- Ganaie, M. and Zulfeqar, M. (2015), "Structural and optical investigation of Cd₄Se_{96-x}S_x (x = 4, 8, 12) chalcogenide thin films", *Journal of Materials Science: Materials in Electronics*, Vol. 26 No. 7, pp. 4816–4822.

- Ganguly, S. and Brock, S.L. (2011), "Toward nanostructured thermoelectrics : synthesis and characterization of lead telluride gels and aerogels", *Journal of Materials Chemistry*, Vol. 21, pp. 8800–8806.
- Ganguly, S., Zhou, C., Morelli, D., Sakamoto, J., Uher, C. and Brock, S.L. (2011), "Synthesis and evaluation of lead telluride/bismuth antimony telluride nanocomposites for thermoelectric applications", *Journal of Solid State Chemistry*, Vol. 184, pp. 3195–3201.
- Gao, B., Zhao, M., Wang, Q., Kang, K.-B., Xu, Z.-G. and Zhang, H.-L. (2013), "Improved synthesis of $\text{PbS}_x\text{Se}_{1-x}$ ternary alloy nanocrystals and their nonlinear optical properties", *New Journal of Chemistry*, Vol. 37 No. 6, pp. 1692–1695.
- Gautam, P., Madathil, D. and Nair, A.N.B. (2013), "Nanotechnology in waste water treatment: a review", *International Journal of ChemTech Research*, Vol. 5 No. 5, pp. 2303–2308.
- Gautam, U.K. and Seshadri, R. (2004), "Preparation of PbS and PbSe nanocrystals by a new solvothermal route", *Materials Research Bulletin*, Vol. 39, pp. 669–676.
- Gayner, C. and Kar, K.K. (2015), "Inherent room temperature ferromagnetism and dopant dependent Raman studies of PbSe, $\text{Pb}_{1-x}\text{Cu}_x\text{Se}$, and $\text{Pb}_{1-x}\text{Ni}_x\text{Se}$ ", *Journal of Applied Physics*, Vol. 117, pp. 103906–103914.
- Ge, J.-P., Wang, J., Zhang, H.-X., Wang, X., Peng, Q. and Li, Y.-D. (2005), "Orthogonal PbS nanowire arrays and networks and their raman scattering", *Chemistry European Journal*, Vol. 11, pp. 1889–1894.
- Gertman, R., Osherov, A., Golan, Y. and Visoly-Fisher, I. (2014), "Chemical bath deposited PbS thin films on ZnO nanowires for photovoltaic applications", *Thin Solid Films*, Vol. 550, pp. 149–155.
- Ghamsari, M.S., Radiman, S., Yarmo, M.A., Abdul-hamid, M.A., Bananej, A. and Rahman, I.A. (2011), "Colloidal PbS nanocrystals with narrow photoluminescence spectra", *Materials Letters*, Vol. 65 No. 9, pp. 1381–1384.
- Ghosh, D., Bagchi, S. and Das, A.K. (2012), "Theoretical study of electronic structure and complexation of $\text{PbII}(\text{S}_2\text{COR})_2$ [R = Me, Et, Ph] complexes", *Molecular Physics*, Vol. 110 No. 1, pp. 37–48.
- Ghosh, D., Sen, K., Bagchi, S. and Das, A.K. (2013), "The nature of lead–sulfur interaction in $[\text{PbII}(\text{S}_2\text{COEt})_n]_{2-n}$ (n = 1,2,3,4) complexes: topological exploration and formation analysis", *New Journal of Chemistry*, Vol. 37, pp. 1408–1416.
- Ghosh, S., Khan, A.H. and Acharya, S. (2012), "Fabrication of highly stable, hybrid PbS nanocomposites in PAMAM dendrimer matrix for photodetection", *The Journal of Physical Chemistry C*, Vol. 116, pp. 6022–6030.
- Göde, F., Güneri, E., Emen, F.M., Emir Kafadar, V. and Ünlü, S. (2014), "Synthesis, structural, optical, electrical and thermoluminescence properties of chemically deposited PbS thin films", *Journal of Luminescence*, Vol. 147, pp. 41–48.
- Goh, K.K.K., Kim, S. and Zard, S.Z. (2013), "A synthesis of (1E, 3 E)-TMS dienes from ketoxanthates via Chugaev- type elimination", *The Journal of Organic Chemistry*, Vol. 78, pp. 12274–12279.

- Golovnev, N.N., Leshok, A.A., Novikova, G. V. and Petrov, A.I. (2010), “Stability of bismuth (III), indium (III), lead (II) and cadmium (II) monocomplexes with selenourea and thiourea”, *Physical Chemistry of Solutions*, Vol. 55 No. 1, pp. 133–135.
- Gondek, E. (2014), “Optical optimization of organic solar cell with bulk heterojunction”, *OptoElectronic Review*, Vol. 22 No. 2, pp. 77–85.
- Grätzel, M. (2001), “Photoelectrochemical cells”, *Insight Review Articles*, Vol. 414, pp. 338–344.
- Green, M.A. and Blakers, A.W. (1983), “Advantages of metal-insulator-semiconductor structures for silicon solar cells.”, *Solar Cells*, Vol. 8, pp. 3–16.
- Gubin, S.P., Kataeva, N.A. and Khomutov, G.B. (2005), “Promising avenues of research in nanoscience: chemistry of semiconductor nanoparticles”, *Russian Chemical Bulletin*, Vol. 54 No. 4, pp. 827–852.
- Guchhait, A., Rath, A.K. and Pal, A.J. (2011), “To make polymer: Quantum dot hybrid solar cells NIR-active by increasing diameter of PbS nanoparticles”, *Solar Energy Materials and Solar Cells*, Vol. 95, pp. 651–656.
- Guo, L., Zhao, X., An, H. and Wang, Y. (2012), “Catalysis by lead oxide for diethyl carbonate synthesis from ethyl carbamate and ethanol”, *Chinese Journal of Catalysis*, Vol. 33 No. 4, pp. 595–600.
- Gupta, K.M. and Gupta, N. (2017), “Carrier transport in semiconductors”, *Advanced Semiconducting Materials and Devices*, pp. 87–144.
- Haiduc, I. and Yoong, L. (2002), “Reactions of *bis*(thiophosphoryl) disulfanes and *bis*(thiophosphinyl) disulfanes with metal species: an alternative, convenient route to metal complex and organometallic dithiophosphates and dithiophosphinates”, *Coordination Chemistry Reviews*, Vol. 224, pp. 151–170.
- Halimehjani, A.Z., Marjani, K. and Ashouri, A. (2010), “Synthesis of dithiocarbamate by Markovnikov addition reaction in aqueous medium”, *Green Chemistry*, Vol. 12 No. 7, pp. 1306–1310.
- Han, P., Mihi, A., Ferre-Borrull, J., Pallarés, J. and Marsal, L.F. (2015), “Interplay between morphology, optical properties, and electronic structure of solution-processed Bi₂S₃ colloidal nanocrystals”, *The Journal of Physical Chemistry C*, Vol. 119 No. 19, pp. 10693–10699.
- Han, Q., Sun, S., Sun, D., Zhu, J. and Wang, X. (2011), “Room-temperature synthesis from molecular precursors and photocatalytic activities of ultralong Sb₂S₃ nanowires”, *RSC Advances*, Vol. 1, pp. 1364–1369.
- Hao, S., Wu, J. and Sun, Z. (2012), “A hybrid tandem solar cell based on hydrogenated amorphous silicon and dye-sensitized TiO₂ film”, *Thin Solid Films*, Vol. 520, pp. 2102–2105.
- Hasegawa, Y., Adachi, T., Tanaka, A., Afzaal, M., O’Brien, P., Doi, T., Tsuyoshi, T.K., Yukio, H., Koji, F. and Katsuhisa, T. (2008), “Remarkable magneto-optical properties of europium selenide nanoparticles with wide energy gaps”, *Journal of the American Chemical Society*, Vol. 195 No. 3, pp. 5710–5715.

- Henderson, W., Nicholson, B.K. and Dinger, M.B. (2003), "Synthesis and crystal structure of the first complex containing a chelating selenourea dianion ligand", *Inorganica Chimica Acta*, Vol. 355, pp. 428–431.
- Hiszpanski, A.M. and Loo, Y.-L. (2014), "Directing the film structure of organic semiconductors via post-deposition processing for transistor and solar cell applications", *Energy and Environmental Science*, Vol. 7, pp. 592–608.
- Holcapek, M., Jandera, P., Fischer, J. and Prokes, B. (1999), "Analytical monitoring of the production of biodiesel by high-performance liquid chromatography with various detection methods", *Journal of Chromatography A*, Vol. 858, pp. 13–31.
- Hsiang, H.-I., Hsu, W.-H., Lu, L.-H., Chang, Y.-L. and Yen, F.-S. (2013), "Cuprous selenide nano-crystal synthesis and characterization", *Materials Research Bulletin*, Vol. 48, pp. 715–720.
- Hursthouse, M.B., Malik, M.A., Motevalli, M. and O'Brien, P. (1992), "The crystal and molecular structure of N,N-diethyldiselenocarbamatocadmium(II): cadmium and zinc diethyldiselenocarbamates as precursors for selenides", *Polyhedron*, Vol. 11 No. 1, pp. 11–14.
- Hussain, A., Begum, A. and Rahman, A. (2013), "Characterization of nanocrystalline lead sulphide thin films prepared by chemical bath deposition technique", *Arabian Journal for Science and Engineering*, Vol. 38, pp. 169–174.
- Hwang, C.S. (2015), "Prospective of semiconductor memory devices: from memory system to materials", *Advanced Electronoc Materials*, Vol. 1, pp. 1400056–1400086.
- Hyun, B.-R., Zhong, Y., Bartnik, A.C., Sun, L., Abrun, H.D., Wise, F.W. and Goodreau, J.D. (2008), "Electron injection from colloidal PbS nanoparticles", *Ascnano*, Vol. 2 No. 11, pp. 2206–2212.
- Ibanez, M., Zamani, R., Gorsse, S., Fan, J., Ortega, S., Cadavid, D. and Morante, J.R. (2013), "Core-shell nanoparticles as building blocks for the bottom-up production of functional nanocomposites: PbTe-PbS thermoelectric properties", *Acs Nano*, Vol. 7 No. 3, pp. 2573–2586.
- Iqbal, P., Preece, J.A. and Mendes, P.M. (2012), "Nanotechnology: the 'top-down' and 'bottom-up' approaches", edited by Gale, P.A. and Steed, J.W. *Supramolecular Chemistry: From Molecules to Nanomaterials*, pp. 1–14.
- Jabalamei, A., Nowek, A., Sullivan, R.H. and Leszczyfiski, J. (1997), "Structures and energies of seleno derivatives of biuret. Ab Initio comparative studies of diselenobiuret, selenobiuret, and selenothiobiuret", *Structural Chemistry*, Vol. 8 No. 4, pp. 245–256.
- Jain, V., Rajbongshi, B.K., Tej, M.A., Bhattacharjya, G., Kumar, I.S.S. and Ramanathan, G. (2008), "Photovoltaic effect in single-layer organic solar cell devices fabricated with two new imidazolin-5-one molecules", *Solar Energy Materials and Solar Cells*, Vol. 92, pp. 1043–1046.
- Jardim, P.L.G., Michels, A.F. and Horowitz, F. (2014), "Spin-coating process evolution and reproducibility for power-law fluids", *Applied Optics*, Vol. 53 No. 9, pp. 1820–1825.

- Jasinski, P., Molin, S., Gazda, M., Petrovsky, V. and Anderson, H.U. (2009), “Applications of spin coating of polymer precursor and slurry suspensions for solid oxide fuel cell fabrication”, *Journal of Power Sources*, Vol. 194, pp. 10–15.
- Ji, C., Zhang, Y., Zhang, X., Wang, P., Shen, H., Gao, W. and Wang, Y. (2017), “Synthesis and characterization of $\text{Ag}_2\text{S}_x\text{Se}_{1-x}$ nanocrystals and their photoelectrochemical property”, *Nanotechnology*, Vol. 28, pp. 2–10.
- Jin, R., Chen, G. and Pei, J. (2012), “PbS/PbSe hollow spheres: solvothermal synthesis, growth mechanism, and thermoelectric transport property”, *The Journal of Physical Chemistry C*, Vol. 116, p. 16207–16216.
- Joshi, R.K., Kanjilal, A. and Sehgal, H.K. (2003), “Size dependence of optical properties in solution-grown $\text{Pb}_{1-x}\text{Fe}_x\text{S}$ nanoparticle”, *Nanotechnology*, Vol. 14, pp. 809–812.
- Jung, Y.K., Kim, J. and Lee, J.-K. (2010), “Thermal decomposition mechanism of single-molecule precursors forming metal sulfide nanoparticles.”, *Journal of the American Chemical Society*, Vol. 132 No. 1, pp. 178–184.
- Kaci, S., Keffous, A., Trari, M., Fellahi, O., Menari, H., Manseri, A. and Guerbois, L. (2010), “Relationship between crystal morphology and photoluminescence in polynanocrystalline lead sulfide thin films”, *Journal of Luminescence*, Vol. 130 No. 10, pp. 1849–1856.
- Kalebaila, K.K. and Brock, S.L. (2012), “Lead selenide nanostructured aerogels and xerogels”, *Journal of Inorganic and General Chemistry*, Vol. 638 No. 15, pp. 2598–2603.
- Kaltenhauser, V., Rath, T., Haas, W., Torvisco, A., Friedel, B., Kunert, B. and Saf, R. (2013), “Bismuth sulfide–polymer nanocomposites from a highly soluble bismuth xanthate precursor”, *Journal of Materials Chemistry C*, Vol. 1, pp. 7825–7832.
- Kalyanikutty, K.P., Gautam, U.K. and Rao, C.N.R. (2006), “Ultra-thin crystalline films of ZnS and PbS formed at the organic – aqueous interface”, *Solid State Sciences*, Vol. 8, pp. 296–302.
- Kang, M.S., Sahu, A., Frisbie, C.D. and Norris, D.J. (2013), “Influence of silver doping on electron transport in thin films of PbSe nanocrystals.”, *Advanced Materials*, Vol. 25 No. 5, pp. 725–731.
- Kariper, E.A. and Özpozan, T. (2013), “Cobalt xanthate thin film with chemical bath deposition”, *Journal of Nanomaterials*, Vol. 2013, pp. 1–10.
- Kayatürk, N., Usanmaz, A. and Önal, A.M. (1999), “Polymerization by bis(ethylxanthato)nickel(II) as an initiator. I. Polymerization of styrene oxide”, *Journal of Macromolecular Science: Pure and Applied Chemistry*, Vol. 36 No. 1, pp. 115–135.
- Kershaw, S. V., Susha, A.S. and Rogach, A.L. (2013), “Narrow bandgap colloidal metal chalcogenide quantum dots: synthetic methods, heterostructures, assemblies, electronic and infrared optical properties”, *Chemical Society Reviews*, Vol. 42, pp. 3033–3087.
- Kevin, P., Alghamdi, Y.G., Lewis, D.J. and Malik, M.A. (2015), “Morphology and band gap controlled AACVD of CdSe and $\text{CdS}_x\text{Se}_{1-x}$ thin films using novel single source precursors: bis(diethyldithio/diselenocarbamate) cadmium (II)”, *Materials Science in Semiconductor Processing*, Vol. 40, pp. 848–854.

- Khalid, S., Malik, M.A., Lewis, D.J., Kevin, P., Ahmed, E., Khan, Y. and O'Brien, P. (2015), "Transition metal doped pyrite (FeS_2) thin films: structural properties and evaluation of optical band gap energies", *Journal of Material Chemistry C*, Vol. 3 No. 46, pp. 12068–12076.
- Khalil, M.M.H., Ismail, E.H., El-Baghdady, K.Z. and Mohamed, D. (2014), "Green synthesis of silver nanoparticles using olive leaf extract and its antibacterial activity", *Arabian Journal of Chemistry*, Vol. 7 No. 6, pp. 1131–1139.
- Khalil, M.M.H., Ismail, E.H. and El-Magdoub, F. (2012), "Biosynthesis of Au nanoparticles using olive leaf extract", *Arabian Journal of Chemistry*, Vol. 5 No. 4, pp. 431–437.
- Khan, A.H., Ji, Q., Ariga, K., Thupakula, U. and Acharya, S. (2011), "Size controlled ultranarrow PbS nanorods: spectroscopy and robust stability", *Journal of Materials Chemistry*, Vol. 21 No. 15, pp. 5671–5676.
- Khanna, P.K., Jun, K.-W., Gokarna, A., Baeg, J.-O. and Seok, S. (2006), "One-step synthesis of TOP capped PbSe pyramidal nanocrystals", *Materials Chemistry and Physics*, Vol. 96, pp. 154–157.
- Kim, D.K., Lai, Y., Vemulkar, T.R. and Kagan, C.R. (2011), "Flexible, low-voltage, and low-hysteresis PbSe nanowire field-effect transistors", *ACS Nano*, Vol. 5 No. 12, pp. 10074–10083.
- Kim, K., Bong, H., Won, J. and Soo, K. (2010), "Poly(ethylenimine)-stabilized silver nanoparticles assembled into 2-dimensional arrays at water–toluene interface", *Journal of Colloid and Interface Science*, Vol. 345, pp. 103–108.
- Kim, W.D., Lee, S., Pak, C., Woo, J.Y., Lee, K., Won, J. and Lee, D.C. (2014), "Metal tips on pyramid-shaped PbSe/CdSe/CdS heterostructure nanocrystal photocatalysts: study of Ostwald ripening and core/shell formation.", *Chemical Communications*, Vol. 50 No. 14, pp. 1719–1721.
- Ko, Y.G., Shin, D.H., Lee, G.S. and Choi, U.S. (2011), "Fabrication of colloidal crystals on hydrophilic/hydrophobic surface", *Colloids and Surfaces A: Physicochemical and Engineering Aspects*, Vol. 385 No. 1–3, pp. 188–194.
- Koca, M., Yildirim, G., Kirilmis, C. and Karaboga, F. (2012), "Density functional theory study on the identification of $\text{Pd}(\text{Me-xanthate})_2$ ", *Arabian Journal for Science and Engineering*, Vol. 37, pp. 1283–1291.
- Koh, Y.W., Lai, C.S., Du, A.Y., Tiekink, E.R.T. and Loh, K.P. (2003), "Growth of bismuth sulfide nanowire using bismuth trisxanthate single source precursors", *Chemistry of Materials*, Vol. 15, pp. 4544–4554.
- Komikado, T., Inoue, A., Masuda, K., Ando, T. and Umegaki, S. (2007), "Multi-layered mirrors fabricated by spin-coating organic polymers", *Thin Solid Films*, Vol. 515, pp. 3887–3892.
- Kosacki, I., Suzuki, T., Petrovsky, V. and Anderson, H.U. (2000), "Electrical conductivity of nanocrystalline ceria and zirconia thin films", *Solid State Ionics*, Vol. 137, pp. 1225–1233.
- Kovalenko, M. V, Talapin, D. V, Loi, M.A., Cordella, F., Hesser, G., Bodnarchuk, M.I. and

- Heiss, W. (2008), “Quasi-seeded growth of ligand-tailored PbSe nanocrystals through cation-exchange-mediated nucleation.”, *Angewandte Chemie*, Vol. 47 No. 16, pp. 3029–3033.
- Kügler, R.T., Beißert, K. and Kind, M. (2016), “On heterogeneous nucleation during the precipitation of barium sulfate”, *Chemical Engineering Research and Design*, Vol. 114, pp. 30–38.
- Kumar, D., Agarwal, G., Tripathi, B., Vyas, D. and Kulshrestha, V. (2009), “Characterization of PbS nanoparticles synthesized by chemical bath deposition”, *Journal of Alloys and Compounds*, Vol. 484 No. 1–2, pp. 463–466.
- Kumar, K.N.C., Pasha, S.K.K., Shakil, M.G. and Chidambaram, D.K.K. (2015), “Influence of nickel on the structural, optical and magnetic properties of PbS thin films synthesized by successive ionic layer adsorption and reaction (SILAR) method”, *Materials Letters*, doi.org/10.1016/j.matlet.2015.10.120.
- Kumar, R., Das, R., Gupta, M. and Ganesan, V. (2014), “Preparation of nanocrystalline Sb doped PbS thin films and their structural, optical, and electrical characterization”, *Superlattices and Microstructures*, Vol. 75, pp. 601–612.
- Kumar, R., Jain, G., Saini, R. and Agarwal, P. (2010), “Compositional effects on properties of $\text{PbS}_{1-x}\text{Se}_x$ thin films”, *Chalcogenide Letters*, Vol. 7 No. 4, pp. 233–240.
- Kumar, S., Khan, Z.H., Majeed Khan, M. A. and Husain, M. (2005), “Studies on thin films of lead chalcogenides”, *Current Applied Physics*, Vol. 5 No. 6, pp. 561–566.
- Kun, W.N., Mlowe, S., Nyamen, L.D., Ndifon, P.T., Malik, M.A., Munro, O.Q. and Revaprasadu, N. (2016), “Heterocyclic bismuth(III) dithiocarbamate complexes as single source precursors for the synthesis of anisotropic Bi_2S_3 nanoparticles”, *ChemPubSoc*, Vol. 22 No. 37, pp. 13127–13135.
- Kungumadevi, L. and Sathyamoorthy, R. (2013), “Synthesis, mechanism, optical and electrical characterization of PbTe micro-needles”, *Materials Research Bulletin*, Vol. 48, pp. 1891–1897.
- Kwon, S., Moon, H.C., Lim, K.-G., Bae, D., Jang, S., Shin, J. and Park, J. (2013), “Improvement of power conversion efficiency of P3HT: CdSe hybrid solar cells by enhanced interconnection of CdSe nanorods via decomposable selenourea”, *Journal of Materials Chemistry A*, Vol. 1, pp. 2401–2405.
- Kwon, S.G. and Hyeon, T. (2011), “Formation mechanisms of uniform nanocrystals via hot injection and heat-up methods”, *Small*, Vol. 7 No. 19, pp. 2685–2702.
- Kwon, S.G., Piao, Y., Park, J., Angappane, S., Jo, Y., Hwang, N.-M. and Park, J.-G. (2007), “Kinetics of monodisperse iron oxide nanocrystal formation by ‘heating-up’ process”, *Journal of the American Chemical Society*, Vol. 129 No. 41, pp. 12571–12584.
- Kyobe, J.W., Mubofu, E.B., Makame, Y.M.M., Mlowe, S. and Revaprasadu, N. (2015), “CdSe quantum dots capped with naturally occurring biobased oils”, *New Journal of Chemistry*, Vol. 39, pp. 7251–7259.

- Labidi, M., Meradji, H., Ghemid, S. and Labidi, S. (2011), “Structural, electronic, optical and thermodynamic properties of Pbs, PbSe and their ternary alloy $PbS_{1-x}Se_x$ ”, *Modern Physics Letters B*, Vol. 25 No. 7, pp. 473–486.
- Landsberg, P.T. and Markvart, T. (2013), “Ideal Efficiencies”, *Solar Cells*, pp. 55–66.
- Larramendi, E.M., Calzadilla, O., Gonzalez-Ariasa, A., Hernandez, E. and Ruiz-Garcia, J. (2001), “Effect of surface structure on photosensitivity in chemically deposited PbS thin films”, *Thin Solid Films*, Vol. 389, pp. 301–306.
- Lee, S., Lee, D.T., Ko, J.-H., Kim, W.-J., Joo, J., Jeong, S. and Mcguire, J.A. (2014), “Slow colloidal growth of PbSe nanocrystals for facile morphology and size control”, *RSC Advances*, Vol. 4, pp. 9842–9850.
- Lee, S.M., Yeon, D.H., Chon, S.S. and Cho, Y.S. (2016), “Effect of double substitutions of Cd and Cu on optical band gap and electrical properties of non-colloidal PbS thin films”, *Journal of Alloys and Compounds*, doi:10.1016/j.jallcom.2016.05.203.
- Lee, W., Jeong, M.-C. and Myoung, J.-M. (2004), “Catalyst-free growth of ZnO nanowires by metal-organic chemical vapour deposition (MOCVD) and thermal evaporation”, *Acta Materialia*, Vol. 52, pp. 3949–3957.
- Lei, S., Ge, L., Najmaei, S., George, A., Koppera, R., Lou, J. and Chhowalla, M. (2014), “Evolution of the electronic band structure and efficient photo-detection in atomic layers of InSe”, *ACS Nano*, Vol. 8 No. 2, pp. 1263–1272.
- Lemberger, M., Thiemann, S., Baunemann, A., Parala, H., Fischer, R. A., Hinz, J. and Bauer, A. J. (2007), “MOCVD of tantalum nitride thin films from TBTEMT single source precursor as metal electrodes in CMOS applications”, *Surface and Coatings Technology*, Vol. 201 No. 22–23, pp. 9154–9158.
- Leuw, C.-C., Chen, S.-T. and Liu, F.-K. (2010), “Spin-coating-derived gold-nanoparticle memory”, *Journal of the American Ceramic Society*, Vol. 93 No. 10, pp. 3142–3147.
- Leventis, H.C., O’Mahony, F., Akhtar, J., Afzaal, M., O’Brien, P. and Haque, S.A. (2010), “Transient optical studies of interfacial charge transfer at nanostructured metal oxide/PbS quantum dot/organic hole conductor heterojunctions”, *Journal of the American Chemical Society*, Vol. 132, pp. 2743–2750.
- Lewis, E.A., Mcnaughten, P.D., Yin, Z., Chen, Y., Brent, J.R., Saah, S.A., Raftery, J., Awudza, J.A.M., O’Brien, P. and Haque, S.A. (2015), “In situ synthesis of PbS nanocrystals in polymer thin films from lead (II) xanthate and dithiocarbamate complexes: evidence for size and morphology control”, *Chemistry of Materials*, Vol. 27 No. 6, pp. 2127–2136.
- Lewis, E., Sarah, H. and O’Brien, P. (2014), “The synthesis of metallic and semiconducting nanoparticles from reactive melts of precursors”, *Journal of Materials Chemistry A*, Vol. 2, pp. 570–580.
- Li, C.-C., Chang, S.-J., Su, F.-J., Lin, S.-W. and Chou, Y.-C. (2013), “Effects of capping agents on the dispersion of silver nanoparticles”, *Colloids and Surfaces A: Physicochemical and Engineering Aspects*, Vol. 419, pp. 209–215.

- Li, G., Li, C., Tang, H., Cao, K. and Chen, J. (2011), “Controlled self-assembly of PbS nanoparticles into macrostar-like hierarchical structures”, *Materials Research Bulletin*, Vol. 46, pp. 1072–1079.
- Li, Q., Mahendra, S., Lyon, D.Y., Brunet, L., Liga, M. V., Li, D. and Alvarez, P.J.J. (2008), “Antimicrobial nanomaterials for water disinfection and microbial control: potential applications and implications”, *Water Research*, Vol. 42, pp. 4591–4602.
- Li, W.-F., Fang, C.-M., Dijkstra, M. and Van Huis, M.A. (2015), “The role of point defects in PbS, PbSe and PbTe: a first principles study”, *Journal of Physics: Condensed Matter*, Vol. 27 No. 35, pp. 355801–3558014.
- Li, X.L., Ge, J.P. and Li, Y.D. (2004), “Atmospheric pressure chemical vapor deposition: an alternative route to large-scale MoS₂ and WS₂ inorganic fullerene-like nanostructures and nanoflowers”, *Chemistry*, Vol. 10 No. 23, pp. 6163–6171.
- Lifshitz, E., Bashouti, M., Kloper, V., Kigel, A., Eisen, M.S. and Berger, S. (2003), “Synthesis and characterization of PbSe quantum wires, multipods, quantum rods and cubes”, *Nano Letters*, Vol. 3 No. 6, pp. 857–862.
- Lifshitz, E., Brumer, M., Kigel, A., Sashchiuk, A., Bashouti, M., Sirota, M. and Galun, E. (2006), “Air-stable PbSe/PbS and PbSe/ PbSe_xS_{1-x} core-shell nanocrystal quantum dots and their applications”, *Journal of Physical Chemistry B*, Vol. 110, pp. 25356–25365.
- Lima, P.J.H. and de Andrade, A.M. (2006), “Morphological analysis of poly (omethoxyaniline) thin-films deposited by spin coating technique”, *Journal of Materials Science: Materials in Electronics*, Vol. 17, pp. 593–596.
- Lin, S., Zhang, X., Shi, X., Wei, J., Lu, D., Zhang, Y. and Kou, H. (2011), “Nanoscale semiconductor Pb_{1-x}Sn_xSe (x=0.2) thin films synthesized by electrochemical atomic layer deposition”, *Applied Surface Science*, Vol. 257 No. 13, pp. 5803–5807.
- Liu, C., Kwon, Y.K. and Heo, J. (2009), “Absorption and photoluminescence of PbS QDs in glasses”, *Journal of Non-Crystalline Solids*, Vol. 355, pp. 1880–1883.
- Liu, C., Li, Y., Lee, M. V., Kumatania, A. and Tsukagoshi, K. (2013), “Self-assembly of semiconductor/insulator interfaces in one-step spin-coating: a versatile approach for organic field-effect transistors”, *Physical Chemistry Chemical Physics*, Vol. 15, pp. 7917–7933.
- Liu, F.-K., Chang, Y.-C., Ko, F.-H., Chu, T.-C. and Dai, B.-T. (2003), “Rapid fabrication of high quality self-assembled nanometer gold particles by spin coating method”, *Microelectronic Engineering*, Vol. 68, pp. 702–709.
- Liu, J., Zheng, X., Yan, L., Zhou, L., Tian, G., Yin, W. and Wang, L. (2015), “Bismuth sulfide nanorods as a precision nanomedicine for in vivo photothermal therapy of tumor”, *ACS Nano*, Vol. 9 No. 1, pp. 696–707.
- Liu, X., Li, Y., Zhou, B., Wang, D., Cartwright, A.N. and Swihart, M.T. (2013), “Formation of IV–VI alloy nanocrystals for application in solution- processed optoelectronic devices: the case of Pb_{1-x}Sn_xS”, *Chemistry of Materials*, Vol. 25, pp. 4409–4415.
- Liu, Z., Peng, S., Xie, Q., Hu, Z., Yang, Y., Zhang, S. and Qian, Y. (2003), “Large-scale synthesis of ultralong Bi₂S₃ nanoribbons via a solvothermal process”, *Advanced Materials*, Vol. 15 No. 11, pp. 936–940.

- Ma, D.-W. and Cheng, C. (2013), “Crystallization behaviors of PbSe quantum dots in silicate glasses”, edited by Pinckney, L. *Journal of the American Ceramic Society*, Vol. 96 No. 5, pp. 1428–1435.
- Ma, W., Luther, J.M., Zheng, H., Wu, Y. and Alivisatos, A.P. (2009), “Photovoltaic devices employing ternary $\text{PbS}_x\text{Se}_{1-x}$ nanocrystals”, *Nano Letters*, Vol. 9 No. 4, pp. 1699–1703.
- Ma, W., Swisher, S.L., Ewers, T., Engel, J., Ferry, V.E., Atwater, H.A. and Alivisatos, A.P. (2011), “Photovoltaic performance of ultrasmall PbSe quantum dots”, *ASC Nano*, Vol. 5 No. 10, pp. 8140–8147.
- Ma, Y., Qi, L., Ma, J. and Cheng, H. (2004), “Hierarchical, star-shaped PbS crystals formed by a simple solution route”, *Crystal Growth and Design*, Vol. 4 No. 2, pp. 351–354.
- Maji, S.K., Dutta, A.K., Dutta, S., Srivastava, D.N., Paul, P., Mondal, A. and Adhikary, B. (2012), “Single-source precursor approach for the preparation of CdS nanoparticles and their photocatalytic and intrinsic peroxidase like activity”, *Applied Catalysis B: Environmental*, Vol. 126, pp. 265–274.
- Maji, S.K., Dutta, A.K., Srivastava, D.N., Paul, P., Mondal, A. and Adhikary, B. (2011), “Effective photocatalytic degradation of organic pollutant by ZnS nanocrystals synthesized *via* thermal decomposition of single-source precursor”, *Polyhedron*, Vol. 30 No. 15, pp. 2493–2498.
- Malik, M.A., Afzaal, M. and O’Brien, P. (2010), “Precursor chemistry for main group elements in semiconducting materials”, *Chemical Reviews*, Vol. 110 No. 7, pp. 4417–4446.
- Malik, M.A. and O’Brien, P. (2005), “Precursors Basic Chemistry of CVD and ALD Precursors”, *Basic Chemistry of CVD and ALD Precursors*, pp. 207–271.
- Maneeprakorn, W., Nguyen, C.Q., Malik, M.A., O’Brien, P. and Raftery, J. (2009), “Synthesis of the nickel selenophosphinates $[\text{Ni}(\text{Se}_2\text{PR}_2)_2]$ (R = ⁱPr, ^tBu and Ph) and their use as single source precursors for the deposition of nickel phosphide or nickel selenide nanoparticles”, *Dalton Transactions*, pp. 2103–2108.
- Mangrola, M.H., Pillai, A.S., Parmar, B.H. and Joshi, V.G. (2013), “Electrical property of transparent thin films TiO_2 and Sr-doped TiO_2 developed by spin coating”, *Advanced Materials Research*, Vol. 665, pp. 263–266.
- Manning, T.D. and Parkin, I.P. (2004), “Atmospheric pressure chemical vapour deposition of tungsten doped vanadium (IV) oxide from VOCl_3 , water and WCl_6 ”, *Journal of Materials Chemistry*, Vol. 14, pp. 2554–2559.
- Marimuthu, G., Ramalingam, K., Rizzoli, C. and Arivanandhan, M. (2012), “Solvothelmal preparation of nano- β -HgS from a precursor, *bis*(dibenzylthiocarbamate)mercury(II)”, *Journal of Nanoparticle Research*, Vol. 14 No. 2, doi.org/10.1007/s11051-011-0710-7.
- Maspero, A., Kani, I., Mohamed, A.A., Omary, M.A., Staples, R.J. and Fackler, J.P. (2003), “Syntheses and structures of dinuclear gold (I) dithiophosphonate complexes and the reaction of the dithiophosphonate complexes with phosphines: diverse coordination types”, *Inorganic Chemistry*, Vol. 42 No. 17, pp. 209–211.

- Mauk, M., Sims, P., Rand, J. and Barnett, A. (2013), *Thin Silicon Solar Cells*. pp. 1-100.
- McIntyre, A. and Brush, L.N. (2010), "Spin-coating of vertically stratified thin liquid films", *Journal of Fluid Mechanics*, Vol. 647, pp. 265–285.
- McNaughter, P.D., Saah, S.A., Akhtar, M., Abdulwahab, K., Malik, M.A., Raftery, J., Awudza, J.A.M. and O'Brien, P. (2016), "The effect of alkyl chain length on the structure of lead(II) xanthates and their decomposition to PbS in melt reactions", *Dalton Transactions*, Vol. 45, pp. 16345–16353.
- Mehmood, S.K., Zaman, S., Ahmed, K. and Asim, M.M. (2010), "Structural and texture studies of PbS thin film", *Key Engineering Materials*, Vol. 442, pp. 123–129.
- Meng, L., Zhao, F., Zhang, J., Luo, R., Chen, A., Sun, L. and Bai, S. (2014), "Preparation of monodispersed PbS quantum dots on nanoporous semiconductor thin film by two-phase method", *Journal of Alloys and Compounds*, Vol. 595, pp. 51–54.
- Merino-Montiel, P., Maza, S., Martos, S., López, Ó., Maya, I. and Fernández-bolaños, J.G. (2013), "Synthesis and antioxidant activity of O -alkyl selenocarbamates, selenoureas and selenohydantoins", *European Journal of Pharmaceutical Sciences*, Vol. 48, pp. 582–592.
- Midgett, A.G., Luther, J.M., Stewart, J.T., Smith, D.K., Padilha, L.A., Klimov, V.I. and Nozik, A.J. (2013), "Size and composition dependent multiple exciton generation efficiency in PbS, PbSe, and PbSSe", *Nano Letters*, Vol. 13, p. 3078–3085.
- Mirkovic, T., Hines, M.A., Nair, P.S. and Scholes, G.D. (2005), "Single-source precursor route for the synthesis of EuS nanocrystals", *Chemistry of Materials*, Vol. 17, pp. 3451–3456.
- Mitzi, D.B., Kosbar, L.L., Murray, C.E., Copel, M. and Afzali, A. (2004), "High-mobility ultrathin semiconducting films prepared by spin coating", *Nature Letters*, Vol. 428, pp. 299–303.
- Miyazaki, Y., Okamoto, K., Kousuke, T. and Ogin, K. (2013), "Fabrication of ordered poly[1,6-bis(3-nonyl-9-carbazolyl)-2,4-hexadiyne] thin film *via* simple spin-coating process", *Chemical Letters*, Vol. 42, pp. 1217–1219.
- Mlowe, S., Nejo, A.A., Pullabhotla, V.S.R.R., Mubofu, E.B., Ngassapa, F.N., O'Brien, P. and Revaprasadu, N. (2013), "Lead chalcogenides stabilized by anacardic acid", *Materials Science in Semiconductor Processing*, Vol. 16 No. 2, pp. 263–268.
- Mlowe, S., Nyamen, L.D., Ndifon, P.T., Malik, M.A., Raftery, J., O'Brien, P. and Revaprasadu, N. (2015), "Aerosol assisted chemical vapor deposition (AACVD) of CdS thin films from heterocyclic cadmium(II) complexes", *Inorganica Chimica Acta*, Vol. 434, pp. 181–187.
- Monshi, A., Foughi, M.R. and Monshi, M.R. (2012), "Modified Scherrer equation to estimate more accurately nano-crystallite size using XRD", *World Journal of Nano Science and Engineering*, Vol. 2, pp. 154–160.
- Moreno-García, H., Nair, M.T.S. and Nair, P.K. (2011), "Chemically deposited lead sulfide and bismuth sulfide thin films and Bi₂S₃/PbS solar cells", *Thin Solid Films*, Vol. 519, pp. 2287–2295.
- Morey, M.S., Grano, S.R. and Ralston, J. (1999), "Pyrite consumption of xanthate in hellyer base metal sulfide pulps", *Minerals Engineering*, Vol. 12 No. 9, pp. 1021–1032.

- Mozafari, M., Moztarzadeh, F., Vashae, D. and Tayebi, L. (2012), "Effects of heat treatment on physical, microstructural and optical characteristics of PbS luminescent nanocrystals", *Physica E: Low-Dimensional Systems and Nanostructures*, Vol. 44, pp. 1429–1435.
- Mthombeni, N.H., Mpenyana-monyatsi, L., Onyango, M.S. and Momba, M.N.B. (2012), "Breakthrough analysis for water disinfection using silver nanoparticles coated resin beads in fixed-bed column", *Journal of Hazardous Materials*, Vol. 217, pp. 133–140.
- Mulik, R.N., Pawar, S.G., More, P.D., Pawar, S.A., Patil, V.B., Shivaji, S. and Barshi, M. (2010), "Nanocrystalline PbS thin films: synthesis, microstructural and optoelectronic properties", Vol. 2 No. 4, pp. 1–6.
- Murphy, J.E., Beard, M.C., Norman, A.G., Ahrenkiel, S.P., Johnson, J.C., Yu, P. and Mic, O.I. (2006), "PbTe colloidal nanocrystals: synthesis, characterization and multiple exciton generation", *Journal of the American Chemical Society*, Vol. 128 No. 10, pp. 865–871.
- Murray, C.B., Noms, D.J. and Bawendi, M.G. (1993), "Synthesis and characterization of nearly monodisperse CdE (E = S, Se, Te) semiconductor nanocrystallites", *Journal of the American Chemical Society*, Vol. 115, pp. 8706–8715.
- Mustafa, S., Hamid, A. and Naeem, A. (2004), "Temperature effect on xanthate sorption by chalcopyrite", *Journal of Colloid and Interface Science*, Vol. 275 No. 2, pp. 368–375.
- Nabi, Z., Abbar, B., Mecabih, S., Khalfi, A. and Amrane, N. (2000), "Pressure dependence of band gaps in PbS, PbSe and PbTe", *Computational Materials Science*, Vol. 18, pp. 127–131.
- Nahar, M.K., Zakaria, Z. and Bari, M.F. (2015), "Green synthesis of silver nanoparticles using *Momordica charantia* fruit extracts", *Advanced Materials Research*, Vol. 1109, pp. 35–39.
- Nair, P.S., Radhakrishnan, T., Revaprasadu, N., Kolawole, G. and O'Brien, P. (2002), "Cadmium ethylxanthate: A novel single-source precursor for the preparation of CdS nanoparticles", *Journal of Materials Chemistry*, Vol. 12 No. 9, pp. 2722–2725.
- Nam, M., Kim, S., Kang, M., Kim, S.-W. and Lee, K.-K. (2012), "Efficiency enhancement in organic solar cells by configuring hybrid interfaces with narrow bandgap PbSSe nanocrystals", *Organic Electronics*, Vol. 13, pp. 1546–1552.
- Ndzebet, E., Schuhmann, D. and Vanel, P. (1994), "Study of the impedance of a galena electrode under conditions similar to those used in sulphide mineral flotation: electrode oxidation and xanthate adsorption", *Pergamon*, Vol. 39 No. 5, pp. 745–753.
- Nedjar, Z. and Barkat, D. (2012), "Characterization of galena surfaces and potassium isoamyl xanthate (KIAX) synthesized adsorption", *Journal of Iran Chemistry Society*, Vol. 9, pp. 709–714.
- Nguyen, B.P., Kim, T. and Park, C.R. (2014), "Nanocomposite-based bulk heterojunction hybrid solar cells", *Journal of Nanomaterials*, Vol. 2014, pp. 1–21.
- Nguyen, C.Q., Afzaal, M., Malik, M.A., Helliwell, M., Raftery, J. and O'Brien, P. (2007), "Novel inorganic rings and materials deposition", *Journal of Organometallic Chemistry*, Vol. 692, pp. 2669–2677.

- Nomoev, A. V., Bardakhanov, S.P., Schreiber, M., Baldanov, B.B. and Romanov, N.A. (2015), "Synthesis, characterization, and mechanism of formation of Janus-like nanoparticles of tantalum silicide-silicon (TaSi₂/Si)", *Nanomaterials*, Vol. 5, pp. 26–35.
- Nowack, B. (2008), "Pollution prevention and treatment using nanotechnology", *Nanotechnology: Environmental Aspects*, Vol. 2, pp. 1–16.
- Nur, A.M., Muhammad, A.A. and Mahmood, M.R. (2012), "Effect of the precursor solution concentration of CuI thin film deposited by spin coating method", *Advanced Materials Research*, Vol. 364, pp. 417–421.
- Nyamen, D.L., Revaprasadu, N. and Ndifon, T.P. (2014), "Low temperature synthesis of PbS and CdS nanoparticles in olive oil", *Materials Science in Semiconductor Processing*, Vol. 27, pp. 191–196.
- Nyamen, L.D., Pullabhotla, V.S.R., Nejo, A.A., Ndifon, P. and Revaprasadu, N. (2011), "Heterocyclic dithiocarbamates: precursors for shape controlled growth of CdS nanoparticles", *New Journal of Chemistry*, Vol. 35, pp. 1133–1139.
- Nyamen, L.D., Pullabhotla, V.S.R.R., Nejo, A.A., Ndifon, P.T., Warner, J.H. and Revaprasadu, N. (2012), "Synthesis of anisotropic PbS nanoparticles using heterocyclic dithiocarbamate complexes", *Dalton Transactions*, Vol. 41, pp. 8297–8302.
- O'Brien, P., Malik, M.A. and Revaprasadu, N. (2005), "Precursor routes to semiconductor quantum dots", *Taylor and Francis*, Vol. 180, pp. 689–712.
- O'Neill, S.A., Parkin, I.P., Clark, R.J.H., Mills, A. and Elliott, N. (2003), "Atmospheric pressure chemical vapour deposition of titanium dioxide coatings on glass", *Journal of Materials Chemistry*, Vol. 13, p. 56–60.
- Obaid, A.S., Mahdi, M.A., Hassan, Z. and Bououdina, M. (2012), "Characterization of nanocrystalline PbS thin films prepared using microwave-assisted chemical bath deposition", *Materials Science in Semiconductor Processing*, Vol. 15 No. 5, pp. 564–571.
- Obaid, A.S., Mahdi, M. A., Hassan, Z. and Bououdina, M. (2013), "PbS nanocrystal solar cells fabricated using microwave-assisted chemical bath deposition", *International Journal of Hydrogen Energy*, Vol. 38 No. 2, pp. 807–815.
- Oener, S.Z., Groep, J.V.D., Macco, B., Bronsveld, P.C.P., Kessels, W.M.M., Polman, A. and Garnett, E.C. (2016), "Metal–insulator–semiconductor nanowire network solar cells", *Nano Letters*, Vol. 16, pp. 3689–3695.
- Oftadeh, M., Aghtar, A., Esfahani, M.N., Salavati-Niasari, M. and Mir, N. (2012), "Fabrication of highly efficient dye-sensitized solar cell and CO₂ reduction photocatalyst using TiO₂ nanoparticles prepared by spin coating-assisted sol–gel method", *Journal of Iran Chemistry Society*, Vol. 9, pp. 143–149.
- Ogi, T., Modesto-lopez, L.B., Iskandar, F. and Okuyama, K. (2007), "Fabrication of a large area monolayer of silica particles on a sapphire substrate by a spin coating method", *Colloids and Surfaces A: Physicochemical and Engineering Aspects*, Vol. 297, pp. 71–78.
- Oh, S.J., Berry, N.E., Choi, J.-H., Gaulding, E.A., Paik, T., Hong, S.-H. and Murray, C.B. (2013), "Stoichiometric control of lead chalcogenide nanocrystal solids to enhance their

- electronic and optoelectronic device performance”, *ASC Nano*, Vol. 7 No. 3, pp. 2413–2421.
- Ohta, M., Chung, D.Y., Kunii, M. and Kanatzidis, M.G. (2014), “Low lattice thermal conductivity in $\text{Pb}_5\text{Bi}_6\text{Se}_{14}$, promising thermoelectric materials in the cannizzarite, lillianite, and galenobismuthite homologous series”, *Journal of Materials Chemistry A*, Vol. 2, pp. 20048–20058.
- Ohzeki, M., Fujii, S., Arai, Y., Yanagidate, T. and Yanagi, Y. (2014), “Performance improvement of flexible bulk heterojunction solar cells using PTB7:PC71BM by optimizing spin coating and drying processes”, *Japanese Journal of Applied Physics*, Vol. 53, pp. 1–6.
- Onicha, A.C., Petchsang, N., Kosel, T.H. and Kuno, M. (2012), “Controlled synthesis of compositionally tunable ternary $\text{PbSe}_x\text{S}_{1-x}$ as well as binary PbSe and PbS nanowires”, *Acs Nano*, Vol. 6 No. 3, pp. 2833–2843.
- Onwudiwe, D.C., Krüger, T.P.J. and Strydom, C.A. (2014), “Laser assisted solid state reaction for the synthesis of ZnS and CdS nanoparticles from metal xanthate”, *Materials Letters*, Vol. 116, pp. 154–159.
- Opoku, F., Asare-Donkor, N.K. and Adimado, A.A. (2015), “Quantum mechanical study of the kinetics, mechanisms and thermodynamics of the gas-phase decomposition of $\text{Pb}[(\text{iPr})_2\text{PSSe}]_2$ single-source precursor”, *Journal of Organometallic Chemistry*, Vol. 787, pp. 33–43.
- Oshero, A., Makai, J.P., Balazs, J., Horvath, Z.J., Gutman, N., Sa, A. and Golan, Y. (2010), “Tunability of the optical band edge in thin PbS films chemically deposited on GaAs(100)”, *Journal of Physics. Condensed Matter: An Institute of Physics Journal*, Vol. 22 No. 26, pp. 262002–262008.
- Otto, T.N. and Yu, D. (2013), “Positive temperature coefficient of resistance and bistable conduction in lead selenide quantum dot thin films”, *The Journal of Physical Chemistry C*, Vol. 117, p. 3713–3717.
- Padilha, L.A., Stewart, J.T., Sandberg, R.L., Bae, W.K., Koh, W.-K., Pietryga, M. and Klimov, V.I. (2013), “Aspect ratio dependence of auger recombination and carrier multiplication in PbSe nanorods”, *Nano Letters*, Vol. 13, pp. 1092–1099.
- Pan, J.H. and Lee, W.I. (2005), “Selective control of cubic and hexagonal mesophases for titania and silica thin films with spin-coating”, *New Journal of Chemistry*, Vol. 29, pp. 841–846.
- Pan, Z., Mora-Seró, I., Shen, Q., Zhang, H., Li, Y., Zhao, K. and Wang, J. (2014), “High efficiency ‘green’ quantum dot solar cells”, *Journal of the American Chemical Society*, Vol. 136, pp. 9203–9210.
- Pandey, O.P. (1988), “Chemistry and mechanism of thermal degradation reactions of zirconium(IV) alkyl xanthate complexes”, *Thermochimica Acta*, Vol. 127, pp. 193–199.
- Panneerselvam, A. and Green, M. (2013), “Recent advances in quantum dot synthesis”, *Nanoscience*, Vol. 1, pp. 208–243.

- Papagiorgis, P., Stavrinadis, A., Othonos, A., Konstantatos, G. and Itskos, G. (2017), “The influence of doping on the optoelectronic properties of PbS colloidal quantum dot solids”, *Scientific Reports*, Vol. 6, pp. 18735–18749.
- Park, J., Joo, J., Kwon, S.G., Jang, Y. and Hyeon, T. (2007), “Synthesis of monodisperse spherical nanocrystals”, *Angewandte Chemie*, Vol. 46, pp. 4630–4660.
- Patel, J.D., Mighri, F., Ajji, A. and Chaudhuri, T.K. (2012), “Morphology and size control of lead sulphide nanoparticles produced using methanolic lead acetate trihydrate – thiourea complex *via* different precipitation techniques”, *Materials Chemistry and Physics*, Vol. 132, pp. 747–755.
- Patil, R.S., Lokhande, C.D., Mane, R.S., Gujar, T.P. and Han, S.-H. (2007), “Room temperature PbS nanoparticle growth, incubation in porous TiO₂ electrode for photosensitization application”, *Journal of Non-Crystalline Solids*, Vol. 353, pp. 1645–1649.
- Patla, I., Acharya, S., Zeiri, L., Israelachvili, J., Efrima, S. and Golan, Y. (2007), “Synthesis, two-dimensional assembly, and surface pressure-induced coalescence of ultranarrow PbS nanowires”, *Nano Letters*, Vol. 7 No. 6, pp. 1459–1462.
- Patra, B.K., Khilari, S., Bera, A., Mehetor, K., Pradhan, D. and Pradhan, N. (2017), “Chemically filled and Au-coupled BiSbS₃ nanorod heterostructures for photoelectrocatalysis”, *Chemistry of Materials*, doi:10.1021/acs.chemmater.6b04266.
- Pawar, A.S., Mlowe, S., Garje, S.S., Akerman, M.P. and Revaprasadu, N. (2017), “Zinc thiosemicarbazone complexes: single source precursors for alkylamine capped ZnS nanoparticles”, *Inorganic Chimica Acta*, doi:10.1016/j.ica.2017.04.009.
- Pawar, S.B., Shaikh, J.S., Devan, R.S., Ma, Y.R., Haranath, D., Bhosale, P.N. and Patil, P.S. (2011), “Facile and low cost chemosynthesis of nanostructured PbS with tunable optical properties”, *Applied Surface Science*, Vol. 258 No. 5, pp. 1869–1875.
- Pedras, M.S.C., Minic, Z. and Hossain, S. (2012), “Discovery of inhibitors and substrates of brassinin hydrolase: Probing selectivity with dithiocarbamate bioisosteres.”, *Bioorganic and Medicinal Chemistry*, Vol. 20, pp. 225–233.
- Pedruza, E., Segura, A., Abargues, R., Bailach, J.B., Chervin, J.C. and Mart, J.P. (2013), “The effect of quantum size confinement on the optical properties of PbSe nanocrystals as a function of temperature and hydrostatic pressure”, *Nanotechnology*, Vol. 24, pp. 205701–205709.
- Pei, Y.-L. and Liu, Y. (2012), “Electrical and thermal transport properties of Pb-based chalcogenides : PbTe, PbSe, and PbS”, *Journal of Alloys and Compounds*, Vol. 514, pp. 40–44.
- Pejova, B., Grozdanov, I., Nesheva, D. and Petrova, A. (2008), “Size-dependent properties of sonochemically synthesized three-dimensional arrays of close-packed semiconducting AgBiS₂ quantum dots”, *Chemistry of Materials*, Vol. 20 No. 8, pp. 2551–2565.
- Peng, Y. and Grano, S. (2010), “Effect of grinding media on the activation of pyrite flotation”, *Minerals Engineering*, Vol. 23 No. 8, pp. 600–605.

- Peng, Y., Wang, B. and Gerson, A. (2012), “The effect of electrochemical potential on the activation of pyrite by copper and lead ions during grinding”, *International Journal of Mineral Processing*, Vol. 102–103, pp. 141–149.
- Perex, J., Bax, L. and Escolano, C. (2005), *Roadmap Report on Nanoparticles*. pp 1-150.
- Pichumani, M., Bagheri, P., Poduska, K.M. and Yethiraj, A. (2013), “Dynamics, crystallization and structures in colloid spin coating”, *Soft Matter*, Vol. 9, pp. 3220–3229.
- Pimanpang, S., Towannang, M., Thiangkaew, A., Maiaugree, W., Uppachai, P., Jareerboon, W. and Amornkitbamrung, V. (2014), “A flexible plastic-stainless steel dye-sensitized solar cell based on organic T-/T₂ electrolyte”, *International Journal of Energy Research*, Vol. 38, pp. 429–435.
- Pitchaimani, P., Mun, K. and Elango, K.P. (2015), “Synthesis, crystal structures, luminescence properties and catalytic application of lanthanide(III) piperidine dithiocarbamate complexes”, *Polyhedron*, Vol. 93, pp. 8–16.
- Plescia, P. (1993), “Study of galena/potassium ethyl xanthate system by X-ray diffractometry and scanning electron microscopy”, *Applied Surface Science*, Vol. 72, pp. 249–257.
- Porento, M. and Hirva, P. (2003), “The adsorption interaction of anionic sulfhydryl collectors on different PbS (100) surface sites”, *Surface Science*, Vol. 539, pp. 137–144.
- Portillo, M.C., Mathew, X., Juárez, H.S., Castillo, M.P., Santiago, A.C. and Moreno, O.P. (2017), “Influence of Li doping on the optical properties of PbS”, *Superlattices and Microstructures*, doi: 10.1016/j.spmi.2017.05.029.
- Pradhan, N., Katz, B. and Efrima, S. (2003), “Synthesis of high-quality metal sulfide nanoparticles from alkyl xanthate single precursors in alkylamine solvents”, *The Journal of Physical Chemistry B*, Vol. 107, pp. 13843–13854.
- Prastani, C., Nanu, M., Nanu, D.E., Rath, J.K. and Schropp, R.E.I. (2013), “Synthesis and conductivity mapping of SnS quantum dots for photovoltaic applications”, *Materials Science and Engineering B*, Vol. 178 No. 9, pp. 656–659.
- Preetha, K.C. and Remadevi, T.L. (2013), “Optimization of PbS thin films using different metal ion sources for photovoltaic applications”, *Journal of Materials Science: Materials in Electronics*, Vol. 24, pp. 489–498.
- Preetha, K.C. and Remadevi, T.L. (2014), “Band gap engineering in PbSe thin films from nearinfrared to visible region by photochemical deposition method”, *Journal of Materials Science: Materials in Electronics*, Vol. 25, pp. 1783–1791.
- Pring, A. and Etschmann, B. (2002), “HRTEM observations of structural and chemical modulations in cosalite and its relationship to the lillianite homologues”, *Mineralogical Magazine*, Vol. 66 No. 3, pp. 451–458.
- Puiso, J., Lindroos, S., Tamulevicius, S., Leskela, M. and Snitka, V. (2003), “Growth of ultra thin PbS films by SILAR technique”, *Thin Solid Films*, Vol. 428, pp. 223–226.
- Puiso, J., Tamulevicius, S., Laukaitis, G., Lindroos, S., Leskela, M. and Snitka, V. (2002), “Growth of PbS thin films on silicon substrate by SILAR technique”, *Thin Solid Films*, Vol. 404, pp. 457–461.

- Qiu, W., Xu, M., Chen, F., Yang, X., Nan, Y. and Chen, H. (2011), "Morphology evolution route of PbS crystals via environment-friendly electrochemical deposition", *CrystEngComm*, Vol. 13 No. 14, pp. 4689–4694.
- Qiu, X., Zhao, Y., Steward, I.M., Dyck, J.S., Burda, C. and Dyck, S. (2010), "Improvement of the thermoelectric power factor through anisotropic growth of nanostructured PbSe thin films", *Dalton Transactions*, Vol. 39, pp. 1095–1100.
- Queiroz, M.L.S., Fernandes, M.D. and Valadares, M.C. (1999), "Neutrophil function in workers exposed to organophosphate and carbamate insecticides", *International Journal of Immunopharmacology*, Vol. 21, pp. 263–270.
- Rafea, M.A. and Roushdy, N. (2010), "Study of optical properties of nanostructured PbS films", *Philosophical Magazine Letters*, Vol. 90 No. 2, pp. 113–120.
- Rajashree, C. and Balu, A.R. (2016), "Tuning the physical properties of PbS thin films towards optoelectronic applications through Ni doping", *Optik*, Vol. 127, pp. 8892–8898.
- Rajashree, C., Balu, A.R. and Nagarethinam, V.S. (2016), "Enhancement in the physical properties of spray deposited nanostructured ternary PbMgS thin films towards optoelectronic applications", *Journal of Materials Science: Materials in Electronics*, doi:10.1007/s10854-016-4396-6.
- Raju, K.M. and Srivastava, R.K. (2010), "Acoustical investigation of lead chalcogenides", *Physica B: Condensed Matter*, Vol. 405, pp. 4855–4857.
- Ramasamy, K., Malik, M.A., O'Brien, P. and Raftery, J. (2010), "Metal complexes of thiobiurets and dithiobiurets: Novel single source precursors for metal sulfide thin film nanostructures", *Dalton Transactions*, Vol. 39, pp. 1460–1463.
- Ramasamy, K., Malik, M.A., Revaprasadu, N. and O'Brien, P. (2013), "Routes to nanostructured inorganic materials with potential for solar energy applications", *Chemistry of Materials*, Vol. 25 No. 18, pp. 3551–3569.
- Ramasamy, K., Nejo, O., Ziqubu, N., Rajasekhar, P.V.S.R., Nejo, A.A., Revaprasadu, N. and O'Brien, P. (2011), "A new route to lead chalcogenide nanocrystals", *European Journal of Inorganic Chemistry*, pp. 5196–5201.
- Ramesh, P., Rajendran, A. and Meenakshisundaram, M. (2014), "Green synthesis of zinc oxide nanoparticles using flower extract *Cassia auriculata*", *Journal of NanoScience and NanoTechnology*, Vol. 2 No. 1, pp. 41–45.
- Raniero, L., Ferreira, C.L., Cruz, L.R., Pinto, A.L. and Alves, R.M.P. (2010), "Photoconductivity activation in PbS thin films grown at room temperature by chemical bath deposition", *Physica B: Condensed Matter*, Vol. 405 No. 5, pp. 1283–1286.
- Rao, C.N.R. and Kalyanikutty, K.P. (2007), "The liquid–liquid interface as a medium to generate nanocrystalline films of inorganic materials", *Accounts of Chemical Research*, Vol. 41 No. 4, pp. 489–499.
- Rao, C.N.R., Vivekchand, S.R.C., Biswas, K. and Govindaraj, A. (2007), "Synthesis of inorganic nanomaterials", *Dalton Transactions*, pp. 3728–3749.

- Rastogi, R.B., Yadav, M. and Singh, K. (2001), "Synthesis and characterization of molybdenum and tungsten complexes of 1-aryl-2,4-dithiobiurets", *Synthesis and Reactivity in Inorganic and Metal-Organic Chemistry*, Vol. 31 No. 6, pp. 1011–1022.
- Rath, T., Maclachlan, A.J., Brown, M.D. and Haque, S.A. (2015), "Structural, optical and charge generation antimony sulfide thin films prepared from metal xanthates", *Journal of Materials Chemistry A*, Vol. 3, pp. 24155–24162.
- Reiss, P. (2008), "Synthesis of semiconductor nanocrystals in organic solvents", *Semiconductor Nanocrystal Quantum Dots*, pp. 35–72.
- Remadevi, T.L. and Preetha, K.C. (2012), "Comparative studies on structural, optoelectronic and electrical properties of SILAR grown PbS thin films from acidic, neutral and alkaline cationic reaction bath", *Journal of Materials Science: Materials in Electronics*, Vol. 23 No. 11, pp. 2017–2023.
- Rimal, G., Pimachev, A.K., Yost, A.J., Poudyal, U., Maloney, S., Wang, W. and Chien, T. (2016), "Giant photocurrent enhancement by transition metal doping in quantum dot sensitized solar cells", *Applied Physics Letters*, Vol. 109, pp. 103901–103906.
- Ritch, J.S., Chivers, T., Ahmad, K., Afzaal, M. and O'Brien, P. (2010), "Synthesis, structures, and multinuclear NMR spectra of tin(II) and lead(II) complexes of tellurium-containing imidodiphosphinate ligands: preparation of two morphologies of phase-pure PbTe from a single-source precursor", *Inorganic Chemistry*, Vol. 49 No. 3, pp. 1198–205.
- Rojas-Chávez, H., Reyes-Carmona, F., Achimovičová, M., Daneu, N. and Jaramillo-Vigueras, D. (2012), "PbSe nanocubes obtained by high-energy milling", *Journal of Nanoparticle Research*, Vol. 14 No. 6, pp. 897–903.
- Romano, B., Plano, D., Encío, I., Antonio, J. and Sanmartín, C. (2015), "In vitro radical scavenging and cytotoxic activities of novel hybrid selenocarbamates", *Bioorganic and Medicinal Chemistry*, Vol. 23 No. 8, pp. 1716–1727.
- Rosmani, C.H., Abdullah, S. and Rusop, M. (2013), "CdSe thin film by using spin-coating", *Advanced Materials Research*, Vol. 626, pp. 401–403.
- Sadovnikov, S.I. and Gusev, A.I. (2013), "Structure and properties of PbS films", *Journal of Alloys and Compounds*, Vol. 573, pp. 65–75.
- Safrani, T. and Golan, Y. (2015), "Compositional tunability in solid solution $\text{PbS}_x\text{Se}_{1-x}$ thin films chemically deposited on GaAs(100)", *CrystEngComm*, No. 17, pp. 3433–3439.
- Sagadevan, S., Pal, K., Hoque, E. and Zaman, Z. (2017), "A chemical synthesized Al-doped PbS nanoparticles hybrid composite for optical and electrical response", *Journal of Materials Science: Materials in Electronics*, doi:10.1007/s10854-017-6869-7 A.
- Saha, S.K., Bera, A. and Pal, A.J. (2015), "Improvement in PbS-based hybrid bulkheterojunction solar cells through band alignment via bismuth doping in the nanocrystals", *Applied Materials and Interfaces*, Vol. 7 No. 16, pp. 8886–8893.
- Saha, S.K. and Pal, A.J. (2015), "Schottky diodes between Bi_2S_3 nanorods and metal nanoparticles in a polymer matrix as hybrid bulk-heterojunction solar cells", *Journal of Applied Physics*, Vol. 118, pp. 1450300–1450310.

- Salavati-Niasari, M., Sobhani, A. and Davar, F. (2010), "Synthesis of star-shaped PbS nanocrystals using single-source precursor", *Journal of Alloys and Compounds*, Elsevier B.V., Vol. 507 No. 1, pp. 77–83.
- Sambandan, K., Nagabalasubramanian, P.B. and Vijayalakshmi, S. (2015), "Green synthesis of silver nanoparticles using leaf extracts of common weeds: a case study from *Lantana camera L.* and *Leucas aspera* (wild) link", *International Journal of Advanced Trends in Computer Science and Engineering*, Vol. 2 No. 1, pp. 12–21.
- Sartale, S.D. and Ansari, A.A. (2013), "Growth of Ag nanoparticles by spin coating", *Journal of Nano Research*, Vol. 24, pp. 163–167.
- Sashchiuk, A., Amirav, L., Bashouti, M., Krueger, M., Sivan, U. and Lifshitz, E. (2004), "PbSe nanocrystal assemblies: synthesis and structural, optical, and electrical characterization", *Nano Letters*, Vol. 4 No. 1, pp. 159–165.
- Sayed-Sweet, Y., Hedstrand, D.M., Spinder, R. and Tomalia, D.A. (1997), "Hydrophobically modified poly (amidoamine) (PAMAM) dendrimers : their properties at the air – water interface and use as nanoscopic container molecules", *Journal of Materials Chemistry*, Vol. 7 No. 7, pp. 1199–1205.
- Scarongella, M., Paraecattil, A.A., Douglas, J.D., Heeney, M., Leclerc, M., Stingelin, N. and Banerji, N. (2014), "The influence of microstructure on charge separation dynamics in organic bulk heterojunction materials for solar cell applications", *Journal of Materials Chemistry A*, Vol. 2, pp. 6218–6230.
- Scheele, M., Oeschler, N., Veremchuk, I., Peters, S.-O., Littig, A., Kornowski, A., Klinke, C., et al. (2011), "Thermoelectric properties of lead chalcogenide core-shell nanostructures", *Ascnano*, Vol. 5 No. 11, pp. 8541–8551.
- Shankaranarayana, M.L. and Patel, C.C. (1961), "Infrared spectra and the structures of xanthates and dixanthogens", *Canadian Journal of Chemistry*, Vol. 39, pp. 1633–1637.
- Shao, G., Chen, G., Zuo, J., Gong, M. and Yang, Q. (2014), "Organometallic synthesis, structure determination, shape evolution, and formation mechanism of hexapod-like ternary $\text{PbSe}_x\text{S}_{1-x}$ nanostructures with tunable compositions", *Langmuir*, Vol. 30 No. 26, pp. 7811–7822.
- Sharma, A.K. (1986), "Thermal behaviour of metal-dithiocarbamates", *Thermochimica Acta*, Vol. 104, pp. 339–372.
- Shavel, A., Ibáñez, M., Luo, Z., De Roo, J., Carrete, A., Dimitrievska, M. and Genç, A., (2016), "Scalable heating-up synthesis of monodisperse $\text{Cu}_2\text{ZnSnS}_4$ nanocrystals", *Chemistry of Materials*, Vol. 28 No. 3, pp. 720–726.
- Shchennikov, V. V., Ovsyannikov, S. V. and Derevskov, A.Y. (2002), "Thermopower of lead chalcogenides at high pressures", *Semiconductors and Dielectrics*, Vol. 44 No. 10, pp. 1845–1849.
- Shi, M., Su, W. and Matsui, H. (2010), "PbSe nanocrystal growth as nanocubes and nanorods on peptide nanotubes via different directed-assembly pathways.", *Nanoscale*, Vol. 2 No. 11, pp. 2373–2376.

- Shyju, T.S., Anandhi, S., Sivakumar, R., Garg, S.K. and Gopalakrishnan, R. (2012), "Investigation on structural, optical, morphological and electrical properties of thermally deposited lead selenide (PbSe) nanocrystalline thin films", *Journal of Crystal Growth*, Vol. 353, pp. 47–54.
- Siddiqui, F.Y., Shaikh, S.U., Desale, D.J., Upadhye, D.S., Mahajan, S. V., Ghule, A. V. and Varshney, P. (2014), "Band gap engineering by substitution of S by Se in nanostructured CdS_{1-x}Se_x thin films grown by soft chemical route for photosensor application", *Materials Science in Semiconductor Processing*, Vol. 27, pp. 404–411.
- Sigman, M.B. and Korgel, B.A. (2005), "Solventless synthesis of Bi₂S₃ (bismuthinite) nanorods, nanowires and nanofabric", *Chemistry of Materials*, Vol. 17, pp. 1655–1660.
- Silvestru, C. and Drake, J.E. (2001), "Tetraorganodichalcogenoimidodiphosphorus acids and their main group metal derivatives", *Coordination Chemistry Reviews*, Vol. 223, pp. 117–216.
- Singh, R. and Green, M.A. (1981), "Review of conductor-insulator-semiconductor (cis) solar cells", *Solar Cells*, Vol. 3, pp. 95–148.
- Sliem, M. A., Chemseddine, A., Bloeck, U. and Fischer, R. A. (2011), "PbSe nanocrystal shape development: oriented attachment at mild conditions and microwave assisted growth of nanocubes", *CrystEngComm*, Vol. 13 No. 2, p. 483-490.
- Smith, D.K., Luther, J.M., Semonin, O.E., Nozik, A.J. and Beard, M.C. (2011), "Tuning the synthesis of ternary lead chalcogenide quantum dots by balancing precursor reactivity", *ACS Nano*, Vol. 5 No. 1, pp. 183–190.
- Song, H., Zhan, X., Li, D., Zhou, Y., Yang, B., Zeng, K. and Zhong, J. (2016), "Rapid thermal evaporation of Bi₂S₃ layer for thin film photovoltaics", *Solar Energy Materials and Solar Cells*, Vol. 146, pp. 1–7.
- Song, T., Cheng, H., Fu, C., He, B. and Li, W. (2016), "Influence of the active layer nanomorphology on device performance for ternary PbS_xSe_{1-x} quantum dots based solution-processed infrared photodetector", *Nanotechnology*, Vol. 27, pp. 165202–165210.
- Sridharan, K., Tamilselvan, V., Yuvaraj, D., Rao, K.N. and Philip, R. (2012), "Synthesis and nonlinear optical properties of Lead telluride nanorods", *Optical Materials*, Vol. 34 No. 4, pp. 639–645.
- Srivastav, A.K., Chawake, N. and Murty, B.S. (2015), "Grain-size-dependent non-monotonic lattice parameter variation in nanocrystalline W: The role of non-equilibrium grain boundary structure", *Scripta Materialia*, Vol. 98, pp. 20–23.
- Stansfield, G.L., Vanitha, P. V., Johnston, H.M., Fan, D., Alqahtani, H., Hague, L. and Grell, M. (2010), "Growth of nanocrystals and thin films at the water–oil interface", *Philosophical Transactions*, Vol. 368, pp. 4313–4330.
- Stavriniadis, A., Pradhan, S., Papagiorgis, P., Itkos, G. and Konstantatos, G. (2017), "Suppressing deep traps in PbS colloidal quantum dots via facile iodide substitutional doping for solar cells with efficiency >10%", *ACS Energy Letters*, doi:10.1021/acseenergylett.7b00091.

- Stavrinadis, A., Rath, A.K., García De Arquer, F.P., Diedenhofen, S.L., Magén, C., Martinez, L. and So, D. (2013), “Heterovalent cation substitutional doping for quantum dot homojunction solar cells”, *Nature Communications*, Vol. 4, pp. 1–9.
- Su, H., Xie, Y., Gao, P., Xiong, Y. and Qian, Y. (2001), “Synthesis of MS/TiO₂ (M =Pb, Zn, Cd) nanocomposites through a mild sol-gel process”, *Journal of Materials Chemistry*, Vol. 11, pp. 684–684.
- Suganya, M., Prabha, D., Balamurugan, S. and Balu, A.R. (2016), “Studies on the spectroscopic, photoconductive properties and antifungal activities of Al-doped PbS nanopowders synthesized by a simple soft chemical route”, *Journal of Materials Science: Materials in Electronics*, No. 1–8, doi.org/10.1007/s10854-016-6193-7.
- Sun, J. and Buhro, W.E. (2008), “The Use of single-source precursors for the solution – liquid – solid growth of metal sulfide semiconductor nanowires”, *Angewandte Chemie*, Vol. 120, pp. 3259–3262.
- Takahashi, H., Nishina, A., Fukumoto, R.-H., Kimura, H., Koketsu, M. and Ishihara, H. (2005), “Selenocarbamates are effective superoxide anion scavengers in vitro”, *European Journal of Pharmaceutical Sciences*, Vol. 24, pp. 291–295.
- Tan, G.-L., Liu, L. and Wu, W. (2014), “Mid-IR band gap engineering of Cd_xPb_{1-x}S nanocrystals by mechanochemical reaction”, *AIP Advances*, Vol. 4, pp. 67107–67110.
- Tan, Z., Zhang, W., Qian, D., Zheng, H., Xiao, S., Yang, Y. and Zhu, T. (2011), “Efficient hybrid infrared solar cells based on P3HT and PbSe nanocrystal quantum dots”, *Materials Science Forum*, Vol. 685, pp. 38–43.
- Tani, K., Ito, C., Hanawa, Y., Uchida, M., Otaguro, K., Horiuchi, H. and Hiratsuka, H. (2008), “Photophysical property and photostability of J-aggregate thin films of thiocyanine dyes prepared by the spin-coating method”, *Journal of Physical Chemistry B*, Vol. 112, pp. 836–844.
- Thanh, N.T.K., Maclean, N. and Mahiddine, S. (2014), “Mechanisms of nucleation and growth of nanoparticles in solution”, *Chemical Reviews*, Vol. 114, p. 7610–7630.
- Thomas, P.J., Mbufub, E. and O’Brien, P. (2013), “Thin films of metals, metal chalcogenides and oxides deposited at the water–oil interface using molecular precursors”, *Chemical Communications*, Vol. 49, pp. 118–127.
- Thomas, P.J., Stansfield, G.L., Komba, N., Cant, D.J.H., Ramasamy, K., Albrasi, E. and AlChaghouri, H. (2015), “Growth of nanocrystalline thin films of metal sulfides [CdS, ZnS, CuS and PbS] at the water–oil interface”, *RSC Advances*, Vol. 5, pp. 62291–62299.
- Thomson, J.W., Wang, X., Hoch, L., Faulkner, D., Petrov, S. and Ozin, G.A. (2012), “Discovery and evaluation of a single source selenium sulfide precursor for the synthesis of alloy PbS_xSe_{1-x} nanocrystals”, *Journal of Materials Chemistry*, Vol. 22, pp. 5984–5989.
- Thupakula, U., Jena, A., Khan, A.H., Dalui, A. and Acharya, S. (2012), “Synthesis, structure and electronic properties of ultranarrow CdS nanorods”, *Journal of Nanoparticle Research*, Vol. 14 No. 1, p. 701-706.

- Tian, L., Tan, H.Y. and Vittal, J.J. (2008), "Morphology-controlled synthesis of Bi₂S₃ nanomaterials via single- and multiple-source approaches", *Crystal Growth and Design*, Vol. 8 No. 2, pp. 734–738.
- Timonen, J.V.I., Seppälä, E.T., Ikkala, O. and Ras, R.H.A. (2011), "From hot-injection synthesis to heating-up synthesis of cobalt nanoparticles: observation of kinetically controllable nucleation.", *Angewandte Chemie*, Vol. 50, pp. 2080–2084.
- Todescato, F., Chesman, A.S.R., Martucci, A., Signorini, R. and Jasieniak, J.J. (2012), "Highly luminescent and temperature stable quantum dot thin films based on a ZnS composite", *Chemistry of Materials*, Vol. 24, pp. 2117–2126.
- Tominaka, S., Hamoudi, H., Suga, T., Bennett, T.D., Cairnsd, A.B. and Cheetham, A.K. (2015), "Topochemical conversion of a dense metal–an amorphous semiconductor", *Chemical Science*, Vol. 6, pp. 1465–1473.
- Toolan, D.T.W., Parnell, A.J., Topham, P.D. and Howse, J.R. (2013), "Directed phase separation of PFO : PS blends during spin-coating using feedback controlled in situ stroboscopic fluorescence microscopy", *Journal of Materials Chemistry A*, Vol. 2, pp. 3587–3592.
- Torres-Blancas, T., Roa-Morales, G., Fall, C., Barrera-Díaz, C., Ureña-Nuñez, F. and Pavón, T.B. (2013), "Improving lead sorption through chemical modification of de-oiled allspice husk by xanthate", *Fuel*, Vol. 110, pp. 4–11.
- Touati, B., Gassoumi, A., Dobryden, I., Maria, M., Vomiero, A. and Kamoun, N. (2016), "Engineering of electronic and optical properties of PbS thin films *via* Cu doping", *Superlattices and Microstructures*, Vol. 97, pp. 519–528.
- Trindade, T. and O'Brien, P. (1997), "Lead(II) dithiocarbamate complexes as precursors for the LP-MOCVD of lead sulfide", *Chemical Vapour Deposition*, Vol. 3 No. 2, pp. 75–77.
- Trindade, T., O'Brien, P. and Pickett, N.L. (2001), "Nanocrystalline semiconductors: synthesis, properties and perspectives", *Chemistry of Materials*, Vol. 13, pp. 3843–3858.
- Trujillo, C., Mo, O., Ya, M., Tortajada, J. and Salpin, J.-Y. (2008), "Selenourea - Ca²⁺ reactions in gas phase. Similarities and dissimilarities with urea and thiourea", *Journal of Physical Chemistry B*, Vol. 112, pp. 5479–5486.
- Turyanska, L., Moro, F., Patanè, A., Barr, J., Köckenberger, W., Williams, H.E.L. and Thomas, N.R. (2016), "Developing Mn-doped lead sulfide quantum dots for MRI labels", *Journal of Materials Chemistry B*, Vol. 4, pp. 6797–6802.
- Tussupbayev, S., Govind, N., Lopata, K. and Cramer, C.J. (2015), "Comparison of real-time and linear-response time-dependent density functional theories for molecular chromophores ranging from sparse to high densities of states", *Journal of Chemical Theory and Computation*, Vol. 11, pp. 1102–1109.
- Valenzuela-Jáuregui, J.J., Ramírez-Bon, R., Mendoza-Galván, A. and Sotelo-Lerma, M. (2003), "Optical properties of PbS thin films chemically deposited at different temperatures", *Thin Solid Films*, Vol. 441 No. 1–2, pp. 104–110.

- Vijayaprasath, G., Murugan, R., Mahalingam, T., Hayakawa, Y. and Ravi, G. (2015), "Preparation of highly oriented Al:ZnO and Cu/Al:ZnO thin films by sol-gel method and their characterization", *Journal of Alloys and Compounds*, Vol. 649, pp. 275–284.
- Wagner, P., Vanderzande, D. and Schepper, L.D.E. (2005), "Absorption phenomena in organic thin films for solar cell applications investigated by photothermal deflection spectroscopy", *Journal of Materials Science*, Vol. 40, pp. 1413–1418.
- Wang, C.-W., Liu, H.-G., Bai, X.-T., Xue, Q. and Chen, X. (2008), "Triangular PbS nanopyrramids, square nanoplates, and nanorods formed at the air", *Crystal Growth and Design*, Vol. 8 No. 8, pp. 2660–2664.
- Wang, D. and Möhwald, H. (2004), "Rapid fabrication of binary colloidal crystals by stepwise spin-coating", *Advanced Materials*, Vol. 16 No. 3, pp. 244–247.
- Wang, L.S. and Hong, R.Y. (2001), "Synthesis, surface modification and characterisation of nanoparticles". pp. 208-212.
- Wang, N., Cao, X., Guo, L., Yang, S. and Wu, Z. (2008), "Facile synthesis of PbS truncated octahedron crystals with high symmetry and their large-scale assembly into route", *ACS Nano*, Vol. 2 No. 2, pp. 184–190.
- Wang, P., Wang, A.-M., Zhang, Z., Fan, L., Lei, Y., Yang, M. and Zhang, Y. (2012), "A solar cell based on a hybrid film of P3HT and magic cubic-like PbS", *Advanced Materials Research*, Vol. 567, pp. 236–239.
- Wang, Y., Tang, A., Li, K., Yang, C., Wang, M., Ye, H. and Hou, Y. (2012), "Shape-controlled synthesis of PbS nanocrystals via a simple one-step process", *Langmuir*, Vol. 28, pp. 16436–16443.
- Wang, Z., Yang, X., Feng, D., Wu, H. and Carrete, J. (2017), "Understanding phonon scattering by nano-precipitates in potassium-doped lead chalcogenides", *ACS Applied Materials and Interfaces*, pp. 1–27.
- Warren, B. E. (1969), "X-ray diffraction.", ISBN 0-486-66317-3. New York.
- Williamson, G. K. and Hall, W. H. (1953), "X-ray line broadening from filed aluminium and wolfram." *Acta Metallurgica*, Vol. 1 No. 1, pp. 22-31.
- Williamson, G. K. and Smallman, R. E. (1956), "Dislocation densities in some annealed and cold-worked metals from measurement on the X-ray debye-scherrer spectrum." *Philosophical Magazine*, Vol. 1, pp. 34-36.
- Witt, E., Witt, F., Trautwein, N., Fenske, D., Neumann, J., Borchert, H. and Parisi, J. (2012), "Synthesis of lead chalcogenide nanocrystals and study of charge transfer in blends of PbSe nanocrystals and poly(3-hexylthiophene).", *Physical Chemistry Chemical Physics*, Vol. 14 No. 33, pp. 11706–11714.
- Woods, L. and Meyers, P. (2002), Atmospheric pressure chemical vapor deposition and jet vapor deposition of CdTe for high efficiency thin film PV devices, pp. 1-44.
- Wu, T., Zhou, X., Zhang, H. and Zhong, X. (2010), "Bi₂S₃ nanostructures: A new photocatalyst", *Nano Research*, Vol. 3, pp. 379–386.

- Xiong, K., Hou, L., Wu, M., Huo, Y., Mo, W. and Yuan, Y. (2015), “From spin coating to doctor blading: a systematic study on the photovoltaic performance of an isoindigo-based polymer”, *Solar Energy Materials and Solar Cells*, Vol. 132, pp. 252–259.
- Yanev, S.G., Kent, U.M., Roberts, E.S., Ballou, D.P. and Hollenberg, P.F. (2000), “Mechanistic studies of cytochrome P450 2B1 inactivation by xanthates”, *Archives of Biochemistry and Biophysics*, Vol. 378 No. 1, pp. 157–166.
- Yang, J., Chen, W., Yu, B., Wang, H. and Yan, D. (2012), “Organic tandem solar cell using active inter-connecting layer”, Vol. 13, pp. 1018–1022.
- Yang, J.L., An, S.J., Park, W.I., Yi, G.-C. and Choi, W. (2004), “Photocatalysis using ZnO thin films and nanoneedles grown by metal-organic chemical vapor deposition”, *Advanced Materials*, Vol. 16 No. 18, pp. 1661–1664.
- Yang, X., Tian, S., Li, R., Wang, W. and Zhou, S. (2017), “Use of single-crystalline Bi₂S₃ nanowires as room temperature ethanol sensor synthesized by hydrothermal approach”, *Sensors and Actuators B: Chemical*, Vol. 241, pp. 210–216.
- Yang, Y.A., Wu, H., Williams, K.R. and Cao, Y.C. (2005), “Synthesis of CdSe and CdTe nanocrystals without precursor injection”, *Angewandte Chemie*, Vol. 117, pp. 6870–6873.
- Yanover, D., Richard, K.C., Rubin-Brusilovski, A., Vaxenburg, R., Grumbach, N., Maikov, G.I. and Solomeshch, O. (2012), “Small-sized PbSe/PbS core/shell colloidal quantum dots”, *Chemistry of Materials*, Vol. 24, p. 4417–4423.
- Yogamalar, N.R., Srinivasan, R. and Bose, A.C. (2009), “Multi-capping agents in size confinement of ZnO nanostructured particles”, *Optical Materials*, Vol. 31 No. 11, pp. 1570–1574.
- Young, R.J. and Kinloch, I.A. (2013), “Graphene and graphene-based nanocomposites”, *Nanoscience*, Vol. 1, pp. 145–179.
- Yu, B., Zhu, C., Xia, H., Chen, H. and Gan, F. (1997), “Optical non-linearities of PbSe microcrystallites doped in glass”, *Journal of Materials Science Letters*, Vol. 16, pp. 2001–2004.
- Yu, C.-C., Jiang, K.-J., Huang, J.-H., Zhang, F. and Bao, X. (2013), “Novel pyrene-based donor–acceptor organic dyes for solar cell application”, *Organic Electronics*, Vol. 14 No. 2, pp. 445–450.
- Yu, H., Wang, J., Wang, T., Yu, H., Yang, J., Guiwu, L. and Qiao, G. (2016), “Scalable colloidal synthesis of uniform Bi₂S₃ nanorods as sensitive material for visible-light photodetectors”, *CrystEngComm*, doi:10.1039/C6CE01879c.
- Yu, K., Ouyang, J., Zhang, Y., Tung, H.-T., Lin, S., Nagelkerke, R.A.L. and Kingston, D. (2011), “Low-temperature noninjection approach to homogeneously-alloyed PbSe_xS_{1-x} colloidal nanocrystals for photovoltaic applications”, *Applied Materials and Interfaces*, Vol. 3, pp. 1511–1520.
- Yücel, E. and Yücel, Y. (2016), “Fabrication and characterization of Sr-doped PbS thin films grown by CBD”, *Ceramics International*, doi:org/10.1016/j.ceramint.2016.09.173.

- Yücel, E. and Yücel., Y. (2017), “Effect of doping concentration on the structural , morphological and optical properties of Ca-doped PbS thin films grown by CBD”, *Optik -International Journal for Light and Electron Optics*, doi.org/10.1016/j.ijleo.2017.04.104.
- Yun, M.H., Jang, J.H., Kim, K.M., Song, H.-E., Lee, J.C. and Kim, J.Y. (2013), “A hybrid solar cell fabricated using amorphous silicon and a fullerene derivative”, *Physical Chemistry Chemical Physics*, Vol. 15, pp. 19913–19918.
- Zaman, S., Asim, M.M., Siddique, S. and Mahmood, S.K. (2010), “Effect of deposition parameters and annealing on the morphology and optical properties of PbS thin films”, *Key Engineering Materials*, Vol. 442, pp. 144–151.
- Zhang, H., Huang, J., Zhou, X. and Zhong, X. (2011), “Single-crystal Bi₂S₃ nanosheets growing via attachment- recrystallization of nanorods”, *Inorganic Chemistry*, Vol. 50, pp. 7729–7734.
- Zhang, J.Z. (2000), “Interfacial charge carrier dynamics of colloidal semiconductor nanoparticles”, *Journal of Physical Chemistry B*, Vol. 104, pp. 7239–7253.
- Zhang, S., Yan, Z., Li, Y., Chen, Z. and Zeng, H. (2015), “Atomically thin arsenene and antimonene: semimetal–semiconductor and indirect – direct band-gap transitions.”, *Angewandte Communications*, Vol. 54, pp. 3112–3115.
- Zhang, Y., Cai, J., Ji, T., Wu, Q., Xu, Y., Wang, X. and Sun, T. (2015), “Superionic conductormediated growth of ternary ZnCdS nanorods over a wide composition range”, *Nano Research*, Vol. 8 No. 2, pp. 584–591.
- Zhao, K., Wu, Z. and Jiang, Y. (2014), “Fabrication and application in hybrid solar cell of ZnO nanorod arrays”, *Journal of Materials Science: Materials in Electronics*, pp. 93–96.
- Zhao, N., Osedach, T.P., Chang, L.-Y., Geyer, S.M., Wanger, D., Binda, M.T. and Arango, A.C. (2010), “Colloidal PbS quantum dot solar cells with high fill factor”, *ASC Nano*, Vol. 102 No. 11, pp. 1–10.
- Zhou, W., Nair, V. and Thiruvengadam, G. (2006), “The impact of high dielectric constant on photonic bandgaps in PbSe nanocrystal based photonic crystal slabs”, *Photonic Crystal Materials and Devices*, Vol. 6128, pp. 1–8.
- Zhu, G. and Liu, P. (2009), “Low-temperature urea-assisted hydrothermal synthesis of Bi₂S₃ nanostructures with different morphologies”, *Crystal Research and Technology*, Vol. 44 No. 7, pp. 713–720.
- Zimmermann, B., Schleiermacher, H.-F., Niggemann, M. and Würfel, U. (2011), “ITO-free flexible inverted organic solar cell modules with high fill factor prepared by slot die coating”, *Solar Energy Materials and Solar Cells*, Vol. 95 No. 7, pp. 1587–1589.
- Ziqubu, N., Ramasamy, K., Rajasekhar, P.V.S.R., Revaprasadu, N. and O’Brien, P. (2010), “Simple route to dots and rods of PbTe nanocrystals”, *Chemistry of Materials Communication*, Vol. 22, pp. 3817–3819.
- Zohir, N., Mustapha, B. and Elbaki, D.A. (2009), “Synthesis and structural characterization of xanthate (KEX) in sight of their utilization in the processes of sulphides flotation”, *Journal of Minerals and Materials Characterization and Engineering*, Vol. 8 No. 6, pp. 469–477.

Zyl, W.E.V. and Woollins, J.D. (2013), “The coordination chemistry of dithiophosphonates: An emerging and versatile ligand class”, *Coordination Chemistry Reviews*, Vol. 257, pp. 718–731.

KNUST

APPENDIX

Research output

- (a) Deposition of PbS, PbSe and $\text{PbS}_x\text{Se}_{(1-x)}$ Thin Films by the Spin Coating and Heating of Molecular Precursors (Submitted to Journal of Materials Science, 2017).
- (b) Paul D. McNaughter, **Selina A. Saah**, Masood Akhtar, Khadijat Abdulwahab, M. Azad Malik, James Raftery, Johannes A. M. Awudza, and Paul O’Brien. *Dalton Transactions*, 2016, 45, 16345-16353.
- (c) Edward A. Lewis, Paul D. McNaughter, Zhongjie Yin, Yiqiang Chen, Jack R. Brent, **Selina A. Saah**, James Raftery, Johannes A. M. Awudza, M. Azad Malik, Paul O’Brien, and Sarah J. Haigh. *Chemistry of Materials*, 2015, 27 (6), 2127–2136.
- (d) Effect of nitrogen adduct on the morphology of bismuth sulfide thin films (manuscript under preparation).
- (e) The facile synthesis of PbS, PbSe and $\text{PbS}_x\text{Se}_{(1-x)}$ nanoparticles from lead thio and/or seleno urea from solution (manuscript under preparation).

- (f) Effect of alkyl chain on the properties of PbS from lead alkyl xanthate complexes using spin coating method (manuscript under preparation).

KNUST

